Fall 2014

Experimental database, analysis and design of noncompact and slender concrete-filled steel tube (CFT) members

Zhichao Lai
Purdue University

Graduate School Form 30
(Revised 08/14)

PURDUE UNIVERSITY
GRADUATE SCHOOL
Thesis/Dissertation Acceptance

This is to certify that the thesis/dissertation prepared

By Zhichao Lai

Entitled
EXPERIMENTAL DATABASE, ANALYSIS AND DESIGN OF NONCOMPACT AND SLENDER CONCRETE-FILLED STEEL TUBE (CFT) MEMBERS

For the degree of Doctor of Philosophy

Is approved by the final examining committee:

Amit H. Varma

Chin-teh Sun

Judy Liu

Robert J. Connor

To the best of my knowledge and as understood by the student in the Thesis/Dissertation Agreement, Publication Delay, and Certification/Disclaimer (Graduate School Form 32), this thesis/dissertation adheres to the provisions of Purdue University's "Policy on Integrity in Research" and the use of copyrighted material.

Amit H. Varma

Approved by Major Professor(s): _____

_____

Approved by: Dulcy M. Abraham 10/10/2014

Head of the Department Graduate Program Date

EXPERIMENTAL DATABASE, ANALYSIS AND DESIGN OF NONCOMPACT AND SLENDER CONCRETE-FILLED STEEL TUBE (CFT) MEMBERS

A Dissertation

Submitted to the Faculty

of

Purdue University

by

Zhichao Lai

In Partial Fulfillment of the

Requirements for the Degree

of

Doctor of Philosophy

December 2014

Purdue University

West Lafayette, Indiana

谨赠我的家人

To my family

ACKNOWLEDGEMENTS

I express my sincere gratitude to my advisor Dr. Amit Varma, for giving me the opportunity to work on this research and for offering me the invaluable guidance during this study. I also gratefully thank Dr. Robert Connor, Dr. Judy Liu, and Dr. Chin-teh Sun for serving as members of my Ph.D. committee.

This research project was partially funded by United States Army Corps of Engineers (USACOE), HDR Inc., and American Institute of Steel Construction (AISC). I would like to thank their support.

I would like to express my heartfelt love and gratitude to my grandparents, Mr. Tianshui Lai and Mrs. Douzhi Huang, who always love me and set me the greatest example of magnanimity. I would also like to express my deepest love and gratitude to my parents, Mr. Congming Lai and Mrs. Suxia Huang, who help me grow up with everything they could ever offer and every bead of sweat they could possibly drip. I also want to thank my dear sister, Xiaocui Lai, and my dear brother Zhiqiang Lai. I dedicate this work to all my family, they together provide me the courage and strength to work, to learn, and to enjoy this work.

I want to thank my special friend Liuling Huang, who supports me all the way in this work. I also thank, Kai Zhang, Yu Tian, Ruoxi Wu, Ying Wang and Yuxing Yang for their friendship.

TABLE OF CONTENTS

Page

Page

LIST OF TABLES

Table Page

LIST OF FIGURES

Figure Page

Figure Page

Figure Page

Figure Page

Figure Page

Figure Page

Figure Page

Figure Page

Figure Page

Figure Page

Figure Page

Figure Page

Figure Page

Figure Page

Figure Page

Figure Page

Figure Page

Figure Page

Figure Page

Figure Page

ABSTRACT

Lai, Zhichao. Ph.D., Purdue University, December 2014. Experimental Database, Analysis and Design of Noncompact and Slender Concrete-Filled Steel Tube (CFT) Members. Major Professor: Amit Varma.

Concrete-filled steel tube beam-columns are categorized as compact, noncompact or slender depending on the governing tube slenderness ratio. AISC 360-10 specifies the provisions for designing noncompact and slender rectangular and circular CFT members under axial compression, flexure, and combined axial and flexural loading. This research presents the development and evaluation of these design provisions. Available experimental databases of CFT members are reviewed, and a new experimental database of tests conducted on noncompact and slender CFT members is compiled. Detailed 3D finite element method (FEM) models are developed for noncompact and slender CFT members, and benchmarked using experimental results. The AISC 360-10 design provisions for noncompact and slender CFT members are then evaluated by both the experimental test results and additional FEM analysis that address the gaps in the experimental database. The current AISC 360-10 P-M interaction equations are updated using the results from comprehensive parametric studies (conducted using the benchmarked FEM model). Effective stress-strain curves for the steel tube and concrete infill are also developed. The validation of these effective stress-strain curves are

confirmed by implementing them in a benchmarked nonlinear fiber analysis based macro model.

CHAPTER 1. INTRODUCTION

1.1 Concrete-Filled Steel Tube (CFT) Members

Concrete-filled steel tube (CFT) members consist of rectangular or circular steel tubes filled with concrete, as shown in Figure 1.1. These composite members optimize the use of both steel and concrete construction materials as compared to steel or reinforced concrete structures. The concrete infill delays the local buckling of the steel tube, while the steel tube provides confinement to the concrete infill. The behavior of CFT members under axial loading, flexure, and combined axial and flexural loading can be more efficient than that of structural steel or reinforced concrete members. Moreover, the steel tube serves as formwork for placing the concrete, which facilitates and expedites construction while reducing labor costs.

CFT members are categorized as compact, noncompact or slender depending on the governing slenderness ratio (width-to-thickness b/t or D/t ratio, λ) of the steel tube wall. AISC 360-10 (2010) specifies the slenderness limits for demarcating the members, as shown in Table 1.1. These slenderness limits are proposed by Varma and Zhang (2009), based on the research of Schilling (1965), Winter (1968), Tsuda et al. (1996), Bradford et al. (1998, 2002), Leon (2007) and Ziemian (2010). Developments of the slenderness limits will be discussed in detail in Chapter 4 and Chapter 5.

For a CFT member, if the governing tube slenderness ratio is less than or equal to λ_p, the member is classified as compact; if the governing tube slenderness ratio is greater than λ_p but less than or equal to λ_r, the member is classified as noncompact; if the governing tube slenderness ratio is greater than λ_r, the member is classified as slender. The tube slenderness ratio is also limited to a maximum permitted value λ_{limit} due to: (i) the lack of experimental data for CFTs with such slender steel tubes, and (ii) potential issues with deflections and stresses in the slender tube walls due to concrete casting pressures and other fabrication processes.

1.2 Applications of CFT

As an innovative and efficient structural component, CFT members are used widely around the world in various types of structures. For example, CFT members are used as columns in composite braced frames in: (i) the Two Union Square building in Seattle, Washington, (ii) Casselden Place project in Melbourne, Australia, (iii) Taipei 101 tower in Taipei, Taiwan, and (iv) Commerzbank in Frankfort, Germany. Figure 1.2 shows a typical application of CFT members as mega columns in composite braced frames.

CFT members are also used as columns in composite moment frames, for example in: (i) 3 Houston Center in Houston, Texas, (ii) Postal Office building in Quanzhou, China, (iii) Wuhan International Financial Center in Wuhan, China, and iv) Shimizu Super High Rise in Tokyo, Japan. Figure 1.3 shows the Shimizu Super High Rise that uses 4 x 2.4 m rectangular CFT columns. This is a 121-story building with the height of 550 m.

CFT members are used as compression chords in composite bridges, for example, in: (i) the Yajisha bridge in Guangzhou, China, (ii) Chunnan Napu bridge in Zhejiang, China, (iii) Pudong Canal bridge in Shanghai, China, (iv) Wuxia Changjiang bridge in Chongqing, China, and (v) Shinsaikai bridge in Sasebo, Japan. In China, CFT members are used in more than three hundred composite bridges. Figure 1.4 shows typical applications of CFT members in half-through arch bridges. The chords, webs, and bracings of the four-pipe truss are all made of CFT members. CFT members are also used as piles, transmission towers, and bracing members in buckling.

1.3 Prior Research and Design of CFT Members

1.3.1 Experimental Research

Since the first documented experimental research on CFT columns by Klöppel and Goder (1957), significant research has been conducted to investigate the behavior of CFT members under various loading conditions. For example:

(1) Axial compression tests have been conducted by Furlong (1967), Knowles and Park (1969), Anslijin and Janss (1974), Bridge (1976), Lin (1988), Sakino and Hayashi (1991), Bridge and Webb (1993), Bergmann (1994), Fujimoto et al. (1995), Yoshioka et al. (1995), O'Shea and Bridge (1996), Song and Kwon (1997), Schneider (1998), Han and Yan (2000), Uy (1998, 2001), Kang et al. (2001), Mursi and Uy (2004), and Guo et al. (2007) among others.

(2) Flexural tests have been conducted by Ichinohe et al. (1991), Lu and Kennedy (1994), Elchalakani et al. (2001, 2004, 2008), Uy (2000), Ichinohe et al. (1991), Han (2004),

Wheeler and Bridge (2004), Han et al. (2006), Lennie et al. (2008), and Jiang et al. (2013) among others.

(3) Combined axial force and flexure (beam-column) tests have been conducted by Bridge (1976), Cai (1991), Prion and Boehme (1994), O'Shea and Bridge (1997a, 1997b, 1997c, 2000), Bridge and O'Shea (1998), Nakahara and Sakino (2000), Sakino and Nakahara (2000), Uy (2001), Mursi and Uy (2004), Varma et al. (2002, 2004), Soundararajan and Shanmugasundaram (2008), and Huang et al. (2011) among others.

Nishiyama et al. (2002), Kim (2005), Gourley et al. (2008), and Hajjar et al. (2013) have independently compiled comprehensive databases of experimental research conducted on rectangular and circular CFTs. The database compiled by Hajjar et al. (2013) (previously, Gourley et al., 2008) is the most comprehensive database of experimental and numerical research performed on CFT members, frames, and systems. The database includes all the tests conducted on compact, noncompact, and slender CFT members with a wide range of material, geometric, and loading parameters. Experimental research show that the strength of CFT members depends on several parameters, namely, the steel yield stress F_y, concrete compressive strength f'_c, tube wall slenderness (b/t or D/t) ratio, column length-to-depth ratio (L/B *or* L/D) and composite interaction between the steel tube and concrete infill, etc.

However, a significant portion of these experimental tests are conducted on compact CFT members. There are fewer, but reasonable number of tests conducted on noncompact and slender CFT members, which are the focus of this research.

1.3.2 Analytical Research

Significant analytical research has also been conducted to investigate the behavior of CFT members, as can be placed in four general categories:

(1) Three-dimensional (3-D) finite element method (FEM) models, as have been developed by Yonezawa et al. (1996), Goto et al. (1998, 2010, 2011), Schneider (1998), Varma et al. (2002b), Lu et al. (2009), Moon et al. (2012), Tao et al. (2013) among others. These FEM models usually account for the material nonlinearity of the steel tube and concrete infill, interactions between steel tube and concrete infill, and local buckling of the steel tube, etc.

(2) Fiber analysis based macro models, as have been developed by Tomii and Sakino (1979a, 1979b), Hajjar and Gourley (1996), Inai and Sakino (1996), Morino et al. (1996), Zhang and Shahrooz (1997), Varma et al. (2005) and Liang (2008) among others. These models are usually used for developing moment-curvature responses and axial load-bending moment (P-M) interaction curves, and conducting parametric studies on CFT beam-columns.

(3) Concentrated-plasticity based FEM models, as have been developed by Hajjar and Gourley (1996, 1997). These models consisted of a 12 degree-of-freedom elastic beam finite element with concentrated plastic hinges at the element ends. Transverse displacements of the element are obtained assuming cubic Hermetian shape function. The element stiffness matrix consisted of element elastic, geometric, and plastic reduction matrices. These models are usually incorporated into a computer program that can be used for conducting monotonic, cyclic, or dynamic analysis of frames structures with CFT columns.

(4) Distributed-plasticity based FEM models for CFT columns, as have been developed by Hajjar et al. (1998a, 1998b). These models were developed using a stiffness-based beam-column finite element formulation. The model uses several finite elements along the length of a CFT beam-column. The ends of each finite element are discretized into a grid of fibers and the stress-strain behavior of the steel and concrete fibers are explicitly monitored during the loading history. The cross-sectional stiffness at the element ends are obtained by numerical integration over the fibers and interpolation functions are used to integrate along the element length. These models are suited for studying the force-deformation behavior of CFT columns as part of composite frames subjected to monotonic and cyclic loading conditions, and for conducting parametric studies of individual CFT columns.

However, most of these analytical studies focus on compact CFT members. Therefore the findings from these studies may not be applicable to noncompact and slender CFT members.

1.3.3 Current Design Codes for CFT members

Several international design codes provide the guidance for designing CFT members. Most design codes specify steel tube slenderness limits (*b/t* or *D/t* ratio) for CFT members. For example, Eurocode 4 (2004) specifies that the steel tube of rectangular CFT columns in compression should satisfy the limit, $b/t \le 52\sqrt{235/F_y}$, where F_y is in MPa, to prevent the local buckling. AS 4100 (2012) permits the occurrence of steel tube local buckling, and provides an effective width method to calculate the axial strength of

slender CFT members. The Japanese code (AIJ 2008) classifies CFT members into three types, i.e., *FA*, *FC*, and *FD* depending on the steel tube slenderness ratio. CFT columns classified as *FC* and *FD* have larger steel tube slenderness ratios and are susceptible to local buckling effects. AIJ 2008 provides an axial load capacity factor to account for the effects of steel tube slenderness (and local buckling) on the axial strength of CFTs.

Eurocode 4 (2004) specifies that the flexural strength of CFT members can be calculated as the plastic moment resistance over the composite cross-section while using: (i) the yield stress (F_y) for steel in compression or in tension, (ii) the compressive strength (f'_c) for concrete in compression, and (iii) neglecting the contribution of concrete in tension. The Australian and Japanese codes (AS 4100 and AIJ 2008) specify tube slenderness ratio dependent stress-strain curves for steel in compression that can be used to calculate the flexural strength of rectangular CFT members.

However, none of these international codes specify tube slenderness (*b/t* or *D/t*) ratio limits to classify CFT members into noncompact or slender CFTs. They also do not have different tube slenderness ratio limits for rectangular or circular CFTs subjected to different loading conditions (axial or flexural loading). The AISC 360-05 (2005) specification also specified the tube slenderness ratio limits only for compact CFTs, and did not include any provisions for classifying or calculating the strength of noncompact or slender CFTs subjected to different loading conditions (axial or flexural loading).

1.4 Research Significance

Due to the lack of both experimental and analytical research, the design and use of noncompact or slender CFT members in the US is limited in scope. However, noncompact or slender CFT members are suitable and sufficient for design in many scenarios, because the behavior and strength of these members are comparable to that of compact CFT members. Figure 1.5 shows typical comparisons of moment-curvature curves of noncompact and slender circular CFT beam-columns with different tube slenderness ratio (D/t) and with the same axial load ratio of 0.2. In this figure, the axial load ratio is obtained by dividing the applied axial load (P) by the nominal axial strength (P_n, which is calculated using the corresponding design equations in AISC 360-10). Comparisons as shown in Figure 1.5 indicate that the ductility of noncompact and slender circular CFT members is excellent, and there is no sign of the occurrence of severe failure mechanisms (for example, local buckling).

Moreover, there is increasing engineering interest in the use of noncompact and slender members nowadays. For example, noncompact concrete-filled spirally welded pipe (CSWP) piles were used for floodwall structures in the extended New Orleans area. These pipe piles are 1371.6 mm in diameter and 19.1 mm in wall thickness, and the resulting tube slenderness ratio (D/t) is 72. These pipes are noncompact because the tube slenderness ratio (72) is greater than the compact limit (λ_p = 44.7, calculated according to Table 1.1, with E_s = 200 GPa, and F_y = 402 MPa). CFT mega columns are also widely used in tall buildings. These columns are likely to be noncompact or slender since: (i) the diameter is significantly large (for example, greater than 3200 mm), and (ii) it is

extremely hard to fabricate tubes with such large thickness (for example, 62 mm) to satisfy the compact limit. Also, the material cost can be significantly reduced if noncompact or slender CFT members instead of compact CFT members are used. Therefore, it is necessary to investigate the behavior of these noncompact and slender CFT members, and propose corresponding design provisions.

1.5 Research Objectives and Scope

The current AISC Specification (AISC 360-10) includes provisions for classifying and calculating the strength of noncompact and slender CFT members (with both rectangular and circular cross sections) subjected to different loading conditions, namely, axial compression, flexure, and combined axial compression and flexure. However, there is no evaluation of these design provisions. The overall objectives of this research are: (i) to evaluate these design provisions comprehensively, (ii) to propose an updated P-M interaction curve for designing noncompact and slender CFT beam-columns, and (iii) to develop effective stress-strain curves for the steel tube and concrete infill for noncompact and slender CFT members.

These overall objectives are fulfilled by completing the following tasks:

(1) To review available experimental databases of CFT members, and compile a new experimental database of tests conducted on noncompact and slender CFT members.

(2) To develop and benchmark detailed 3D finite element method (FEM) models for further evaluating the behavior of noncompact and slender CFT members.

(3) To present the development of the AISC 360-10 provisions for designing noncompact and slender CFT members, and evaluate these design provisions by both the experimental database and FEM models.

(4) To propose an updated P-M interaction curve for designing noncompact and slender CFT beam-columns based on the comprehensive parametric studies using the benchmarked FEM models.

(5) To develop effective stress-strain curves for the steel tube and concrete infill for CFT members based on the results from comprehensive parametric analysis using the benchmarked FEM models.

1.6 Dissertation Outline

Chapter 2 presents the experimental database of tests conducted on noncompact and slender rectangular CFT members subjected to different loading conditions (axial compression, flexure, combined axial force and flexure). This database included tests from the database of Gourley et al. (2008) and Hajjar (2013), and additional tests from other databases and literature as applicable. Gaps in the databases are also identified. The database provides essential information to: (i) evaluate the design provisions by AISC 360-10 Specification (as presented in Chapter 4, Chapter 5, and Chapter 6) and (ii) benchmark the detailed 3D FEM models (as presented in Chapter 3).

Chapter 3 presents the development and benchmarking of detailed 3D FEM models. These FEM models account for plastic hardening and local buckling of the steel tube, compression plasticity and isotropic tensile cracking of the concrete infill, geometric

imperfections, contact interactions between the steel tube and concrete infill, as well as interactions between local steel tube buckling and global column buckling. The benchmarked FEM models are used to conduct additional analysis to: (i) further evaluate the AISC 360-10 design provisions (as presented in Chapter 4, Chapter 5, and Chapter 6) by addressing the gaps in the experimental database, (ii) develop the updated P-M interaction curve in Chapter 6, and (iii) develop effective stress-strain curves of the steel tube and concrete infill for noncompact and slender CFT members in Chapter 7.

Chapter 4 presents the development of the AISC 360-10 specification that includes provisions for classifying and calculating the axial strength of noncompact and slender CFT columns. Details of the slenderness classifications are presented first, followed by the development of the AISC 360-10 design equations. The conservatism of these design provisions is established by using them to predict the axial compressive strength of CFT columns in the experimental database and additional FEM models.

Chapter 5 presents the development of the AISC 360-10 specification that includes provisions for classifying and calculating the flexural strength of noncompact and slender CFT beams. Details of the slenderness classifications are presented first, followed by the development of the AISC 360-10 design provisions. The conservatism of these design provisions is established by using them to predict the flexural strength of CFT beams in the experimental database and additional FEM models.

Chapter 6 presents the development of an updated P-M interaction curve for noncompact and slender CFT beam-columns. The current AISC 360-10 equations for designing noncompact and slender CFT beam-columns are evaluated first, by using them to predict the strength of CFT beam-columns in the experimental database. The evaluations show that the current AISC 360-10 bilinear P-M interaction curve is over-conservative. Comprehensive analytical studies using the benchmarked FEM models are then conducted to investigate the effects of several parameters on the behavior of CFT beam-columns. These parameters include tube slenderness ratio (width-to-thickness b/t or D/t ratio, λ), material strength ratio (F_y/f'_c), axial load ratio (α), and member length-to-depth ratio (L/B or L/D). The updated P-M interaction curve is then proposed based on the findings from the analytical studies.

Chapter 7 presents the development and verification of effective stress-strain curves for the steel tube and concrete infill for noncompact and slender CFT members. These effective stress-strain curves are developed based on comprehensive analytical studies using the benchmarked FEM models. The developed effective stress-strain curves account for the effects of steel tube local buckling, steel hoop stresses and concrete confinement from the interactions between the steel tube and concrete infill, and geometric imperfections. These effective stress-strain curves could be implemented in fiber analysis based macro models or commercial analysis programs to analyze composite (CFT) structural systems.

Finally Chapter 8 presents the summary and conclusions of this research, and recommendations for further work.

Table 1.1 Slenderness Limits for CFT Members

Loading	Description of Element	Width-to-Thickness Ratio	λ_p Compact/ Noncompact	λ_r Noncompact/ Slender	λ_{limit} Maximum Permitted
Axial compression	Steel tube walls of Rectangular CFT Members	*b/t*	$2.26\sqrt{\frac{E_s}{F_y}}$	$3.00\sqrt{\frac{E_s}{F_y}}$	$5.00\sqrt{\frac{E_s}{F_y}}$
	Steel tube wall of Circular CFT Members	*D/t*	$0.15\frac{E_s}{F_y}$	$0.19\frac{E_s}{F_y}$	$0.31\frac{E_s}{F_y}$
Flexure	Flanges of Rectangular CFT Members	*b/t*	$2.26\sqrt{\frac{E_s}{F_y}}$	$3.00\sqrt{\frac{E_s}{F_y}}$	$5.00\sqrt{\frac{E_s}{F_y}}$
	Webs of Rectangular CFT Members	*h/t*	$3.00\sqrt{\frac{E_s}{F_y}}$	$5.70\sqrt{\frac{E_s}{F_y}}$	$5.70\sqrt{\frac{E_s}{F_y}}$
	Steel tube wall of Circular CFT Members	*D/t*	$0.09\frac{E_s}{F_y}$	$0.31\frac{E_s}{F_y}$	$0.31\frac{E_s}{F_y}$

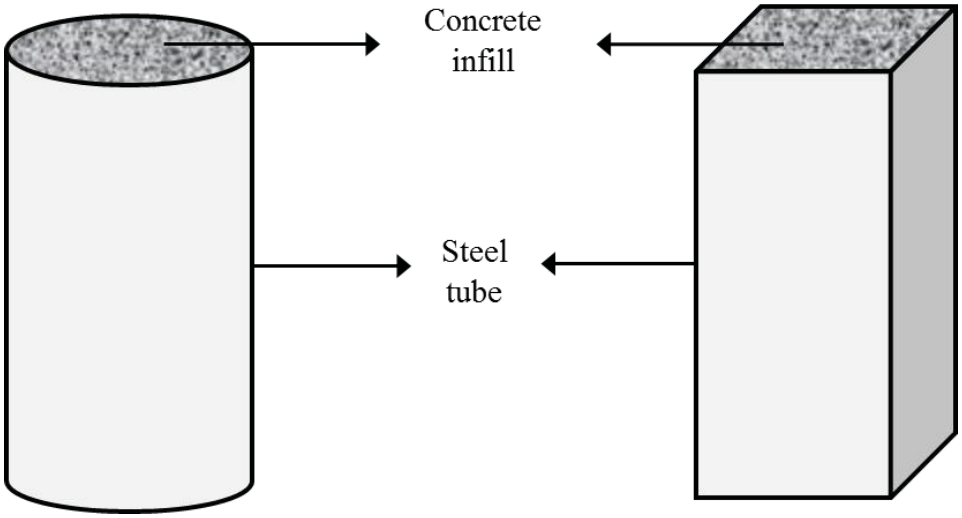

Figure 1.1 Typical CFT Members

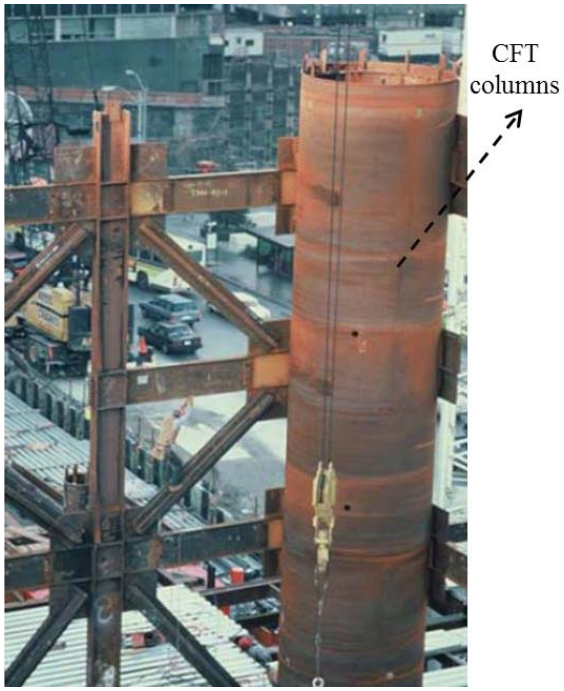

Figure 1.2 A Typical Application of CFT Members as Mega Columns in Composite Braced Frames

Figure 1.3 Shimizu Super High Rise

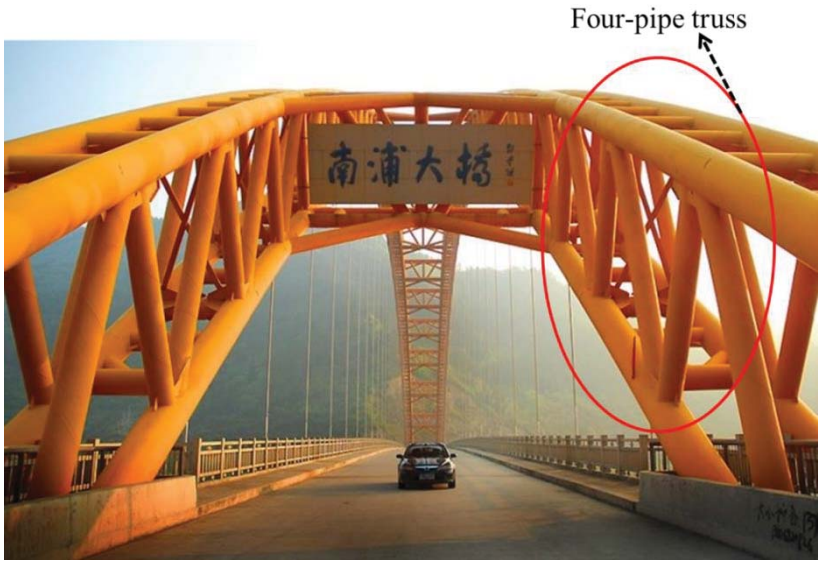

Figure 1.4 Typical Applications of CFT Members in Half-Through Arch Bridges

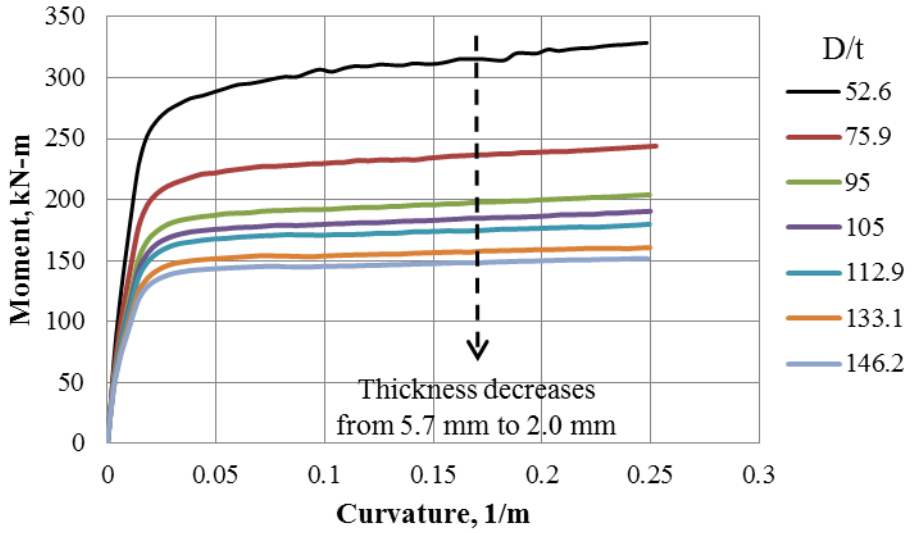

Figure 1.5 Effects of Tube Thickness on the Moment-Curvature Response of Circular CFT Beam-Columns (F_y = 420 MPa, E_s = 200 GPa)

CHAPTER 2. EXPERIMENTAL DATABASE

Several experimental databases have been developed for tests conducted on CFT members, for example, Nishiyama et al. (2002), Kim (2005), Gourley et al. (2008), and Hajjar (2013). These databases usually include tests on CFT columns, beams, beam-columns, connections, and frames. The database compiled by Gourley et al. (2008) and Hajjar (2013) are the most comprehensive, and include the material, geometric, and loading parameters, and brief description of all tests. In this chapter, a new experimental database of tests conducted on noncompact and slender CFT members subjected to axial compression, flexure, and combined axial compression and flexure is compiled. The database includes tests from the database of Gourley et al. (2008) and Hajjar (2013), and additional tests from other databases and literature as applicable.

2.1 Experimental Tests of Noncompact and Slender CFT Columns

Forty-one rectangular and forty-seven circular noncompact and slender CFT column tests were included into the experimental database. In these tests, the axial loads were applied to the specimen using load or displacement control. Table 2.1 and Table 2.2 summarize the noncompact and slender rectangular and circular CFT column tests that were included. These tables include the relevant parameters for the specimens included in the database.

Table 2.1 includes the length (L), width (B), depth (H), flange thickness (t_f), web thickness (t_w), governing tube slenderness ratio (b/t_f and h/t_w), and the slenderness coefficient (λ_{coeff}) obtained by dividing the governing slenderness ratio with $\sqrt{E_s/F_y}$ for rectangular columns. Table 2.2 includes the length (L), diameter (D), tube thickness (t), tube slenderness ratio (D/t), and the slenderness coefficient (λ_{coeff}) obtained by dividing the governing slenderness ratio with E_s/F_y for circular columns. These tables also include the measured steel yield stress (F_y) and concrete strength (f'_c) where reported by the researchers. The experimental axial load capacity (P_{exp}) is included in the tables along with the nominal strength (P_n) calculated using AISC 360-10 design equations (Equations 4.1-4.13) as applicable.

2.2 Experimental Tests of Noncompact and Slender CFT Beams

Four rectangular and forty-two circular noncompact and slender CFT beams were included in the experimental database. The four point loading scheme as shown in Figure 2.1 was used for all specimens. Table 2.3 and Table 2.4 summarize the rectangular and circular noncompact and slender CFT beam tests that were compiled into the experimental database. These tables include the relevant parameters for the specimens included in the database.

Table 2.3 includes the length (L), width (B), depth (H), flange thickness (t_f), web thickness (t_w), governing tube slenderness ratio (b/t_f and h/t_w), and the coefficient (λ_{coeff}) obtained by dividing the governing slenderness ratio with $\sqrt{E_s/F_y}$ for rectangular CFT

beams. The shear span to depth ratio (a/H) is also included in the Table. Table 2.4 includes the length (L), diameter (D), tube thickness (t), tube slenderness ratio (D/t), and the slenderness coefficient (λ_{coeff}) obtained by dividing the governing slenderness ratio with E_s/F_y for circular CFT beams. The shear span to depth ratio (a/D) is also included in the Table. These tables also includes the measured steel yield stress (F_y) and concrete strength (f'_c) where reported by the researchers. The experimental flexural capacity (M_{exp}) is included in these tables along with the nominal flexural strength (M_n) calculated using AISC 360-10 design provisions as applicable.

2.3 Experimental Tests of Noncompact and Slender CFT Beam-Columns

Seventeen rectangular and thirty-six circular noncompact and slender CFT beam-column tests were compiled into the experimental database. Three types of loading schemes (Type-1, Type-2 and Type-3) as shown in Figure 2.2 were used in the beam-column tests. In Type-1 loading: concentric axial load is applied first and maintained constant. The bending moment is increased monotonically to failure by applying lateral loads. In Type-2 loading: concentric axial loading is applied first and maintained constant. The bending moment is applied monotonically to failure. In Type-3 loading, eccentric axial load is applied and increased monotonically, which results in both axial force and bending moment increasing proportionally to failure. Type-1 and Type-2 loading are fundamentally the same; therefore they are called Type-A loading hereafter. Type-3 loading is called Type-B loading hereafter. Table 2.5 and Table 2.6 summarize the noncompact and slender CFT beam-column tests that were compiled into the

experimental database. These tables include the relevant parameters for the specimens included in the database.

Table 2.5 includes the length (L), width (B), flange thickness (t_f), governing tube slenderness ratio (b/t_f), the slenderness coefficient (λ_{coeff}) obtained by dividing the governing tube slenderness ratio by $\sqrt{E_s/F_y}$, and the relative strength ratio (ξ) for rectangular CFT beam-columns. Table 2.6 includes the length (L), diameter (D), tube thickness (t), tube slenderness ratio (D/t), the slenderness coefficient (λ_{coeff}) obtained by dividing the governing tube slenderness ratio by E_s/F_y, and the relative strength ratio (ξ) for circular CFT beam-columns. These tables also include the measured steel yield stress (F_y) and concrete strength (f'_c) where reported by the researchers. The experimental axial load strength (P_{exp}) and flexural strength (M_{exp}) are included along with the nominal strength (P_n and M_n). It should be noted that all specimens in included in Table 2.5 are beam-columns with square sections. The depth (H) is equal to width (B); the web thickness (t_w) is equal to flange thickness (t_f). Therefore these two parameters were not included in Table 2.5.

2.4 Gap Identifications

The experimental database provides valuable data points to evaluate the AISC 360-10 design provisions, as will be presented in Chapter 4, Chapter 5, and Chapter 6. However, there were some gaps in the experimental database, i.e., the available data points in the databases did not cover the whole range of noncompact and slender CFT members (for

example, λ_{coeff} = 2.26 to 5.0 for rectangular CFT columns). These gaps are identified in Figures 2.3–2.8. In these figures, the ordinate represents the number of tests in the database, while the abscissa represents the normalized slenderness coefficient (λ_{coeff}).

For example, for axial compression, there are no data points for rectangular columns with λ_{coeff} in the range of 4.0 and 5.0, and the data points for circular columns with slender sections ($\lambda_{coeff} \geq 0.19$) are limited. For flexure, there are only four data points with slender sections ($\lambda_{coeff} \geq 3.0$) for rectangular beams, and the data points for circular CFT beams with λ_{coeff} greater than 0.16 are limited. For combined axial compression and flexure, additional data points are also required for both rectangular and circular beam-columns with different tube slenderness ratios. It was important to address these gaps in the database to further evaluate the design provisions. The finite element analysis approach as will be presented in Chapter 3 is selected to address these gaps in the experimental database, and to develop additional data points to evaluate the design provisions.

Table 2.1 Noncompact and Slender Rectangular CFT Column Tests

Reference	Specimen ID	L (mm)	B (mm)	t_f (mm)	b/t_f	H (mm)	t_w (mm)	h/t_w	λ_{coeff}	L/H	F_y (MPa)	f'_c (MPa)	E_c (GPa)	P_n (kN)	P_{exp} (kN)	P_{exp}/P_n
Janss and Anslijn (1974)	21	1318.3	329.9	4.47	71.8	329.9	4.47	71.8	3.09	4.0	370.3	31.6	26.60	4272.9	4363.3	1.02
	22	1328.4	331.0	4.47	72.0	331.0	4.47	72.0	3.10	4.0	370.3	27.4	24.76	3979.2	4411.7	1.11
	23	1320.8	331.0	4.50	71.6	331.0	4.50	71.6	3.08	4.0	370.3	27.4	24.76	4013.7	4656.8	1.16
	24	1318.3	331.0	4.50	71.6	331.0	4.50	71.6	3.08	4.0	370.3	31.6	26.60	4315.1	4411.7	1.02
	25	1318.3	333.0	6.38	50.2	333.0	6.38	50.2	2.37	4.0	444.7	31.6	26.60	6262.6	5862.8	0.94
	26	1318.3	331.0	6.30	50.5	331.0	6.30	50.5	2.38	4.0	444.7	31.6	26.60	6150.2	5843.2	0.95
	27	1318.3	331.0	6.32	50.3	331.0	6.32	50.3	2.37	4.0	444.7	27.4	24.76	5835.4	5833.4	1.00
	28	1320.8	331.0	6.32	50.3	331.0	6.32	50.3	2.37	4.0	444.7	27.4	24.76	5835.1	5637.2	0.97
Lin (1988)	D10	800.0	150.0	1.40	105.1	150.0	1.40	105.1	3.70	5.3	247.3	22.5	2.93	468.5	711.5	1.52
	D12	800.0	150.0	2.10	69.4	150.0	2.10	69.4	2.45	5.3	248.5	22.5	2.95	671.4	792.8	1.18
	D16	800.0	200.0	1.40	140.9	150.0	1.40	105.1	4.95	5.3	247.0	22.5	3.88	537.3	881.0	1.64
	D18	800.0	200.0	2.10	93.2	150.0	2.10	69.4	3.29	5.3	248.3	22.5	4.34	739.3	843.8	1.14
	E10	800.0	150.0	1.40	105.1	150.0	1.40	105.1	3.70	5.3	247.3	35.3	4.06	653.8	973.1	1.49
	E15	480.0	200.0	1.40	140.9	150.0	1.40	105.1	4.95	3.2	247.0	33.7	4.14	766.8	1191.7	1.55
	E18	800.0	200.0	2.10	93.2	150.0	2.10	69.4	3.29	5.3	248.3	35.3	4.35	984.6	1288.4	1.31
Fujimoto et al. (1995)	CR4-D-2	485.1	323.1	4.37	72.0	323.1	4.37	72.0	2.60	1.5	261.3	25.4	23.84	3316.6	3365.5	1.01
	CR4-D-4-1	485.1	323.1	4.37	72.0	323.1	4.37	72.0	2.60	1.5	261.3	41.0	30.32	4464.6	4949.1	1.11
	CR4-D-4-2	485.1	323.1	4.37	72.0	323.1	4.37	72.0	2.60	1.5	261.3	41.0	30.32	4464.6	4828.5	1.08
	CR4-D-8	485.1	323.6	4.37	72.1	323.6	4.37	72.1	2.61	1.5	261.3	80.1	42.37	7344.6	7478.4	1.02
	CR6-D-2	477.5	319.0	6.35	48.2	319.0	6.35	48.2	2.68	1.5	616.4[a]	25.4	23.84	6618.9	6318.7	0.95
	CR6-D-4-1	477.5	318.5	6.35	48.2	318.5	6.35	48.2	2.67	1.5	616.4[a]	41.0	30.32	7671.8	7777.3	1.01
	CR6-D-4-2	477.5	318.3	6.35	48.1	318.3	6.35	48.1	2.67	1.5	616.4[a]	41.0	30.32	7664.7	7470.3	0.97
	CR6-D-8	477.5	318.5	6.35	48.2	318.5	6.35	48.2	2.67	1.5	616.4[a]	84.9	43.62	10658.3	10353.7	0.97
	CR8-D-2	396.2	264.9	6.48	38.9	264.9	6.48	38.9	2.51	1.5	832.9[a]	25.4	23.84	6795.9	6544.2	0.96

Table 2.1 continued.

Fujimoto et al. (1995)	CR8-D-4-1	396.2	263.9	6.48	38.7	263.9	6.48	38.7	2.50	1.5	832.9[a]	41.0	30.32	7523.6	7114.5	0.95
	CR8-D-4-2	396.2	264.4	6.48	38.8	264.4	6.48	38.8	2.51	1.5	832.9[a]	41.0	30.32	7539.1	7169.6	0.95
	CR8-D-8	396.2	264.9	6.48	38.9	264.9	6.48	38.9	2.51	1.5	832.9[a]	84.9	43.62	9682.5	8987.2	0.93
Song and Kwon (1997)	US15	660.4	222.8	3.00	72.3	222.8	3.00	72.3	2.86	3.0	313.7	30.1	25.98	1816.6	2412.7	1.33
Uy (1998)	NS1	558.0	186.0	3.00	60.0	186.0	3.00	60	2.32	3.0	300	32.0	26.77	1507.1	1555.0	1.03
	NS7	738.0	246.0	3.00	80.0	246.0	3.00	80	3.10	3.0	300	38.0	29.17	2341.0	3095.0	1.32
	NS13	918.0	306.0	3.00	100.0	306.0	3.00	100	3.87	3.0	300	38.0	29.17	3034.9	4003.0	1.32
	NS14	918.0	306.0	3.00	100.0	306.0	3.00	100	3.75	3.0	281	47.0	32.44	3597.5	4253.0	1.18
	NS15	918.0	306.0	3.00	100.0	306.0	3.00	100	3.75	3.0	281	47.0	32.44	3597.5	4495.0	1.25
	NS16	918.0	306.0	3.00	100.0	306.0	3.00	100	3.75	3.0	281	47.0	32.44	3597.5	4658.0	1.29
Schneider (1998)	R1	600.0	152.3	3.00	48.8	76.6	3.00	23.5	2.32	7.8	430.0	30.5	26.61	806.4	819.0	1.02
Uy (2001)	HSS14	630.0	210.0	5.00	40.0	210.0	5.00	40	2.45	3.0	750[a]	30.0	25.92	3908.8	3710.0	0.95
	HSS15	630.0	210.0	5.00	40.0	210.0	5.00	40	2.45	3.0	750[a]	30.0	25.92	3908.8	3483.0	0.89
Kang et al. (2001)	KOM2001	599.4	199.9	3.20	60.5	199.9	3.20	60.5	2.41	3.0	317.9	24.8	23.55	1530.6	1577.8	1.03
	KOM2001	749.3	249.9	3.20	76.1	249.9	3.20	76.1	3.03	3.0	317.9	24.8	23.55	2001.0	2123.1	1.06
	KOM2001	899.2	300.0	3.20	91.7	300.0	3.20	91.7	3.66	3.0	317.9	24.8	23.55	2297.4	2749.9	1.20
	KOM2001	599.4	199.9	3.20	60.5	199.9	3.20	60.5	2.41	3.0	317.9	30.3	26.07	1695.6	2463.0	1.45
	KOM2001	899.2	300.0	3.20	91.7	300.0	3.20	91.7	3.66	3.0	317.9	30.3	26.07	2632.2	4590.6	1.74
Mursi and Uy (2004)	SH-C210	730.0	220.0	5.00	42.0	220.0	5.00	42	2.59	3.3	761[a]	20.0	21.16	3818.0	3609.0	0.95
	SH-C260	880.0	270.0	5.00	42.0	270.0	5.00	52	2.59	3.3	761[a]	20.0	21.16	4350.7	3950.0	0.91

Table 2.2 Noncompact and Slender Circular CFT Column Tests

Reference	Specimen ID	L (mm)	D (mm)	t (mm)	D/t	λ_{coeff}	L/D	F_y (MPa)	f'_c (MPa)	E_c (GPa)	P_n (kN)	P_{exp} (kN)	P_{exp}/P_n
Furlong (1967)	N.A.	914.4	152.4	1.55	98.0	0.16	6.0	331.0	21.0	36.50	533.1	682.4	1.28
	N.A.	914.4	152.4	1.55	98.0	0.16	6.0	331.0	25.9	32.62	598.4	721.5	1.21
	N.A.	914.4	152.4	1.55	98.0	0.16	6.0	331.0	25.9	32.62	598.4	733.1	1.22
Lin (1988)	D1	480.0	150.0	0.70	214.0	0.27	3.2	248.2	22.5	2.19	344.5	538.0	1.56
	D2	800.0	150.0	0.70	214.0	0.27	5.3	248.2	22.5	3.36	336.1	513.5	1.53
	E1	480.0	150.0	0.70	214.0	0.27	3.2	248.2	33.7	3.96	476.2	743.8	1.56
Luksha and Nesterovich (1991)	SB-5	2460.0	820.0	8.93	92.0	0.15	3.0	331.0	45.0	31.75	28327.7	33600.0	1.19
	SB-9	3060.0	1020.0	9.64	106.0	0.18	3.0	336.0	16.9	19.46	19778.7	30000.0	1.52
Bridge and Webb (1993)	D	750.0	250.0	2.00	125.0	0.16	3.0	260.0	59.5	36.50	2692.5	3400.0	1.26
Yoshioka et al., (1995)	CC4-D-2	1348.7	450.1	2.97	151.0	0.21	3.0	283.4	25.4	32.62	3891.2	4413.5	1.13
	CC4-D-4-1	1348.7	449.8	2.97	151.0	0.21	3.0	283.4	41.0	50.42	5574.4	6867.6	1.23
	CC4-D-4-2	1348.7	450.1	2.97	151.0	0.21	3.0	283.4	41.0	50.42	5581.2	6983.3	1.25
	CC4-D-8	1348.7	449.8	2.97	151.0	0.21	3.0	283.4	84.9	50.42	10265.1	11661.9	1.14
	CC6-C-2	716.3	238.5	4.55	52.0	0.15	3.0	578.5	25.4	50.42	2936.0	3034.1	1.03
	CC6-C-4-1	713.7	238.3	4.55	52.0	0.15	3.0	578.5	40.4	31.75	3540.1	3582.2	1.01
	CC6-C-4-2	713.7	238.0	4.55	52.0	0.15	3.0	578.5	40.4	19.45	3547.1	3646.2	1.03
	CC6-C-8	713.7	237.7	4.55	52.0	0.15	3.0	578.5	76.8	22.47	5032.4	5576.3	1.11
	CC6-D-2	1082.0	360.7	4.55	79.0	0.22	3.0	578.5	25.4	22.47	4555.4	5631.4	1.24
	CC6-D-4-1	1082.0	360.7	4.55	79.0	0.22	3.0	578.5	41.0	27.48	5607.7	7257.7	1.29
	CC6-D-4-2	1079.5	360.2	4.55	79.0	0.22	3.0	578.5	41.0	21.70	5594.1	7043.3	1.26
	CC6-D-8	1082.0	360.4	4.55	79.0	0.22	3.0	578.5	84.9	24.06	8514.4	11501.8	1.35
	CC8-D-2	1010.9	336.8	6.48	52.0	0.2	3.0	834.3	25.4	24.06	6938.9	8472.5	1.22
	CC8-D-4-1	1008.4	336.6	6.48	52.0	0.2	3.0	834.3	41.0	23.84	7820.0	9665.5	1.24
	CC8-D-4-2	1010.9	336.8	6.48	52.0	0.2	3.0	834.3	41.0	30.31	7839.6	9832.3	1.25

Table 2.2 continued.

Yoshioka et al., (1995)	CC8-D-8	1010.9	336.6	6.48	52.0	0.2	3.0	834.3	84.9	30.31	10303.8	13772.6	1.34
O'Shea and Bridge (1996)	S16CS	661.5	190.0	1.55	123.0	0.18	3.5	315.3	113.5	31.17	2457.2	3260.0	1.33
	S12CS	660.0	190.0	1.15	165.0	0.17	3.5	184.8	113.5	31.17	2478.0	3058.0	1.23
	S10CS	662.0	190.0	0.95	200.0	0.23	3.5	211.2	113.5	31.17	2263.6	3070.0	1.36
O'shea and Bridge (1997)	R12CF1	662.0	190.0	1.11	171.2	0.18	3.5	203.1	110.0	32.50	2227.7	3030.0	1.36
	R12CF2	656.0	190.0	1.11	171.2	0.18	3.5	203.1	110.0	32.50	2228.7	2940.0	1.32
	R12CF3	662.0	190.0	1.11	171.2	0.18	3.5	203.1	110.0	32.50	2227.7	3140.0	1.41
	R12CF4	662.0	190.0	1.11	171.2	0.18	3.5	203.1	94.7	29.60	1939.3	2462.0	1.27
	R12CF5	664.0	190.0	1.11	171.2	0.18	3.5	203.1	110.0	32.50	2227.4	3055.0	1.37
	R12CF7	660.0	190.0	1.11	171.2	0.18	3.5	203.1	110.0	32.50	2228.0	3000.0	1.35
	S10CL10C	664.0	190.0	0.86	220.9	0.26	3.5	210.7	91.7	31.10	1847.6	2553.0	1.38
	S12CL10A	661.5	190.0	1.13	168.1	0.18	3.5	185.7	113.6	32.50	2375.9	3220.0	1.36
	S12CL10C	662.5	190.0	1.13	168.1	0.18	3.5	185.7	91.7	31.10	1948.8	2630.0	1.35
	S16CL10C	658.0	190.0	1.52	125.0	0.18	3.5	306.1	91.7	31.10	2012.4	2830.0	1.41
O'shea and Bridge (2000)	S16CS50B	664.5	190.0	1.52	125.0	0.18	3.5	306.1	48.3	21.21	1193.4	1695.0	1.42
	S12CS50A	664.5	190.0	1.13	168.0	0.18	3.5	185.7	41.0	17.81	944.8	1377.0	1.46
	S10CS50A	659.0	190.0	0.86	221.0	0.26	3.5	210.7	41.0	17.81	886.7	1350.0	1.52
	S16CS80A	663.5	190.0	1.52	125.0	0.18	3.5	306.1	80.2	28.45	1795.4	2602.0	1.45
	S12CS80A	662.5	190.0	1.13	168.0	0.18	3.5	185.7	80.2	28.45	1721.9	2295.0	1.33
	S10CS80B	663.5	190.0	0.86	221.0	0.26	3.5	210.7	74.7	27.58	1526.8	2451.0	1.61
	S16CS10A	661.5	190.0	1.52	125.0	0.18	3.5	306.1	108.0	29.82	2313.8	3260.0	1.41
	S12CS10A	660.0	190.0	1.13	168.0	0.18	3.5	185.7	108.0	29.82	2264.4	3058.0	1.35
	S10CS10A	662.0	190.0	0.86	221.0	0.26	3.5	210.7	108.0	29.82	2149.2	3070.0	1.43

Table 2.3 Noncompact and Slender Rectangular CFT Beam Tests

Reference	Specimen ID	L (mm)	B (mm)	t_f (mm)	b/t_f	H (mm)	t_w (mm)	h/t_w	λ_{coeff}	a/H	F_y (MPa)	f'_c (MPa)	E_c (GPa)	M_n (kN-m)	M_{exp} (kN-m)	M_{exp}/M_n
Han et al. (2006)	SVB-1	1400.0	200.0	1.90	103.3	200.0	1.90	105.3	3.86	1.75	282.0	81.3	42.67	32.9	42.3	1.29
	SVB-2	1400.0	200.0	1.90	103.3	200.0	1.90	105.3	3.86	1.75	282.0	81.3	42.67	32.9	54.9	1.67
	SSCB-1	1400.0	200.0	1.90	103.3	200.0	1.90	105.3	3.86	1.75	282.0	81.3	42.67	32.9	56.7	1.72
Jiang et al. (2013)	S-150-2.0	2000.0	150.0	2.00	73.0	150.0	2.00	75.0	3.18	4.67	397.0	56.0	37.42	26.3	31.1	1.18

Table 2.4 Noncompact and Slender Circular CFT Beam Tests

Reference	Loading Type	Specimen ID	L (mm)	D (mm)	t (mm)	D/t	λ_{coeff}	a/D	F_y (MPa)	f'_c (MPa)	E_c (GPa)	M_n (kN-m)	M_{Exp} (kN-m)	M_{Exp}/M_n
Prion and Boehme (1993)	Monotonic loading	BP1	1100.0	152.0	1.70	89.4	0.12	3.9	262.0	73.0	40.2	13.5	19.9	1.48
		BP2	1100.0	152.0	1.70	89.4	0.12	3.0	262.0	73.0	40.2	13.5	17.9	1.33
		BP3	1100.0	152.0	1.70	89.4	0.12	2.0	262.0	73.0	40.2	13.5	20.8	1.55
		BP4	1100.0	152.0	1.70	89.4	0.12	0.0	262.0	73.0	40.2	13.5	19.0	1.41
	Cyclic	BP16	2120.0	152.0	1.70	89.4	0.15	4.0	328.0	92.0	45.1	16.1	21.0	1.30
Elchalakani et al. (2001)	Monotonic loading	CVB-1	1400.0	200.0	1.90	105.3	0.15	1.5	282.0	81.3	42.4	28.2	32.4	1.15
		CVB-2	1400.0	200.0	1.90	105.3	0.15	1.5	282.0	81.3	42.4	28.2	33.9	1.20
		CSCB-1	1400.0	200.0	1.90	105.3	0.15	1.5	282.0	81.3	42.4	28.2	36.6	1.30
Han et al. (2004)		CBC0-C	1500.0	109.9	1.00	109.9	0.23	1.8	400.0	23.4	22.7	5.2	7.6	1.47
		CBC0-B	1500.0	110.4	1.25	88.3	0.18	1.8	400.0	23.4	22.7	6.6	9.1	1.38
		CBC0-A	1500.0	110.9	1.50	73.9	0.15	1.8	400.0	23.4	22.7	8.0	11.0	1.38
Ichinohe et al. (1991)		C06F0M	2000.0	300.0	6.23	48.2	0.10	2.3	436.0	58.8	36.0	280.8	320.0	1.14
		C06F0MA	2000.0	300.0	5.65	53.1	0.11	2.3	403.0	63.4	37.4	241.6	273.6	1.13
		C06S0M	2000.0	300.0	6.16	48.7	0.10	2.3	406.0	66.2	38.2	264.2	303.0	1.15

Table 2.4 continued.

Wheeler and Bridge (2004)	Monotonic loading	TPB002	3800.0	406.0	6.40	63.4	0.11	3.2	350.0	40.0	29.7	432.0	489.0	1.13
		TPB003	3800.0	406.0	6.40	63.4	0.11	3.2	350.0	55.0	34.9	444.2	498.0	1.12
		TPB005	3800.0	456.0	6.40	71.3	0.12	2.9	350.0	48.0	32.6	556.9	630.0	1.13
		TPB006	3800.0	456.0	6.40	71.3	0.12	2.9	350.0	56.0	35.2	564.6	647.0	1.15
Elchalakani et al. (2004)	Cyclic loading with constant amplitude	F03A6	1500.0	109.3	0.68	160.7	0.35	3.2	430.0	23.1	22.6	3.6	4.1	1.13
		F08A6	1500.0	99.3	1.45	68.5	0.14	3.5	414.0	23.1	22.6	5.9	6.7	1.14
		F04A8	1500.0	110.2	1.15	95.8	0.21	3.2	430.0	23.1	22.6	6.1	6.4	1.04
		F06A8	1500.0	98.6	1.08	91.3	0.19	3.6	414.0	23.1	22.6	4.5	4.9	1.09
		F08A8	1500.0	99.3	1.45	68.5	0.14	3.5	414.0	23.1	22.6	5.9	6.9	1.17
		F01A10	1500.0	109.3	1.05	104.1	0.24	3.2	457.0	23.1	22.6	6.0	5.7	0.95
		F05A10	1500.0	98.3	1.54	63.8	0.13	3.6	410.0	23.1	22.6	6.0	7.6	1.25
		F06A10	1500.0	98.6	1.08	91.3	0.19	3.6	414.0	23.1	22.6	4.5	4.9	1.10
		F09A10	1500.0	99.7	1.63	61.1	0.13	3.5	414.0	23.1	22.6	6.6	7.4	1.12
		F10A10	1500.0	100.8	2.17	46.4	0.10	3.5	414.0	23.1	22.6	8.6	10.7	1.24
		F10A10-S	1500.0	100.8	2.17	46.4	0.10	3.5	414.0	23.1	22.6	8.6	11.4	1.33
		F12A10-S	1500.0	100.6	2.09	48.1	0.10	3.5	414.0	23.1	22.6	8.3	10.2	1.22
		F11A12	1500.0	87.3	2.28	38.3	0.09	4.0	473.0	23.1	22.6	7.3	8.1	1.11
		F09A12	1500.0	99.7	1.63	61.1	0.13	3.5	414.0	23.1	22.6	6.6	7.7	1.17
Lennie et al. (2008)	Cyclic loading with varying amplitude	1	9144.0	609.6	12.70	48.0	0.10	6.0	399.9	27.6	24.7	2062.5	2692.8	1.31
		2	9144.0	609.6	12.70	48.0	0.10	4.5	399.9	27.6	24.7	2062.5	2698.4	1.31
		3	9144.0	609.6	12.70	48.0	0.10	6.0	399.9	27.6	24.7	2062.5	2752.7	1.33
		4	9144.0	609.6	12.70	48.0	0.10	4.5	399.9	27.6	24.7	2062.5	2576.4	1.25
		5	9144.0	609.6	12.70	48.0	0.10	6.0	399.9	27.6	24.7	2062.5	2847.6	1.38
		6	9144.0	609.6	12.70	48.0	0.10	4.5	399.9	27.6	24.7	2062.5	2440.8	1.18
		7	9144.0	609.6	12.70	48.0	0.10	6.0	399.9	27.6	24.7	2062.5	2712.0	1.31
		8	9144.0	609.6	12.70	48.0	0.10	4.5	399.9	27.6	24.7	2062.5	2644.2	1.28
		9	9144.0	609.6	12.70	48.0	0.10	6.0	399.9	27.6	24.7	2062.5	2779.8	1.35
		10	9144.0	609.6	12.70	48.0	0.10	4.5	399.9	27.6	24.7	2062.5	2508.6	1.22

Table 2.5 Noncompact and Slender Rectangular CFT Beam-Column Tests

Reference	Load Type	Specimen ID	L (mm)	B (mm)	t_f (mm)	b/t_f	λ_{coeff}	ξ	F_y (MPa)	f'_c (MPa)	E_c (GPa)	P_n (kN)	P_{exp} (kN)	P_{exp}/P_n	M_n (kN-m)	M_{exp} (kN-m)	M_{exp}/M_n
Sakino and Nakahara (2000)	Monotonic, Type-B	ER4-D-4-06	969.0	323.0	4.38	71.7	2.56	0.36	262.0	41.1	30.34	4520.1	3306.0	0.73	209.7	201.0	0.96
		ER4-D-4-20	969.0	323.0	4.38	71.7	2.56	0.36	262.0	41.1	30.34	4520.1	1479.0	0.33	209.7	297.0	1.42
		ER6-D-4-10	954.0	318.0	6.36	48.0	2.63	1.28	618.0	41.1	30.34	7725.2	4100.0	0.53	614.3	408.0	0.66
		ER6-D-4-30	957.0	319.0	6.36	48.2	2.64	1.27	618.0	41.1	30.34	7752.8	1967.0	0.25	617.6	593.0	0.96
Nakahara and Sakino (2000)	Monotonic, Type-A	BR4-3-10-02	600.0	200.0	3.17	61.1	2.41	0.17	310.0	119.0	51.62	4330.3	1049.0	0.24	72.0	136.0	1.89
		BR4-3-10-04-1	600.0	200.0	3.17	61.1	2.41	0.17	310.0	119.0	51.62	4330.3	2108.0	0.49	72.0	136.0	1.89
		BR4-3-10-04-2	600.0	200.0	3.17	61.1	2.41	0.17	310.0	119.0	51.62	4330.3	2108.0	0.49	72.0	139.0	1.93
		BR8-3-10-02	600.0	200.0	3.09	62.7	3.92	0.43	781.0	119.0	51.62	4242.7	1294.0	0.30	144.2	195.0	1.35
		BR8-3-10-04	600.0	200.0	3.09	62.7	3.92	0.43	781.0	119.0	51.62	4242.7	2569.0	0.61	144.2	143.0	0.99
		BRA4-2-5-02	600.0	200.0	2.04	96.0	3.42	0.22	253.0	47.6	32.65	1594.2	380.0	0.24	31.9	62.7	1.96
		BRA4-2-5-04	600.0	200.0	2.04	96.0	3.42	0.22	253.0	47.6	32.65	1594.2	761.0	0.48	31.9	69.1	2.16
	Cyclic, Type-A	BRA4-2-5-02-C	600.0	200.0	2.04	96.0	3.42	0.22	253.0	47.6	32.65	1594.2	380.0	0.24	31.9	63.5	1.99
		BRA4-2-5-04-C	600.0	200.0	2.04	96.0	3.42	0.22	253.0	47.6	32.65	1594.2	761.0	0.48	31.9	71.5	2.24
Uy (2001)	Monotonic, Type- B	HSS16	630.0	210.0	5.00	40.0	2.45	2.40	750.0	32.0	26.77	4077.3	3106.0	0.76	249.1	77.7	0.31
		HSS17	630.0	210.0	5.00	40.0	2.45	2.40	750.0	32.0	26.77	4077.3	2617.0	0.64	249.1	130.9	0.53
Mursi and Uy (2004)	Monotonic, Type-B	SH-C210	2416.0	220.0	5.00	42.0	2.59	3.71	761.0	20.0	21.16	3539.3	2939.0	0.83	265.5	58.8	0.22
		SH-C260	2817.0	270.0	5.00	52.0	3.21	2.98	761.0	20.0	21.16	4122.9	3062.0	0.74	368.3	76.6	0.21

Table 2.6 Noncompact and Slender Circular CFT Beam-Column Tests

Reference	Load Type	Specimen ID	L (mm)	D (mm)	t (mm)	D/t	λ_{coeff}	ξ	F_y (MPa)	f'_c (MPa)	E_c (GPa)	P_n (kN)	P_{exp} (kN)	P_{exp}/P_n	M_n (kN-m)	M_{Exp} (kN-m)	M_{Exp}/M_n
Ichinohe et al. (1991)	Type A	C04F5M	2000.0	300.0	4.25	70.6	0.15	0.39	438.0	66.2	38.5	5262.6	3069.5	0.58	197.8	329.0	1.66
		C06F3M	2000.0	300.0	5.83	51.5	0.11	0.54	420.0	64.3	38.0	5706.9	1932.0	0.34	258.2	348.0	1.35
		C06F5M	2000.0	300.0	5.83	51.5	0.11	0.56	420.0	61.9	37.2	5583.1	3216.6	0.58	257.2	326.0	1.27
		C06F5MA	2000.0	300.0	5.65	53.1	0.11	0.52	403.0	61.9	37.2	5445.5	2981.0	0.55	241.1	318.0	1.32
		C06F7M	2000.0	300.0	5.65	53.1	0.11	0.51	419.0	66.2	38.5	5736.2	4560.0	0.79	250.5	256.0	1.02
		C06F3C	2000.0	300.0	6.23	48.2	0.10	0.58	436.0	66.2	38.5	6021.6	1961.0	0.33	283.7	418.7	1.48
		C06F5C	2000.0	300.0	5.65	53.1	0.11	0.51	419.0	66.2	38.5	5736.2	3255.8	0.57	250.5	402.0	1.60
		C06S5M	2000.0	300.0	6.16	48.7	0.10	0.54	406.0	66.2	38.5	5854.3	3285.0	0.56	264.2	405.0	1.53
		C06S5C	2000.0	300.0	5.70	52.6	0.11	0.52	431.0	66.2	38.5	5806.1	3305.0	0.57	258.5	391.0	1.51
		C06SVC	2000.0	300.0	5.70	52.6	0.11	0.52	431.0	66.2	38.5	5806.1	4628.7	0.80	258.5	327.0	1.26
		C06SVC	2000.0	300.0	5.70	52.6	0.11	0.52	431.0	66.2	38.5	5806.1	1981.0	0.34	258.5	416.0	1.61
		DC04S5M	2000.0	165.2	4.35	38.0	0.11	1.01	588.0	66.2	38.5	1856.1	1285.0	0.69	76.0	99.0	1.30
		DC04S5C	2000.0	165.2	4.35	38.0	0.11	1.01	588.0	66.2	38.5	1856.1	1285.0	0.69	76.0	99.0	1.30
Prion and Boehme (1993)	Type A	BP11	2120.0	152.0	1.70	89.4	0.15	0.17	328.0	92.0	45.4	1341.1	470.0	0.35	16.6	29.7	1.79
		BP12	2120.0	152.0	1.70	89.4	0.15	0.17	328.0	92.0	45.4	1341.1	570.0	0.43	16.6	32.1	1.93
		BP13	2120.0	152.0	1.70	89.4	0.15	0.17	328.0	92.0	45.4	1341.1	670.0	0.50	16.6	28.5	1.71
		BP14	2120.0	152.0	1.70	89.4	0.15	0.17	328.0	92.0	45.4	1341.1	820.0	0.61	16.6	29.2	1.76
		BP15	2120.0	152.0	1.70	89.4	0.15	0.17	328.0	92.0	45.4	1341.1	970.0	0.72	16.6	30.5	1.83
		BP17	2120.0	152.0	1.70	89.4	0.15	0.17	328.0	92.0	45.4	1341.1	270.0	0.20	16.6	30.1	1.81
		BP18	2120.0	152.0	1.70	89.4	0.15	0.17	328.0	92.0	45.4	1341.1	270.0	0.20	16.6	30.8	1.85
		BP19	2120.0	152.0	1.70	89.4	0.15	0.17	328.0	92.0	45.4	1341.1	670.0	0.50	16.6	34.8	2.09
	Type B	BP20	1071.0	152.0	1.70	89.4	0.15	0.17	328.0	92.0	45.4	1655.1	1273.0	0.77	16.6	21.4	1.29
		BP21	1071.0	152.0	1.70	89.4	0.15	0.17	328.0	92.0	45.4	1655.1	1451.0	0.88	16.6	13.8	0.83
		BP22	1071.0	152.0	1.70	89.4	0.15	0.17	328.0	92.0	45.4	1655.1	1309.0	0.79	16.6	15.9	0.96
O'shea and Bridge (1997c)	Type B	S12E210B	662.0	190.0	1.13	168.1	0.18	0.04	185.7	113.9	32.3	2731.1	2438.0	0.89	10.8	20.7	1.92
O'shea and Bridge (2004)	Type B	S12E250A	663.5	190.0	1.13	168.1	0.18	0.11	185.7	41.0	17.8	1073.4	1229.0	1.14	10.2	10.5	1.02
		S10E250A	662.0	190.0	0.86	220.9	0.26	0.09	210.7	41.0	17.8	886.6	1219.0	1.37	8.7	9.0	1.04
		S16E150B	662.0	190.0	1.52	125.0	0.18	0.21	306.1	48.3	21.2	1270.2	1260.0	0.99	21.0	19.5	0.93
		S12E150A	664.0	190.0	1.13	168.1	0.18	0.11	185.7	41.0	17.8	1073.4	1023.0	0.95	10.2	19.3	1.90
		S10E150A	663.0	190.0	0.86	220.9	0.26	0.09	210.7	41.0	17.8	886.5	1017.0	1.15	8.7	14.1	1.63
		S10E280B	665.5	190.0	0.86	220.9	0.26	0.05	210.7	74.4	27.6	1521.0	1910.0	1.26	9.0	16.4	1.82
		S16E180A	663.5	190.0	1.52	125.0	0.18	0.13	306.1	80.2	28.4	1921.6	1925.0	1.00	21.9	27.5	1.26
		S10E180B	665.0	190.0	0.86	220.9	0.26	0.05	210.7	74.7	27.6	1526.6	1532.0	1.00	9.1	27.4	3.03
		S10E210B	660.5	190.0	0.86	220.9	0.26	0.03	210.7	112.7	31.5	2238.7	2112.0	0.94	9.3	8.5	0.91
		S16E110B	660.5	190.0	1.52	125.0	0.18	0.09	306.1	112.7	31.5	2578.3	2420.0	0.94	22.5	31.2	1.39
		S12E110B	662.0	190.0	1.13	168.1	0.18	0.04	185.7	112.7	31.5	2702.2	1925.0	0.71	10.8	32.9	3.05

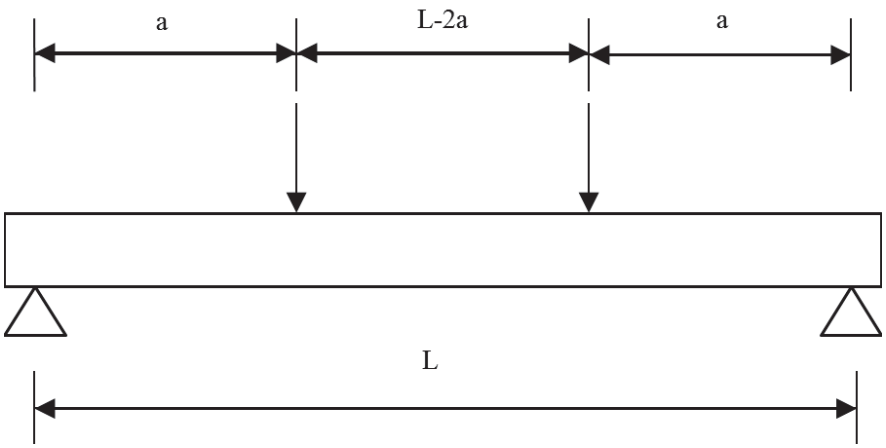

Figure 2.1 Typical Four Point Loading Scheme for CFT Beam Tests

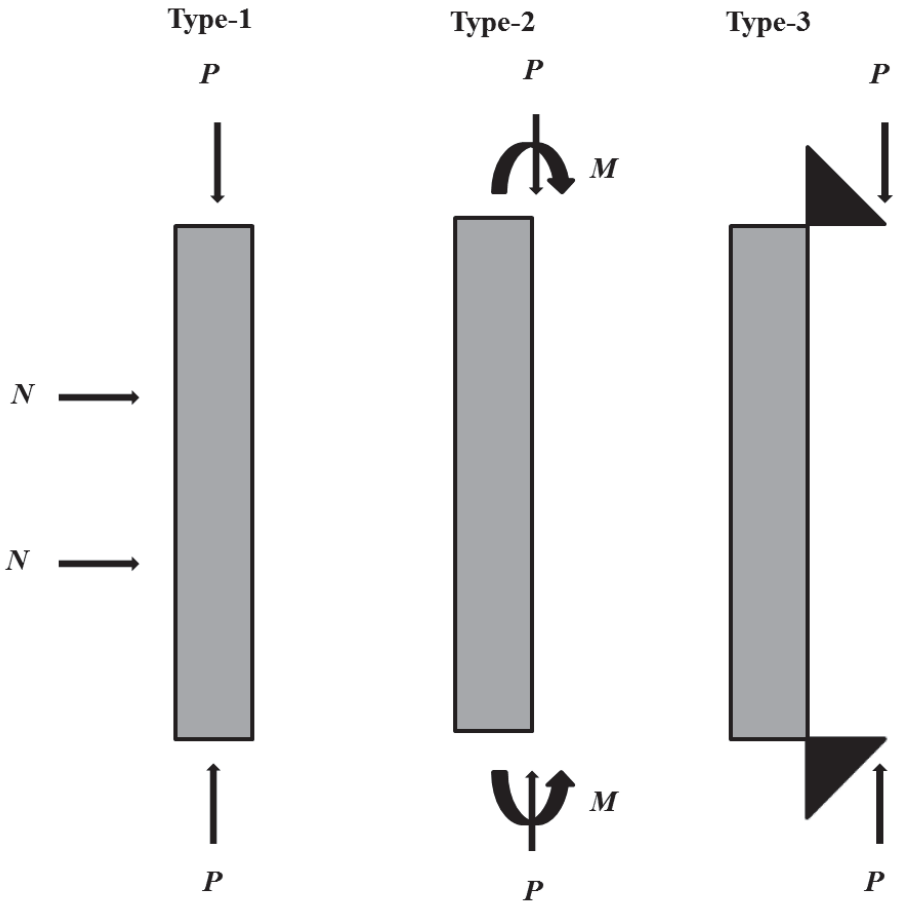

Figure 2.2 Typical Loading Schemes for CFT Beam-Column Tests

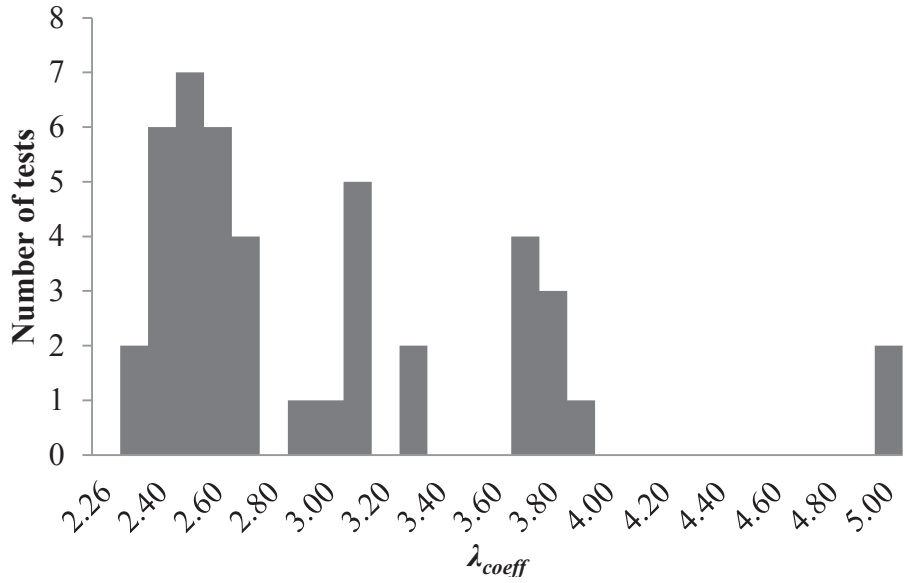

Figure 2.3 Distributions of Test Data for Rectangular CFT Columns

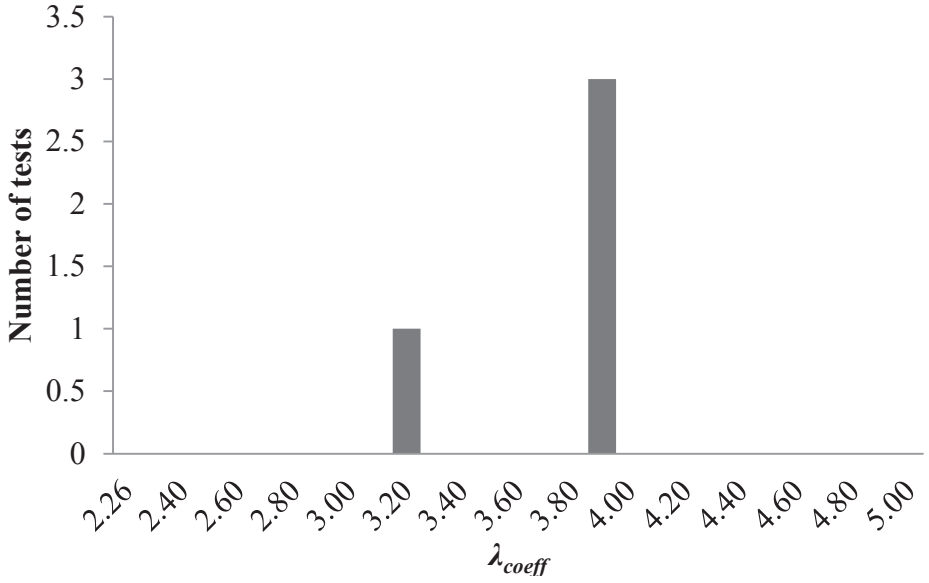

Figure 2.4 Distributions of Test Data for Circular CFT Columns

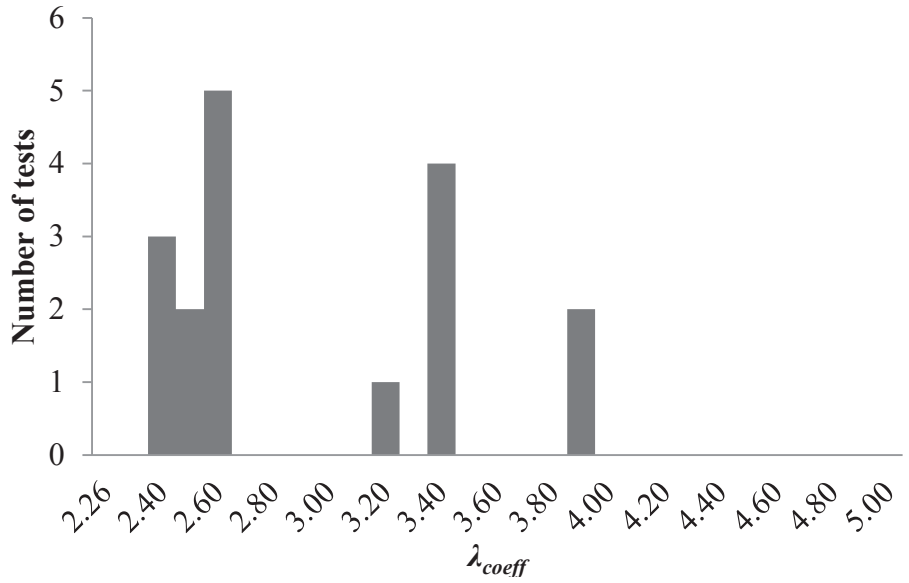

Figure 2.5 Distributions of Test Data for Rectangular CFT Beams

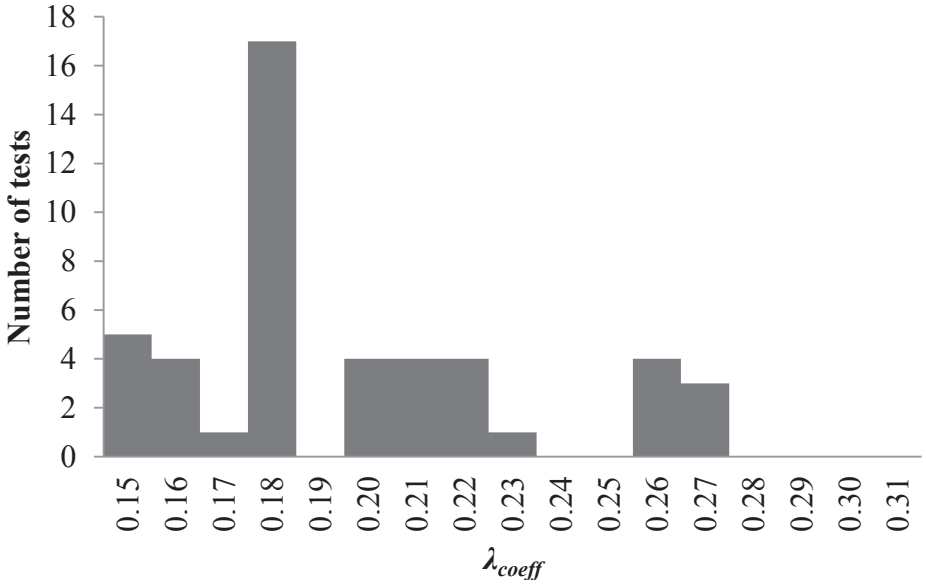

Figure 2.6 Distributions of Test Data for Circular CFT Beams

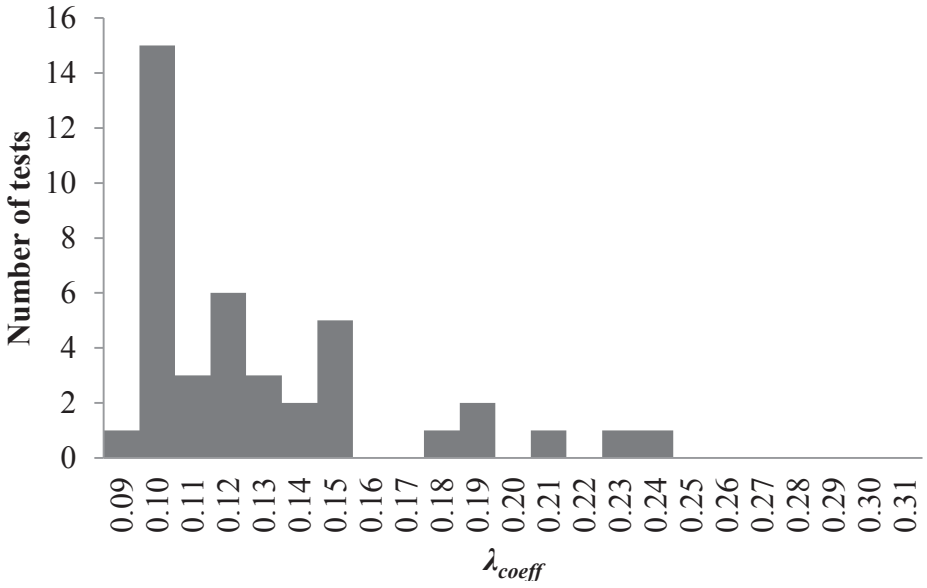

Figure 2.7 Distributions of Test Data for Rectangular CFT Beam-Columns

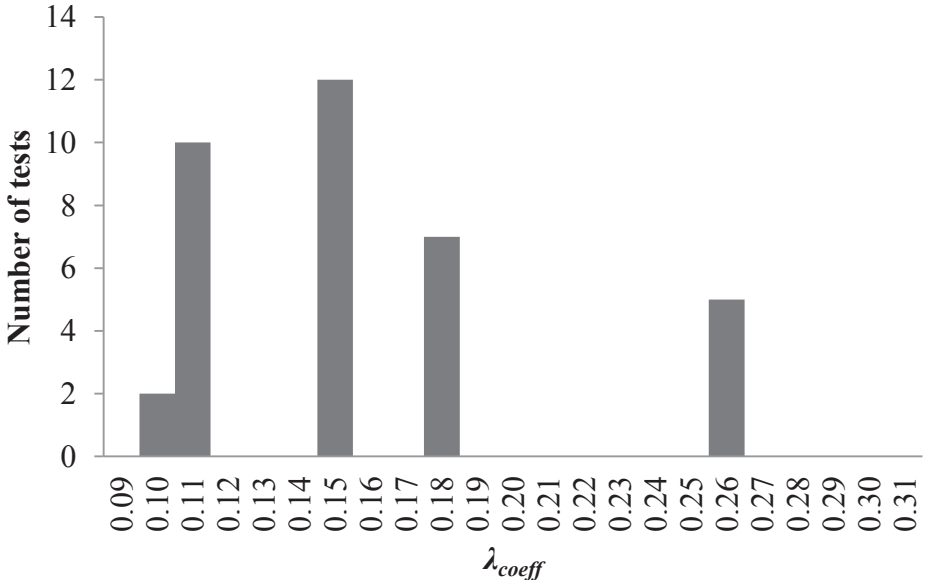

Figure 2.8 Distributions of Test Data for Circular CFT Beam-Columns

CHAPTER 3. DEVELOPMENT AND BENCHMARKING OF FEM MODELS

This chapter presents details of the 3D finite element method (FEM) models are presented first, followed by the benchmarking of these models using experimental results from the database. The FEM models were developed and analyzed using ABAQUS (2012), which is a general-purpose commercial finite element analysis program. ABAQUS was selected because it has: (i) the capabilities for modeling steel tube local buckling, contact interactions between steel tube and concrete infill, as well as interaction between local buckling and global column buckling, (ii) versatile material models that can account for steel kinematic strain hardening, concrete confinement in compression, and concrete cracking in tension, and (iii) different analysis techniques and solution algorithms like modified-Riks arc length method, modified Newton method, and implicit or explicit dynamic analysis method to account for the nonlinear behavior of CFT members.

The benchmarked FEM models are used to conduct additional analysis to: (i) further evaluate the AISC 360-10 design provisions in Chapters 4-6 by addressing the gaps in the database identified in Chapter 2, and (ii) develop the updated P-M interaction curve for noncompact and slender CFT beam-columns in Chapter 6, and (iii) develop effective stress-strain curves for the steel tube and concrete infill for CFT members in Chapter 7.

3.1 FEM Model Details

3.1.1 Element Types

The steel tubes of the CFT members were modeled using a fine mesh of 4-node S4R shell elements. These elements have: (i) six degrees of freedom per node, (ii) three or five section points to compute the stress and strain variations through the thickness, and (iii) reduced integration in the plan of the elements. These elements model thick shell behavior, but converge to Kirchhoff's thin plate bending theory with reducing thickness. These elements also account for finite membrane strains and arbitrarily large rotations; therefore, they are suitable for large-strain analysis, for example, the analysis of CFT members with the occurrence of local buckling of the steel tube.

The concrete infill of CFT members was modeled using eight-node solid elements with reduced integration (C3D8R). These elements have three degrees of freedom per node and reduced integration to calculate the stresses and strains in the elements. The C3D8R elements are computationally effective for modeling concrete cracking.

3.1.2 Contact Interactions

The contact interactions between the steel tube and concrete infill of CFT members were modeled in both the normal and tangential directions. The hard contact pressure-overclosure relationship with penalty constraint method was used for interaction in the normal direction. The penalty friction formulation with coulomb friction coefficient equal to 0.55 and maximum interfacial shear stress equal to 0.41 MPa (60 psi, as suggested by AISC 360-10) was used for interaction in the tangential direction. There was no

additional bond (adhesive or chemical) between the steel tube and the concrete infill in the model. The steel tube and concrete infill could slip relative to each other when the applied interfacial shear stress (τ_{app}) exceeded 0.55 times the contact pressure (p).

3.1.3 Geometric Imperfections

Geometric imperfections were defined to initiate local buckling in the steel tube models. As recommended by Varma (2000), the shape of the geometric imperfection was developed by conducting eigenvalue buckling analysis and the amplitude (magnitude) of the geometric imperfection was set equal to 0.1 times the tube thickness. Figure 3.1 shows the first buckling eigenmode shape used to define the geometric imperfection for rectangular and circular CFT members.

3.1.4 Boundary Conditions

The boundary conditions and constraints used for the FEM models were designed to simulate those achieved in the experiments, i.e., by using kinematic coupling constrains. Figure 3.2 shows an example of the coupling constraints used to simulate the boundary conditions of a circular CFT column test with Pin-Pin end restraints. Two reference points (i.e., Reference Point A and Reference Point B) were defined first, and each of them was coupled to one of the column ends (i.e., left end or right end) using kinematic coupling constraints. The translational and rotational degrees of freedom (U_1, U_2, U_3, UR_1, UR_2, and UR_3) of the column ends were then coupled to the corresponding reference point. The Pin-Pin boundary conditions on the column ends were prescribed by applying displacement constraints ($U_1 = U_2 = 0$, $UR_2 = UR_3 = 0$) on both reference points.

The axial loading was then applied to the column by applying axial force (P) or axial displacement (U_3) to Reference Point A, and restraining the axial displacement of Reference Point B (i.e., $U_3 = 0$).

3.1.5 Material Models

The steel material multiaxial behavior was defined using the Von Mises yield surface, associated flow rule, and kinematic hardening. An idealized bilinear curve as shown in Figure 3.3 was used to specify the uniaxial stress-strain behavior of steel. The elastic modulus (E_s) was assumed to be 200 GPa, and the post-yield hardening modulus (E_t) was assumed to be $E_s/100$.

The concrete material multiaxial behavior was modeled using the damaged plasticity (CDP) material model developed by Lee and Fenves (1998). This model accounts for multiaxial behavior using a special compression yield surface developed earlier by Lubliner et al. (1988) and modified by Lee and Fenves (1998) to account for different evolution of strength in tension and compression.

The CDP model accounts for the non-associated plastic flow behavior of concrete in compression (Chen and Han, 2007) using: (i) the Drucker-Prager hyperbolic function as the flow potential G, (ii) dilation angle ψ, and (iii) eccentricity ratio e. The value of the dilation angle ψ was calibrated by Prabhu et al. (2009) using experimental data for axial and lateral stress-strain behavior reported by other researchers. The resulting value of the dilation angle for unconfined concrete was 15 degrees (15^o). For rectangular CFT

members, this dilation angle (15^o) was used because of the limited dilation and confinement of the concrete infill. For circular CFT members, the value of the dilation angle was selected differently for columns, beams and beam-columns.

For circular CFT columns, the value of the dilation angle being used in the FEM models is dependent on the concrete compressive strength (i.e., normal strength or high strength). According to AISC 360-10, concrete with the compressive strength (f'_c) greater than 10 MPa is defined as high strength concrete. High strength concrete develops its compressive stress linearly up to f'_c under axial compression without significant volumetric dilation. Therefore, the dilation angle was selected as 15^o for CFT columns filled with high strength concrete. Normal strength concrete develops its compressive stress linearly up to $0.70f'_c$, followed by significant amount of volumetric dilation. Thus, the dilation angle was selected as 40^o for CFT columns filled with normal strength concrete.

For circular CFT beams, the dilation angle of 15^o was used because: (i) the flexural behavior was dominated by the steel tube of the steel tube; and (ii) the beneficial effects of confinement on the strain ductility and strength increase of the concrete do not have significant effect of the overall flexural behavior.

For circular CFT beam-columns, confinement of the concrete on the compressive side of the neutral axis can have a significant influence on the flexural behavior and strength. However, preliminary finite element analyses indicated that increasing the dilation angle

alone (for example, ψ up to 40^o) was incapable of modeling the beneficial effects of confinement on the strain ductility of normal strength concrete because of the limitations of the material model formulation. The compressive stress-strain behavior of normal strength (only) had to be modified to be elastic-perfectly plastic, and the dilation angle of 15^o was used. For circular CFT beam-columns, the dilation angle of 15^o was also used. The selected value of the dilation angle and concrete stress-strain curves are reasonable for all specimens, as shown later in the benchmarking of the FEM models. Table 3.1 summarizes the values of dilation angle used in the analysis. The selections of both the dilation angle values and concrete stress-strain curves are reasonable for all specimens, as shown later in the benchmarking of the FEM models in Section 3.2.

Other parameters required to define the multiaxial plasticity model are: the eccentricity ratio e, the ratio of biaxial compressive strength to uniaxial strength f'_{bc}/f'_c, and the ratio of compressive to tensile meridians of the yield surface in π (deviatoric stress) space K_c. The default value of 0.1 was specified for the eccentricity ratio (e). The default value of e indicates that the dilation angle converges to ψ reasonably quickly with increasing hydrostatic compression pressure (p). f'_{bc}/f'_c was assumed to be equal to 1.16 based on Kupfer and Gerstle (1973). K_c was assumed to be equal to 0.67 based on Chen and Han (2007).

Two types of stress-strain curve were used to specify the uniaxial compressive behavior of the concrete infill, as summarized in Table 3.2. For rectangular CFT members, circular CFT columns and beams, and circular CFT beam-columns with high strength concrete,

the empirical stress-strain curve proposed by Popovics (1973) was used, as shown in Figure 3.4(a). For circular CFT beam-columns, an elastic perfectly plastic (EPP) curve was used as discussed previously. The smeared cracking behavior in tension was specified using a stress-crack opening displacement curve that is based on fracture energy principles and empirical models developed by CEB-FIB (2010), as shown in Figure 3.4(b).

3.1.6 Analysis Method

The fracture behavior of concrete in tension makes it virtually impossible to obtain converged results using standard (predictor-corrector) nonlinear solution strategies like the full Newton or modified Newton-Raphson iteration approaches. Even arc-length based techniques like the modified-Riks method cannot provide converged results due to the brittle fracture behavior of concrete in tension. Implicit dynamic analysis based methods also become unstable and cannot provide results after significant cracking. Therefore, the explicit dynamic analysis method was used. The primary advantage and reason for using this method is that it can find results up to failure, particularly when brittle materials (like concrete in tension) and failures are involved. The explicit dynamic analysis method was used to perform quasi-static analyses simulating the experiments.

3.2 Benchmarking of the FEM Models

The developed FEM models were used to predict the behavior of the specimens in the experimental database. Some of the specimens in the experimental database could not be modeled because the corresponding references did not include all critical information (i.e.,

specimen length, loading protocol, boundary conditions, etc.) needed to develop the finite element models. Ninety-two (noncompact or slender) CFT member tests from the database were used to benchmark the finite element models. These include 33 column tests, 20 beam tests, and 39 beam-column tests. Comparisons of the strengths from the finite element analysis and the corresponding tests are shown in Figure 3.5 – Figure 3.8, where the ordinate is the ratio of experimental strength to that predicted by FEM analysis, and the abscissa is the slenderness coefficient.

The strengths from the finite element analyses were defined appropriately for different loading conditions (axial compression, flexure, and combined axial and flexure) as follows. For CFT columns, the axial strength from the finite element analysis (P_{FEM}) was defined as the maximum load value obtained from the analysis and the corresponding comparisons are shown in Figure 3.5. For CFT beams, if the method of determining the flexural strength was specified in the corresponding experimental paper (for example, Han (2004) defined flexural strength as the moment corresponding to 1% strain in the extreme compression fibers), then the same method was used to define the flexural strength (M_{FEM}) from the finite element analysis. Otherwise, the flexural strength from finite element analysis (M_{FEM}) was defined as the maximum moment obtained from the analysis for rectangular beams, and as the applied moment value corresponding to an average curvature of 0.05/m for circular CFT beams. The corresponding comparisons are shown in Figure 3.6.

For beam-columns with Type-A loading (constant axial loading), only comparisons of the flexural strength were required. The flexural strength from finite element analysis (M_{FEM}) was defined in the same way as that for CFT beams. For CFT beam-columns with Type-B loading (eccentric axial loading), comparisons of both axial and flexural strength were required. The axial strength (P_{FEM}) was defined as the maximum value obtained from the analysis, and the flexural strength (M_{FEM}) was defined as the bending moment corresponding to P_{FEM} including second order effects. The resulting comparisons are shown in Figure 3.7 (for rectangular CFT beam-columns) and Figure 3.8 (for circular CFT beam-columns).

Figure 3.9 – Figure 3.17 show typical comparisons of experimental and analytical load-displacement responses for noncompact and slender CFT beams. These figures include comparisons of: (i) the moment-midspan deflection curves for Specimens S-150-2.0, CVB-1, TPB002, TPB003, TPB005, TPB006, and 1, (ii) the moment-curvature response for Specimen C06F0M, and (iii) the moment-rotation response for Specimen C06FS0M.

Figure 3.18 – Figure 3. 25 show typical comparisons of experimental and analytical load-displacement responses for noncompact and slender CFT beam-columns. These figures include comparisons of: (i) the moment-curvature response for Specimens BRA4-2-5-02, BRA4-2-5-04, C06F3M, C06F5M, C06F5MA, C06F7M, and BP17, and (ii) the moment-rotation response for Specimen C06S5M.

The comparisons shown in Figure 3.9 - Figure 3.25 are typical and representative of the comparisons between experimental and analytical load-displacement responses. As shown in these figures, the finite element models predict the behavior and strengths of CFT columns, beams, and beam-columns reasonably well.

Table 3.1 Values of the Dilation Angle

	Member Type / Concrete Strength	Columns	Beams	Beam-columns
Rectangular	Normal strength concrete	15	15	15
	High strength concrete	15	15	15
Circular	Normal strength concrete	40	15	15
	High strength concrete	15	15	15

Table 3.2 Compressive Stress-Strain Curve of the Concrete

	Member Type / Concrete Strength	Columns	Beams	Beam-columns
Rectangular	Normal strength concrete	Popovics	Popovics	Popovics
	High strength concrete	Popovics	Popovics	Popovics
Circular	Normal strength concrete	Popovics	Popovics	EPP
	High strength concrete	Popovics	Popovics	Popovics

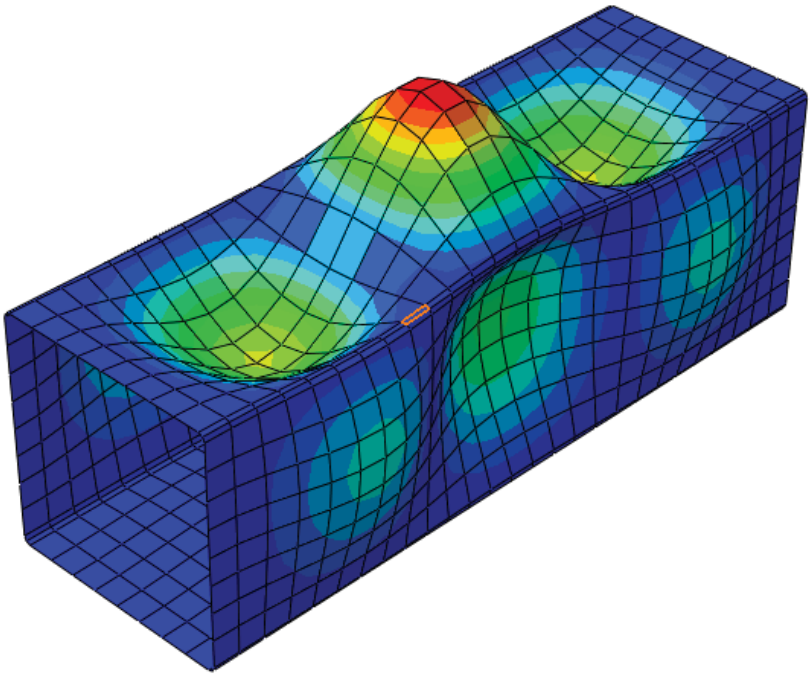

(a) Rectangular

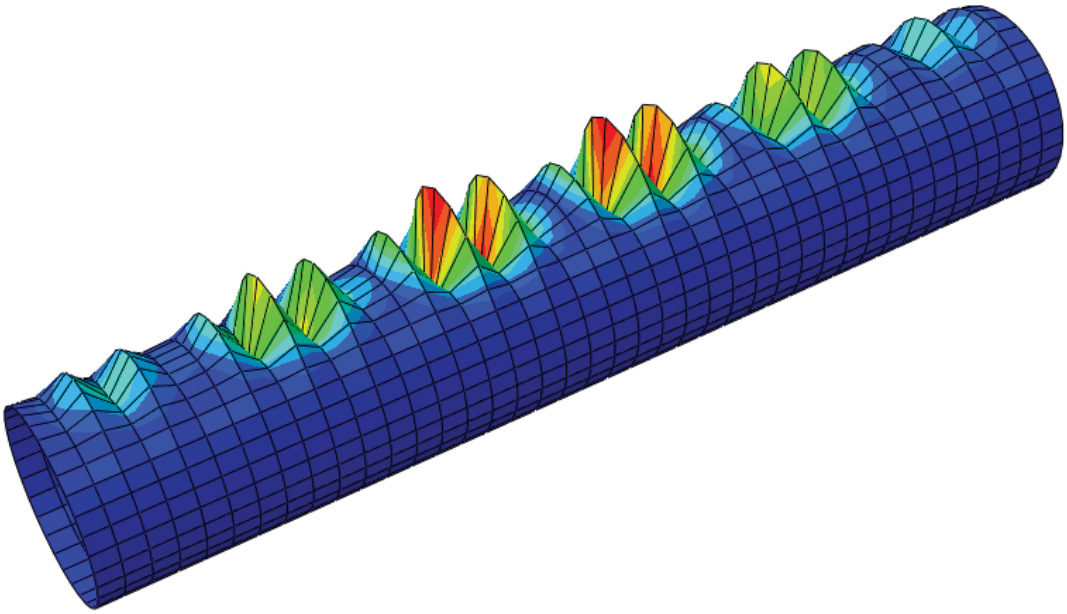

(b) Circular

Figure 3.1 First Buckling Eigenmode from Eigenvalue Analysis

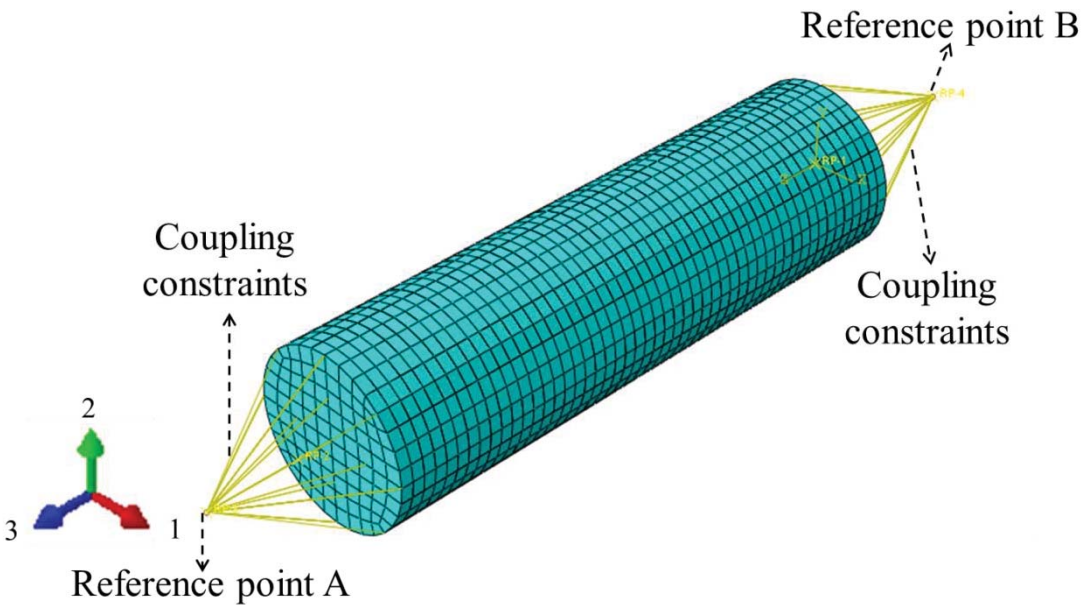

Figure 3.2 Example of Boundary Conditions, Couplings and Constraints, and Mesh in the FEM Models

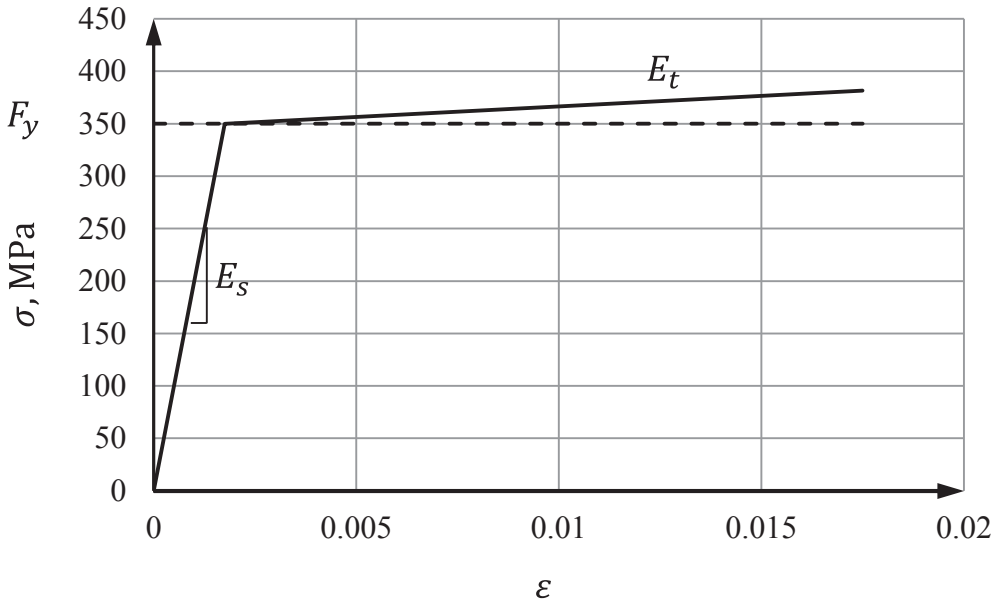

Figure 3.3 Idealized Bilinear Stress-Strain Curve for the Steel Tube (F_y = 350 MPa)

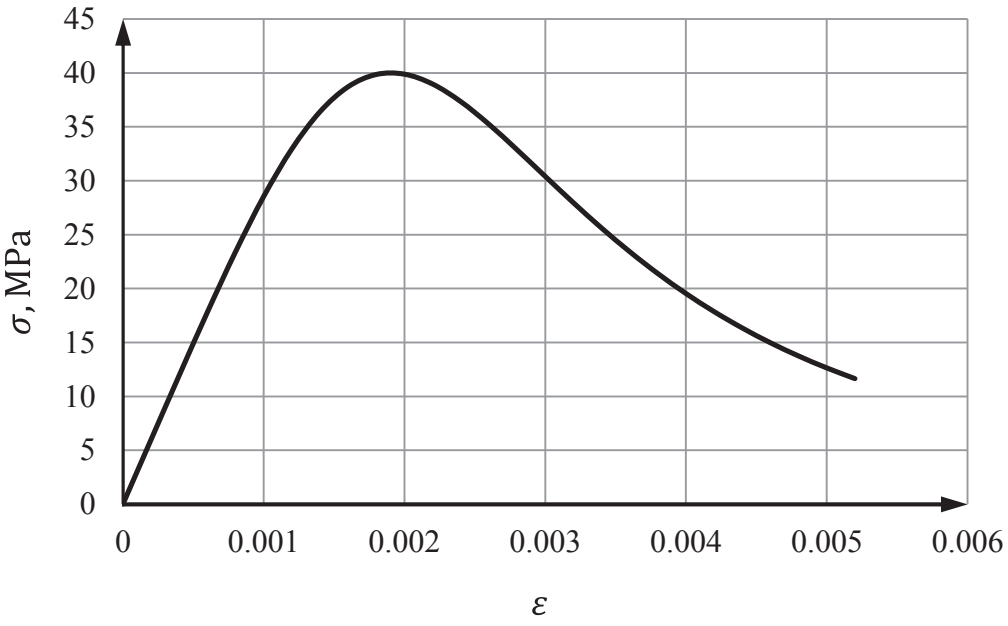

(a) Compressive Stress-Strain Curve (f'_c = 40 Mpa)

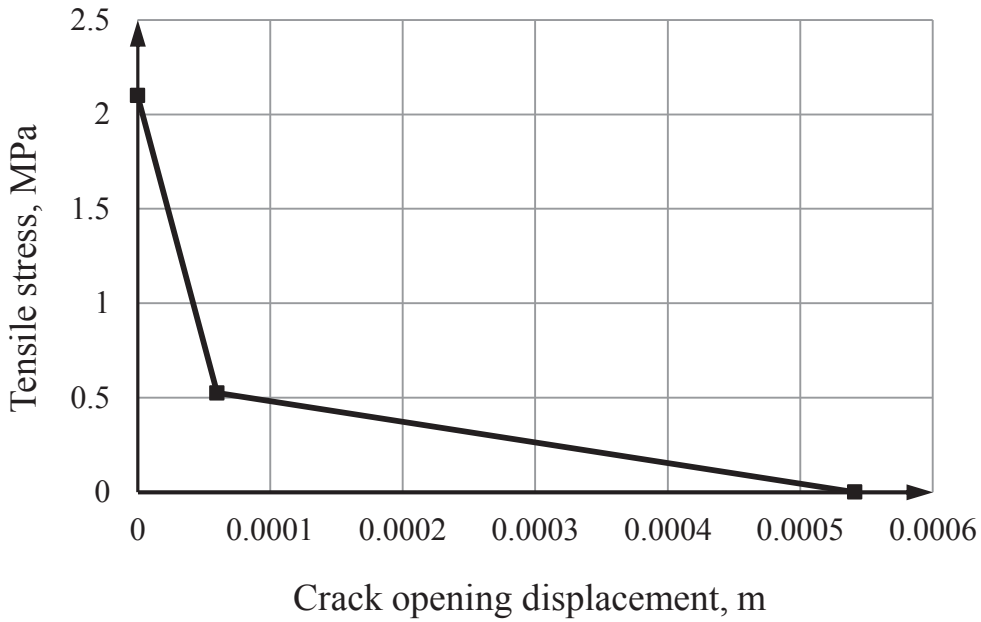

(b) Tensile Stress-Crack Opening Displacement Curve (f'_c = 40 Mpa)

Figure 3.4 Stress-Strain Curves for the Concrete Infill

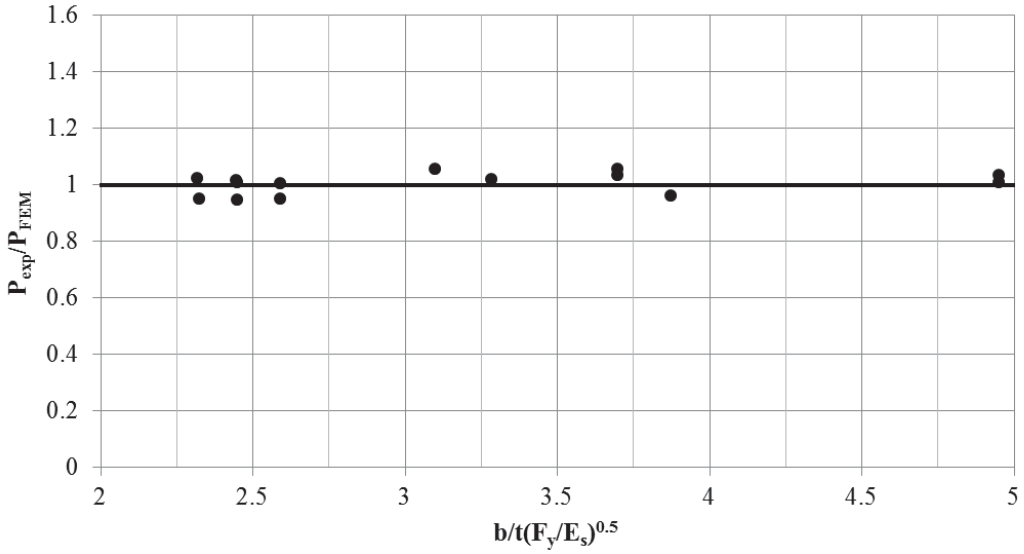

(a) Rectangular

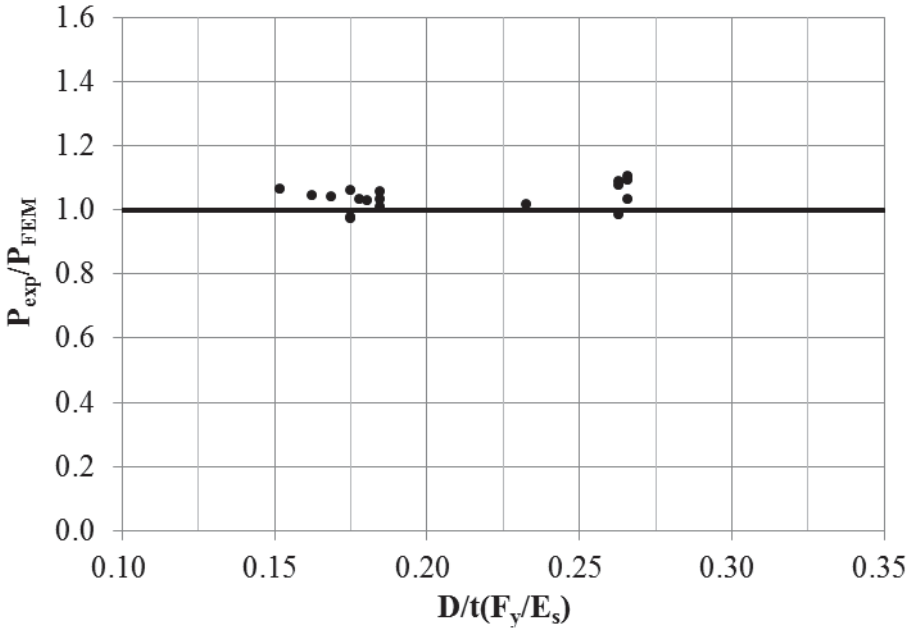

(b) Circular

Figure 3.5 Comparisons of Axial Strengths from the FEM Analyses with the Corresponding Experimental Results for Noncompact and Slender CFT Columns

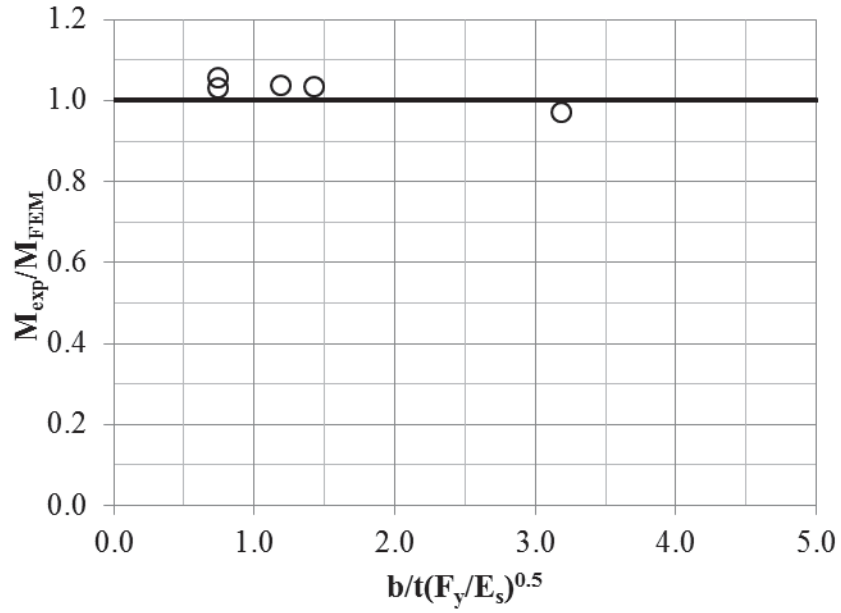

(a) Rectangular

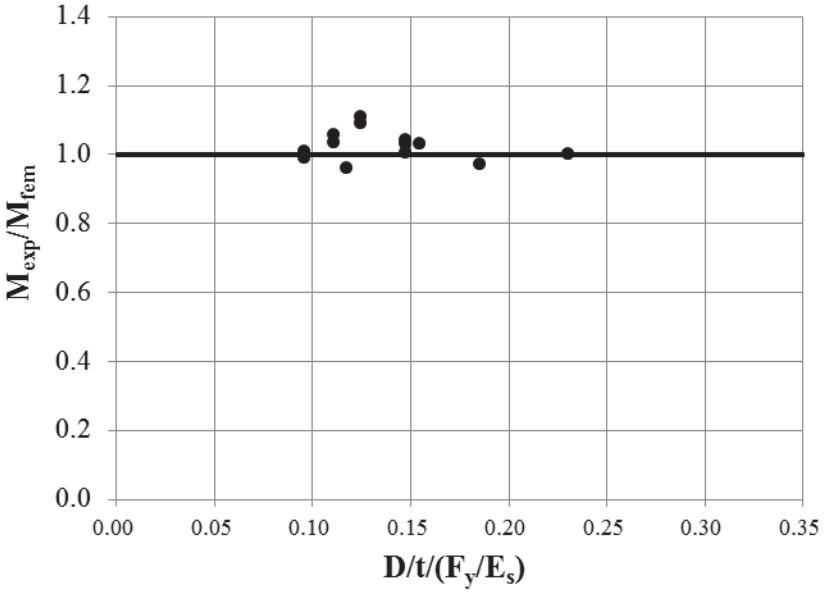

(b) Circular

Figure 3.6 Comparisons of Flexural Strengths from the FEM Analyses with the Corresponding Experimental Results for Noncompact and Slender CFT Beams

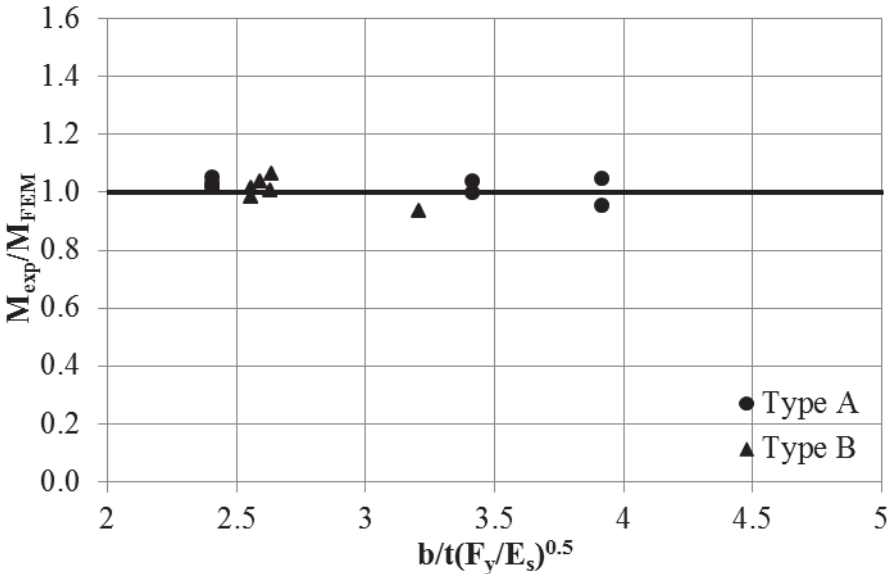

(a) Rectangular CFT Beam-Columns with Type A and Type B Loading

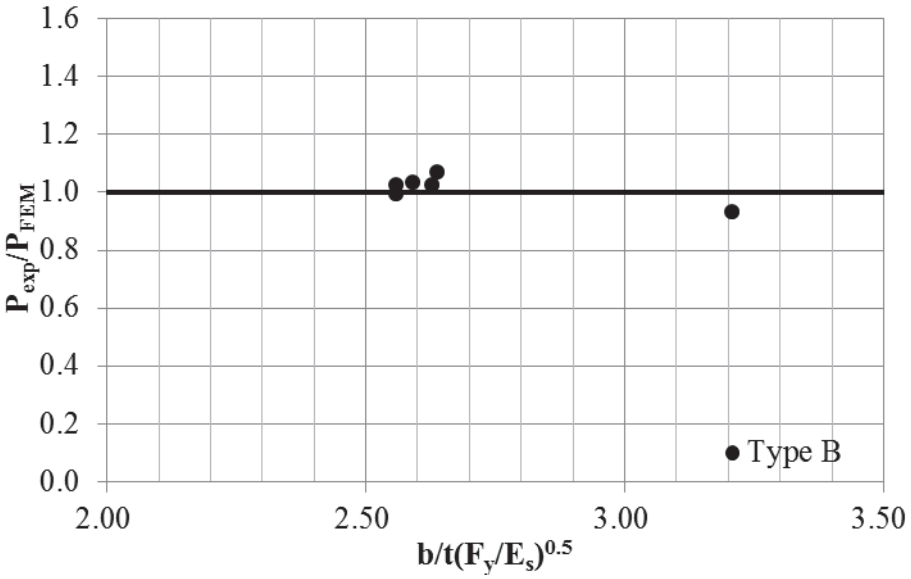

(b) Rectangular CFT Beam-Columns with Type B Loading

Figure 3.7 Comparisons of Strengths from the FEM Analyses with the Corresponding Experimental Results for Rectangular Noncompact and Slender CFT Beam-Columns

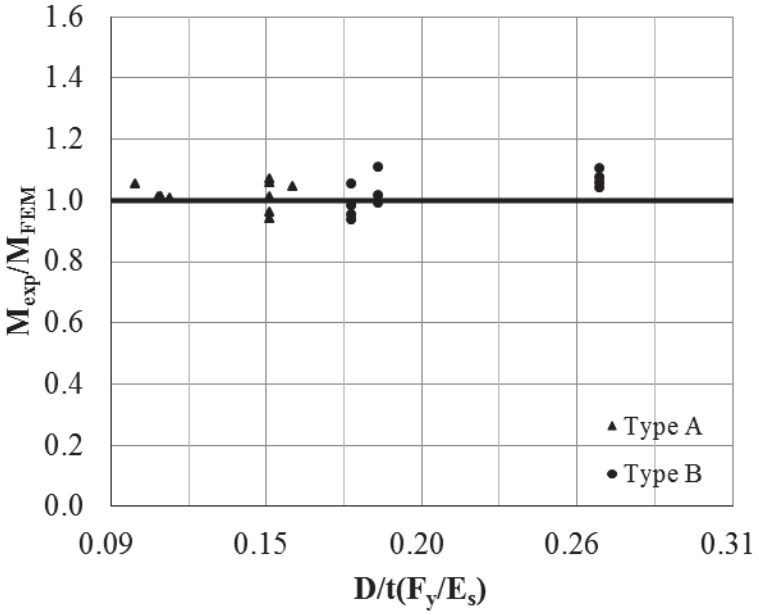

(a) Circular CFT Beam-Columns with Type A and Type B Loading

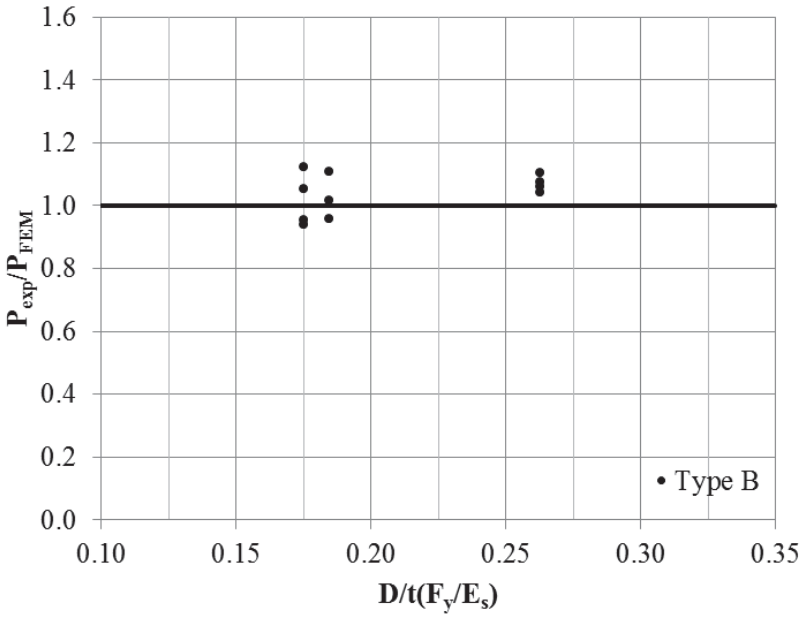

(b) Circular CFT beam-columns with Type A and Type B loading
Figure 3.7 Continued

Figure 3.8 Comparisons of Strengths from the FEM Analyses with the Corresponding Experimental Results for Circular Noncompact and Slender CFT Beam-Columns

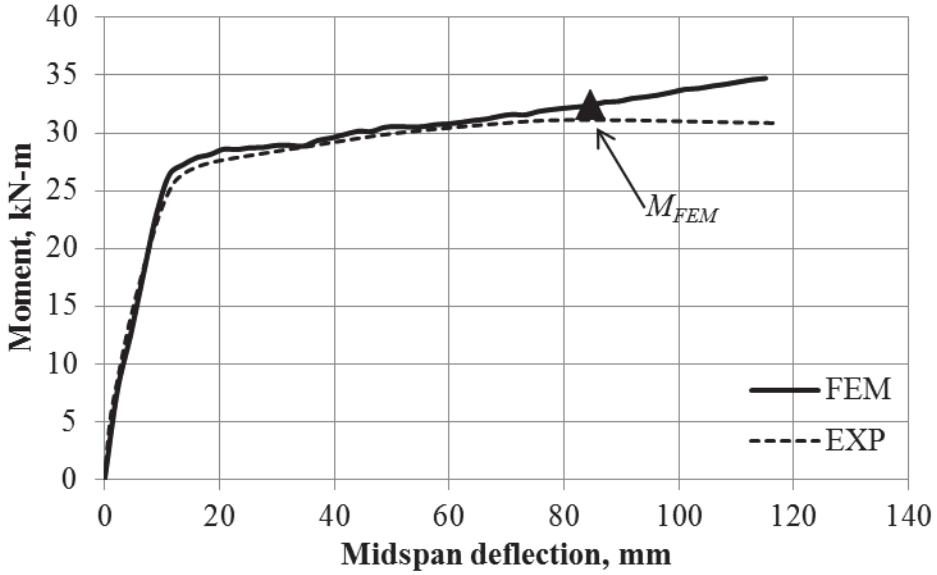

Figure 3.9 Comparisons of Experimental and Analytical Moment-Midspan Deflection Response for Specimen S-120-2.0

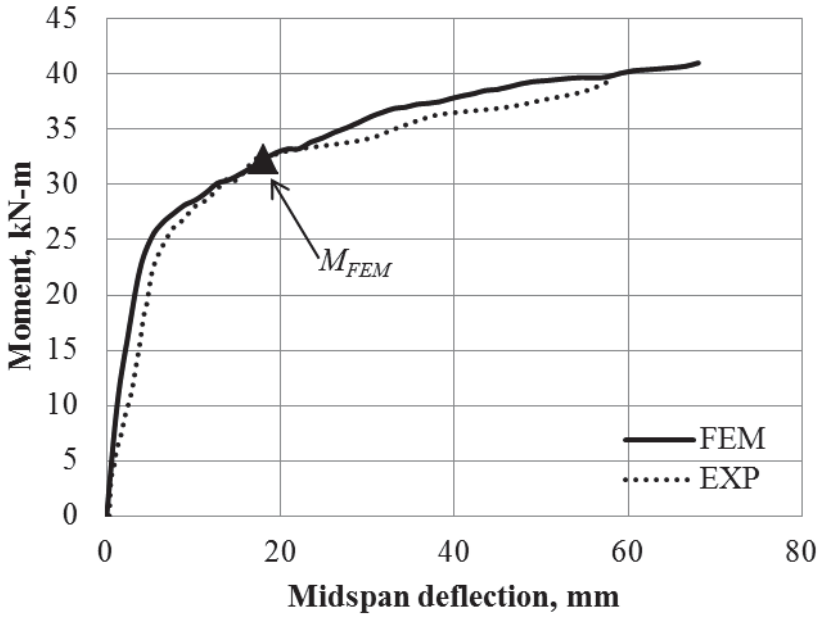

Figure 3.10 Comparisons of Experimental and Analytical Moment-Midspan Deflection Response for Specimen CVB-1

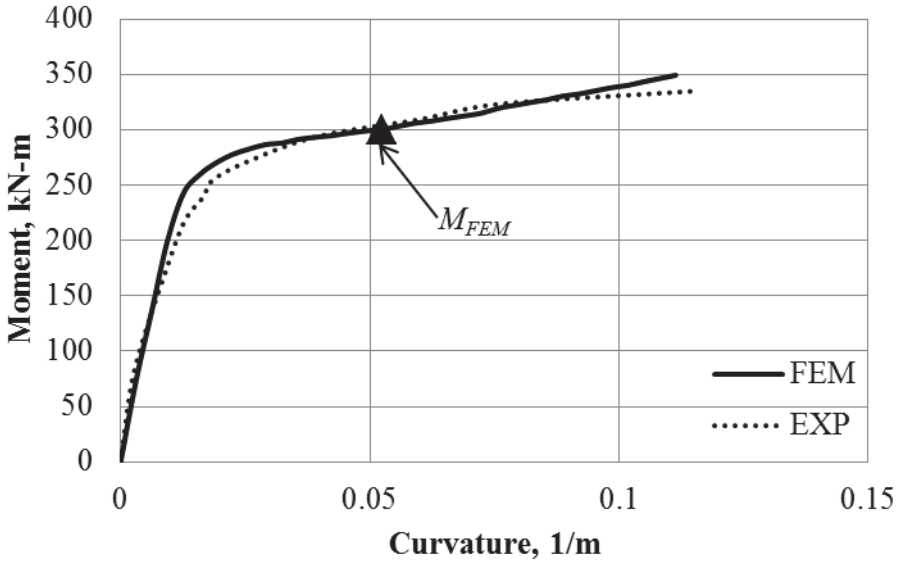

Figure 3.11 Comparisons of Experimental and Analytical Moment-Curvature Response for Specimen C06F0M

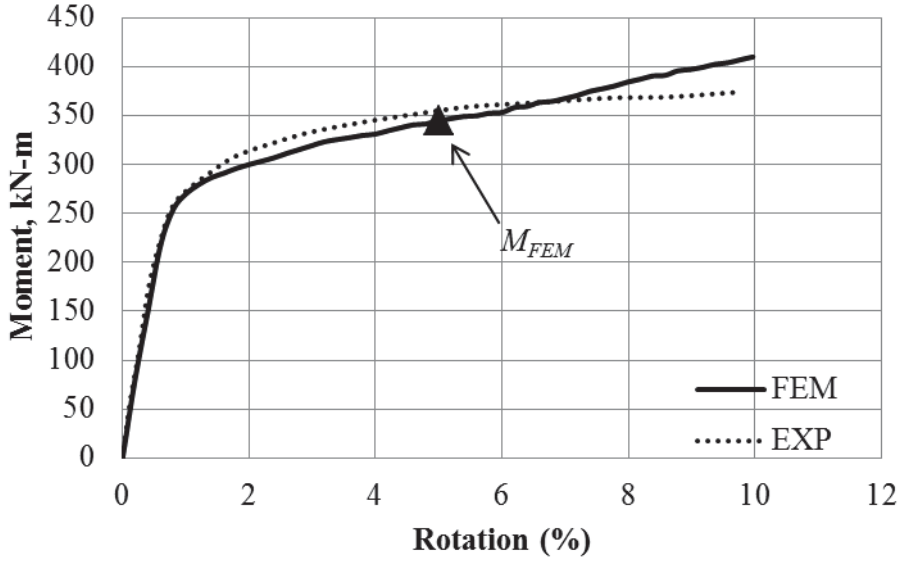

Figure 3.12 Comparisons of Experimental and Analytical Moment-Rotation Response for Specimen C06FS0M

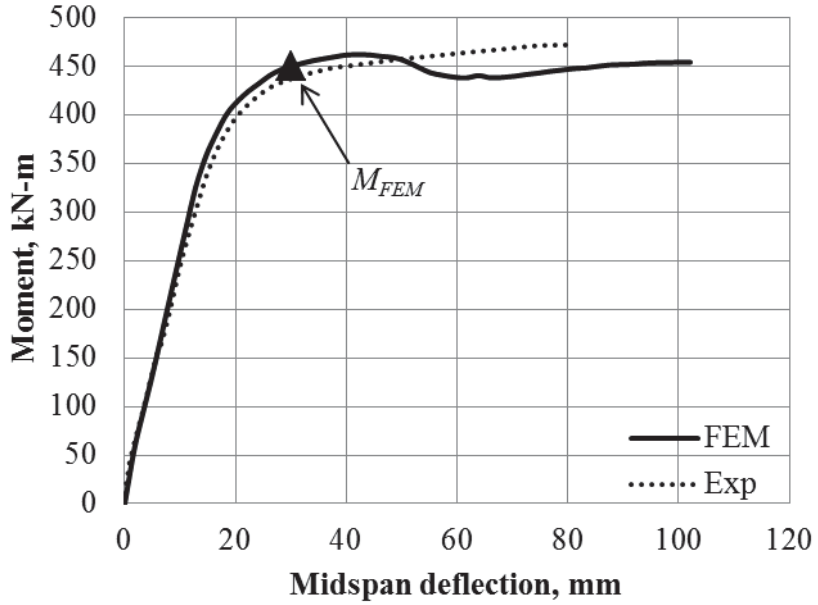

Figure 3.13 Comparisons of Experimental and Analytical Moment-Midspan Deflection Response for Specimen TPB002

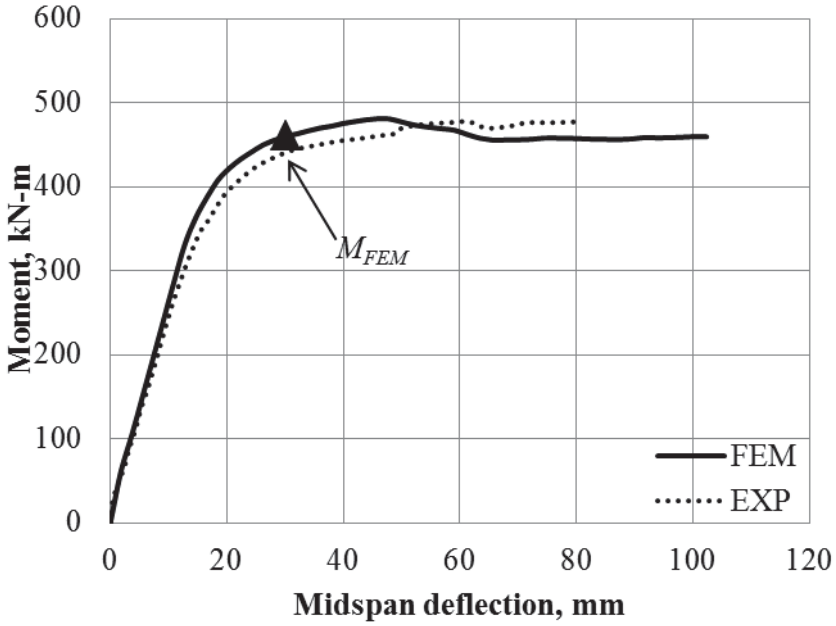

Figure 3.14 Comparisons of Experimental and Analytical Moment-Midspan Deflection Response for Specimen TPB003

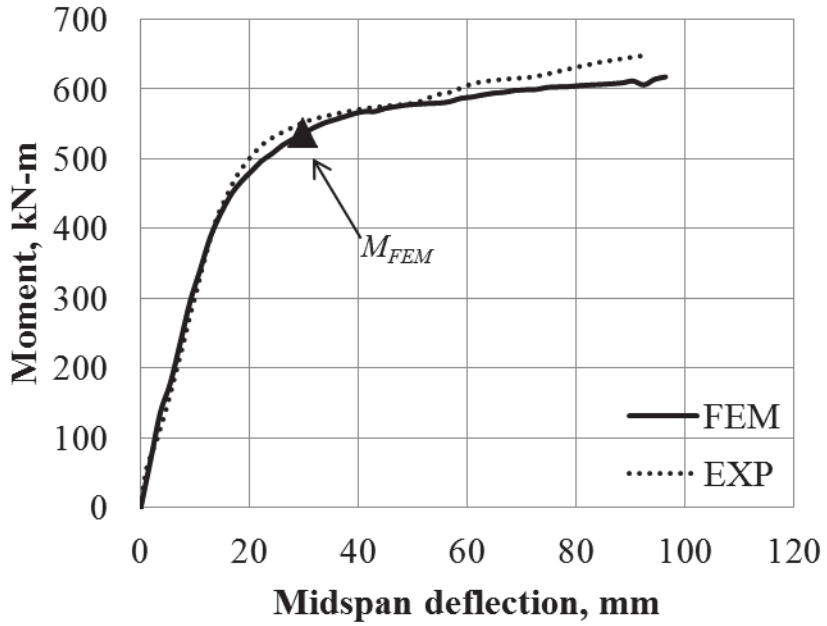

Figure 3.15 Comparisons of Experimental and Analytical Moment-Midspan Deflection Response for Specimen TPB005

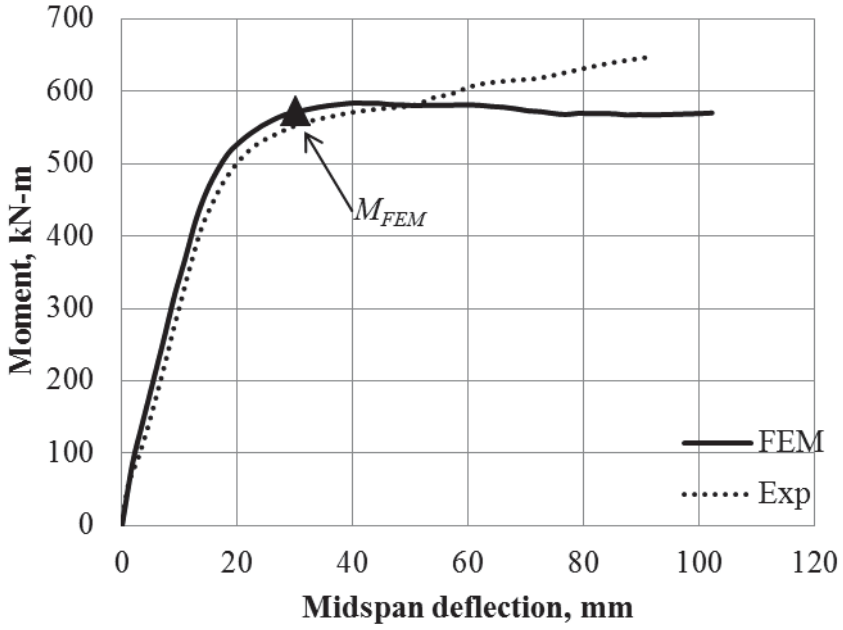

Figure 3.16 Comparisons of Experimental and Analytical Moment-Midspan Deflection Response for Specimen TPB006

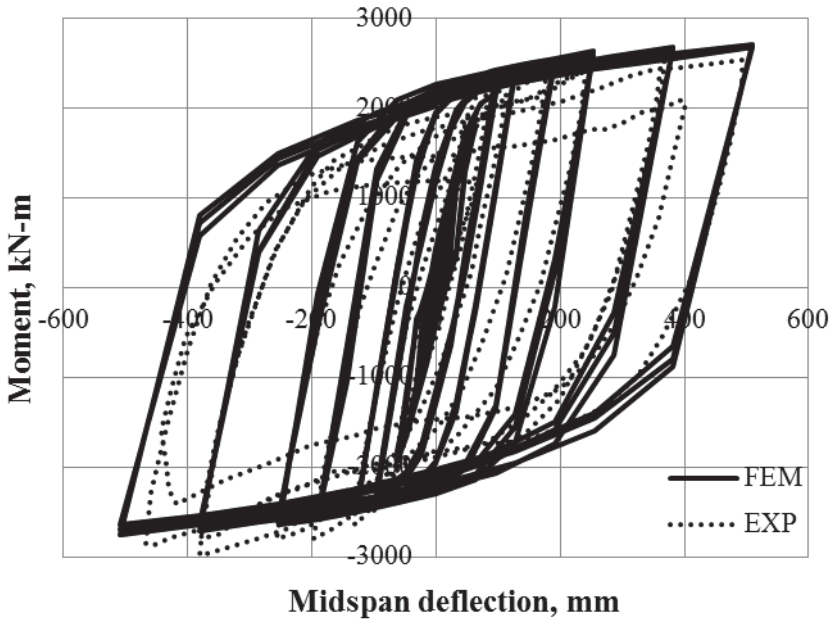

Figure 3.17 Comparisons of Experimental and Analytical Moment-Midspan Deflection Response for Specimen 1

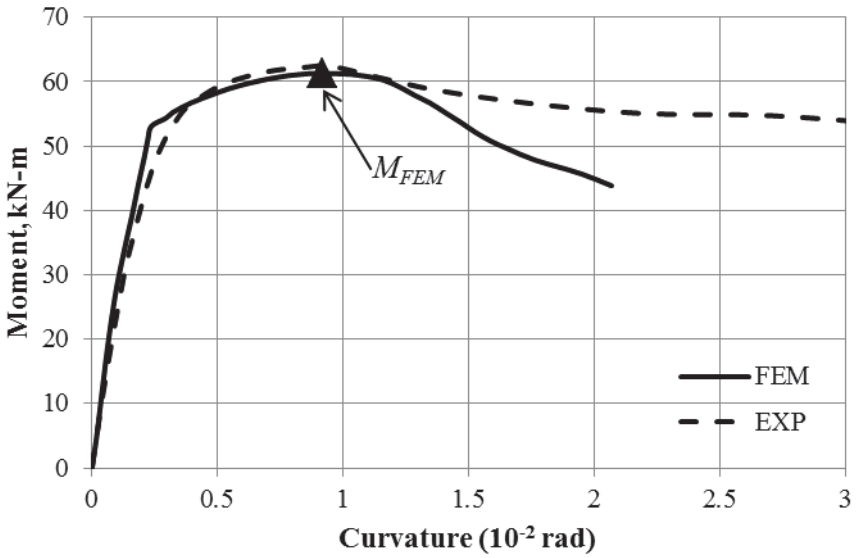

Figure 3.18 Comparisons of Experimental and Analytical Moment-Curvature Response for BRA4-2-5-02

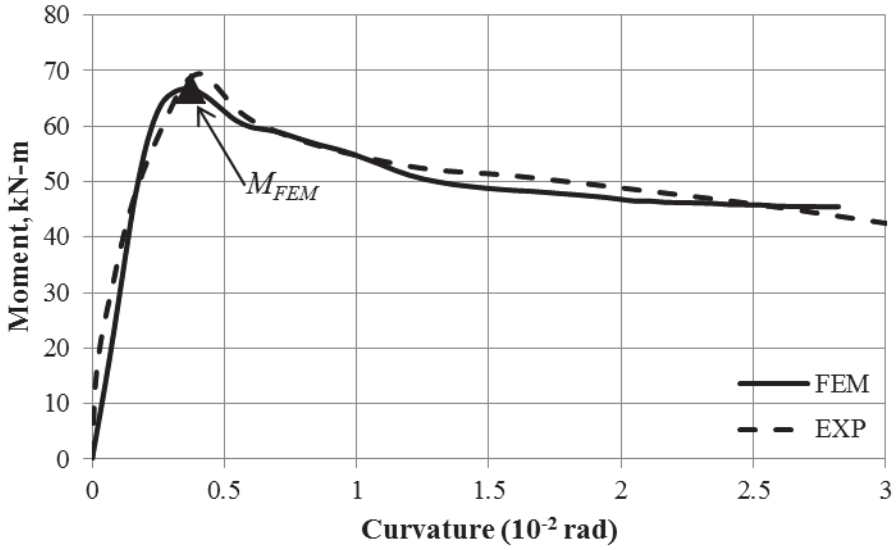

Figure 3.19 Comparisons of Experimental and Analytical Moment-Curvature Response for BRA4-2-5-04

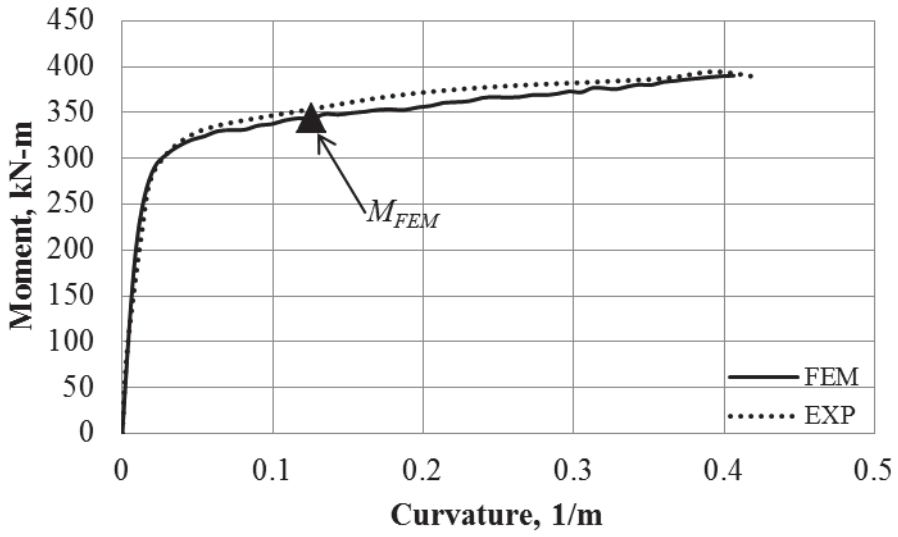

Figure 3.20 Comparisons of Experimental and Analytical Moment-Curvature Response for C06F3M

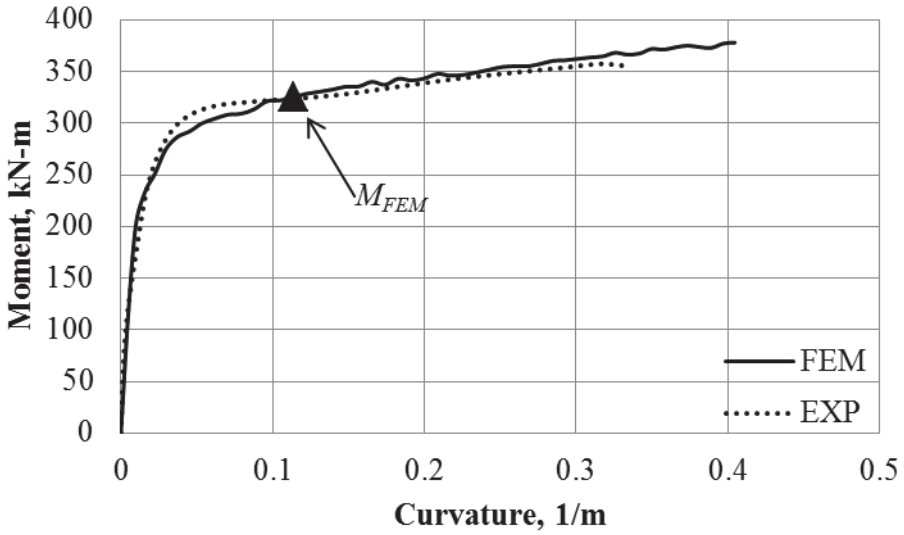

Figure 3.21 Comparisons of Experimental and Analytical Moment-Curvature Response for C06F5M

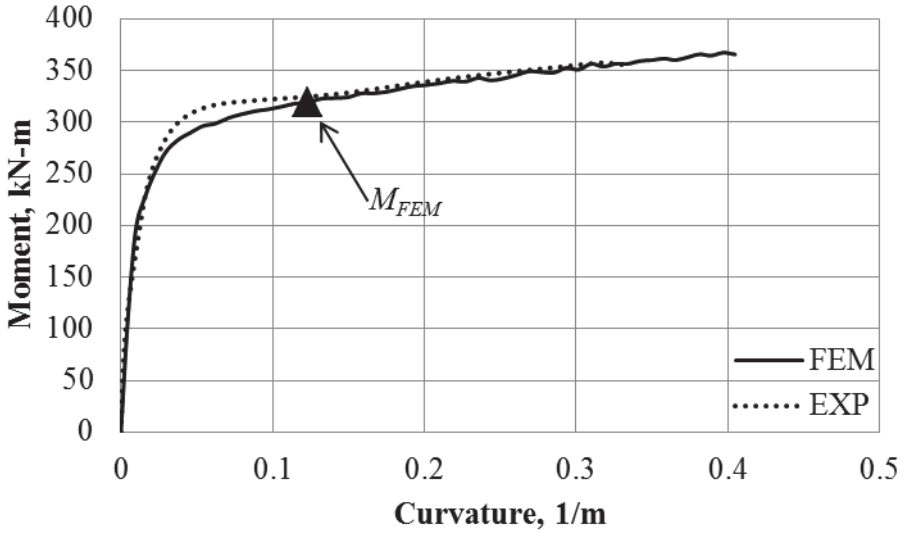

Figure 3.22 Comparisons of Experimental and Analytical Moment-Curvature Response for C06F5MA

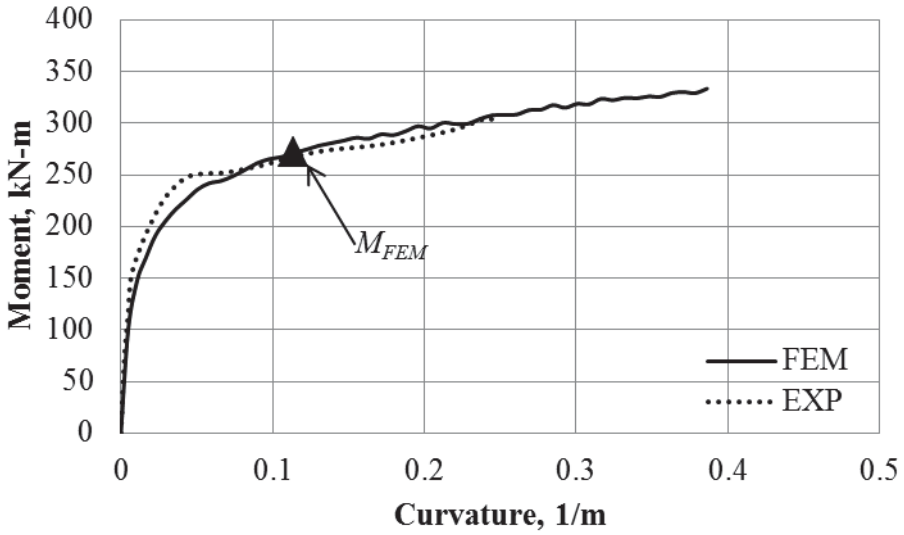

Figure 3.23 Comparisons of Experimental and Analytical Moment-Curvature Response for C06F7M

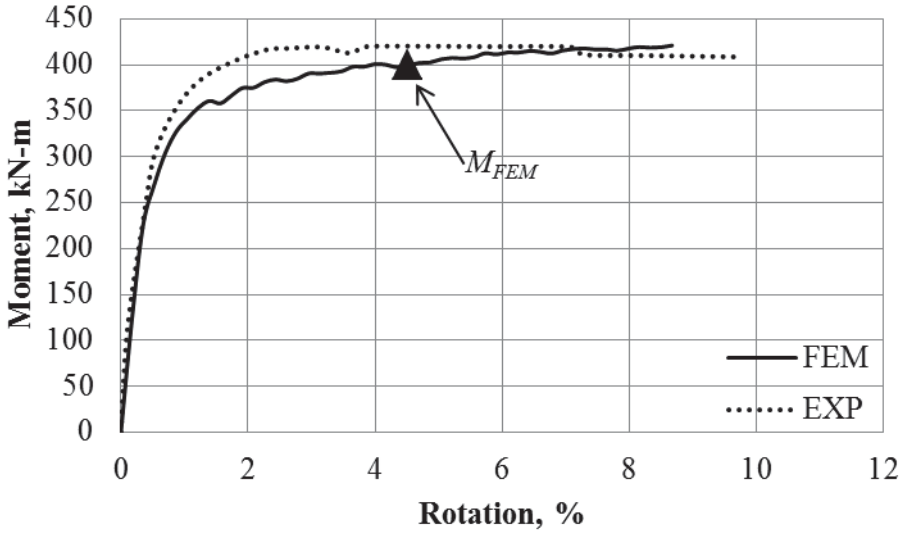

Figure 3.24 Comparisons of Experimental and Analytical Moment-Rotation Response for C06S5M

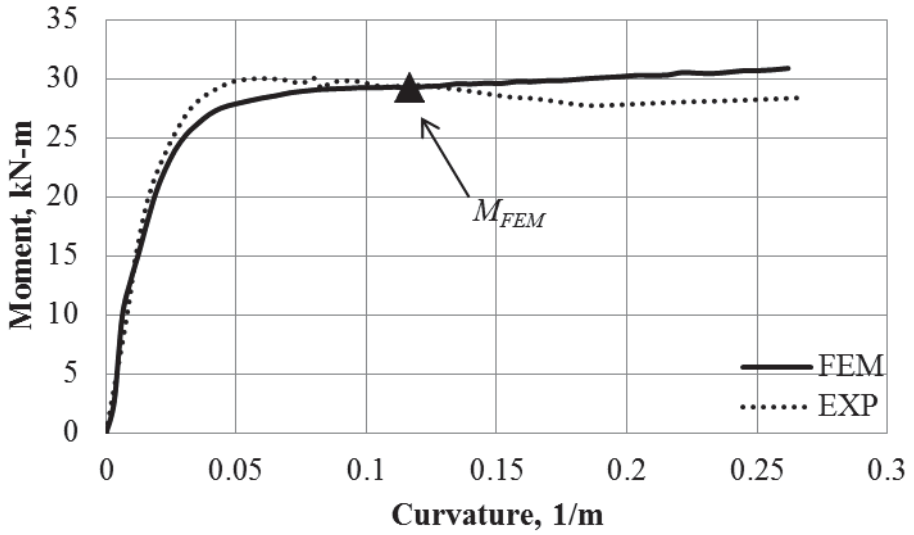

Figure 3.25 Comparisons of Experimental and Analytical Moment-Curvature Response for BP17

CHAPTER 4. DESIGN OF NONCOMPACT AND SLENDER CFT COLUMNS

The tube slenderness ratio (width-to-thickness b/t or D/t ratio, λ) governs local buckling behavior of CFT members, and the confinement of the concrete infill. CFT members are categorized as compact, noncompact or slender depending on the governing slenderness ratio of the steel tube wall. The AISC 360-10 specifies the slenderness limits for classifying CFT members, and the provisions for calculating the strength of noncompact and slender CFT members subjected to different loading conditions. This chapter focuses on CFT columns. Details of the slenderness classifications are presented first, followed by the development of the AISC 360-10 design equations. The conservatism of these design equations is then evaluated by using them to predict the strength of: (i) CFT columns in the experimental database presented in Section 2.1, and (ii) CFT columns from additional FEM models that address the gaps in the experimental database. The development and evaluation of the AISC 360-10 provisions for noncompact and slender CFT beams is presented in Chapter 5.

4.1 Slenderness Limits for CFT Columns

4.1.1 Slenderness Limits for Rectangular CFT Columns

The behavior of CFT members is fundamentally different from that of hollow structural shape (HSS) members. The concrete infill changes the buckling mode of the steel tube by preventing it from buckling inward, as shown in Figure 4.1. The post-buckling behavior

of CFT members is more ductile than that of equivalent HSS members due to the larger wavelength of the buckling mode, spreading of plastic deformation, and slight increase in the moment of inertia of the steel tube due to the outward buckling shape.

The elastic local buckling behavior of the steel tube walls of rectangular CFT members subjected to axial compression was investigated analytically by Bradford et al. (1998) using the Rayleigh-Ritz method. The assumed local buckling mode shape accounted for the effects of concrete infill, i.e., no inward displacements as shown in Figure 4.1.

The resulting equation for local buckling is shown in Equation 4.1. In this equation, F_{cr} is the critical stress for elastic local buckling, E_s is the modulus of elasticity of the steel tube, ν is the Poisson's ratio for steel, and *b/t* is the governing (larger) slenderness ratio. The parameter *k* accounts for the local buckling mode. Bradford et al. (1998) showed that *k* was equal to 10.6 for the mode shape shown in Figure 4.1. The critical buckling stress F_{cr} simplifies to $9.6E_s/(b/t)^2$ after substituting the value of *k* equal to 10.6, and Poisson's ratio for steel equal to 0.3. The critical buckling stress (F_{cr}) reaches the yield stress (F_y) when the slenderness ratio (*b/t*) becomes equal to $3.10\sqrt{E_s/F_y}$.

$$F_{cr} = \frac{k\pi^2 E_s}{12\left(1-\nu^2\right)\left(\frac{b}{t}\right)^2} \tag{4.1}$$

$$P_{no} = P_p = A_s F_y + 0.85 f'_c A_c \tag{4.2}$$

Previous researchers (Leon et al., 2007) used the existing experimental database to show that when the tube wall slenderness (*b/t*) ratio is less than or equal to $2.26\sqrt{E_s/F_y}$, the axial compressive strength of rectangular CFT stub (short) columns could be calculated conservatively using Equation 4.2, which consists of superposition of the yield strength of the steel tube and compressive strength of the concrete infill. Therefore, this slenderness ratio, $2.26\sqrt{E_s/F_y}$, was established as the compactness limit (λ_p) for rectangular CFT columns in AISC 360-10.

In AISC 360-10, the noncompactness limit (λ_r) was established conservatively as $3.00\sqrt{E_s/F_y}$ based on Bradford et al. (1998) as explained above. Rectangular CFT columns with steel tube slenderness ratio greater than λ_p ($2.26\sqrt{E_s/F_y}$) but less than or equal to λ_r ($3.00\sqrt{E_s/F_y}$) are classified as noncompact. Rectangular CFT columns with steel tube slenderness ratio greater than λ_r ($3.00\sqrt{E_s/F_y}$) are classified as slender. AISC 360-10 also specifies the maximum permitted tube slenderness ratio (λ_{limit}) as $5.00\sqrt{E_s/F_y}$ for rectangular CFT columns.

4.1.2 Slenderness Limits for Circular CFT Columns

Previous research by Schilling (1965), Winter (1968) and Ziemian (2010) showed that the slenderness limit for demarcating the elastic local buckling of circular hollow steel tube is $\lambda_r = 0.11E_s/F_y$. For axially loaded CFT members, the existence of concrete infill

prevents the steel tube wall from buckling inward, as shown in Figure 4.2. Analytical research by Bradford et al. (2002) showed that the critical local buckling stress for filled circular tube is $\sqrt{3}$ (or 1.73) times that for an unfilled circular tube. It is therefore reasonable to define the noncompact/slender limit λ_r for circular CFT 1.73 times that for circular HSS tubes as $\lambda_r = 0.19E_s/F_y$.

$$P_{no} = P_p = A_s F_y + 0.95 f'_c A_c \tag{4.3}$$

Previous researchers (Leon et al., 2007) used the experimental database to show that when the slenderness ratio (D/t) is less than or equal to $0.15E_s/F_y$, the axial compressive strength of circular CFT column could be calculated conservatively using Equation 4.3. Therefore this slenderness ratio, $0.15E_s/F_y$, was established as the limit λ_p for compact/noncompact sections. Circular CFT columns with slenderness ratio less than or equal to λ_p are classified as compact. Circular CFT columns with slenderness ratio greater than λ_p ($0.15E_s/F_y$) but less than or equal to λ_r ($0.19E_s/F_y$) are categorized as noncompact. Circular CFT columns with slenderness ratio greater than λ_r ($0.19E_s/F_y$) are classified as slender. AISC 360-10 also specifies the maximum permitted tube slenderness ratio (λ_{limit}) as $0.31E_s/F_y$ for circular CFT columns.

4.2 Development of the AISC 360-10 Design Provisions for CFT Columns

CFT columns with slenderness ratios less than or equal to λ_p are classified as compact sections. CFT columns with compact sections can develop yielding before local buckling and provide adequate confinement of the concrete infill to develop its compressive

strength up to $0.85f'_c$ for rectangular CFT columns and $0.95f'_c$ for circular CFT columns. The axial compressive strength of rectangular and circular stub (short) CFT columns with compact sections is calculated using Equation 4.2 and Equation 4.3, respectively. In these two equations, A_s and A_c is the cross-sectional area of the steel tube and concrete infill, respectively. The axial compressive strength is calculated as the superposition of the yield strength of steel tube and compressive strength of concrete infill.

CFT columns with steel tube slenderness ratio greater than λ_p but less than or equal to λ_r are classified as noncompact. Noncompact CFT sections can reach the yield stress (F_y) of the steel tube with local buckling, but cannot provide adequate confinement to the concrete infill to reach its full compressive strength. The concrete infill has significant volumetric dilation after the compressive stress exceeds $0.70f'_c$ (Chen and Han, 2007). The volumetric dilation of concrete infill cannot be confined adequately by the noncompact steel tube undergoing local buckling. As a result, the compressive strength of both rectangular and circular CFT stub (short) columns with noncompact sections (slenderness ratio = λ_r) is limited to that calculated using Equation 4.4.

$$P_{no} = P_y = A_s F_y + 0.70 f'_c A_c \tag{4.4}$$

CFT columns with tube slenderness ratio greater than λ_r are classified as slender. Slender CFT sections undergo elastic local buckling, and the critical buckling stress F_{cr} can be calculated conservatively using: (i) Equation 4.6 for rectangular CFT columns, which is based on Bradford et al. (1998) as explained above, and (ii) Equation 4.7 for circular CFT

columns, which is based on Varma and Zhang (2009). The post-local buckling behavior of the steel tube is constrained by the concrete infill while it is in the elastic range. However, the concrete has significant volumetric dilation after the compressive stress exceeds $0.70f'_c$. This volumetric dilation exacerbates the post local buckling deterioration of the steel tube, which cannot confine it as well. Therefore, the compressive strength of both rectangular and circular CFT stub (short) columns with slender sections (slenderness ratio > λ_r) is limited to that calculated using Equation 4.5.

$$P_{no} = P_{cr} = A_s F_{cr} + 0.70 f'_c A_c \tag{4.5}$$

$$F_{cr} = \frac{9E_s}{(b/t)^2} \tag{4.6}$$

$$F_{cr} = \frac{0.72F_y}{\left(\left(D/t\right)\frac{F_y}{E_s}\right)^{0.2}} \tag{4.7}$$

The use of slender CFTs with tube slenderness ratio greater than λ_{limit} is not permitted by AISC 360-10 due to: (i) the lack of experimental data in the database for CFTs with such slender steel tubes, and (ii) potential issues with deflections and stresses in the slender tube walls due to concrete casting pressures and other fabrication processes. Table 1.1 summarizes the slenderness limits (λ_p and λ_r), and the maximum permitted slenderness ratio (λ_{limit}) for steel tubes of CFTs under axial compression.

Figure 4.3 shows a graphical representation of the nominal axial compressive strength (P_{no}) of CFT stub (short) columns as a function of the tube slenderness ratio, λ (λ = *b/t*

for rectangular CFTs and $\lambda = D/t$ for circular CFTs). As shown, the nominal axial compressive strength (P_{no}) of noncompact CFT stub (short) columns (with slenderness ratio λ between λ_p and λ_r) can be calculated using Equation 4.8, which has a quadratic variation between P_p (Equation 4.2 or Equation 4.3) and P_y (Equation 4.4) with the tube slenderness ratio (λ). This nonlinear variation accounts for the fact that steel tubes need to be closer to the compactness limit λ_p to confine the concrete, and increase its compressive strength contribution from $0.70f'_c$ at P_y to: (i) $0.85f'_c$ at P_p for rectangular CFT columns, or (ii) $0.95f'_c$ at P_p for circular CFT columns. A linear variation between P_y and P_p was considered initially, but found to be unconservative for some of the experimental results.

$$P_{no} = P_p - \frac{P_p - P_y}{(\lambda_r - \lambda_p)^2}(\lambda - \lambda_p)^2 \tag{4.8}$$

Equations 4.9 - 4.13 are specified by AISC 360-10 to calculate the nominal compressive strength of CFT columns accounting for length effects, member slenderness, and residual stresses. In these Equations: P_n is the nominal compressive strength including length effects; P_{no} is the nominal compressive strength of the section accounting for tube slenderness using Equations 4.2, 4.3, 4.4, 4.5 or 4.8; P_e is the elastic (Euler) buckling load of the column calculated using the column length (KL) and effective flexural stiffness (EI_{eff}). The effective flexural stiffness includes contributions of both steel and concrete, and accounts for the effects of concrete cracking.

When $\frac{P_{no}}{P_e} \leq 2.25$ $\qquad P_n = P_{no}[0.658^{\frac{P_{no}}{P_e}}]$ (4.9)

When $\frac{P_{no}}{P_e} > 2.25$ $$P_n = 0.877 P_e \quad (4.10)$$

Where, $$P_e = \pi^2 \frac{EI_{eff}}{(KL)^2} \quad (4.11)$$

$$EI_{eff} = E_s I_s + C_3 E_c I_c \quad (4.12)$$

$$C_3 = 0.6 + [\frac{A_s}{A_c + A_s}] \leq 0.9 \quad (4.13)$$

4.3 Evaluation of the AISC 360-10 Design Provisions for CFT Columns

As discussed in Section 2.1, forty-one rectangular and forty-seven circular noncompact and slender CFT column tests were included into the experimental database. These tests provided essential information to evaluate the conservatism of the AISC 360-10 design equations. However, there were some gaps in the experimental database, as identified in Section 2.4. It was important to address these gaps in the database to further evaluate and confirm the conservatism of the design equations.

The finite element analysis approach was selected to address these gaps in the experimental database, and to develop additional data points to confirm the design equations. Prototype specimens were selected from the experimental database for CFT columns. Additional analyses were performed using the benchmarked models (presented in Chapter 3) of these prototype CFT specimens by varying the tube slenderness ratios. The slenderness ratios were varied by changing the tube wall thickness.

The prototype selected for rectangular CFT columns was Specimen E10 by Lin (1988). Thirteen additional analyses were conducted for different tube slenderness ratios in the range of noncompact and slender (λ_{coeff} = 2.26 to 5.0) CFT columns. The prototype selected for circular CFT columns was Specimen D2 by Lin (1988). Seven additional analyses were conducted for different tube slenderness ratios (λ_{coeff} = 0.23 to 0.31). Details of the CFT columns in these additional analyses are shown in Table 4.1 (for rectangular columns) and Table 4.2 (for circular columns).

Figure 4.4 shows the comparisons of the nominal and experimental strengths for all rectangular CFT columns in the database. The nominal strength (P_n) was calculated using the AISC 360-10 design provisions. In Figure 4.4, the ordinate represents the ratio of experimental-to-calculated axial load strength (P_{exp}/P_n), while the abscissa represents the normalized slenderness coefficient (λ_{coeff}). These comparisons indicate that: (1) the AISC 360-10 design provisions estimate the axial strength of rectangular CFT columns conservatively except for the data set labeled as "high strength steel". This data set includes eleven data points with steel yield stress greater than 525 MPa, which are not permitted by the AISC specifications and identified in Table 2.1 with superscript a. (2) The design equations are more conservative for rectangular CFT columns with slender sections, as compared to rectangular CFT columns with noncompact sections. And, (3) the degree of conservatism of the design equations varies even for specimens with the same slenderness ratio. For example, the P_{exp}/P_n ratio changes from 1.20 to 1.74 for columns with slenderness coefficient of 3.66.

These observations are explained using CFT behavior mechanics. As discussed previously, the interaction between the steel tube wall and concrete infill produces hoop stresses in the steel tube wall and confinement of the concrete infill (Varma et al., 2002b). These hoop stresses reduce the axial stress required to cause yielding of the steel, and the confinement of the concrete infill also increases its compressive strength. For rectangular CFT members, concrete confinement occurs at the corners and in the core. AISC 360-10 does not account for these effects directly while calculating the axial strength of CFT columns. As a result, the strength contribution of steel tube may be overestimated, while the strength contribution of the concrete infill may be slightly underestimated. The degree of conservatism of the design equations is therefore dependent on the tube wall slenderness ratio and the relative material strengths of steel and concrete, i.e., the relative strength ratio ξ defined in Equation 6.3. The tube slenderness ratio governs the local buckling of the steel tube, the relative area of the steel tube and concrete infill A_s/A_c, and the hoop stresses induced in the steel tube. As a result, the AISC 360-10 design equations are more conservative for specimens with larger slenderness ratio. For the same slenderness ratio, high strength steel tubes are more susceptible to local buckling than conventional strength steel tubes (Varma et al., 2002a, 2002b). As a result, AISC 360-10 design equations are not recommended for specimens with high strength steel. The variation in P_{exp}/P_n ratios in Figure 4.3 for the same normalized slenderness ratio is due to the fact that the design equation does not account for the relative strength ratio ξ, which governs the relative areas and strengths of the steel tube and concrete infill.

Since AISC 360-10 specifies the steel yield stress in CFT columns to be less than 525 MPa, the eleven points with steel yield stress greater than 525 MPa were eliminated from the comparisons. The resulting updated comparisons are shown in Figure 4.5 (data points labeled as "EXP"). In Figure 4.5, the data points from the additional finite element analyses to address the gaps in the experimental database were included also (data points labeled as "Additional FEM"). These comparisons verify that the AISC 360-10 design provisions conservatively estimate the nominal strength of noncompact and slender rectangular CFT columns.

As for circular CFT columns, Figure 4.6 shows the comparisons of the nominal axial strength calculated using the AISC 360-10 design provisions with: (i) the experimental strength (data points labeled as "EXP") for all circular CFT columns in the database, and (ii) the analysis results from additional finite element analyses (data points labeled as "Additional FEM"). The ordinate represents the ratio of: (i) experimental-to-calculated value (P_{exp}/P_n) for data points labeled as "EXP", or (ii) analytical-to-calculated value (P_{FEM}/P_n) for data points labeled as "Additional FEM"; while the abscissa represents the normalized slenderness coefficient (λ_{coeff}).

These comparisons indicate that: (i) the design equations calculate the axial strength conservatively for all circular CFT columns. (ii) The design equations are more conservative for circular CFT columns with slender sections, as compared to circular CFT columns with noncompact sections. And, (iii) the degree of conservatism of the design equations varies even for specimens with the same slenderness ratio. For example,

the P_{exp}/P_n ratio changes from 1.27 to 1.45 for columns with slenderness coefficient (λ_{coeff}) of 0.18. These observations are due to the CFT behavior mechanics as explained previously for rectangular CFT columns.

Table 4.1 Details of the Rectangular CFT Columns in the Additional FEM Analyses

NO.	L (mm)	B (mm)	t_f (mm)	b/t_f	λ_{coeff}	F_y (MPa)	f'_c (MPa)	P_n (kN-m)	P_{FEM} (kN-m)	P_{FEM}/P_n
1	800.0	151.6	2.20	66.9	2.35	247.3	22.5	627.1	905.2	1.44
2	800.0	151.3	2.05	71.8	2.52	247.3	22.5	615.0	898.9	1.46
3	800.0	151	1.90	77.5	2.72	247.3	22.5	603.9	888.0	1.47
4	800.0	150.6	1.70	86.6	3.04	247.3	22.5	593.6	875.7	1.48
5	800.0	150.4	1.60	92.0	3.24	247.3	22.5	584.1	866.9	1.48
6	800.0	150.2	1.50	98.1	3.45	247.3	22.5	575.4	860.7	1.50
7	800.0	150	1.40	105.1	3.70	247.3	22.5	950.2	1058.8	1.11
8	800.0	149.8	1.30	113.2	3.98	247.3	22.5	915.0	1015.1	1.11
9	800.0	149.7	1.25	117.8	4.14	247.3	22.5	863.1	1006.8	1.17
10	800.0	149.6	1.20	122.7	4.31	247.3	22.5	759.6	961.8	1.27
11	800.0	149.5	1.15	128.0	4.50	247.3	22.5	720.0	949.5	1.32
12	800.0	149.4	1.10	133.8	4.71	247.3	22.5	684.9	915.8	1.34
13	800.0	149.3	1.05	140.2	4.93	247.3	22.5	654.2	913.8	1.40

Table 4.2 Details of the Circular CFT Columns in the Additional FEM Analyses

NO.	L (mm)	D (mm)	t (mm)	D/t	λ_{coeff}	F_y (MPa)	f'_c (MPa)	P_n (kN-m)	P_{FEM} (kN-m)	P_{FEM}/P_n
1	800.0	150.2	0.80	185.8	0.23	248.2	22.5	366.8	513.5	1.40
2	800.0	150.2	0.78	191.7	0.24	248.2	22.5	363.9	509.5	1.40
3	800.0	150.1	0.75	198.1	0.25	248.2	22.5	361.0	505.8	1.40
4	800.0	150.1	0.73	205.0	0.25	248.2	22.5	358.1	501.7	1.40
5	800.0	149.9	0.65	228.6	0.28	248.2	22.5	349.3	489.6	1.40
6	800.0	149.9	0.63	237.8	0.30	248.2	22.5	331.5	485.6	1.46
7	800.0	149.8	0.60	247.7	0.31	248.2	22.5	328.4	481.5	1.47

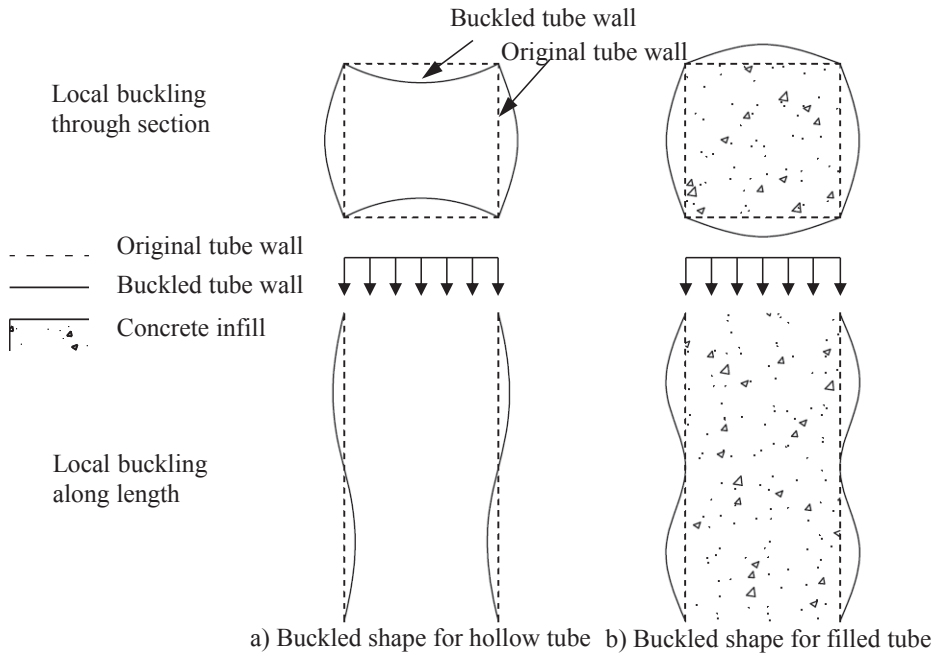

Figure 4.1 Effects of Concrete Infill on Local Buckling of Rectangular Hollow Tubes

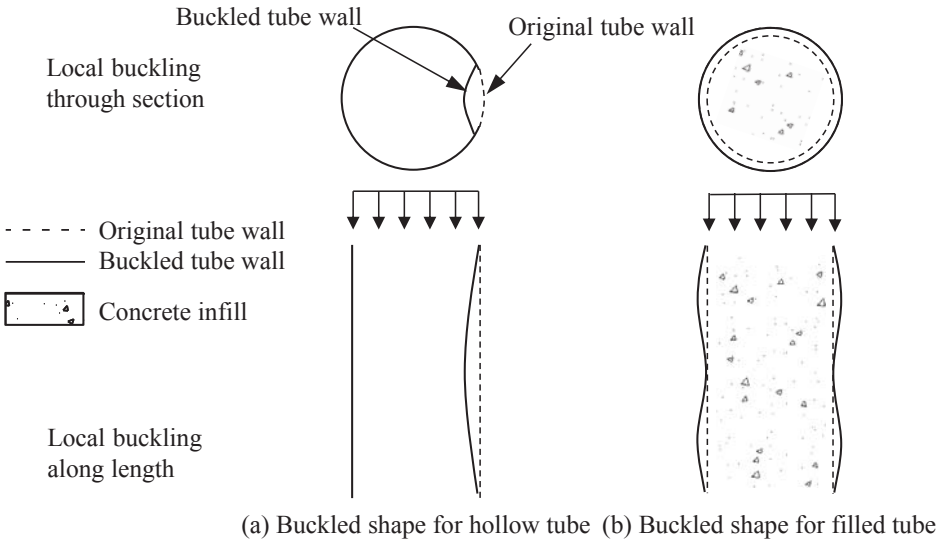

Figure 4.2 Effects of Concrete Infill on Local Buckling of Circular Hollow Tubes

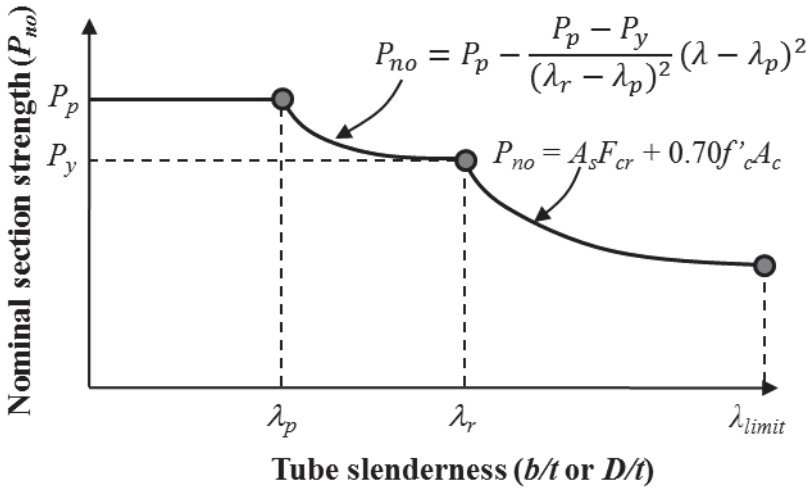

Figure 4.3 Variation of the Nominal Axial Compressive Strength With Respect to the Tube Slenderness Ratio

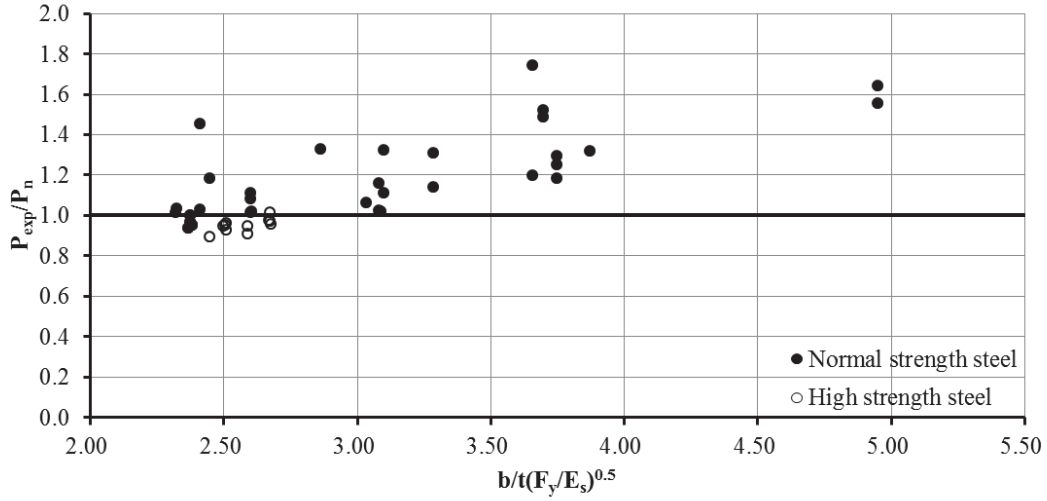

Figure 4.4 Comparisons of the Nominal and Experimental Strengths tor Noncompact and Slender Rectangular CFT Columns

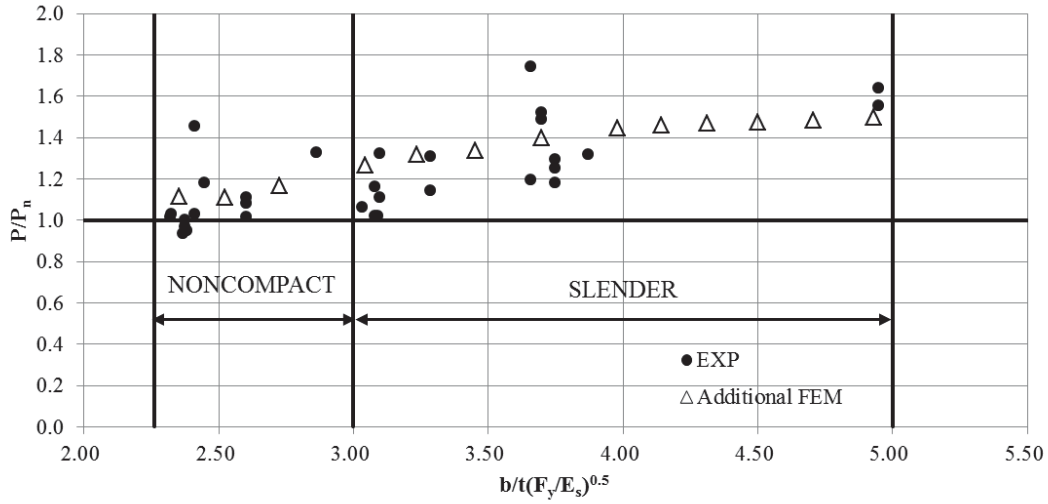

Figure 4.5 Comparisons of the Nominal Strengths with Experimental and Analytical Strengths for Noncompact and Slender Rectangular CFT Columns (with Normal Strength Steel Only)

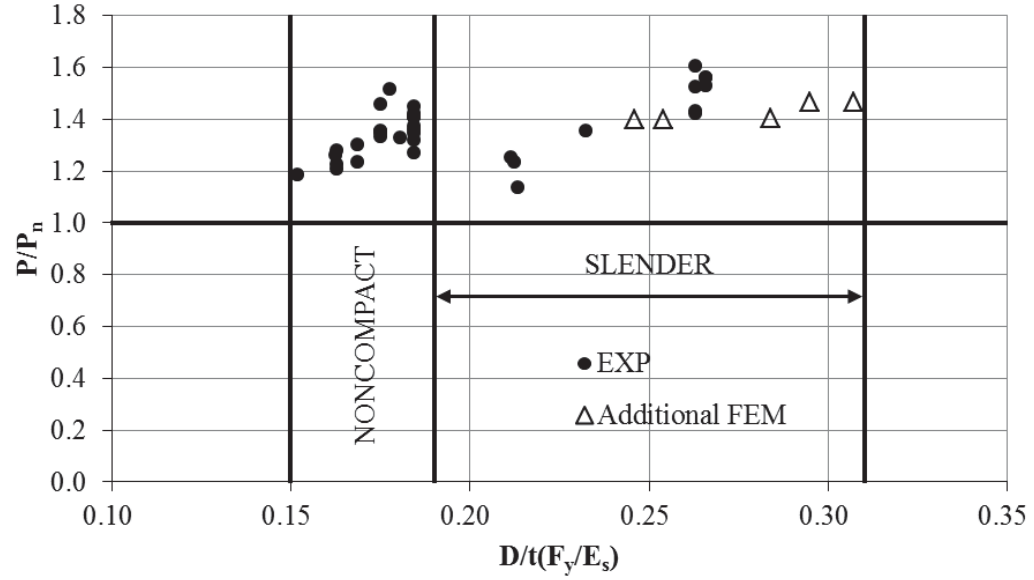

Figure 4.6 Comparisons of the Nominal Strengths with Experimental and Analytical Strengths for Noncompact and Slender Circular CFT Columns

CHAPTER 5. DESIGN OF NONCOMPACT AND SLENDER CFT BEAMS

The AISC 360-10 specifies the slenderness limits and design provisions to calculate the strength of CFT beams. However, it does not provide design equations to calculate the flexural strength of CFT members explicitly. In this chapter, details of the slenderness classifications are presented first, followed by the development of: (i) closed form solution for design equations to calculate the flexural strength of rectangular CFT beams, and (ii) fiber analysis procedures for calculating the flexural strength of circular CFT beams. Both (i) and (ii) are developed using the design provisions specified in the AISC 360-10. These design provisions are evaluated by using them to predict the strength of: (i) CFT beams in the experimental database presented in Section 2.1, and (ii) CFT beams from additional FEM models that address the gaps in the experimental database.

5.1 Slenderness Limits for CFT beams

5.1.1 Slenderness Limits for Rectangular CFT beams

For rectangular CFT members subjected to flexure, the tube slenderness ratios are defined by the *b/t* ratio of the flanges and the *h/t* ratio of the webs. Table 1.1 includes the slenderness limits (λ_p and λ_r), and the maximum permitted slenderness ratio (λ_{limit}) for the flanges and webs of rectangular CFT members subjected to flexure. The local buckling of the steel tube flanges in compression due to flexure is similar to the local

buckling of the tube walls of CFTs in compression. Therefore, as shown in Table 1.1, the slenderness limits for the flanges of rectangular CFT beams are identical to the limits for steel tube walls of CFTs subjected to axial compression.

However, the webs are subjected to stress gradients over their depth (H). The portion of the web subjected to compressive stresses (above the neutral axis) is much shorter than the depth (H), and subjected to linearly varying compressive strains. As shown in Ziemian (2010), the elastic local buckling equation for this case is the same as Equation 4.1 but with the k factor equal to 23.9. Therefore, the compactness limit (λ_p) for the webs was set conservatively as $3.00\sqrt{E_s/F_y}$, and the noncompactness limit (λ_r) was set as $5.70\sqrt{E_s/F_y}$. The maximum slenderness ratio for the webs was also set as $5.70\sqrt{E_s/F_y}$ due to the lack of experimental data and other concerns such as concrete placement.

Thus, rectangular CFT members subjected to flexure may have: (i) compact, noncompact, or slender flanges, but (ii) only compact or noncompact webs. However, CFT members with slender flanges and noncompact webs are still classified as slender for flexure.

5.1.2 Slenderness Limits for Circular CFT beams

AISC 360-10 defines the slenderness limits λ_p and λ_r for circular HSS tubes subjected to flexure as $\lambda_p = 0.07E_s/F_y$ and $\lambda_r = 0.31E_s/F_y$. These values are based on Sherman (1976), Sherman and Tanavde (1984), and Ziemian (2010). The behavior of CFT members in

flexure is fundamentally different from that of the HSS members. However, there is no theoretical development for the slenderness limits for circular filled sections in flexure. The local buckling behavior of CFT beams is much better than that of HSS beams since the limit states of local ovalization and denting (inwards) are not applicable. Therefore, the λ_p for filled sections was increased conservatively only by 25% over hollow circular tubes, i.e., $\lambda_p = 0.09E_s/F_y$. The λ_r was taken conservatively the same as that for HSS sections. Due to the lack of experimental data and concrete placement concerns for thinner filled HSS cross sections, the maximum permitted limit was conservatively taken as the same as λ_r.

Circular CFT beams with tube slenderness ratio less than or equal to λ_p are classified as compact, while circular CFT beams with tube slenderness ratio greater than λ_p but less than or equal to λ_r are classified as noncompact. Circular CFT beams with tube slenderness greater than λ_r are classified as slender. However, no slender section is allowed for circular CFTs in flexure in the AISC 360-10.

5.2 Development of the AISC 360-10 Design Provisions for CFT Beams

The flexural resistance of CFT members is provided by the concrete infill in compression, and the steel tube in both tension and compression. The concrete contribution in tension is ignored due to cracking, which occurs at early stages of loading. The concrete infill prevents the steel tube from buckling inwards, and the outward buckling mode slightly increases the section moment of inertia and spreads plastic deformations providing more stable post-buckling behavior for CFT beams than HSS tubular beams. The steel tube

provides nominal confinement to the concrete infill, but this confinement varies significantly with tube slenderness. Experimental results indicate that the shear span-to-depth (*a/H* or *a/D*) ratio and slip between the steel tube and concrete infill do not have a significant influence on the moment capacity (Lu and Kennedy, 1994; Han et al., 2006). The flexural behavior and capacity of CFT members is governed by yielding of the steel tube in tension, followed by local buckling in compression and concrete crushing failure depending on the material strength and tube slenderness ratio.

Previous researchers (Leon et al., 2007) showed that the nominal flexural strength (M_n) of CFT members with compact sections could be calculated as the plastic moment (M_p) strength of the cross-section using the plastic stress distribution method in AISC 360-10 Section I2.2a. This method assumes rigid-plastic behavior for the steel and concrete materials with the steel yield stress equal to F_y in compression and tension, and the concrete strength equal to $0.85f'_c$ (for rectangular CFT members) or $0.95f'_c$ (for circular CFT members) in compression and zero in tension. This indicates that the compact steel tube can develop its yield stress F_y in compression and tension, and confine the concrete infill adequately to develop its compressive strength of $0.85f'_c$ (for rectangular CFT members) or $0.95f'_c$ (for circular CFT members).

The flexural strength of noncompact and slender CFT members in flexure is calculated using the principles of the lower bound theorem of plasticity. The lower bound capacity of the composite section is calculated using admissible stress blocks that satisfy the equations of equilibrium, boundary conditions, and do not violate the yield criterion

(stress > yield stress F_y) anywhere. For noncompact CFT members in flexure, this method assumes: (i) elastic-plastic behavior for the steel in tension and elastic behavior in compression up to the yield stress F_y, (ii) elastic behavior for concrete in compression up to $0.70f'_c$ and no contribution in tension. For slender CFT members in flexure, this method assumes: (i) elastic behavior for the steel in tension up to the yield stress F_y and elastic behavior in compression up to the local buckling stress F_{cr}, and (ii) elastic behavior for concrete in compression up to $0.70f'_c$ and no contribution in tension. The local buckling critical stress (F_{cr}) is given by Equation 4.6 (for rectangular CFT members) and Equation 4.7 (for circular CFT members).

Due to their slenderness, noncompact and slender steel tubes can neither sustain the compressive stress after local buckling, nor adequately confine the concrete to reach it compressive strength ($0.85f'_c$ for rectangular CFT members, or $0.95f'_c$ for circular CFT members). As mentioned earlier, concrete has significant volumetric dilation after the compressive stress exceeds $0.70f'_c$, which exacerbates the post local buckling deterioration of the noncompact steel tube and its inability to confine the concrete. Therefore, the concrete is assumed to have maximum compressive stress equal to $0.70f'_c$.

5.2.1 Development of the AISC 360-10 Design Provisions for Rectangular CFT Beams

Figure 5.1 shows the stress blocks for calculating the plastic moment (M_p) for rectangular CFT beams. The distance of the neutral axis (a_p) from the compression face is calculated by establishing axial force equilibrium over the cross-section, and the plastic moment strength (M_p) is calculated using this neutral axis location. The resulting Equation 5.1 and

Equation 5.2 for a_p and M_p are given below. The variables in these equations are defined graphically in Figure 5.1. In these equations H, b, t_w, t_f are the tube depth, width, web thickness, and flange thickness respectively:

$$a_p = \frac{2F_y H t_w + 0.85f'_c b t_f}{4F_y t_w + 0.85f'_c b} \tag{5.1}$$

$$\text{If } \lambda \le \lambda_p, \qquad M_n = M_p = F_y b t_f (a_p - \frac{t_f}{2}) + F_y b t_f (H - a_p - \frac{t_f}{2}) + F_y a_p 2t_w (\frac{a_p}{2}) + F_y (H - a_p) 2t_w (\frac{H - a_p}{2}) + 0.85f'_c (a_p - t_f) b (\frac{a_p - t_f}{2}) \tag{5.2}$$

Figure 5.2 shows the admissible stress blocks for estimating the lower-bound capacity of noncompact sections with tube slenderness equal to λ_r. As shown, the steel tube is assumed to undergo yielding and plasticification in tension and reach the yield stress F_y in compression. The concrete is assumed to have maximum compressive stress equal to $0.70f'_c$. The distance of the neutral axis (a_y) from the compression face is calculated by establishing axial force equilibrium over the cross-section, and the moment capacity ($M_n = M_y$) is calculated using this neutral axis location as shown in Equation 5.3 and Equation 5.4.

$$a_p = \frac{2F_y H t_w + 0.85f'_c b t_f}{4F_y t_w + 0.85f'_c b} \tag{5.1}$$

$$a_y = \frac{2F_y H t_w + 0.35f'_c b t_f}{4F_y t_w + 0.35f'_c b} \tag{5.3}$$

$$\text{If } \lambda = \lambda_r, \qquad M_n = M_y = F_y b t_f (a_y - \frac{t_f}{2}) + F_y b t_f (H - a_y - \frac{t_f}{2}) + 0.5F_y a_y 2t_w (\frac{2a_y}{3}) + 0.5F_y a_y 2t_w (\frac{2a_y}{3}) + F_y (H - 2a_y) 2t_w (\frac{d}{2}) + 0.35f'_c (a_y - t_f) b [\frac{2(a_y - t_f)}{3}] \tag{5.4}$$

$$\lambda_p < \lambda \le \lambda_r \qquad M_n = M_p - \frac{(M_p - M_y)}{(\lambda_r - \lambda_p)}(\lambda - \lambda_p) \tag{5.5}$$

For noncompact sections with tube slenderness (λ) greater than λ_p but less than or equal to λ_r, the nominal moment capacity (M_n) can be calculated using Equation 5.5, which assumes a linear variation between the moment capacities (M_p corresponding to λ_p, and M_y corresponding to λ_r) and tube slenderness. This linear interpolation is adequate because the concrete contribution to the flexural strength is generally smaller than that of the steel tube. This is in contrast to the axial load strength of noncompact CFT columns where the concrete contribution can be much higher than that of the steel tube, and a nonlinear variation was recommended in Equation 4.8.

The admissible stress blocks for estimating the lower bound capacity of slender sections with tube slenderness greater than or equal to λ_r are shown in Figure 5.3. As shown, the steel tube is assumed to just reach the yield stress F_y in tension and the critical buckling stress F_{cr} in compression. The concrete is assumed to have maximum compressive stress equal to $0.70f'_c$. The distance of the neutral axis (a_{cr}) from the compression face is calculated by establishing axial force equilibrium over the cross-section, and the moment capacity ($M_n = M_{cr}$) is calculated using this neutral axis location as shown in Equation 5.6 and Equation 5.7.

$$a_{cr} = \frac{F_y H t_w + (0.35f'_c + F_y - F_{cr})bt_f}{t_w(F_{cr} + F_y) + 0.35f'_c b} \tag{5.6}$$

$$\text{If } \lambda \geq \lambda_r, \qquad M_n = M_{cr} = F_{cr} b t_f (a_{cr} - \frac{t_f}{2}) + F_y b t_f (d - a_{cr} - \frac{t_f}{2}) + 0.5 F_{cr} a_{cr} 2 t_w (\frac{2a_{cr}}{3}) + 0.5 F_y (d - a_{cr}) 2 t_w [\frac{2(d - a_{cr})}{3}] + 0.35 f'_c (a_{cr} - t_f) b [\frac{2(a_{cr} - t_f)}{3}] \tag{5.7}$$

Finally, Figure 5.4 shows the variation of the nominal flexural strength for rectangular CFT beams with respect to the tube slenderness. For rectangular CFT members with compact sections, the nominal flexural strength (M_n) is equal to the plastic moment strength (M_p) calculated using Equation 5.2. For rectangular CFT members with noncompact sections, the nominal flexural strength (M_n) is calculated using: (i) M_p calculated using Equation 5.2, (ii) M_y calculated using Equation 5.4, and (iii) linear interpolation using Equation 5.5. For rectangular CFT members with slender sections, the nominal flexural strength (M_n) is equal to the M_{cr} calculated using Equation 5.7.

5.2.2 Development of the AISC 360-10 Design Provisions for Circular CFT Beams

Figure 5.5 shows the stress blocks for calculating the plastic moment (M_p) for circular CFT beams. The distance of the neutral axis (a_p) from the compression face is calculated by establishing axial force equilibrium over the cross-section, and the plastic moment capacity (M_p) is calculated using this neutral axis location.

Figure 5.6 shows the admissible stress blocks for estimating the lower bound capacity (M_y) of noncompact sections with tube slenderness equal to λ_r. As shown, the steel tube is assumed to undergo yielding and plasticification in tension and reach the yield stress F_y in compression. The concrete is assumed to have maximum compressive stress equal to

$0.70f'_c$. The distance of the neutral axis (a_y) from the compression face is calculated by establishing axial force equilibrium over the cross-section, and the moment capacity ($M_n = M_y$) is calculated using this neutral axis location.

Due to the circular shape of the cross-section, closed form solutions for a_p and a_y could not be obtained directly (i.e., iterations were required). A fiber analysis approach was implemented to calculate the flexural capacity associated with the stress blocks in Figure 5.5 and Figure 5.6. Bruneau et al. (2011) indicate that the flexural capacity of circular CFT members can be calculated using: (i) free-body diagrams with an iterative solution approach, or (ii) approximate geometry methods with closed form solutions. The fiber analysis procedure in this section extends the approach (i) to noncompact circular CFT sections. As shown in Figure 5.5 and Figure 5.6, the circular cross-section is discretized into horizontal fibers. The algorithm used to compute the position of the neutral axis (i.e., a_p or a_y) and the corresponding flexural capacity (M_p or M_y) is summarized in Figure 5.7. As shown in Figure 5.7, the algorithm consists of iterating for the neutral axis location, while establishing force equilibrium over the cross-section within selected tolerance level using the fiber discretization and stress blocks Figure 5.5 and Figure 5.6 as appropriate.

Finally, Figure 5.8 shows the variation of the nominal flexural strength (M_n) for circular CFT beams (obtained using the fiber analysis procedure) with respect to the tube slenderness. For circular CFT members with compact sections, the nominal flexural strength (M_n) is equal to the plastic moment strength (M_p). For circular members with noncompact sections, the nominal flexural strength (M_n) is calculated using: (i) M_p

calculated using the fiber analysis procedure and the stress blocks shown in Figure 5.5, (ii) M_y calculated using the fiber analysis procedure and the stress blocks shown in Figure 5.6, and (iii) linear interpolation using Equation 5.5. The use of circular CFT beams with slender sections is not permitted by the AISC 360-10.

5.3 Evaluation of the AISC 360-10 Design Provisions for CFT Beams

As discussed in Section 2.1, four rectangular and 42 circular noncompact and slender CFT beams tests were included into the experimental database. These tests provided essential information to evaluate the conservatism of the AISC 360-10 design provisions. However, there were some gaps in the experimental database, as identified in Section 2.4. It was important to address these gaps in the database to further evaluate and confirm the conservatism of the design equations.

The finite element analysis approach was selected to address these gaps in the experimental database, and to develop additional data points to confirm the design equations. Prototype specimens were selected from the experimental database for CFT beams. Additional analyses were performed using the benchmarked models (presented in Chapter 3) of these prototype CFT specimens by varying the tube slenderness ratios. The slenderness ratios were varied by changing the tube wall thickness.

The prototype selected for rectangular CFT beams was Specimen S-150-2.0 tested by Jiang (2013). Fourteen additional analyses were conducted for different tube slenderness ratios in the range of noncompact and slender (λ_{coeff} = 2.26 to 5.0) CFT beams. Figure 3.8

showed the comparisons of the experimental and analytical results for this specimen. The prototype selected for circular CFT beams was Specimen TPB005 by Wheeler and Bridge (2004). Ten additional analyses were conducted for different tube slenderness ratios (λ_{coeff} =0.18 to 0.31). Figure 3.14 showed the comparisons of the experimental and analytical results for this specimen. Details of the CFT beams in these additional analyses are shown in Table 5.1 (for rectangular beams) and Table 5.2 (for circular beams).

Figure 5.9 and Figure 5.10 show the comparisons of the c nominal and experimental strengths for all rectangular and circular CFT beams in the database. The nominal strength (M_n) was calculated using the AISC 360-10 design provisions. The ordinate represents: (i) the ratio of experimental-to-calculated flexural strength (M_{exp}/M_n) for data points labeled as "EXP", or (ii) analytical-to-calculated flexural strength (M_{FEM}/M_n) for data points labeled as "Additional FEM"; while the abscissa represents the normalized slenderness coefficient (λ_{coeff}). These comparisons indicate that the AISC 360-10 design provisions estimate the flexural strength conservatively for noncompact and slender CFT members.

Table 5.1 Details of the Rectangular CFT Beams in the Additional FEM Analyses

NO.	L (mm)	B (mm)	t_f (mm)	b/t_f	λ_{coeff}	F_y (MPa)	f'_c (MPa)	M_n (kN-m)	M_{FEM} (kN-m)	M_{FEM}/M_n
1	2000.0	151.6	2.80	52.1	2.27	397.0	56.0	44.1	43.9	0.99
2	2000.0	151.3	2.65	55.1	2.40	397.0	56.0	41.3	41.5	1.00
3	2000.0	151.0	2.50	58.4	2.55	397.0	56.0	38.5	39.1	1.02
4	2000.0	150.7	2.35	62.1	2.71	397.0	56.0	35.7	37.1	1.04
5	2000.0	150.4	2.20	66.4	2.89	397.0	56.0	33.0	34.7	1.05
6	2000.0	150.2	2.10	69.5	3.03	397.0	56.0	28.0	30.7	1.10
7	2000.0	150.0	2.00	73.0	3.18	397.0	56.0	26.3	28.9	1.10
8	2000.0	149.8	1.90	76.8	3.35	397.0	56.0	24.7	27.4	1.11
9	2000.0	149.6	1.80	81.1	3.54	397.0	56.0	23.2	26.4	1.14
10	2000.0	149.4	1.70	85.9	3.74	397.0	56.0	21.7	24.8	1.14
11	2000.0	149.2	1.60	91.3	3.98	397.0	56.0	20.3	23.5	1.16
12	2000.0	149.0	1.50	97.3	4.24	397.0	56.0	18.9	22.2	1.17
13	2000.0	148.8	1.40	104.3	4.55	397.0	56.0	17.6	20.7	1.18
14	2000.0	148.6	1.28	114.1	4.97	397.0	56.0	16.0	18.1	1.13

Table 5.2 Details of the Circular CFT Beams in the Additional FEM Analyses

NO.	L (mm)	D (mm)	t (mm)	D/t	λ_{coeff}	F_y (MPa)	f'_c (MPa)	M_n (kN-m)	M_{FEM} (kN-m)	M_{FEM}/M_n
1	3800.0	406.0	4.00	101.5	0.18	350.0	40.0	274.1	304.2	1.11
2	3800.0	406.0	3.80	106.8	0.19	350.0	40.0	260.5	288.0	1.11
3	3800.0	406.0	3.60	112.8	0.20	350.0	40.0	246.9	275.5	1.12
4	3800.0	406.0	3.40	119.4	0.21	350.0	40.0	233.2	263.3	1.13
5	3800.0	406.0	3.20	126.9	0.22	350.0	40.0	219.5	246.5	1.12
6	3800.0	406.0	3.00	135.3	0.24	350.0	40.0	205.7	236.0	1.15
7	3800.0	406.0	2.80	145.0	0.25	350.0	40.0	191.9	218.7	1.14
8	3800.0	406.0	2.60	156.2	0.27	350.0	40.0	177.9	208.2	1.17
9	3800.0	406.0	2.40	169.2	0.30	350.0	40.0	164.0	190.7	1.16
10	3800.0	406.0	2.30	176.5	0.31	350.0	40.0	157.0	184.7	1.18

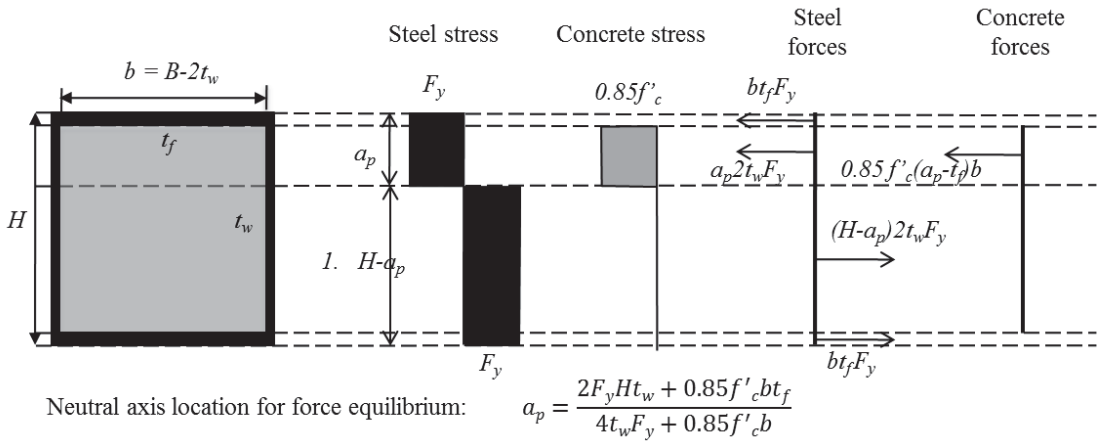

Figure 5.1 Stress blocks for calculating the plastic moment (M_p) for rectangular CFT beams

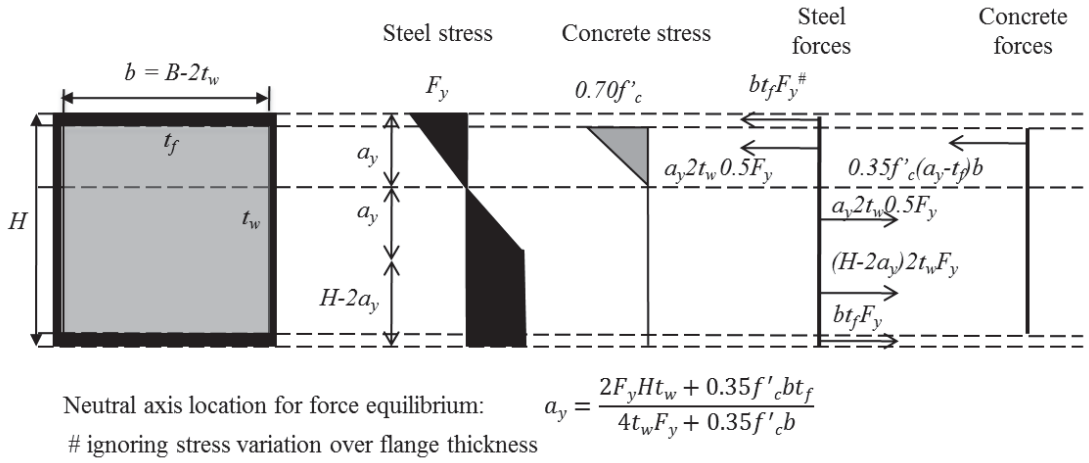

Figure 5.2 Stress Blocks for Calculating the M_y For Rectangular CFT Beams

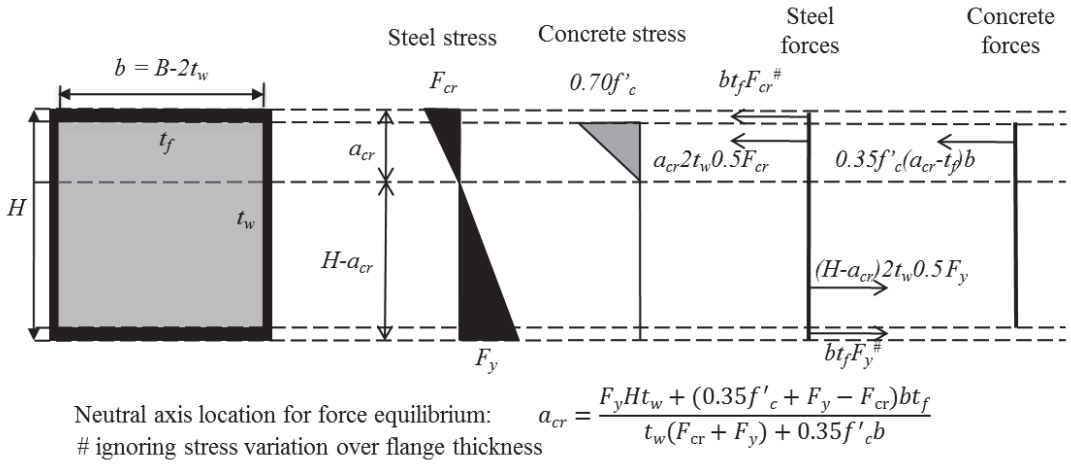

Figure 5.3 Stress blocks for Calculating the M_{cr} for Rectangular CFT Beams

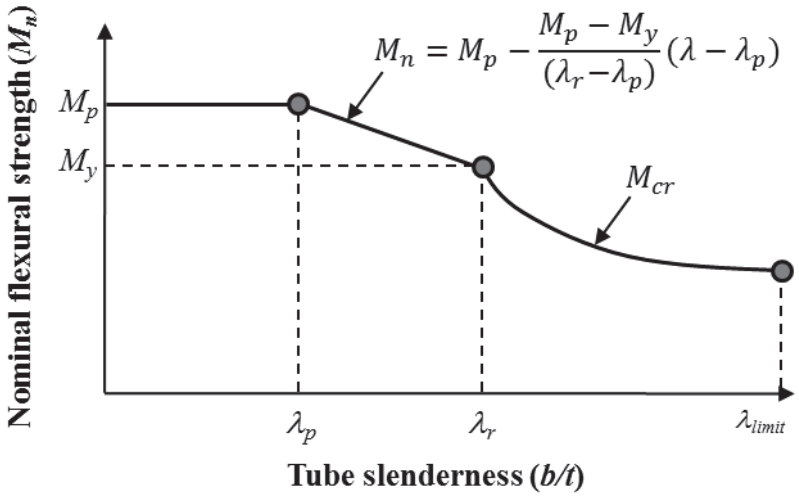

Figure 5.4 Variation of Moment Capacity with Respect to Tube Slenderness Ratio

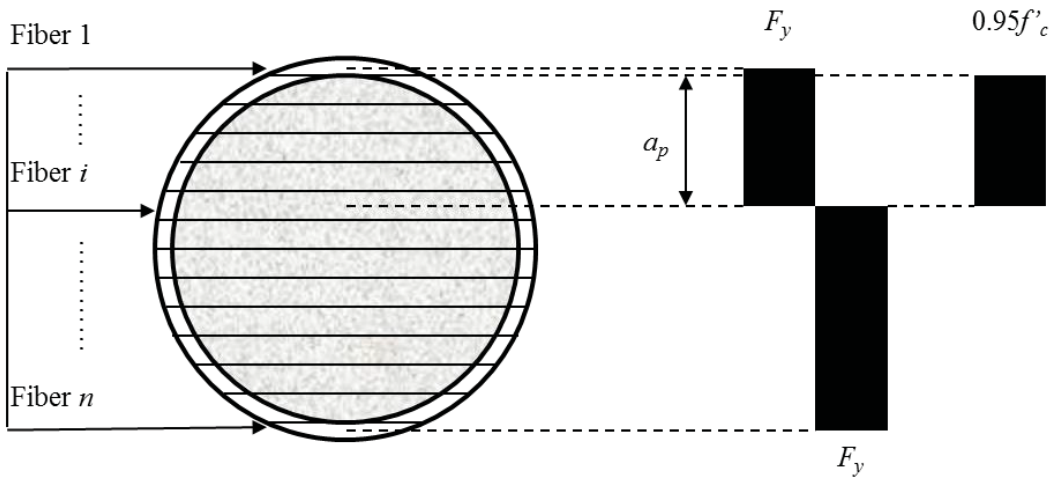

Figure 5.5 Stress blocks for Calculating the Plastic Moment (M_p) for Circular CFT Beams

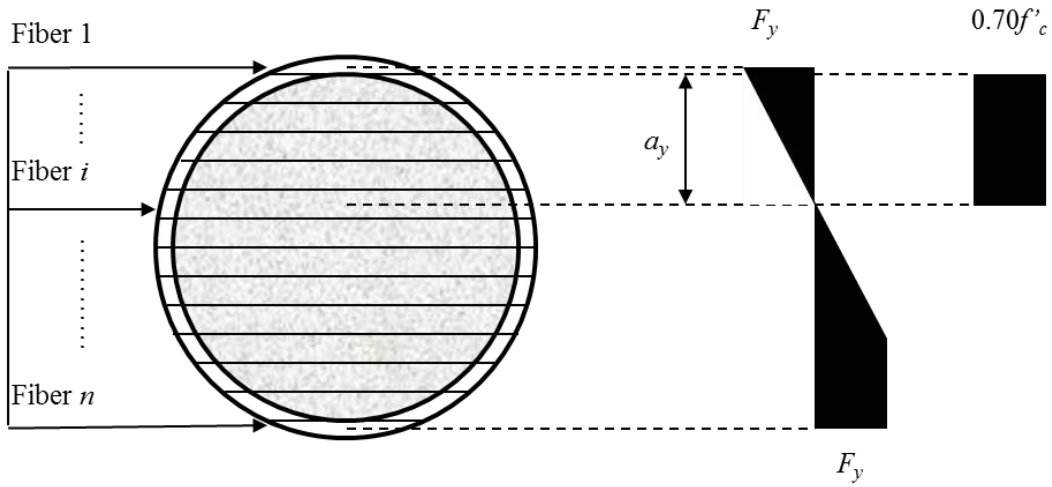

Figure 5.6 Stress blocks for Calculating the M_y for Circular CFT Beams

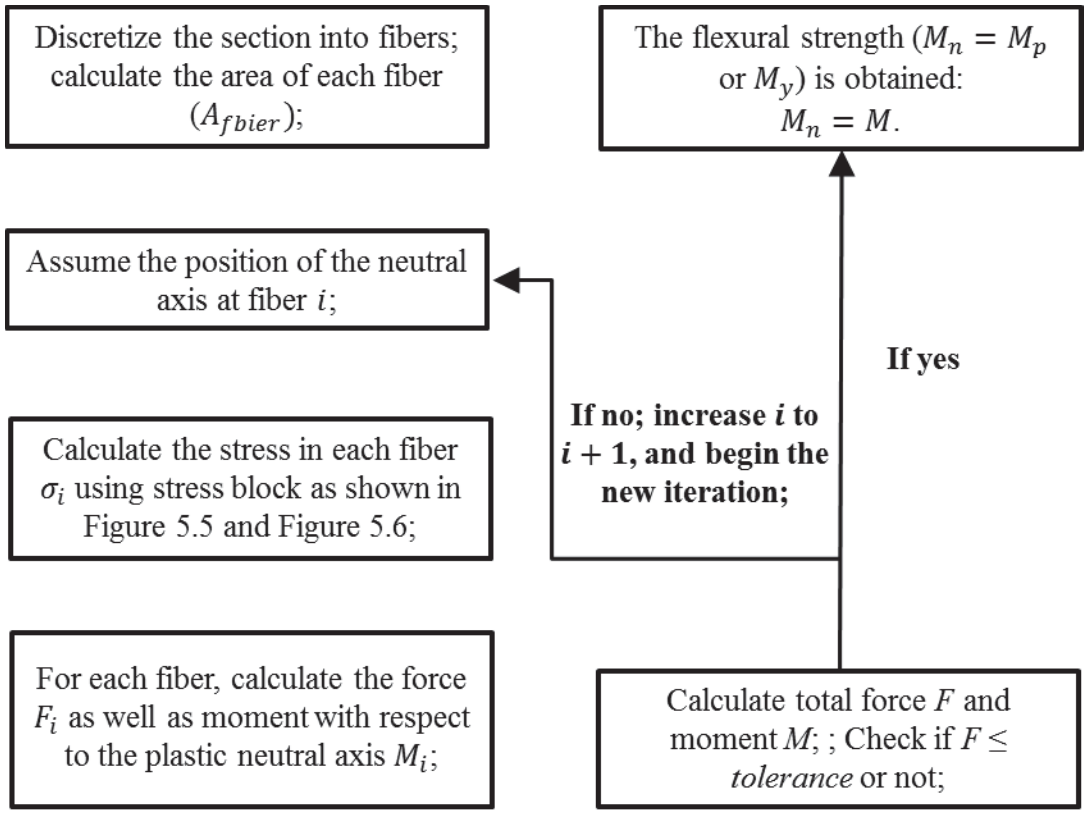

Figure 5.7 Algorithms to Calculate the Flexural Strength M_n of Circular CFT Beams

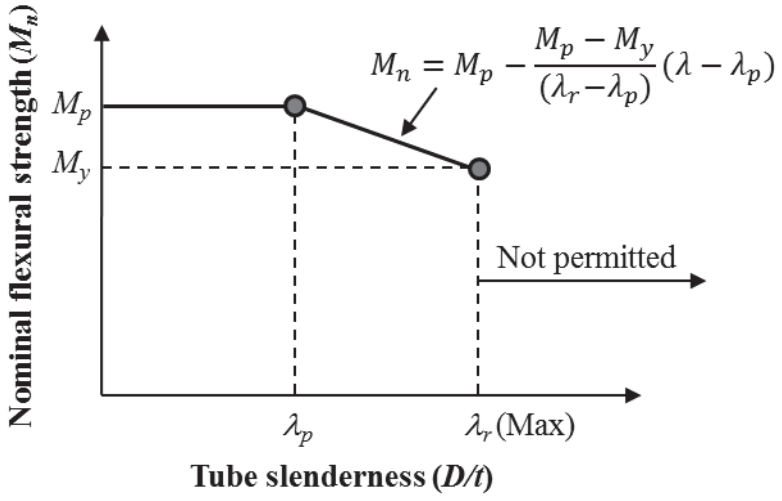

Figure 5.8 Variation of Moment Capacity with Respect to Tube Slenderness Ratio

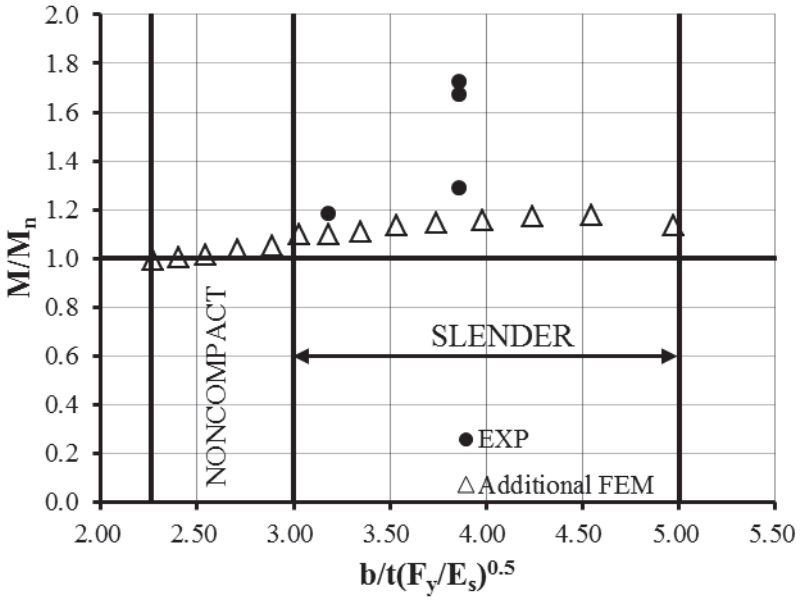

Figure 5.9 Comparisons of the Nominal Strengths with Experimental and Analytical Strengths for Noncompact and Slender Rectangular CFT Beams

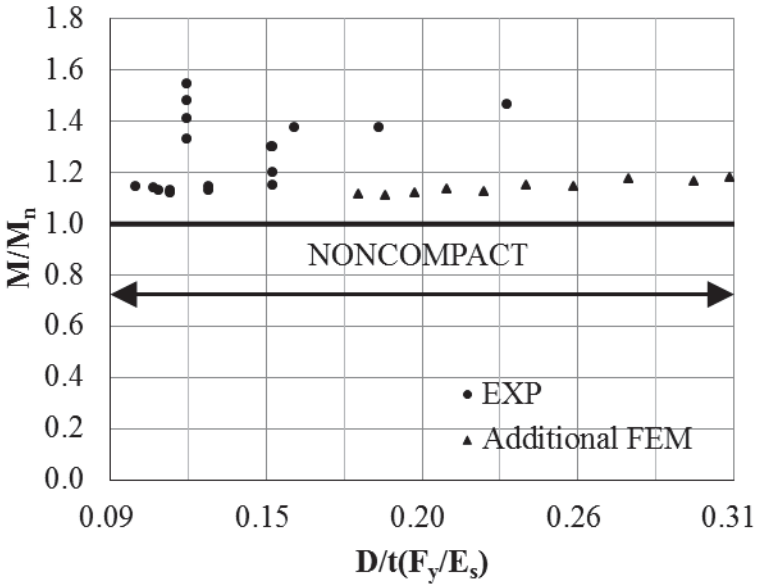

Figure 5.10 Comparisons of the Nominal Strengths with Experimental and Analytical Strengths for Noncompact and Slender Circular CFT Beams

CHAPTER 6. DESIGN OF NONCOMPACT AND SLENDER CFT BEAM-COLUMNS

The AISC 360-10 specifies the slenderness limits and design equations for calculating the strength of CFT beams-columns. This chapter presents details of the slenderness classifications are presented first, followed by the evaluation of the design equations for noncompact and slender CFT beam-columns. The evaluations show that the current AISC 360-10 bilinear P-M interaction curve is over-conservative. Comprehensive parametric are conducted studies using the benchmarked FEM models to investigate the effects of several parameters on the behavior and strength of CFT beam-columns. These parameters include the tube slenderness ratio (width-to-thickness b/t or D/t ratio, λ), material strength ratio (F_y/f'_c), axial load ratio (α), and member length-to-depth ratio (L/B or L/D). An updated P-M interaction curve is then developed and proposed using the results from the parametric studies. This chapter presents the primary results and findings from these parametric studies. It includes verification of the updated P-M interaction equations with results from the finite element analyses and experimental tests. The chapter only includes representative results and typical comparisons. Comprehensive results from the parametric studies are included in the companion analytical database (Lai, 2014).

6.1 Slenderness Classifications

CFT members are categorized as compact, noncompact or slender depending on the slenderness ratio (width-to-thickness *b/t* or *D/t* ratio, λ) of the steel tube wall. AISC 360-10 specifies the slenderness limits for demarcating the CFT members, as shown in Table 1.1. The developments of these slenderness limits were discussed previously in Chapter 4 and Chapter 5.

For a CFT column or beam, if the governing tube slenderness ratio is less than or equal to λ_p, the member is classified as compact; if the governing tube slenderness ratio is greater than λ_p but less than or equal to λ_r, the member is classified as noncompact; if the governing tube slenderness ratio is greater than λ_r, the member is classified as slender. The tube slenderness ratio is also limited to a maximum permitted value λ_{limit} due to: (i) the lack of experimental data for CFTs with such slender steel tubes, and (ii) potential issues with deflections and stresses in the slender tube walls due to concrete casting pressures and other fabrication processes.

For a CFT beam-column, if the governing tube slenderness ratio is less than or equal to λ_p for columns or beams (whichever is smaller), the member is classified as compact; if the governing tube slenderness ratio is greater than λ_p but less than or equal to λ_r for columns or beams (whichever is smaller), the member is classified as noncompact; if the governing tube slenderness ratio is greater than λ_r for columns or beams (whichever is

smaller), the member is classified as slender. The maximum permitted tube slenderness ratio is also limited to λ_{limit} of columns or beams (whichever is smaller).

6.2 Development of the AISC 360-10 Design Provisions for CFT Beam-Columns

AISC 360-10 provides Equation 6.1 and Equation 6.2 for developing P-M interaction curves and designing noncompact and slender CFT beam-columns. These equations are based on those for steel members, and do not account for the expected beneficial effects of axial compression on the flexural strength, which is quite conservative. This conservatism was included to account for: (i) the potentially complex behavior of noncompact and slender CFT beam-columns, which are more susceptible to local buckling effects and lack of concrete confinement, and (ii) the lack of significant experimental data.

When $\frac{P_r}{\phi_c P_n} \geq 0.2$ $$\frac{P_r}{\phi_c P_n} + \frac{8}{9}\frac{M_r}{\phi_b M_n} \leq 1.0 \quad (6.1)$$

When $\frac{P_r}{\phi_c P_n} < 0.2$ $$\frac{P_r}{2\phi_c P_n} + \frac{M_r}{\phi_b M_n} \leq 1.0 \quad (6.2)$$

where P_r is the required axial compressive strength, M_r is the required flexural strength, P_n is the nominal axial strength, M_n is the nominal flexural strength, and ϕ_c is the resistance factor for compression ($\phi_c = 0.75$). The calculations of P_n and M_n for CFT members are specified in AISC 360-10 and presented previously in Chapter 4 and Chapter 5: (i) P_n are calculated using Equations 4.2 – 4.13, and (ii) M_n are calculated using Equations 5.1 – 5.7 and the fiber analysis procedure developed in Section 5.2.2.

Figure 6.1 shows an example of the resulting P-M interaction curve for designing noncompact and slender CFT beam-columns. As shown, only the axial strength (P_n) and flexural strength (M_n) are required to develop the P-M interaction curve.

6.3 Evaluation of the AISC 360-10 Design Equations for CFT Beam-Columns

As discussed in Section 2.1, 53 noncompact and slender CFT beam-column tests were included into the experimental database. These 53 test specimens included 17 rectangular specimens and 36 circular specimens. The AISC 360-10 beam-column design equations (Equation 6.1 and Equation 6.2) were used to predict the strength of these 53 test specimens. The comparisons are shown in Figure 6.2 for rectangular CFT beam-columns and Figure 6.3 for circular CFT beam-columns. In these figures, the ordinate represents the ratio of experimental-to-calculated axial strength (P_{exp}/P_n), while the abscissa represents the ratio of experimental-to-calculated flexural strength (M_{exp}/M_n).

These comparisons indicate that Equation 6.1 and Equation 6.2 are very conservative for most test specimens except for some rectangular CFT specimens with relative strength ratio (ξ, defined in Equation 6.3) greater than 1.0 (i.e., 1.27, 1.28, 2.4, 2.98 and 3.71). These rectangular specimens are composed of high strength steel (i.e., F_y >= 525 MPa, as specified in the AISC 360-10). This research is limited to CFT beam-columns with normal (conventional) strength steel, since AISC 360-10 does not permit the use of CFT members with high strength steel. Therefore these specimens are not included in the study presented hereafter.

For CFT members with normal strength steel, there are two primary reasons for the over-conservatism of the AISC 360-10 beam-column design equations. The first reason is that the AISC 360-10 is conservative in evaluating the axial (P_n) and flexural (M_n) strength of noncompact and slender CFT columns and beams, as shown previously in Figure 4.4, Figure 4.5, Figure 5.9 and Figure 5.10.

The second reason is that AISC 360-10 uses the bilinear interaction curve for bare steel members to design CFT beam-columns. Similar to steel beam-columns, the tube slenderness ratio (λ) governs the local buckling behavior of the steel tubes. Similar to steel or reinforced beam- columns, the behavior of CFT beam-columns is dependent on the axial load ratio and member length-to-depth ratio. The axial load ratio α (α=P/P_n, where P and P_n is the applied axial load and nominal axial strength of the CFT columns, respectively) governs the axial load-bending moment (P-M) interaction behavior of CFT beam-column. When the axial load ratio (α) is low, i.e., below the balance point on the P-M interaction curve, flexural behavior dominates the response. When α is high, i.e., above the balance point, axial compression behavior dominates the response. The member length-to-depth ratio determines the effects of secondary moments and imperfections.

However, the effects of tube slenderness ratio, axial load ratio and member length-to-depth ratio on the behavior of CFT beam-columns are different than that of bare steel beam-columns or reinforced concrete columns. The shape of the P-M interaction curve for CFT beam-columns is influenced by the relative strength ratio ξ defined in Equation

6.3, where A_s and A_c are the total areas of the steel tube and concrete infill, respectively. This relative strength ratio incorporates the effects of both tube slenderness ratio (λ) and material strength ratio (F_y/f'_c). CFT beam-columns with larger ξ values have P-M interaction curves that are more comparable to those for steel columns, while beam-columns with smaller ξ have P-M interaction curves that are more comparable to those for reinforced concrete columns, as shown in Figure 6.4.

$$\xi = \frac{A_s F_y}{A_c f_c^{'}} \tag{6.3}$$

Therefore, two tasks should be completed in order to improve the AISC 360-10 design equations for noncompact and slender CFT beam-columns. The first task is to improve the design equations for calculating P_n and M_n, and the second task is to improve the bilinear interaction diagram. This research focuses on the second task.

Attempts were made by several researchers to improve the interaction curve for CFT beam-columns, namely, Hajjar and Gourley (1996), Choi (2004) and Han and Yang (2007). However, the findings from those researchers are applicable to CFT members with compact sections. Their findings may not be applicable to noncompact and slender CFT members. In order to complete the second task, the effects of tube slenderness ratio, material strength ratio, axial load ratio, and member length-to-depth ratio on the behavior and strength of noncompact and slender CFT beam-columns, as well as the effect of the relative strength ratio and member length-to-depth ratio on the shape of the interaction curve should be investigated explicitly. This is accomplished in this research by

performing comprehensive parametric studies using the benchmarked FEM models presented in Chapter 3. Details of these parametric studies are presented in the following section.

6.4 Behavior of Noncompact and Slender CFT Beam-columns

As discussed in the previous section, the purposes of the parametric studies are to: (i) understand the fundamental behavior of noncompact and slender CFT beam-columns, including the effects of tube slenderness ratio, material strength ratio, axial load ratio, and member length-to-depth ratio, and (ii) propose P-M interaction equations for noncompact and slender CFT beam-columns, based on the understanding of how the shape of the P-M interaction curve is influenced by the relative strength ratio and member length-to-depth ratio. This section focuses on understanding the fundamental behavior of noncompact and slender CFT beam-columns. Only repetitive results and findings from the parametric studies are presented in this chapter. Comprehensive results from the parametric studies are included in the companion analytical database (Lai, 2014).

Prototype specimens were selected from the experimental database. Parametric studies were performed using the benchmarked FEM models of these prototype CFT specimens by varying the tube slenderness ratios, material strength ratios, axial load ratios and member length-to-depth ratios. The tube slenderness ratios ($\lambda = b/t$ or D/t) were varied by changing the tube thickness (t). The material strength ratios (F_y/f'_c) were varied by changing the steel yield stress (F_y) or concrete compressive strength (f'_c). The axial load ratios (P/P_n) were varied by changing the applied axial load level (P), and recalculating

the ratio using the axial strength P_n (calculated using the AISC 360-10 equations). The member length-to-depth ratios (L/B or L/D) were varied by changing the member length (L).

The prototype selected for rectangular CFT beam-columns was Specimen BRA4-2-5-04 by Nakahara and Sakino (2000). Figure 3.18 showed the comparisons of the experimental and analytical results for this specimen. The steel yield stress F_y and the concrete compressive strength f'_c of this specimen is 253 MPa and 47.6 MPa, respectively. Type-2 loading was used to load this specimen. Other details of Specimen BRA4-2-5-04 were shown previously in Table 2.5.

The prototype selected for circular CFT beam-columns was Specimen C06F3M by Ichinohe et al. (1991). Figure 3.19 showed the comparisons of the experimental and analytical results for this specimen. The steel yield stress F_y is 420 MPa and the concrete compressive strength f'_c is 64.3 MPa. Type-1 loading was used to load this specimen. Other details of Specimen C06F3M were shown previously in Table 2.6.

A total of 207 analyses were conducted in the parametric studies. Tables 6.1- 6.6 summarize the details of the beam-columns in these parametric analyses. These details include the length (L), width (B, for rectangular members), diameter (D, for circular members), length-to-depth ratio (L/B for rectangular members and L/D for circular members), flange thickness (t_f for rectangular members), tube thickness (t, for circular members), governing tube slenderness ratio (b/t_f for rectangular members and D/t for

circular members), slenderness coefficient (λ_{coeff}), or relative strength ratio (ξ). The axial strength from finite element analysis (P_f), applied axial load (P), and actual axial load ratio (P/P_f) are also included. The nomenclature used in these tables (for example, R-70-5-0-3, C-51-7-0-7) consists of the cross section type (R represents a rectangular member while C represents a circular member), tube slenderness ratio (b/t_f for rectangular CFT members and D/t for circular CFT member), material strength ratio (F_y/f'_c), nominal axial load ratio (P/P_n), and length-to-depth-ratio (L/B for rectangular CFT members and L/D for circular CFT members). The values for the tube slenderness ratio, material strength ratio and length-to-depth-ratio are round off numbers.

6.4.1 Effect of Tube Slenderness Ratio (λ) and Axial Load ratio (α)

To investigate the effect of tube slenderness ratio on the behavior of noncompact and slender CFT beam-columns, seven different tube slenderness ratios were selected for both prototype specimens. For Specimen BRA4-2-05-04, the resulting slenderness coefficients are 2.49, 2.68, 2.90, 3.17, 3.87, 4.36 and 4.98. For Specimen C06F3M, the resulting slenderness coefficients are 0.11, 0.16, 0.20, 0.22, 0.24, 0.28 and 0.31. These slenderness coefficients cover the whole slenderness range for noncompact and slender sections.

For both prototype specimens, different axial load ratios were selected as follows. Five different axial load ratios (0, 0.2, 0.4, 0.6 and 1.0) were selected for Specimen BRA4-2-05-04 and six different axial load ratios (0, 0.2, 0.4, 0.6, 0.8 and 1.0) were selected for Specimen C06F3M. Beam-columns with axial load ratio of 0 (i.e., columns) were subjected to bending moments only to get the flexural strength M_f. Beam-columns with

axial load ratio of 1.0 (i.e., beams) were subjected to axial compressive force only to get the axial capacity P_f.

Thus, a total of 72 analyses were conducted using the corresponding benchmarked FEM models. These 72 analyses included 35 rectangular beam-column analyses and 42 circular beam-column analyses. In these analyses, the material strength ratios and length-to-depth ratios were kept the same as that of the corresponding prototype specimens. Details of the beam-columns in these parametric analyses are shown in Table 6.1 (for rectangular beam-columns) and Table 6.2 (for circular beam-columns). For all rectangular beam-columns included in Table 6.1, the member length (L), steel yield stress (F_y), and concrete compressive strength (f'_c) were kept the same as that of the prototype specimen BRA4-2-05-04 (for example, L = 600 mm, F_y = 253 MPa, and f'_c = 47.6 MPa). The resulting member length-to-depth ratio and material strength ratio is 3.0 and 5.3, respectively. For all circular beam-columns included in Table 6.2, the member length (L), steel yield stress (F_y), and concrete compressive strength (f'_c) were kept the same as that of the prototype specimen C06F3M (for example, L = 2000 mm, F_y = 420 MPa, and f'_c = 64.3 MPa). The resulting member length-to-depth ratio and material strength ratio is 6.7 and 6.5, respectively.

Figures 6.5 - 6.8 show the effect of tube slenderness ratio on the moment-midspan deflection responses of rectangular CFT beam-columns at different axial load ratios (i.e., α = 0, 0.2, 0.4 and 0.6). These figures indicate that: (i) the stiffness and strength of rectangular CFT beam-columns decreases with increasing tube slenderness ratios, and (ii)

the flexural strength of rectangular CFT beam-columns with axial loads applied (i.e., α = 0.2, 0.4, and 0.6) decreases after failure (for example, local buckling of the steel compression flange) occurs. The reason for the first observation is quite obvious, since both the flexural stiffness and flexural strength of CFT members is proportional to the steel tube thickness. The second observation is explained using CFT behavior mechanics as follows.

For CFT beam-columns, the axial compression force (P) is sustained by both the steel tube wall and concrete infill in the compression, while the bending moment (M) is sustained by: (i) the steel tube wall and concrete infill in the compression, and (ii) the steel tube wall in tension. For all rectangular CFT beam-columns analyzed in this section, local buckling of the steel compression flange was the governing failure mode, as shown in Figure 6.9. To make the local buckling more visible, the deformed shape was shown in Figure 6.9 with a scale factor of 5. After local buckling occurred, a portion of the compressive forces from the steel compression flange was redistributed to the concrete infill in the compression region. For beam-columns with the axial load of 0 (i.e., pure bending specimens): (i) the concrete infill in the compression region was able to sustain the additional compression forces shed from the buckled steel tube before its compressive strength was reached, (ii) the buckled steel tube wall (with part of the compressive forces shed to the concrete infill in compression) was able to continue providing confinement to the concrete infill, and (iii) the steel tube in tension was able to develop strain hardening. Therefore, the flexural strengths of these members did not decrease.

For beam-columns with axial loads applied, however: (i) the concrete infill was subjected to compressive force from the applied axial force and bending moment; and it was not able to sustain the addition compressive forces shed form the buckled steel tube and (ii) the buckled steel tube wall was not able to confine the concrete infill that is undergoing significant volumetric dilation. Therefore, the flexural strengths of these members decreased after local buckling occurred. It should be noted that the local buckling in these members propagated to the webs as loading continued. This propagation of local buckling was shown in Figure 6. 10. To make the local buckling more visible, the deformed shape was shown in Figure 6.10 with a scale factor of 5.

Figures 6.11 - 6.15 show the effect of tube slenderness ratio on the moment-curvature responses of circular CFT beam-columns at different axial load ratios (i.e., α = 0, 0.2, 0.4 0.6 and 0.8). These figures indicate that: (i) the stiffness and strength of circular CFT beam-columns decreases with increasing tube slenderness ratios, and (ii) the moment-curvature responses of circular CFT beam-columns are ductile, i.e., there is no decrease of flexural capacity with continued applied loading. The first observation is obvious, as discussed previously for rectangular beam-columns. The second observation is explained as follows.

For circular CFT beam-columns, the axial compression force (P) is sustained by the steel tube wall and concrete infill in the compression, while the bending moment (M) is sustained by: (i) the steel tube wall and concrete infill in the compression, and (ii) the steel tube wall in tension. This force transfer mechanics is similar to that for rectangular

beam-columns, as presented previously. However, local buckling did not occur for circular beam-columns due to the existence of the concrete infill. With continued applied loading: (i) the steel tube wall in both compression and tension was able to yield, with strain hardening developed, (ii) the concrete infill in compression was able to develop its compressive strength, and (iii) the steel tube wall was able to provide continued confinement to the concrete confinement. This confinement increased the strength and ductility of the concrete infill. Therefore, the flexural strength of circular beam-columns increased with continued applied loading.

Figure 6.16 shows the effect of axial load ratio on the moment-midspan deflection responses of rectangular CFT beam-columns with tube slenderness ratio (b/t_f) of 70.0. In this figure, the actual axial load ratio (P/P_f) instead of the nominal axial load ratio (P/P_n) was used. This figure indicates that: (i) when the ratio P/P_f is less than 0.36, the stiffness and strength of CFT beam-columns increases as the ratio P/P_f increases, (ii) the stiffness and strength of the beam-column with P/P_f of 0.54 is decreased as compared to that of the beam-column with P/P_f of 0.36, and (iii) the moment-midspan response drops more rapidly as P/P_f increases due to the earlier occurrence of local buckling. The effects of axial load ratio on the moment-midspan deflection responses of rectangular CFT beam-columns with other slenderness ratios are similar to what Figure 6.16 indicates, and the corresponding comparisons are shown in the companion analytical database (Lai, 2014).

Figure 6.17 shows the effect of axial load ratio on the moment-curvature responses of circular CFT beam-columns with tube slenderness ratio (D/t) of 52.6. In this figure, the

actual axial load ratio (P/P_f) instead of the nominal axial load ratio (P/P_n) was used. This figure indicates that: (i) when the ratio P/P_f is less than 0.39, the stiffness and strength of CFT beam-columns increases as the ratio P/P_f increases, (ii) when the ratio P/P_f is greater than 0.39, the stiffness and strength of CFT beam-columns decreases as ratio P/P_f increases, and (iii) yielding of the compression flange occurs earlier as P/P_f increases. The effects of axial load ratio on the moment-curvature responses of circular CFT beam-columns with other slenderness ratios are similar to what Figure 6.17 indicates, and the corresponding comparisons are shown in the companion analytical database (Lai, 2014).

6.4.2 Effect of Material Strength Ratio (F_y/f'_c) and Axial Load Ratio (α)

To investigate the effect of tube slenderness ratio on the behavior of noncompact and slender CFT beam-columns, ten different material strength ratios were selected for both prototype specimens. For Specimen BRA4-2-05-04, the material strength ratio increases from 3.6 to 25.0. For Specimen C06F3M, the material strength ratio increases from 6.0 to 25.0. The material strength ratios were varied by changing the steel yield stress (F_y) from 253 MPa to 525 MPa, or the concrete compressive strength (f'_c) from 21 MPa to 70 MPa, since AISC 360-10 specifies the material strength limit for CFT members as: the steel yield stress shall be no more than 525 MPa, and concrete compressive strength shall be no less than 21 MPa nor no more than 70 MPa.

Different axial load ratios were selected both prototype specimens. For Specimen BRA4-2-05-04, five different axial load ratios (0, 0.2, 0.4, 0.6 and 1.0) were selected. For Specimen C06F3M, six different axial load ratios (0, 0.2, 0.4, 0.6, 0.8 and 1.0) were

selected. Thus, a total of 110 analyses were conducted using the corresponding benchmarked FEM models. These analyses included 50 rectangular beam-column analyses and 60 circular beam-column analyses. In these analyses, the tube slenderness ratios and length-to-depth ratios were kept the same as that of the corresponding prototype specimens. Details of the beam-columns in these parametric analyses are shown in Table 6.3 (for rectangular beam-columns) and Table 6.4 (for circular beam-columns). For all rectangular beam-columns included in Table 6.3, the member length (L), flange interior with (b), flange thickness (t_f), and web thickness (t_w) were kept the same as that of the prototype Specimen BRA4-2-05-04 (for example, L = 600 mm, b = 195.9 mm, t_f = 2.8 mm, and t_w = 2.8 mm). The resulting member tube slenderness ratio and length-to-depth ratio is 70.0 and 3.0, respectively. For all circular beam-columns included in Table 6.4, the member length (L), interior diameter (d_i, $d_i = D\text{-}2t$), and tube thickness (t) were kept the same as that of the prototype Specimen C06F3M (for example, L = 2000 mm, d_i = 288.3 mm, and t = 5.7 mm). The resulting tube slenderness ratio and length-to-depth ratio is 52.6 and 6.7, respectively.

Figures 6.18 - 6.25 show the effect of material strength ratio on the moment-midspan deflection responses of rectangular CFT beam-columns at different axial load ratios (i.e., α = 0, 0.2, 0.4 and 0.6). In Figures 6.18- 6.21, the stress yield strength (F_y) decreased from 525 MPa to 317 MPa (525 MPa, 473 MPa, 421 MPa, 369 MPa and 317 MPa), while concrete compressive strength (f'_c) was kept constant at 21 MPa. These four figures indicate that as the material strength ratio decreased: (i) the stiffness of rectangular CFT beam-columns was not changed, and (ii) the strength of rectangular CFT beam-columns

decreased. In Figures 6.22-6.25, the stress yield strength (F_y) was kept constant at 253 MPa, while concrete compressive strength (f'_c) increased from 21 MPa to 70 MPa (21MPa, 30 MPa, 40 MPa, 60 MPa and 70 MPa). These four figures indicate that as the material strength ratio decreased: (i) the stiffness of rectangular CFT beam-columns increased, and (ii) the strength of rectangular CFT beam-columns increased. Observations from Figures 6.18- 6.21 and Figures 6.22-6.25 may seem to be contradicted with each other at first glance. However, these observations are explained as follows.

For the observations regarding stiffness: the stiffness of CFT beam columns depends on the stiffness of both steel tube and concrete infill. In the FEM models, the elastic modulus (E_s) of the steel was assumed to be constant at 200 GPa, while the elastic modulus (E_c) of the concrete infill was assumed to be $4700\sqrt{f_c'}$ in MPa ($57{,}000\sqrt{f_c'}$ in psi, according to ACI 318-11). Therefore, as the steel yield stress (F_y) decreased, the material strength ratio (F_y/f'_c) decreased and the stiffness remained the same (as shown in Figures 6.18-6.21). However, as the concrete compressive strength (f'_c) increased, the material strength ratio decreased and the stiffness increased (as shown in Figures 6.22-6.25). It should be noted that the effect of concrete compressive strength on the stiffness is less significant for beam-columns with lower axial load ratio, as also shown in Figures 6.22-6.25. This is due to the fact the stiffness contribution from the concrete to the overall stiffness decreases as the bending increases (i.e., applied axial load ratio decreases).

For the observations regarding the strength: the strength of CFT members depends on material strength. As the steel yield stress (F_y) decreased, the material strength ratio (F_y/f'_c) decreased and the strength decreased. However, as the concrete compressive strength (f'_c) increased, the material strength ratio decreased and the strength increased. Figures 6.26-6.35 show the effect of material strength ratio on the moment-curvature responses of circular CFT beam-columns at different axial load ratios (i.e., α = 0, 0.2, 0.4, 0.6 and 0.8). In Figures 6.26-6.30, the stress yield strength (F_y) decreased from 525 MPa to 317 MPa (525 MPa, 473 MPa, 421 MPa, 369 MPa and 317 MPa), while concrete compressive strength (f'_c) was kept constant at 21 MPa. These five figures indicate that as the material strength ratio decreased: (i) the stiffness of circular CFT beam-columns was not changed, and (ii) the strength of circular CFT beam-columns decreased. In Figures 6.31-6.35, the stress yield strength (F_y) was kept constant at 420 MPa, while concrete compressive strength (f'_c) increased from 30 MPa to 70 MPa (30 MPa, 40 MPa, 50 MPa, 60 MPa and 70 MPa). These five figures indicate that as the material strength ratio decreased: (i) the stiffness of rectangular CFT beam-columns increased, and (ii) the strength of rectangular CFT beam-columns increased. These observations are similar to that of the rectangular CFT beam-columns presented previously in this section, and they can be explained using the discussions for rectangular CFT beam-columns also.

Figure 6.36 shows the effect of axial load ratio on the moment-midspan deflection responses of rectangular CFT beam-columns with material strength ratio of 25.0 (F_y = 525 MPa, and f'_c = 21 MPa). In this figure, the actual axial load ratio (P/P_f) instead of the nominal axial load ratio (P/P_n) was used. This figure indicates that: (i) when the ratio

P/P_f is less than 0.15, the stiffness and strength of CFT beam-columns increases as the ratio P/P_f increases, (ii) when the ratio P/P_f is greater than 0.15, the stiffness and strength of the beam-column decreases as the ratio P/P_f increases, and (iii) the moment-midspan response drops more rapidly as P/P_f increases due to the earlier occurrence of local buckling. The effects of axial load ratio on the moment-midspan deflection responses of rectangular CFT beam-columns with other material strength ratios are similar to what Figure 6.36 indicates, and the corresponding comparisons are shown in the companion analytical database (Lai, 2014). These observations agree with the discussion presented previously in Section 6.4.1, which showed the effect of axial load ratio for CFT rectangular beam-columns with different tube slenderness ratios.

Figure 6.37 shows the effect of axial load ratio on the moment-curvature responses of circular CFT beam-columns with material strength ratio of 25.0 (F_y = 525 MPa, and f'_c = 21 MPa). In this figure, the actual axial load ratio (P/P_f) instead of the nominal axial load ratio (P/P_n) was used. This figure indicates that: (i) when the ratio P/P_f is less than 0.17, the stiffness and strength of CFT beam-columns increases as the ratio P/P_f increases, (ii) when the ratio P/P_f is greater than 0.17, the stiffness and strength of CFT beam-columns decreases as ratio P/P_f increases, the and (iii) yielding of the compression flange occurs earlier as P/P_f increases. The effects of axial load ratio on the moment-curvature responses of circular CFT beam-columns with other slenderness ratios are similar to what Figure 6.37 indicates, and the corresponding comparisons are shown in the companion analytical database (Lai, 2014). These observations agree with the discussion presented

previously in Section 6.4.1, which showed the effect of axial load ratio for CFT circular beam-columns with different tube slenderness ratios.

6.4.3 Effect of Length-to-depth ratio (*L/B* or *L/D*) and Axial Load Ratio (α)

The member length-to-depth ratio determines the effect of second-order moments on the behavior of beam-columns. This effect is more significant for CFT members with greater tube slenderness ratios (i.e., thinner tube wall), and is therefore investigated analytically in this section for the selected prototype beam-column specimens with the minimum permitted tube thickness (i.e., with maximum permitted slenderness coefficient, $\lambda_{coeff} = \lambda_{limit}$). The resulting tube thickness is 1.4 mm. for Specimen BRA4-2-05-04 and 2.0 mm. for Specimen C06F3M.

For both prototype specimens, 15 analyses were conducted for three different length-to-depth ratios (*L/B*=3.0, 9.9, and 19.8 for Specimen BRA4-2-05-04, and *L/D*=6.8, 13.7, and 20.5 for Specimen C06F3M) and five different axial load ratios (0, 0.2, 0.4, 0.6 and 1.0). In these analyses, the material strength ratios were kept the same as that of the corresponding prototype specimens. Details of the beam-columns in these parametric analyses are shown in Table 6.5 (for rectangular beam-columns) and Table 6.6 (for circular beam-columns). It should be noted that rectangular specimens with *L/B* of 3.0 and circular specimens with *L/D* of 6.8 were analyzed previously in Section 6.4.1; details of these specimens were included here again in Table 6.5 and Table 6.6 for the convenience of comparisons.

For all rectangular beam-columns included in Table 6.5, the flange interior with (b), steel yield stress (F_y), and concrete compressive strength (f'_c) were kept the same as that of the prototype specimen BRA4-2-05-04 (for example, b = 195.9 mm, F_y = 253 MPa, and f'_c = 47.6 MPa). The resulting member tube slenderness ratio and material strength ratio is 139.9 and 5.3, respectively. For all circular beam-columns included in Table 6.6, the interior diameter (d_i, $d_i = D-2t$), steel yield stress (F_y), and concrete compressive strength (f'_c) were kept the same as that of the prototype specimen C06F3M (for example, d_i = 195.9 mm, F_y = 420 MPa, and f'_c = 64.3 MPa). The resulting tube slenderness ratio and material strength ratio is 146.2 and 6.5, respectively.

Figures 6.38 – 6.41 show the effect of member length-to-depth ratio on the moment-midspan deflection responses of rectangular CFT beam-columns at different axial load ratios (i.e., α = 0, 0.2, 0.4 and 0.6). These figures indicate that: (i) the member length-to-depth ratio has no significant effect on the stiffness and strength of rectangular CFT beam-columns, and (ii) the failure occurs earlier as the member length-to-depth ratio increases, due to the earlier occurrence of local buckling of the steel compression flange. As the loading continued, the local buckling propagated into the webs as shown in Figure 6.42. This is similar to the failure modes presented previously in Section 6.4.1. To make the local buckling more visible, the deformed shape was shown in Figure 6.42 with a scale factor of 5.

Figures 6.43-6.46 show the effect of member length-to-depth ratio on the moment-curvature responses of circular CFT beam-columns at different axial load ratios (i.e., α =

0, 0.2, 0.4, 0.6 and 0.8). These figures indicate that: (i) the member length-to-depth ratio has no significant effect on the stiffness of circular CFT beam-columns, and (ii) the strength increases slightly as the member length-to-depth ratio increases, due to the strain hardening of the steel tube. No local buckling was observed in the analysis. Figure 6.47 shows the deformed shape of the circular beam-column (C-146-7-6-21) at the curvature of 0.054/m. The tube slenderness ratio (D/t), material strength ratio (F_y/f'_c), actual axial load ratio (P/P_f), and length-to-depth ratio (L/D) is 146.2, 6.5, 0.37, and 20.5, respectively. The deformed shapes of other circular CFT beam-columns are similar to what Figure 6.47 represents. Therefore the corresponding figures are not shown here for brevity.

Figure 6.48 shows the effect of axial load ratio on the moment-midspan deflection responses of rectangular CFT beam-columns with length-to-depth ratio (L/B) of 3.0. In this figure, the actual axial load ratio (P/P_f) instead of the nominal axial load ratio (P/P_n) was used. This figure indicates that: (i) when the ratio P/P_f is less than 0.38, the stiffness and strength of CFT beam-columns increases as the ratio P/P_f increases, and (ii) the moment-midspan response drops more rapidly as P/P_f increases due to the earlier occurrence of local buckling. The effects of axial load ratio on the moment-midspan deflection responses of rectangular CFT beam-columns with other length-to-depth ratios are similar to what Figure 6.48 indicates, and the corresponding comparisons are shown in the companion analytical database (Lai, 2014). These observations agree with the discussion presented previously in Section 6.4.1 and Section 6.4.2, which showed the

effect of axial load ratio for CFT rectangular beam-columns with different tube slenderness ratios and material strength ratios.

Figure 6.49 shows the effect of axial load ratio on the moment-curvature responses of circular CFT beam-columns with length-to-depth ratio (L/D) of 6.7. In this figure, the actual axial load ratio (P/P_f) instead of the nominal axial load ratio (P/P_n) was used. This figure indicates that when the ratio P/P_f is less than 0.50, the stiffness and strength of CFT beam-columns increases as the ratio P/P_f increases. The effects of axial load ratio on the moment-curvature responses of circular CFT beam-columns with other length-to-depth ratios are similar to what Figure 6.49 indicates, and the corresponding comparisons are shown in the companion analytical database (Lai, 2014). These observations agree with the discussion presented previously in Section 6.4.1 and Section 6.4.2, which showed the effect of axial load ratio for CFT circular beam-columns with different tube slenderness ratios and material strength ratios.

6.5 Shape of the P-M Interaction Curve of Noncompact and Slender CFT Members

The behavior noncompact and slender CFT beam-columns depend on parameters such as: the tube slenderness ratio (λ), steel yield stress (F_y), concrete compressive strength (f'_c), and member length-to-depth ratio (L/B or L/D). These parameters influence the shape of the P-M interaction curve for noncompact and slender CFT beam-columns. In this section, the strengths of both rectangular and circular CFT beam-columns obtained from the parametric analyses presented previously in Section 6.4 are used to generate the P-M interaction curves of CFT beam-columns.

As discussed previously in Section 6.3, the over-conservatism of the AISC P-M interaction equations (Equation 6.1 and Equation 6.2) for designing noncompact and slender rectangular and circular CFT beam-columns is due to: (i) the conservative estimation of the axial and flexural strength (P_n and M_n) by the AISC 360-10; and (ii) the use of bilinear interaction curve which is the same as that used for steel beam-columns. The primary focus of this research is to improve the bilinear interaction curve. Therefore, the conservatism due to (i) was eliminated by using the axial and flexural strength (P_f and M_f) obtained from the finite element analysis to normalize the results from the parametric analyses.

Figure 6.50 and Figure 6.51 show the effect of tube slenderness ratio on the shape of the P-M interaction curve for rectangular and circular CFT-columns, respectively. In these figures, the ordinate is the ratio of applied axial load (P_{FEM}) to the axial strength (P_f), and the abscissa is the ratio of the applied moment (M_{FEM}) to the flexural strength (M_f). These two figures indicate that the P-M interaction curve for both rectangular and circular CFT beam-columns is more convex as the tube slenderness ratio (λ) increases. For example, both P_{FEM}/P_f and M_{FEM}/M_f ratios of the balance point increases as λ increases. The balance point is the point where the maximum flexural strength of a CFT beam-column is reached.

Figure 6.52 shows the effect of steel yield stress (F_y) on the shape of the P-M interaction curve for rectangular CFT-columns. This figure indicate that the P-M interaction curve for rectangular CFT beam-columns is more convex the as the steel yield stress (F_y)

decreases. Figure 6.53 shows the effect of concrete compressive strength (f'_c) on the shape of the P-M interaction curve for rectangular CFT-columns. This figure indicates that the P-M interaction curve for rectangular CFT beam-columns is more convex as the concrete compressive strength (f'_c) increases. These two figures indicate that the P-M interaction curve for rectangular CFT beam-columns is more convex as the material strength ratio (F_y/f'_c) increases, as shown in Figure 6.54. Figure 6.54 combines the results from both Figure 6.52 and Figure 6.53, meaning it includes the results of all fifty beam-columns included in Table 6.3.

Figure 6.55 and Figure 6.56 show the effect of steel yield stress (F_y) and concrete compressive strength (f'_c) on the shape of the P-M interaction curve for circular CFT-columns. Similar to rectangular CFT beam-columns, the P-M interaction curve for circular CFT beam-columns is more convex as the material strength ratio (F_y/f'_c) increases, as shown in Figure 6.57. Figure 6.57 combines the results from both Figure 6.55 and Figure 6.56, meaning it includes the results of all sixty beam-columns included in Table 6.4.

Figure 6.58 and Figure 6.59 show the effect of length-to-depth ratio (*L/B* or *L/D*) on the shape of P-M interaction curves of rectangular and circular CFT beam-columns, respectively. Figure 6.58 indicates that the M_{FEM}/M_f ratio of the balance point decrease slightly as the *L/B* ratio increases. This is due to the earlier occurrence of local buckling as *L/B* increases, as explained previously in Section 6.4.3. Figure 6.59 indicates that the

M_{FEM}/M_f ratio of the balance point increases slightly as the *L/B* ratio increases. This is due to the strain hardening of the steel tube, as also explained previously in Section 6.4.3.

The effect of length-to-depth ratio up to 20.0 could be ignored because: (i) the decrease of M_{FEM}/M_f ratio for the balance point of rectangular CFF beam-columns is only 1.7% (the corresponding M_{FEM}/M_f ratio is 1. 69 with *L/B* of 3.0, and 1.66 with *L/B* ratio of 19.9); (ii) the increase of M_{FEM}/M_f ratio for the balance point of circular CFF beam-columns is only 2.0% (the corresponding M_{FEM}/M_f ratio is 1.69 with *L/D* of 3.0, and 1.66 with *L/D* ratio of 19.9), and this increase could be ignored conservatively; and (iii) the shape of the interaction curve is not changed significantly by the member length up to length-to-depth ratio of about 20.0 (19.8 for rectangular beam-columns, and 20.5 for circular beam-columns).

6.6 Updated P-M Interaction Equations

6.6.1 Development of the Updated P-M Interaction Equations

As presented in the previous section (Section 6.5), the P-M interaction curve for rectangular and circular noncompact and slender CFT beam-columns is more convex with increasing tube slenderness ratio (*b/t* or *D/t*) and material strength ratio (F_y/f'_c) . Therefore it is reasonable to propose a new factor that includes the effects of both tube slenderness ratio and material strength ratio. The relative strength ratio as defined previously in Equation 6.3 and rewritten here for convenience was therefore selected.

$$\xi = \frac{A_s F_y}{A_c f_c'} \tag{6.3}$$

where A_s and A_c are the total areas of the steel tube and concrete infill, respectively. In this factor, the tube slenderness ratio is included by the A_s/A_c ratio, and the material strength ratio is included explicitly. For example, the A_s/A_c ratio for a square CFT member with equal flange and web thickness is related to tube slenderness ratio (b/t) as:

$$\frac{A_s}{A_c} = \frac{4\,b/t + 1}{\left(b/t\right)^2} \tag{6.4}$$

and the A_s/A_c ratio for a circular CFT member is related to tube slenderness ratio (D/t) as:

$$\frac{A_s}{A_c} = \left(\frac{D/t}{D/t - 2} \right)^2 - 1 \tag{6.5}$$

The relative strength ratio decreases with increasing slenderness ratio and material strength ratio.

In Section 6.5, the effects of tube slenderness ratio and material strength ratio are shown in Figure 6.50 and Figure 6.54 for rectangular and Figure 6.51 and Figure 6.57 for circular CFT beam-columns. The results shown in these figures are further combined here to show the effect of the relative strength ratio. For example, Figure 6.60 shows the effect of relative strength ratio on the shape of the P-M interaction curve for rectangular CFT beam-columns. This figure combines the results from Figure 6.50 and Figure 6.54, meaning it includes the results of all eighty-five beam-columns included in Table 6.1 and Table 6.3. This figure indicates that the P-M interaction curve for rectangular noncompact and slender CFT beam-columns is more convex with decreasing relative strength ratio.

Figure 6.61 shows the effect of relative strength ratio on the P-M interaction curve for circular CFT beam-columns. This figure combines the results from both Figure 6.51 and Figure 6.57, meaning it includes the results of all one hundred and two beam-columns included in Table 6.2 and Table 6.4. This figure indicates that the P-M interaction curve for rectangular noncompact and slender CFT beam-columns is also more convex with decreasing relative strength ratio.

The observations from Figure 6.60 and Figure 6.61 means that the shape of the P-M interaction curves for both rectangular and circular CFT beam-columns is determined by the relative strength ratio (ξ). As discussed previously in Section 6.5, the effect of length-to-depth ratio (up to 20.0) on the shape of the P-M interaction curve for both rectangular and circular CFT beam-columns could be ignored. Therefore, the P-M interaction curve could be improved by focusing on the effect of ξ only.

Several design methods could be used to improve the bilinear P-M interaction curve used by AISC 360-10, as shown in Figure 6.62. Method A uses polynomial equation to represent the shape of the P-M interaction curve defined by analysis and tests. Method B simplifies Method A by using a trilinear curve (Line ACDB), which is similar to the approach discussed in the commentary of AISC 360-10, Section I5. Method C further simplifies Method B by using a bilinear curve (Line ADB). Method C is recommended because: (i) it captures the basic P-M behavior of noncompact and slender CFT beam-columns; and (ii) the bilinear form of Method C is similar to the current AISC 360-10 interaction curve, and is convenient for design.

For Method C, Point A is the axial strength, Point B is the flexural strength, and Point D is the balance point which corresponds to the largest increase in flexural strength, i.e., M_{FEM}/M_f ratio. To use Method C, factors β_1 and β_2 for the ordinate and abscissa of Point D need to be determined. Figure 6.60 and Figure 6.61 showed that the maximum M_{FEM}/M_f ratio (β_2) and the corresponding P_{FEM}/P_f ratio (β_1) increases as the relative strength ratio (ξ) increases. Statistical analyses were used to evaluate the β_1- ξ relationship and β_2- ξ relationship. These analyses showed that:

For Rectangular CFT beam-columns:

$$\beta_1 = 0.17\xi^{-0.4} \tag{6.6}$$

When $\xi \geq 0.5$ $$\beta_2 = 1.06\xi^{-0.11} \tag{6.7}$$

When $\xi < 0.5$ $$\beta_2 = 0.90\xi^{-0.36} \tag{6.8}$$

For Circular CFT beam-columns:

$$\beta_1 = 0.27\xi^{-0.4} \tag{6.9}$$

When $\xi \geq 0.5$ $$\beta_2 = 1.10\xi^{-0.08} \tag{6.10}$$

When $\xi < 0.5$ $$\beta_2 = 0.95\xi^{-0.32} \tag{6.11}$$

Equations 6.6 – 6.11 are applicable to noncompact and slender CFT beam-columns with: (i) normal strength steel, i.e., $F_y \leq 525$ MPa, (ii) normal strength concrete, i.e., 21 MPa $\leq f'_c \leq 70$ MPa, and (iii) Length-to-depth ratio (L/B or L/D) no greater than 20.0. Also, Equations 6.6 - 6.8 are applicable to noncompact and slender rectangular CFT beam-columns with relative strength ratio (ξ) no less than 0.153 and no greater than 1.445, and

Equations 6.9 - 6.11 are applicable to noncompact and slender rectangular CFT beam-columns with relative strength ratio (ξ) no less than 0.182 and no greater than 2.016.

To make these equations (Equations 6.6-6.11) more straightforward for design, the equations for β_2 were further simplified by linear approximation. For example, Equation 6.7 and Equation 6.8 were simplified to Equation 6.12, and Equation 6.10 and Equation 6.11 were simplified to Equation 6.13.

$$\beta_2 = 2 - 2\xi \geq 1.0 \tag{6.12}$$

$$\beta_2 = 1.8 - 1.6\xi \geq 1.0 \tag{6.13}$$

The AISC 360-10 interaction curve (Equation 6.1 and Equation 6.2) for noncompact and slender CFT beam-columns can be now updated as:

When $\frac{P_r}{\phi_c P_n} \geq \beta_1$ $$\frac{P_r}{\phi_c P_n} + \frac{1-\beta_1}{\beta_2}\frac{M_r}{\phi_b M_n} \leq 1.0 \tag{6.14}$$

When $\frac{P_r}{\phi_c P_n} < \beta_1$ $$\frac{1-\beta_2}{\beta_1}\frac{P_r}{\phi_c P_n} + \frac{M_r}{\phi_b M_n} \leq 1.0 \tag{6.15}$$

where β_1 and β_2 is calculated using Equation 6.6 and Equation 6.12 for rectangular CFT beam-columns, and Equations 6.9 and Equation 6.13 for circular CFT beam-columns. For example, the relative strength ratio (ξ) for a typical noncompact circular CFT beam-column (with diameter D = 406.4 mm, thickness t = 6.35 mm, steel elastic modulus E_s = 200000 MPa, steel yield stress F_y = 345 MPa, and concrete compressive f'_c = 28 MPa) is 0.82. The resulting β_1 calculated using Equation 6.9 is 0.32, and β_2 calculated using Equation 6.13 is 1.0.

6.6.2 Verification of the Updated P-M Interaction Equations

The updated P-M interaction equations (Equations 6.6-6.15) were verified by using them to calculate the P-M interaction curves for all beam-columns included in Tables 6.1-6.4. Representative comparisons of the updated interaction curves (with solid lines) obtained using these equations with interaction curves (with dashed lines) from the parametric studies are shown in Figures 6.63 and Figure 6.64 (for rectangular beam columns) and Figures 6.65 and Figure 6.66 (for circular beam columns). All other comparisons are shown in the companion analytical database (Lai, 2014). In these figures, the solid black curves are calculated using the exact equations for β_2, and the solid red curves are calculated using the simplified equations for β_2. The relative strength ratios (ξ) are also included on the top right corner in all these figures. These comparisons indicate that: (i) the updated interaction curves evaluated using the exact equations compare favorably with the analysis results, and (ii) the updated interaction curves evaluated using the simplified equations also compare well with the analysis results, and are more conservative.

To further evaluate the simplified design equations, the P-M interaction curves (dashed color lines) evaluated using these equations are compared to the experimental results for all specimens (except the specimens with high strength steel) in the database (as shown in Table 2.5 and Table 2.6). The comparisons are showed in Figure 6.67 for rectangular CFT beam-columns and Figure 6.68 for circular CFT beam-columns. In these two figures, the current AISC 360-10 P-M interaction curves are also included (solid black line). These comparisons: (i) confirmed the conservatism of the updated interaction curves, and

(ii) indicate that the updated interaction curves significantly reduced the over-conservatism by the current AISC 360-10 P-M interaction curves (especially for specimens with high relative strength factor).

6.7 Direct Analysis Method

The current AISC 360-10 uses the direct analysis method as the primary means to address the stability requirements for the design of steel structures. In this method, the required strengths are determined from second-order elastic analysis that considers: (i) P-Δ and P-δ effects, (ii) geometric imperfections, and (iii) stiffness reduction due to inelasticity. The validation of this method for CFT members has been verified by Denavit (2012). However, the conclusions of his work apply only to the design of compact CFT beam-columns (which uses plastic stress distribution method to calculate the available strengths). Therefore, further work need to be conducted to calibrate and verify the applicability of the updated P-M interaction equations (Equation 6.14 and Equation 6.15) in estimating the available strengths of noncompact and slender CFT members in the direct analysis.

6.8 Summary and Conclusions

AISC 360-10 specifies the provisions for designing noncompact and slender rectangular and circular CFT beam-columns. These provisions include the slenderness classifications presented in Section 6.1, and the P-M interaction equations (Equation 6.1 and Equation 6.2) presented in Section 6.2. These provisions were evaluated in Section 6.3 by using them to predict the strength of the 53 beam-columns in the experimental database

compiled by the author (presented in Section 2.3). The comparisons with experimental results showed that the AISC 360-10 P-M interaction equations are over-conservative. The over-conservatism of the design equations is due to the conservative estimation of axial and flexural strength, and the use of the bilinear P-M interaction curve for steel beam-columns. The conservatism of the axial (and flexural) strength was shown previous in Chapter 4 (and Chapter 5) in the corresponding evaluation. The conservatism of the bilinear P-M interaction curve is due to the fact this curve does not account for the beneficial effects of axial compression on the flexural strength of CFT members.

This research focused on improving the bilinear P-M interaction curve by conducting analytical parametric studies (presented in Section 6.4) using FEM models benchmarked against experimental data. In these parametric studies, the effect of several parameters on the behavior of noncompact and slender rectangular and circular CFT beam-columns was evaluated, with a total of 207 beam-column analyses on 34 CFT members conducted. These parameters included the tube slenderness ratio (b/t or D/t), material strength ratio (F_y/f'_c), and member length-to-depth ratio (L/B or L/D). The results from the parametric studies indicate that the shape of the P-M interaction curve for noncompact and slender CFT members depends on the tube slenderness ratio and material strength ratio, and that the effect of length-to-depth ratio (up to 20.0) on the shape of the P-M interaction curve for noncompact and slender CFT members could be neglected.

The relative strength ratio (ξ) which includes the effect of both the tube slenderness ratio and material strength ratio was then defined in Section 6.6.1 (Equation 6.1). The bilinear

interaction curve was improved by including factors β_1 and β_2 in the updated versions (Equation 6.14 and Equation 6.15). The equations for β_1 and β_2 were determined using the results from parametric studies focusing on the effects of relative strength ratio. For rectangular CFT members, Equation 6.6 and Equation 6.12 are given to calculate β_1 and β_2, respectively. For circular CFT members, Equation 6.9 and Equation 6.13 are given to calculate β_1 and β_2, respectively.

The updated P-M interaction curve preserves the bilinear form of the current AISC 360-10 interaction curve, while capturing the basic behavior of noncompact and slender CFT beam-columns. Comparisons with the results from both finite element analysis and experimental tests showed that the updated P-M interaction equations were able to predict the strength of noncompact and slender CFT beam-columns quite well. Further work need to be conducted to calibrate and verify the applicability of these equations in estimating the available strengths of noncompact and slender CFT members in the direct analysis.

Table 6.1 Analysis Matrix for Rectangular CFT Beam-Columns with Different Tube Slenderness Ratios and Axial Load Ratios

ID.	B (mm)	t_f (mm)	b/t_f	λ_{coeff}	ξ	P_f (kN)	P (kN)	P/P_f
R-70-5-0-3	201.5	2.8	70.0	2.49	0.31	2324.7	0.0	0.00
R-70-5-2-3	201.5	2.8	70.0	2.49	0.31	2324.7	415.7	0.18
R-70-5-4-3	201.5	2.8	70.0	2.49	0.31	2324.7	831.4	0.36
R-70-5-6-3	201.5	2.8	70.0	2.49	0.31	2324.7	1247.1	0.54
R-70-5-10-3	201.5	2.8	70.0	2.49	0.31	2324.7	2324.7	1.00
R-75-5-0-3	201.1	2.6	75.4	2.68	0.29	2278.4	0.0	0.00
R-75-5-2-3	201.1	2.6	75.4	2.68	0.29	2278.4	395.2	0.17
R-75-5-4-3	201.1	2.6	75.4	2.68	0.29	2278.4	790.5	0.35
R-75-5-6-3	201.1	2.6	75.4	2.68	0.29	2278.4	1185.7	0.52
R-75-5-10-3	201.1	2.6	75.4	2.68	0.29	2278.4	2278.4	1.00
R-82-5-0-3	200.7	2.4	81.6	2.90	0.26	2233.4	0.0	0.00
R-82-5-2-3	200.7	2.4	81.6	2.90	0.26	2233.4	363.6	0.16
R-82-5-4-3	200.7	2.4	81.6	2.90	0.26	2233.4	727.2	0.33
R-82-5-6-3	200.7	2.4	81.6	2.90	0.26	2233.4	1090.7	0.49
R-82-5-10-3	200.7	2.4	81.6	2.90	0.26	2233.4	2233.4	1.00
R-89-5-0-3	200.3	2.2	89.1	3.17	0.24	2158.2	0.0	0.00
R-89-5-2-3	200.3	2.2	89.1	3.17	0.24	2158.2	333.2	0.15
R-89-5-4-3	200.3	2.2	89.1	3.17	0.24	2158.2	666.5	0.31
R-89-5-6-3	200.3	2.2	89.1	3.17	0.24	2158.2	999.7	0.46
R-89-5-10-3	200.3	2.2	89.1	3.17	0.24	2158.2	2158.2	1.00
R-109-5-0-3	199.5	1.8	108.8	3.87	0.20	2109.2	0.0	0.00
R-109-5-2-3	199.5	1.8	108.8	3.87	0.20	2109.2	297.6	0.14
R-109-5-4-3	199.5	1.8	108.8	3.87	0.20	2109.2	595.2	0.28
R-109-5-6-3	199.5	1.8	108.8	3.87	0.20	2109.2	892.7	0.42
R-109-5-10-3	199.5	1.8	108.8	3.87	0.20	2109.2	2109.2	1.00
R-123-5-0-3	199.1	1.6	122.5	4.36	0.18	2072.9	0.0	0.00
R-123-5-2-3	199.1	1.6	122.5	4.36	0.18	2072.9	284.7	0.14
R-123-5-4-3	199.1	1.6	122.5	4.36	0.18	2072.9	569.4	0.27
R-123-5-6-3	199.1	1.6	122.5	4.36	0.18	2072.9	854.1	0.41
R-123-5-10-3	199.1	1.6	122.5	4.36	0.18	2072.9	2072.9	1.00
R-140-5-0-3	198.7	1.4	139.9	4.98	0.15	2043.4	0.0	0.00
R-140-5-2-3	198.7	1.4	139.9	4.98	0.15	2043.4	274.7	0.13
R-140-5-4-3	198.7	1.4	139.9	4.98	0.15	2043.4	549.4	0.27
R-140-5-6-3	198.7	1.4	139.9	4.98	0.15	2043.4	824.0	0.40
R-140-5-10-3	198.7	1.4	139.9	4.98	0.15	2043.4	2043.4	1.00

Table 6.2 Analysis Matrix for Circular CFT Beam-Columns with Different Tube Slenderness Ratios and Axial Load Ratios

ID.	D (mm)	t (mm)	D/t	λ_{coeff}	ξ	P_f (kN)	P (kN)	P/P_f
C-53-7-0-7	299.7	5.7	52.6	0.11	0.53	5987.9	0.0	0.00
C-53-7-2-7	299.7	5.7	52.6	0.11	0.53	5987.9	1179.6	0.20
C-53-7-4-7	299.7	5.7	52.6	0.11	0.53	5987.9	2359.1	0.39
C-53-7-6-7	299.7	5.7	52.6	0.11	0.53	5987.9	3538.7	0.59
C-53-7-8-7	299.7	5.7	52.6	0.11	0.53	5987.9	4718.2	0.79
C-53-7-10-7	299.7	5.7	52.6	0.11	0.53	5987.9	5987.9	1.00
C-76-7-0-7	296.1	3.9	75.9	0.16	0.36	5686.7	0.0	0.00
C-76-7-2-7	296.1	3.9	75.9	0.16	0.36	5686.7	960.4	0.17
C-76-7-4-7	296.1	3.9	75.9	0.16	0.36	5686.7	1920.8	0.34
C-76-7-6-7	296.1	3.9	75.9	0.16	0.36	5686.7	2881.2	0.51
C-76-7-8-7	296.1	3.9	75.9	0.16	0.36	5686.7	3841.6	0.68
C-76-7-10-7	296.1	3.9	75.9	0.16	0.36	5686.7	5686.7	1.00
C-95-7-0-7	294.5	3.1	95.0	0.20	0.28	5375.5	0.0	0.00
C-95-7-2-7	294.5	3.1	95.0	0.20	0.28	5375.5	788.1	0.15
C-95-7-4-7	294.5	3.1	95.0	0.20	0.28	5375.5	1576.2	0.29
C-95-7-6-7	294.5	3.1	95.0	0.20	0.28	5375.5	2364.3	0.44
C-95-7-8-7	294.5	3.1	95.0	0.20	0.28	5375.5	3152.4	0.59
C-95-7-10-7	294.5	3.1	95.0	0.20	0.28	5375.5	5375.5	1.00
C-105-7-0-7	293.9	2.8	105.0	0.22	0.26	5259.4	0.0	0.00
C-105-7-2-7	293.9	2.8	105.0	0.22	0.26	5259.4	765.1	0.15
C-105-7-4-7	293.9	2.8	105.0	0.22	0.26	5259.4	1530.3	0.29
C-105-7-6-7	293.9	2.8	105.0	0.22	0.26	5259.4	2295.4	0.44
C-105-7-8-7	293.9	2.8	105.0	0.22	0.26	5259.4	3060.6	0.58
C-105-7-10-7	293.9	2.8	105.0	0.22	0.26	5259.4	5259.4	1.00
C-113-7-0-7	293.5	2.6	112.9	0.24	0.24	5179.2	0.0	0.00
C-113-7-2-7	293.5	2.6	112.9	0.24	0.24	5179.2	749.9	0.14
C-113-7-4-7	293.5	2.6	112.9	0.24	0.24	5179.2	1499.7	0.29
C-113-7-6-7	293.5	2.6	112.9	0.24	0.24	5179.2	2249.6	0.43
C-113-7-8-7	293.5	2.6	112.9	0.24	0.24	5179.2	2999.4	0.58
C-113-7-10-7	293.5	2.6	112.9	0.24	0.24	5179.2	5179.2	1.00
C-133-7-0-7	292.7	2.2	133.1	0.28	0.20	5018.7	0.0	0.00
C-133-7-2-7	292.7	2.2	133.1	0.28	0.20	5018.7	719.3	0.14
C-133-7-4-7	292.7	2.2	133.1	0.28	0.20	5018.7	1438.6	0.29
C-133-7-6-7	292.7	2.2	133.1	0.28	0.20	5018.7	2157.9	0.43
C-133-7-8-7	292.7	2.2	133.1	0.28	0.20	5018.7	2877.2	0.57

Table 6.2 continued.

C-133-7-10-7	292.7	2.2	133.1	0.28	0.20	5018.7	5018.7	1.00
C-146-7-0-7	292.3	2	146.2	0.31	0.18	4968.2	0.0	0.00
C-146-7-2-7	292.3	2	146.2	0.31	0.18	4968.2	704.0	0.14
C-146-7-4-7	292.3	2	146.2	0.31	0.18	4968.2	1408.1	0.28
C-146-7-6-7	292.3	2	146.2	0.31	0.18	4968.2	2112.1	0.43
C-146-7-8-7	292.3	2	146.2	0.31	0.18	4968.2	2816.2	0.57
C-146-7-10-7	292.3	2	146.2	0.31	0.18	4968.2	4968.2	1.00

Table 6.3 Analysis Matrix for Rectangular CFT Beam-Columns with Different Material Strength Ratios and Axial Load Ratios

ID.	F_y (MPa)	f'_c (MPa)	F_y/f'_c	ξ	P_f (kN)	P (kN)	P/P_f
R-70-25-0-3	525	21	25	1.45	1854.1	0.0	0.00
R-70-25-2-3	525	21	25	1.45	1854.1	275.3	0.15
R-70-25-4-3	525	21	25	1.45	1854.1	550.6	0.30
R-70-25-6-3	525	21	25	1.45	1854.1	825.9	0.45
R-70-25-10-3	525	21	25	1.45	1854.1	1854.1	1.00
R-70-23-0-3	473	21	22.52	1.31	1789.8	0.0	0.00
R-70-23-2-3	473	21	22.52	1.31	1789.8	275.3	0.15
R-70-23-4-3	473	21	22.52	1.31	1789.8	550.6	0.31
R-70-23-6-3	473	21	22.52	1.31	1789.8	825.9	0.46
R-70-23-10-3	473	21	22.52	1.31	1789.8	1789.8	1.00
R-70-20-0-3	421	21	20.05	1.16	1715.1	0.0	0.00
R-70-20-2-3	421	21	20.05	1.16	1715.1	275.3	0.16
R-70-20-4-3	421	21	20.05	1.16	1715.1	550.6	0.32
R-70-20-6-3	421	21	20.05	1.16	1715.1	825.9	0.48
R-70-20-10-3	421	21	20.05	1.16	1715.1	1715.1	1.00
R-70-18-0-3	369	21	17.57	1.02	1616.7	0.0	0.00
R-70-18-2-3	369	21	17.57	1.02	1616.7	275.3	0.17
R-70-18-4-3	369	21	17.57	1.02	1616.7	550.6	0.34
R-70-18-6-3	369	21	17.57	1.02	1616.7	825.9	0.51
R-70-18-10-3	369	21	17.57	1.02	1616.7	1616.7	1.00
R-70-15-0-3	317	21	15.1	0.88	1500.3	0.0	0.00
R-70-15-2-3	317	21	15.1	0.88	1500.3	264.8	0.18
R-70-15-4-3	317	21	15.1	0.88	1500.3	529.6	0.35
R-70-15-6-3	317	21	15.1	0.88	1500.3	794.5	0.53
R-70-15-10-3	317	21	15.1	0.88	1500.3	1500.3	1.00
R-70-12-0-3	253	21	12.05	0.70	1358.8	0.0	0.00
R-70-12-2-3	253	21	12.05	0.70	1358.8	246.4	0.18
R-70-12-4-3	253	21	12.05	0.70	1358.8	492.8	0.36
R-70-12-6-3	253	21	12.05	0.70	1358.8	739.1	0.54
R-70-12-10-3	253	21	12.05	0.70	1358.8	1358.8	1.00
R-70-8-0-3	253	30	8.433	0.49	1661.3	0.0	0.00
R-70-8-2-3	253	30	8.433	0.49	1661.3	303.7	0.18
R-70-8-4-3	253	30	8.433	0.49	1661.3	607.4	0.37
R-70-8-6-3	253	30	8.433	0.49	1661.3	911.1	0.55
R-70-8-10-3	253	30	8.433	0.49	1661.3	1661.3	1.00

Table 6.3 continued.

R-70-6-0-3	253	40	6.325	0.37	2037.2	0.0	0.00
R-70-6-2-3	253	40	6.325	0.37	2037.2	367.4	0.18
R-70-6-4-3	253	40	6.325	0.37	2037.2	734.7	0.36
R-70-6-6-3	253	40	6.325	0.37	2037.2	1102.1	0.54
R-70-6-10-3	253	40	6.325	0.37	2037.2	2037.2	1.00
R-70-4-0-3	253	40	4.217	0.24	2785.9	0.0	0.00
R-70-4-2-3	253	40	4.217	0.24	2785.9	494.5	0.18
R-70-4-4-3	253	40	4.217	0.24	2785.9	988.9	0.35
R-70-4-6-3	253	40	4.217	0.24	2785.9	1483.4	0.53
R-70-4-10-3	253	40	4.217	0.24	2785.9	2785.9	1.00
R-70-3-0-3	253	40	3.614	0.21	3158.9	0.0	0.00
R-70-3-2-3	253	40	3.614	0.21	3158.9	555.8	0.18
R-70-3-4-3	253	40	3.614	0.21	3158.9	1111.6	0.35
R-70-3-6-3	253	40	3.614	0.21	3158.9	1667.3	0.53
R-70-3-10-3	253	40	3.614	0.21	3158.9	3158.9	1.00

Table 6.4 Analysis Matrix for Circular CFT Beam-Columns with Different Material Strength Ratios and Axial Load Ratios

ID.	F_y (MPa)	f'_c (MPa)	F_y/f'_c	ξ	P_f (kN)	P (kN)	P/P_f
C-53-25-0-7	525	21	25	2.02	4494	0.0	0.00
C-53-25-2-7	525	21	25	2.02	4494	770.7	0.17
C-53-25-4-7	525	21	25	2.02	4494	1541.3	0.34
C-53-25-6-7	525	21	25	2.02	4494	2312.0	0.51
C-53-25-8-7	525	21	25	2.02	4494	3082.6	0.69
C-53-25-10-7	525	21	25	2.02	4494	4494.0	1.00
C-53-23-0-7	473	21	22.52	1.82	4036	0.0	0.00
C-53-23-2-7	473	21	22.52	1.82	4036	721.4	0.18
C-53-23-4-7	473	21	22.52	1.82	4036	1442.8	0.36
C-53-23-6-7	473	21	22.52	1.82	4036	2164.2	0.54
C-53-23-8-7	473	21	22.52	1.82	4036	2885.6	0.71
C-53-23-10-7	473	21	22.52	1.82	4036	4036.3	1.00
C-53-20-0-7	421	21	20.05	1.62	3709	0.0	0.00
C-53-20-2-7	421	21	20.05	1.62	3709	671.8	0.18
C-53-20-4-7	421	21	20.05	1.62	3709	1343.5	0.36
C-53-20-6-7	421	21	20.05	1.62	3709	2015.3	0.54
C-53-20-8-7	421	21	20.05	1.62	3709	2687.0	0.72
C-53-20-10-7	421	21	20.05	1.62	3709	3708.9	1.00
C-53-18-0-7	369	21	17.57	1.42	3461	0.0	0.00
C-53-18-2-7	369	21	17.57	1.42	3461	621.8	0.18
C-53-18-4-7	369	21	17.57	1.42	3461	1243.5	0.36
C-53-18-6-7	369	21	17.57	1.42	3461	1865.3	0.54
C-53-18-8-7	369	21	17.57	1.42	3461	2487.0	0.72
C-53-18-10-7	369	21	17.57	1.42	3461	3460.7	1.00
C-53-15-0-7	317	21	15.1	1.22	3067	0.0	0.00
C-53-15-2-7	317	21	15.1	1.22	3067	571.4	0.19
C-53-15-4-7	317	21	15.1	1.22	3067	1142.7	0.37
C-53-15-6-7	317	21	15.1	1.22	3067	1714.1	0.56
C-53-15-8-7	317	21	15.1	1.22	3067	2285.5	0.75
C-53-15-10-7	317	21	15.1	1.22	3067	3066.9	1.00
C-53-14-0-7	420	30	14	1.13	4232	0.0	0.00
C-53-14-2-7	420	30	14	1.13	4232	774.1	0.18
C-53-14-4-7	420	30	14	1.13	4232	1548.3	0.37
C-53-14-6-7	420	30	14	1.13	4232	2322.4	0.55
C-53-14-8-7	420	30	14	1.13	4232	3096.5	0.73

Table 6.4 continued.

C-53-14-10-7	420	30	14	1.13	4232	4231.6	1.00
C-53-11-0-7	420	40	10.5	0.85	4899	0.0	0.00
C-53-11-2-7	420	40	10.5	0.85	4899	888.0	0.18
C-53-11-4-7	420	40	10.5	0.85	4899	1775.9	0.36
C-53-11-6-7	420	40	10.5	0.85	4899	2663.9	0.54
C-53-11-8-7	420	40	10.5	0.85	4899	3551.8	0.73
C-53-11-10-7	420	40	10.5	0.85	4899	4899.0	1.00
C-53-8-0-7	420	50	8.4	0.68	5404	0.0	0.00
C-53-8-2-7	420	50	8.4	0.68	5404	1000.8	0.19
C-53-8-4-7	420	50	8.4	0.68	5404	2001.7	0.37
C-53-8-6-7	420	50	8.4	0.68	5404	3002.5	0.56
C-53-8-8-7	420	50	8.4	0.68	5404	4003.3	0.74
C-53-8-10-7	420	50	8.4	0.68	5404	5404.0	1.00
C-53-7-0-7	420	60	7	0.56	5404	0.0	0.00
C-53-7-2-7	420	60	7	0.56	5404	1112.8	0.21
C-53-7-4-7	420	60	7	0.56	5404	2225.6	0.41
C-53-7-6-7	420	60	7	0.56	5404	3338.4	0.62
C-53-7-8-7	420	60	7	0.56	5404	4451.2	0.82
C-53-7-10-7	420	60	7	0.56	5404	5700.0	1.05
C-53-6-0-7	420	70	6	0.48	5404	0.0	0.00
C-53-6-2-7	420	70	6	0.48	5404	1112.8	0.21
C-53-6-4-7	420	70	6	0.48	5404	2225.6	0.41
C-53-6-6-7	420	70	6	0.48	5404	3338.4	0.62
C-53-6-8-7	420	70	6	0.48	5404	4451.2	0.82
C-53-6-10-7	420	70	6	0.48	5404	5898.3	1.09

Table 6.5 Analysis Matrix for Rectangular CFT Beam-Columns with Different Length-to-Depth Ratios and Axial Load Ratios

ID.	L (mm)	B (mm)	L/B	P_f (kN)	P (kN)	P/P_f
R-140-5-0-3	600	201.5	3.0	2153.1	0.0	0.00
R-140-5-2-3	600	201.5	3.0	2153.1	274.7	0.13
R-140-5-4-3	600	201.5	3.0	2153.1	549.4	0.26
R-140-5-6-3	600	201.5	3.0	2153.1	824.0	0.38
R-140-5-10-3	600	201.5	3.0	2153.1	2153.1	1.00
R-140-5-0-10	2000	201.5	9.9	2020.2	0.0	0.00
R-140-5-2-10	2000	201.5	9.9	2020.2	260.6	0.13
R-140-5-4-10	2000	201.5	9.9	2020.2	521.3	0.26
R-140-5-6-10	2000	201.5	9.9	2020.2	781.9	0.39
R-140-5-10-10	2000	201.5	9.9	2020.2	2020.2	1.00
R-140-5-0-20	4000	201.5	19.8	1986.5	0.0	0.00
R-140-5-2-20	4000	201.5	19.8	1986.5	219.2	0.11
R-140-5-4-20	4000	201.5	19.8	1986.5	438.4	0.22
R-140-5-6-20	4000	201.5	19.8	1986.5	657.6	0.33
R-140-5-10-20	4000	201.5	19.8	1986.5	1986.5	1.00

Table 6.6 Analysis Matrix for Circular CFT Beam-Columns with Different Length-to-Depth Ratios and Axial Load Ratios

ID.	L (mm)	D (mm)	L/D	P_f (kN)	P (kN)	P/P_f
C-146-7-0-7	2000	292.3	6.8	4225.2	0.0	0.00
C-146-7-2-7	2000	292.3	6.8	4225.2	704.4	0.17
C-146-7-4-7	2000	292.3	6.8	4225.2	1408.8	0.33
C-146-7-6-7	2000	292.3	6.8	4225.2	2113.2	0.50
C-146-7-10-7	2000	292.3	6.8	4225.2	4225.2	1.00
C-146-7-0-13	4000	292.3	13.7	4107.2	0.0	0.00
C-146-7-2-13	4000	292.3	13.7	4107.2	605.0	0.15
C-146-7-4-13	4000	292.3	13.7	4107.2	1210.0	0.29
C-146-7-6-13	4000	292.3	13.7	4107.2	1814.9	0.44
C-146-7-10-13	4000	292.3	13.7	4107.2	4107.2	1.00
C-146-7-0-21	6000	292.3	20.5	3852.6	0.0	0.00
C-146-7-2-21	6000	292.3	20.5	3852.6	469.5	0.12
C-146-7-4-21	6000	292.3	20.5	3852.6	938.9	0.24
C-146-7-6-21	6000	292.3	20.5	3852.6	1408.4	0.37
C-146-7-10-21	6000	292.3	20.5	3852.6	3852.6	1.00

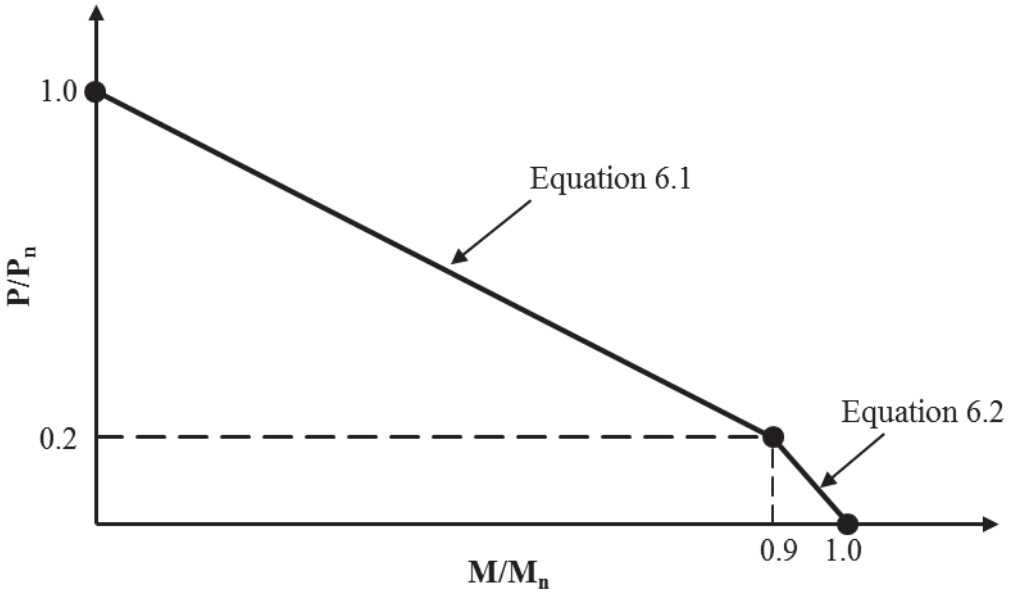

Figure 6.1 Example of the AISC 360-10 P-M Interaction Curve for Designing Noncompact and Slender CFT Beam-Columns

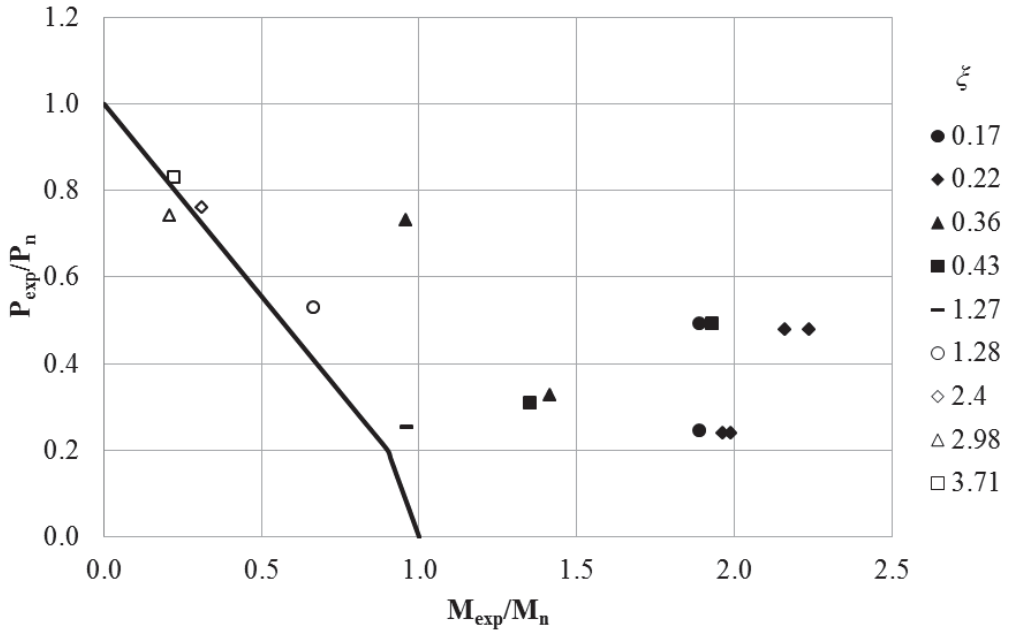

Figure 6.2 Comparisons of the AISC 360-10 P-M Interaction Curve with Experimental Results for Rectangular Noncompact and Slender CFT Beam-Columns

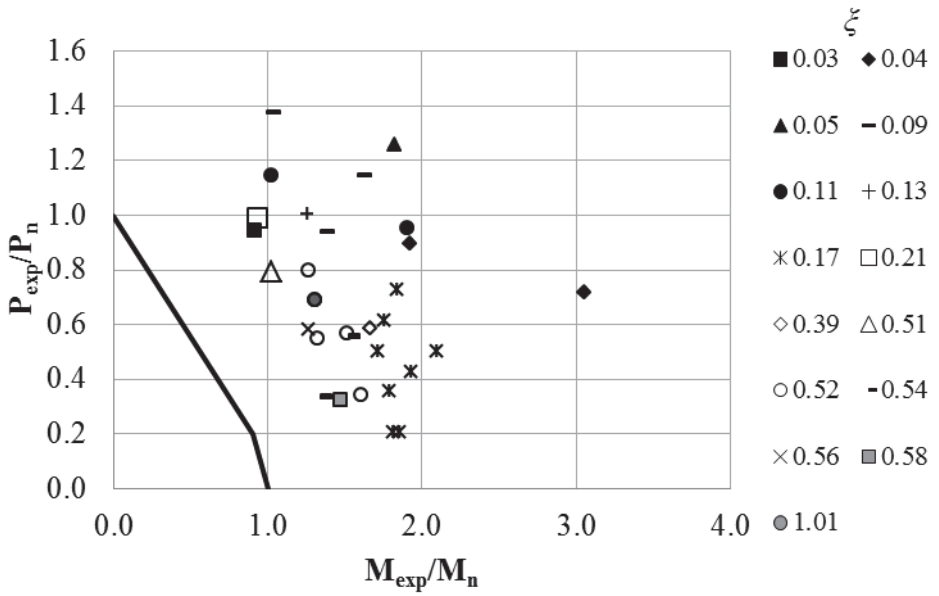

Figure 6.3 Comparisons of the AISC 360-10 P-M Interaction Curve with Experimental Results for Circular Noncompact and Slender CFT Beam-Columns

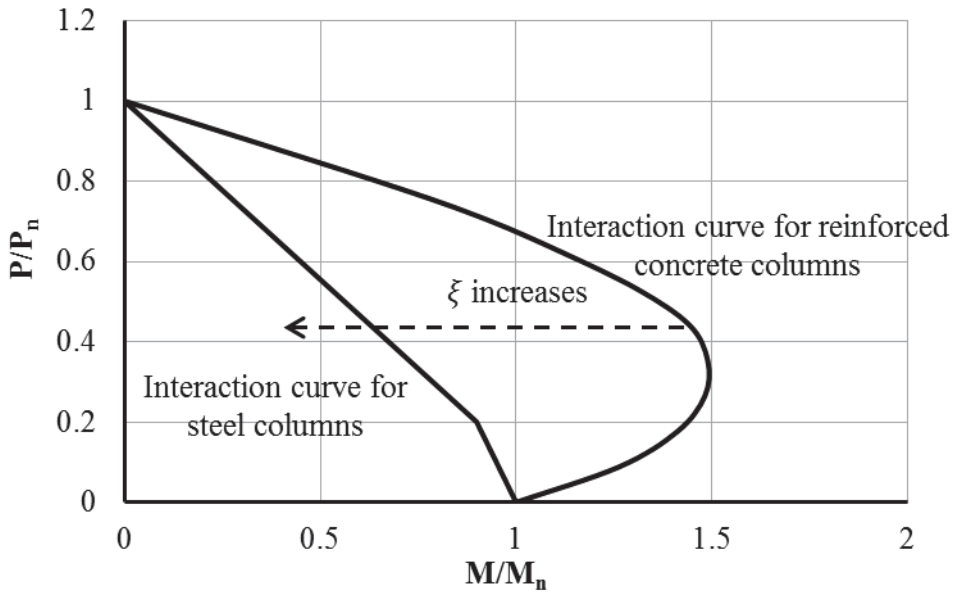

Figure 6.4 Effect of the Relative strength ratio ξ on the Shape of CFT Beam-Column Interaction Curve

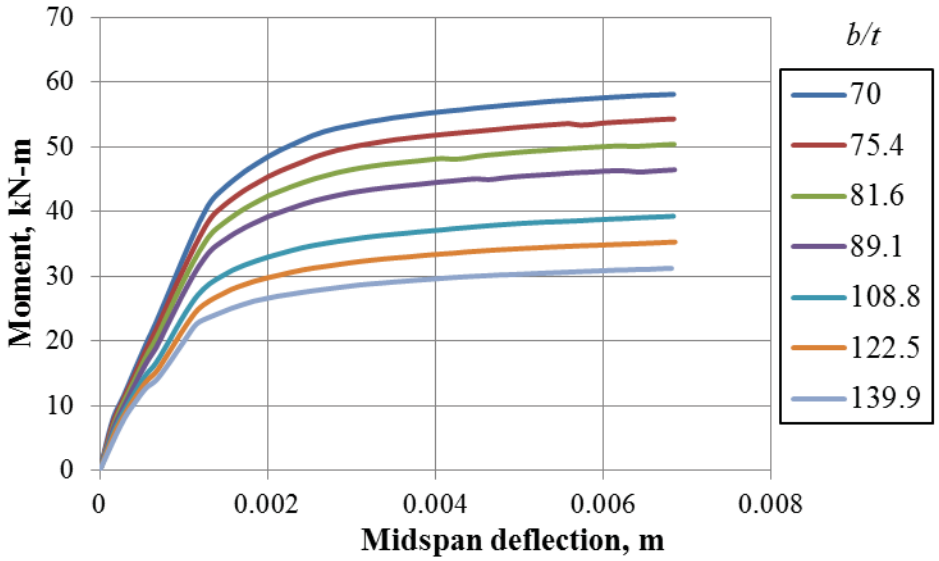

Figure 6.5 Effect of Tube Slenderness Ratio on the Moment-Midspan Deflection Responses of Rectangular CFT Beam-Columns at Axial Load Ratio (P/P_n) of 0 (L/B = 3.0, F_y = 253 MPa, f'_c = 47.6 MPa, and F_y/f'_c = 5.3)

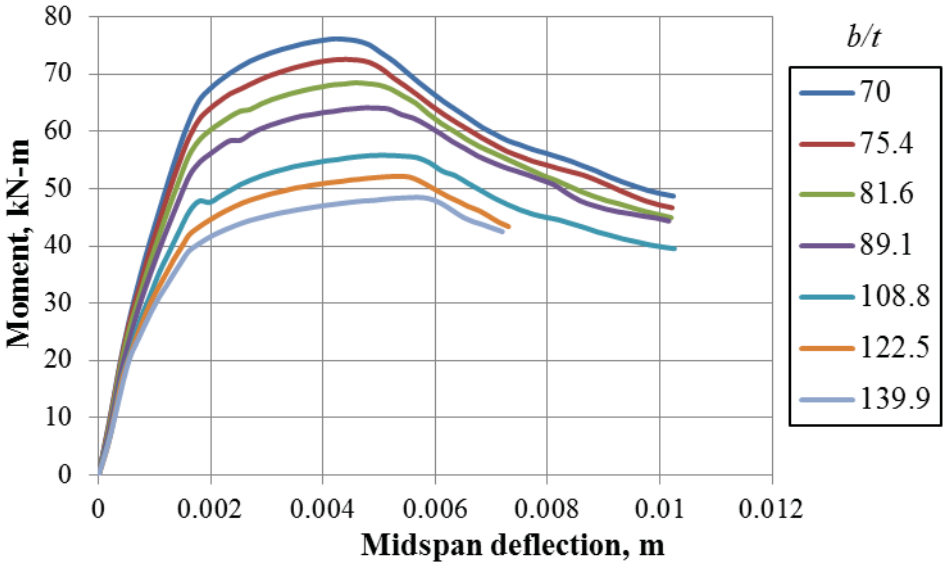

Figure 6.6 Effect of Tube Slenderness Ratio on the Moment-Midspan Deflection Responses of Rectangular CFT Beam-Columns at Axial Load Ratio (P/P_n) of 0.2 (L/B = 3.0, F_y = 253 MPa, f'_c = 47.6 MPa, and F_y/f'_c = 5.3)

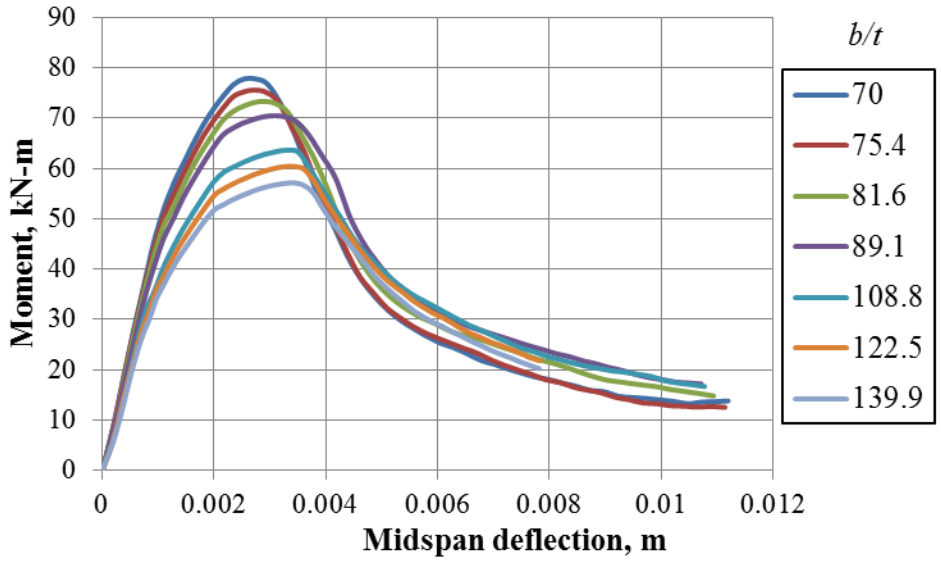

Figure 6.7 Effect of Tube Slenderness Ratio on the Moment-Midspan Deflection Responses of Rectangular CFT Beam-Columns at Axial Load Ratio (P/P_n) of 0.4 (L/B = 3.0, F_y = 253 MPa, f'_c = 47.6 MPa, and F_y/f'_c = 5.3)

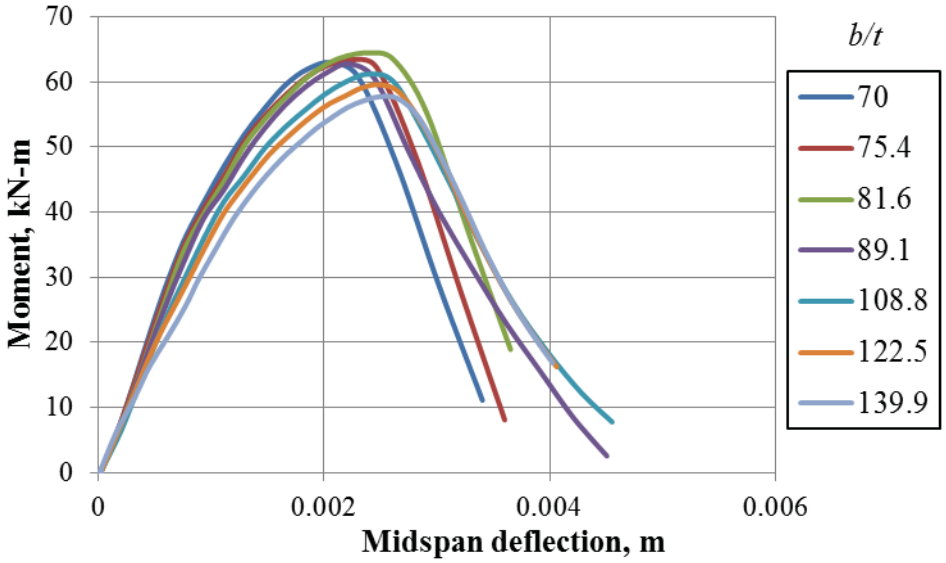

Figure 6.8 Effect of Tube Slenderness Ratio on the Moment-Midspan Deflection Responses of Rectangular CFT Beam-Columns at Axial Load Ratio (P/P_n) of 0.6 (L/B = 3.0, F_y = 253 MPa, f'_c = 47.6 MPa, and F_y/f'_c = 5.3)

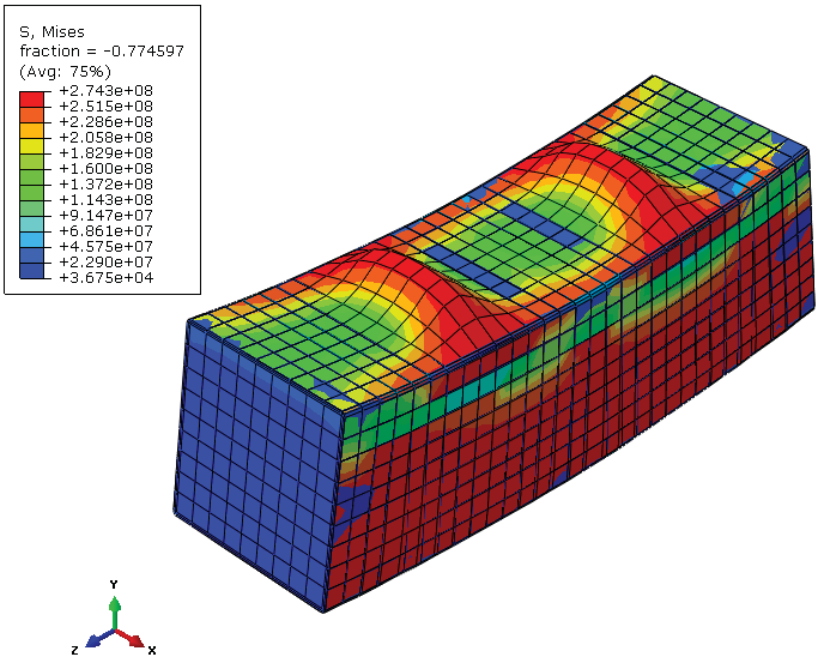

Figure 6.9 Local Buckling of the Steel Compression Flange

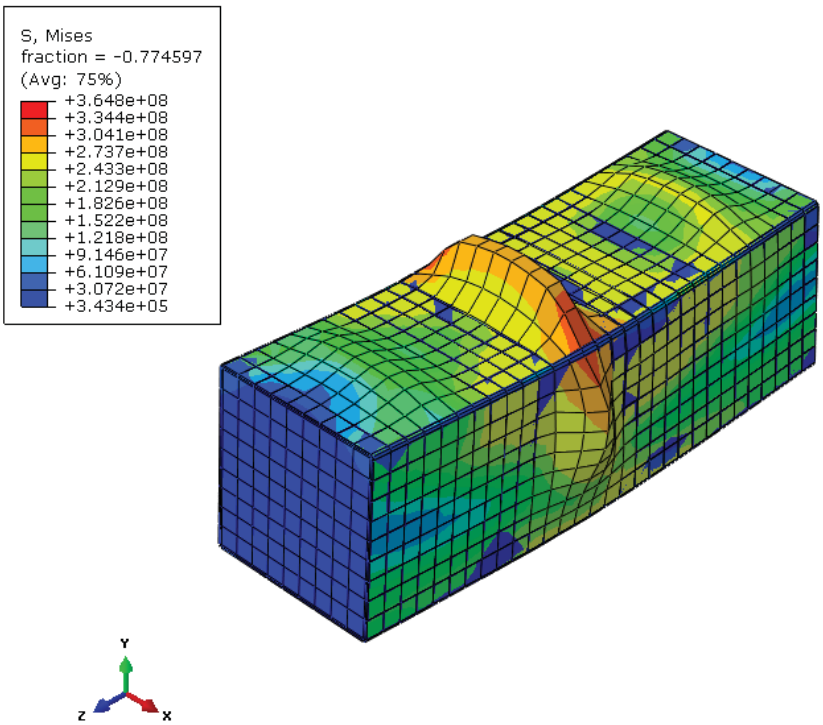

Figure 6.10 Propagation of the Local Buckling to the Webs

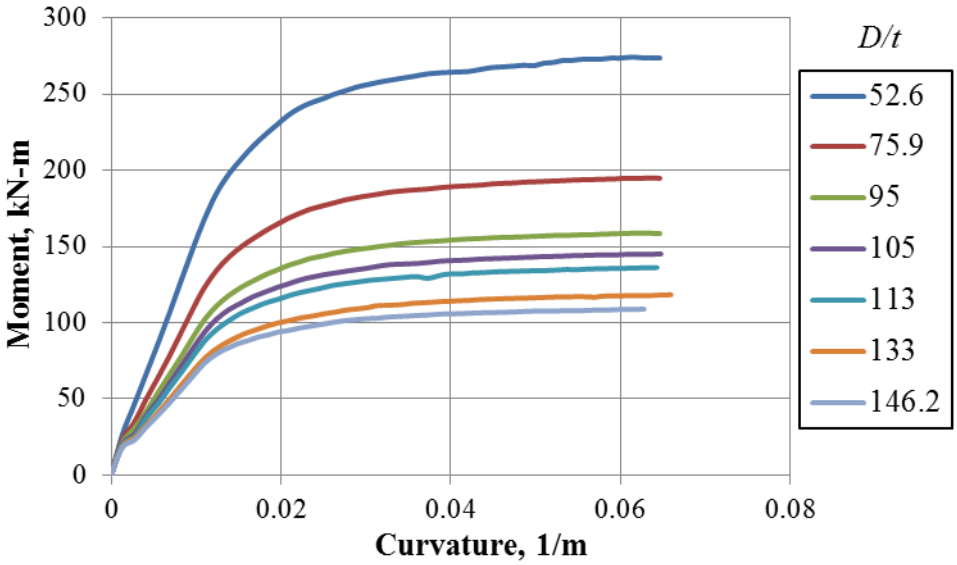

Figure 6.11 Effect of Tube Slenderness Ratio on the Moment-Curvature Responses of Circular CFT Beam-Columns at Axial Load Ratio (P/P_n) of 0 (L/D = 6.7, F_y = 420 MPa, f'_c = 64.3 MPa, and F_y/f'_c = 6.5)

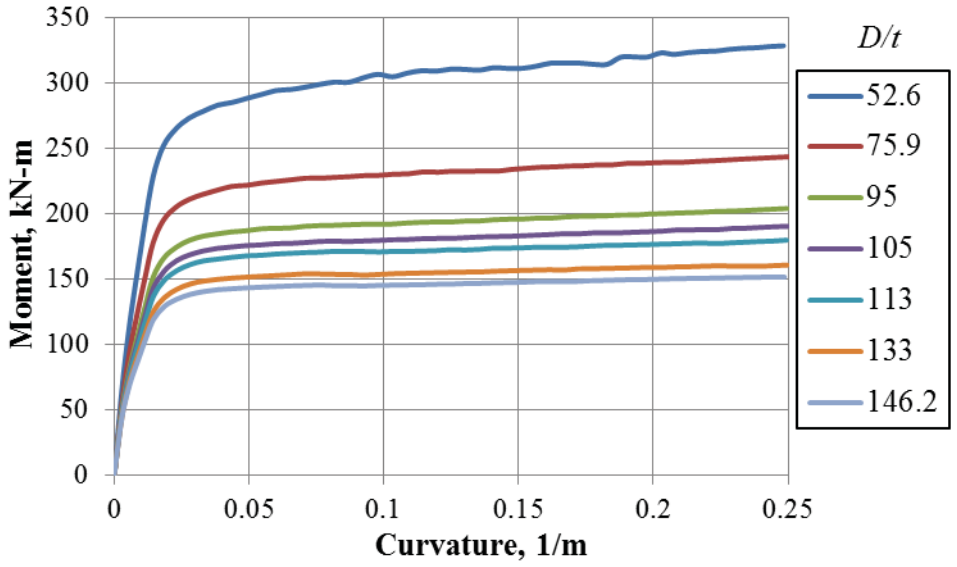

Figure 6.12 Effect of Tube Slenderness Ratio on the Moment-Curvature Responses of Circular CFT Beam-Columns at Axial Load Ratio (P/P_n) of 0.2 (L/D = 6.7, F_y = 420 MPa, f'_c = 64.3 MPa, and F_y/f'_c = 6.5)

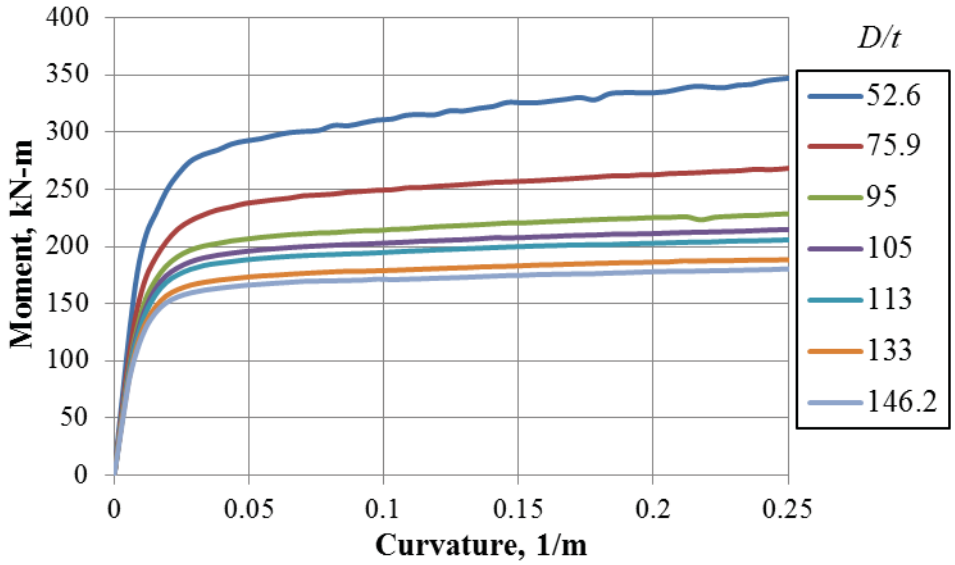

Figure 6.13 Effect of Tube Slenderness Ratio on the Moment-Curvature Responses of Circular CFT Beam-Columns at Axial Load Ratio (P/P_n) of 0.4 (L/D = 6.7, F_y = 420 MPa, f'_c = 64.3 MPa, and F_y/f'_c = 6.5)

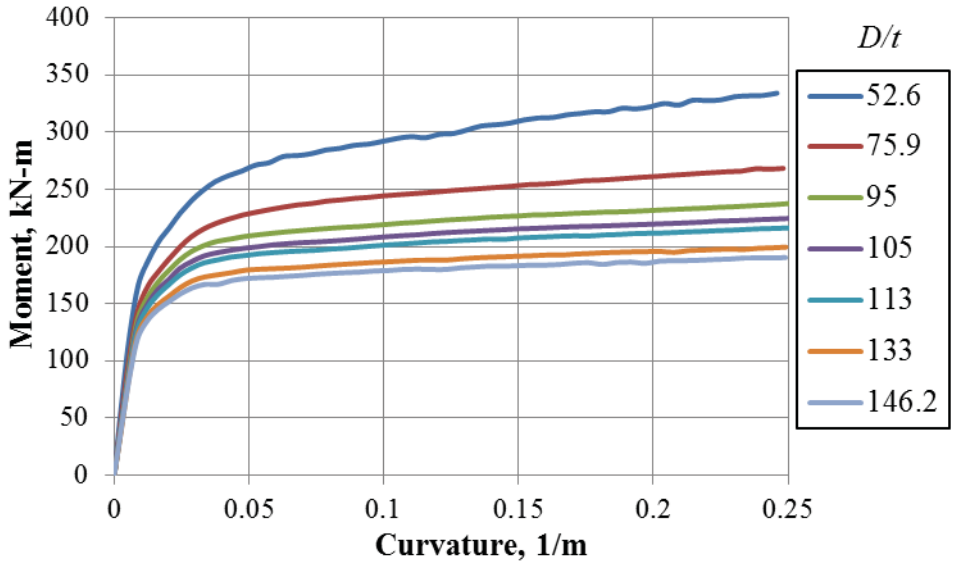

Figure 6.14 Effect of Tube Slenderness Ratio on the Moment-Curvature Responses of Circular CFT Beam-Columns at Axial Load Ratio (P/P_n) of 0.6 (L/D = 6.7, F_y = 420 MPa, f'_c = 64.3 MPa, and F_y/f'_c = 6.5)

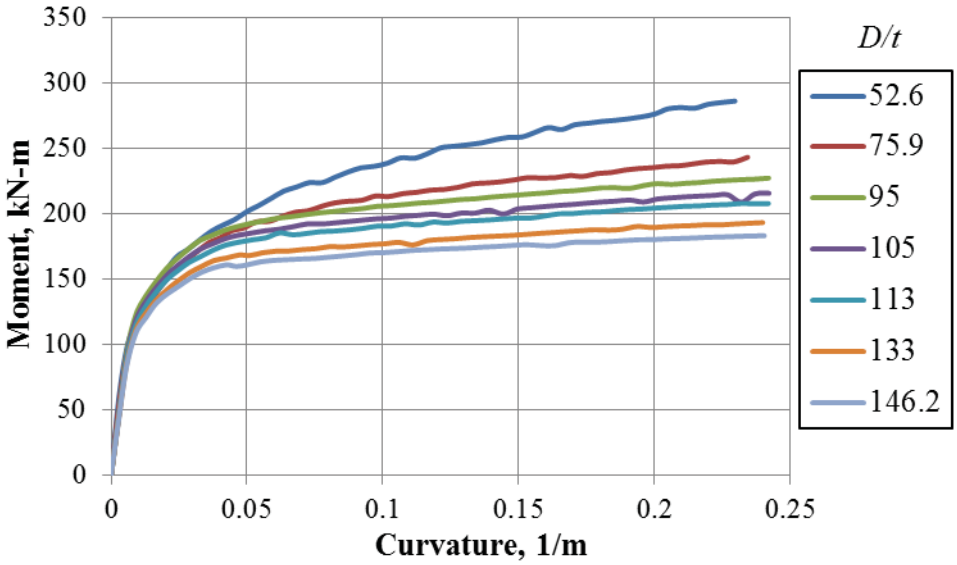

Figure 6.15 Effect of Tube Slenderness Ratio on the Moment-Curvature Responses of Circular CFT Beam-Columns at Axial Load Ratio (P/P_n) of 0.8 (L/D = 6.7, F_y = 420 MPa, f'_c = 64.3 MPa, and F_y/f'_c = 6.5)

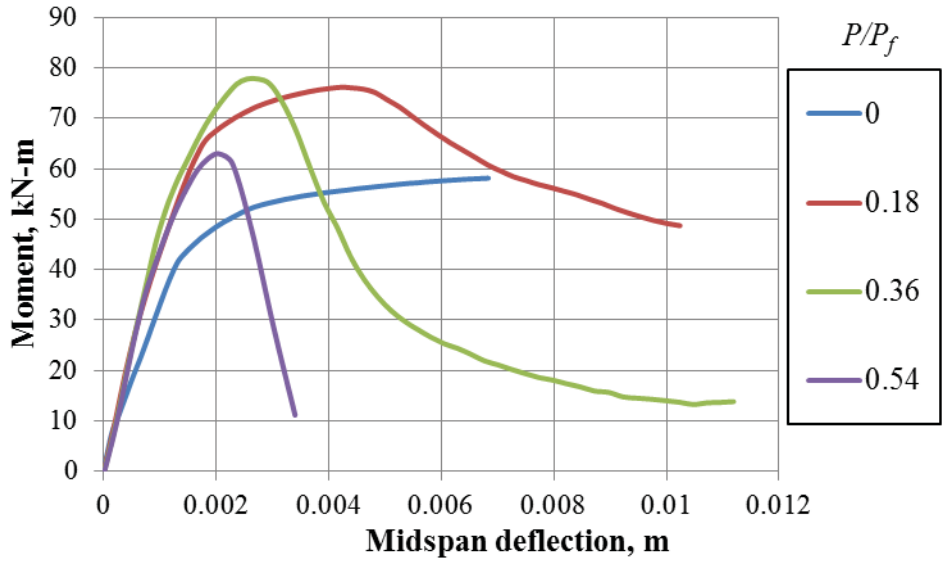

Figure 6.16 Effect of Axial Load Ratio on the Moment-Midspan Deflection Responses of Rectangular CFT Beam-Columns with Tube Slenderness Ratio (b/t_f) of 70.0 (L/B = 3.0, F_y = 253 MPa, f'_c = 47.6 MPa, and F_y/f'_c = 5.3)

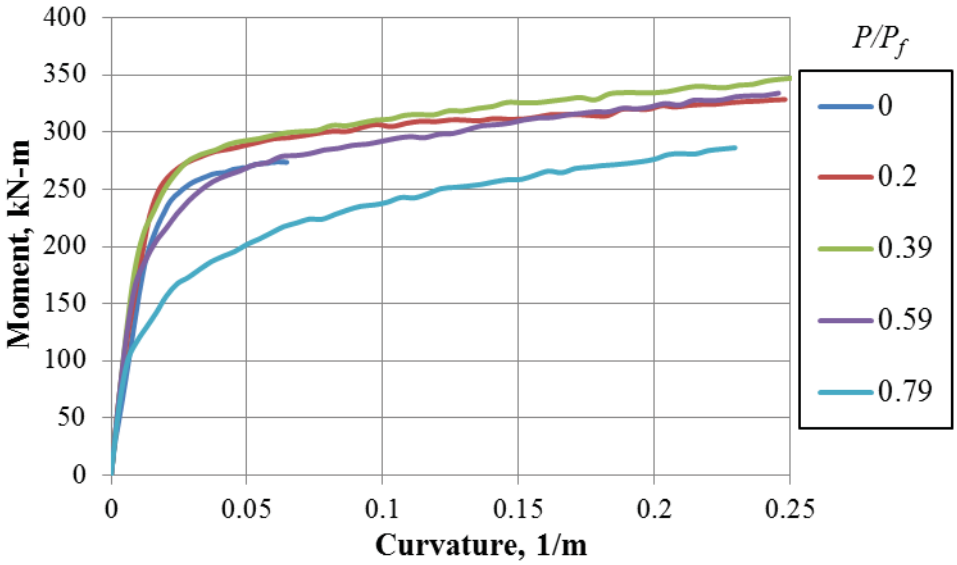

Figure 6.17 Effect of Axial Load Ratio on the Moment-Curvature Responses of Circular CFT Beam-Columns with Tube Slenderness Ratio (D/t) of 52.6 (L/D = 6.7, F_y = 420 MPa, f'_c = 64.3 MPa, and F_y/f'_c = 6.5)

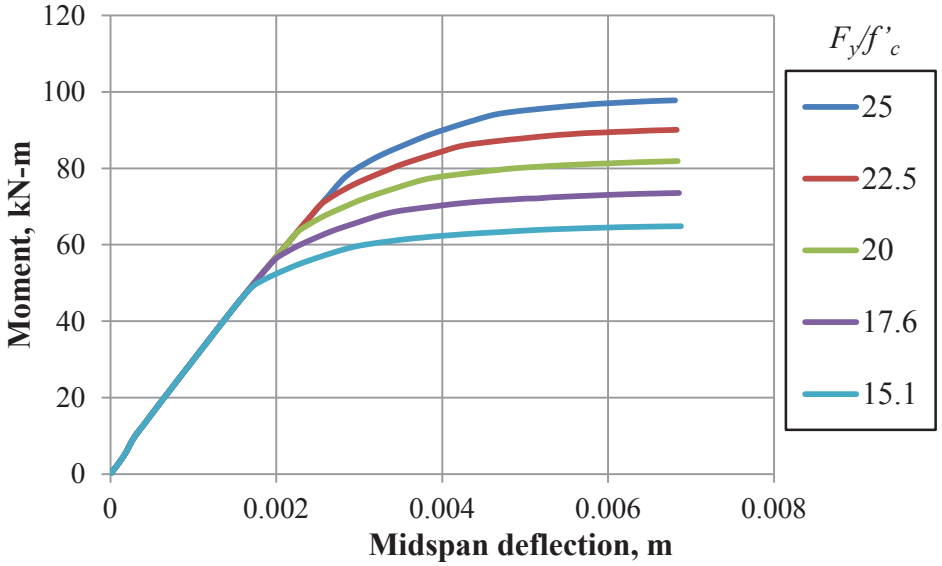

Figure 6.18 Effect of Material Strength Ratios on the Moment-Midspan Deflection Responses of Rectangular CFT Beam-Columns at Different Axial Load Ratios (P/P_n = 0) (B = 201.5 mm, t_f = 2.8 mm, b/t_f = 70.0, L/B = 3.0, and $f'c$ = 21 MPa)

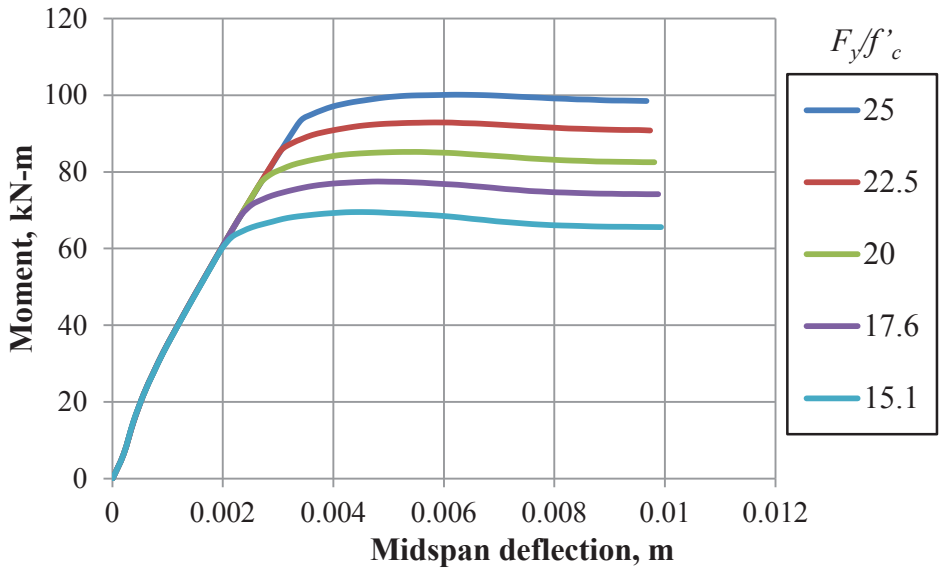

Figure 6.19 Effect of Material Strength Ratios on the Moment-Midspan Deflection Responses of Rectangular CFT Beam-Columns at Different Axial Load Ratios (P/P_n = 0.2) (B = 201.5 mm, t_f = 2.8 mm, b/t_f = 70.0, L/B = 3.0, and $f'c$ = 21 MPa)

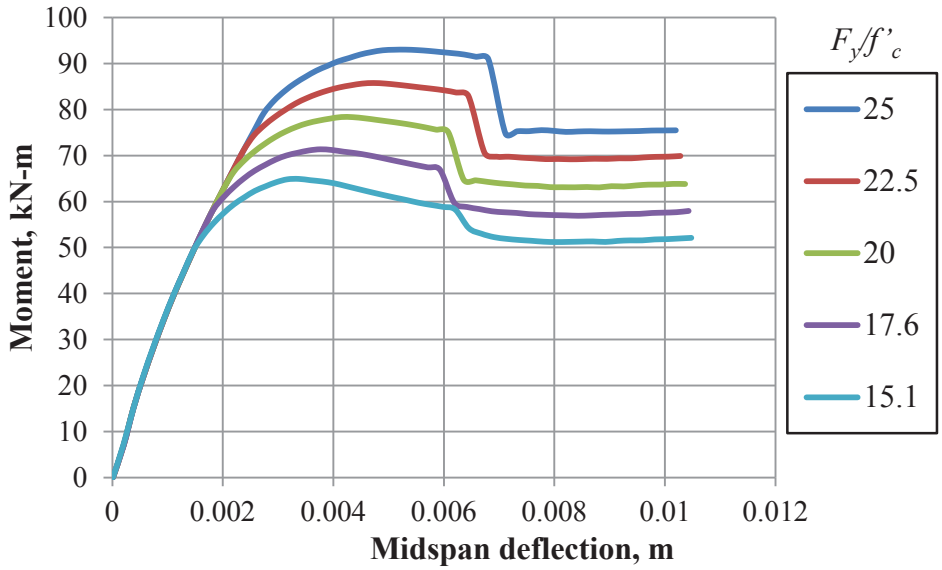

Figure 6.20 Effect of Material Strength Ratios on the Moment-Midspan Deflection Responses of Rectangular CFT Beam-Columns at Different Axial Load Ratios (P/P_n = 0.4) (B = 201.5 mm, t_f = 2.8 mm, b/t_f = 70.0, L/B = 3.0, and $f'c$ = 21 MPa)

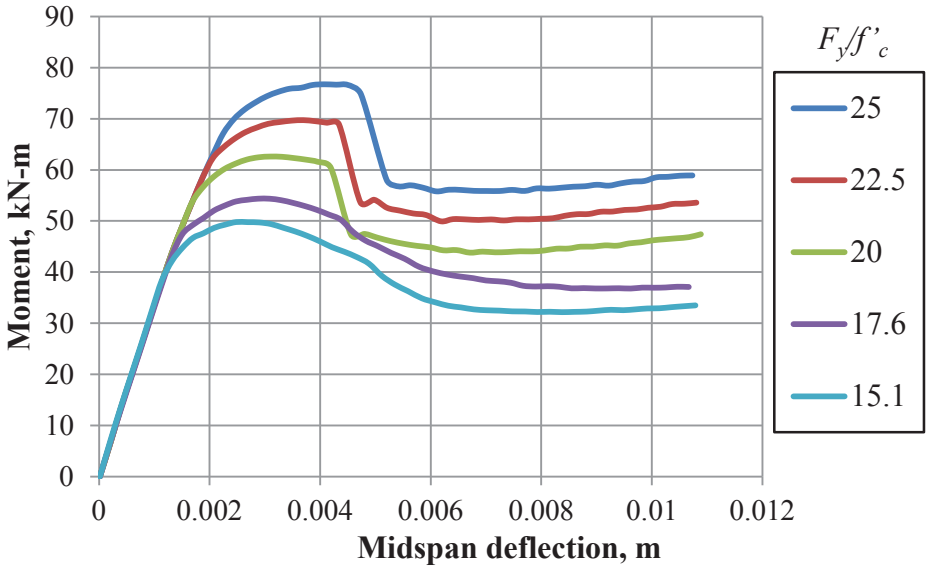

Figure 6.21 Effect of Material Strength Ratios on the Moment-Midspan Deflection Responses of Rectangular CFT Beam-Columns at Different Axial Load Ratios (P/P_n = 0.6) (B = 201.5 mm, t_f = 2.8 mm, b/t_f = 70.0, L/B = 3.0, and $f'c$ = 21 MPa)

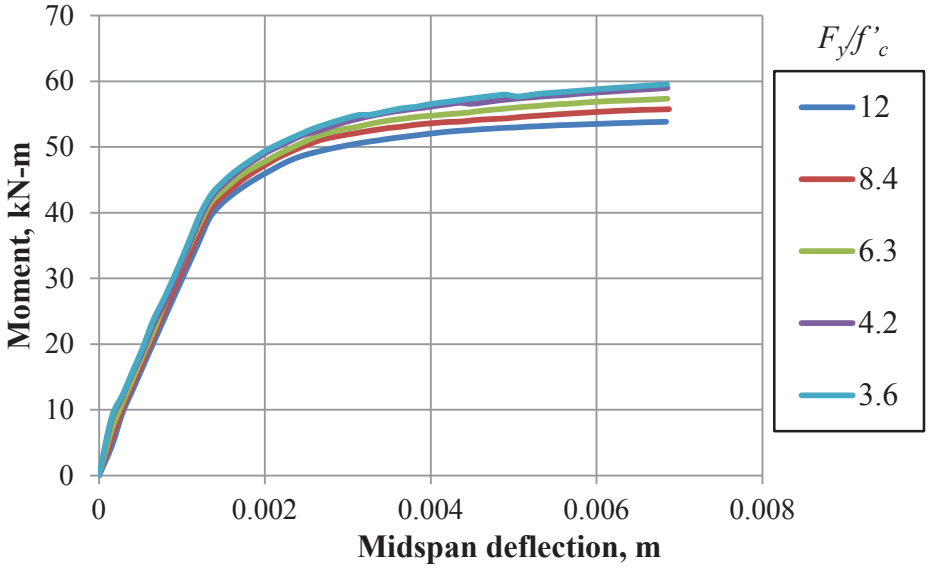

Figure 6.22 Effect of Material Strength Ratios on the Moment-Midspan Deflection Responses of Rectangular CFT Beam-Columns at Different Axial Load Ratios (P/P_n = 0) (B = 201.5 mm, t_f = 2.8 mm, b/t_f = 70.0, L/B = 3.0, and F_y = 253 MPa)

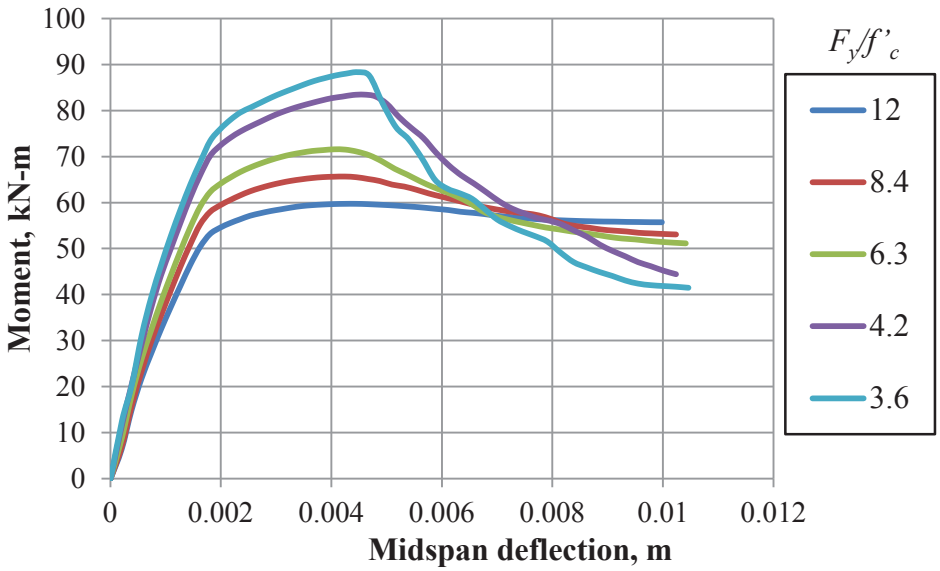

Figure 6.23 Effect of Material Strength Ratios on the Moment-Midspan Deflection Responses of Rectangular CFT Beam-Columns at Different Axial Load Ratios (P/P_n = 0.2) (B = 201.5 mm, t_f = 2.8 mm, b/t_f = 70.0, L/B = 3.0, and F_y = 253 MPa)

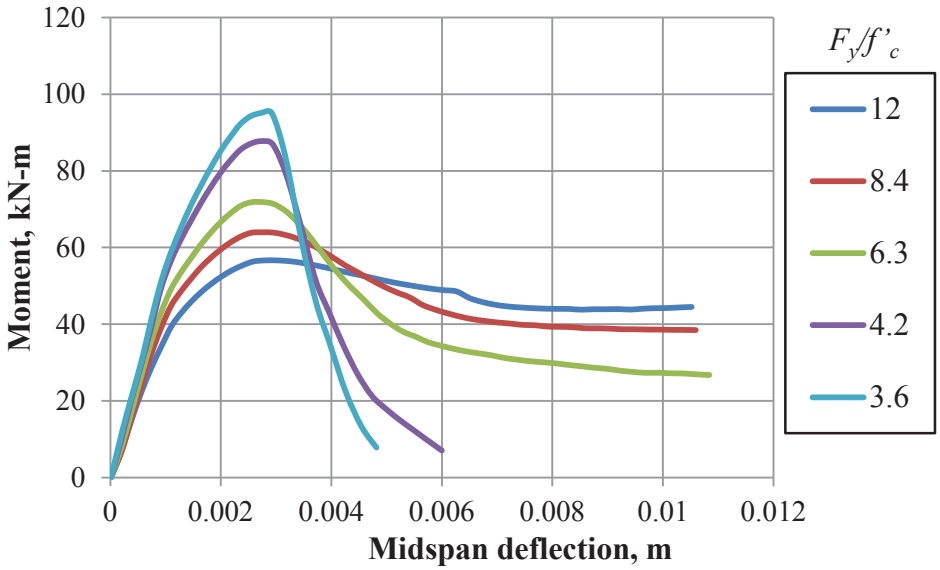

Figure 6.24 Effect of Material Strength Ratios on the Moment-Midspan Deflection Responses of Rectangular CFT Beam-Columns at Different Axial Load Ratios (P/P_n = 0.4) (B = 201.5 mm, t_f = 2.8 mm, b/t_f = 70.0, L/B = 3.0, and F_y = 253 MPa)

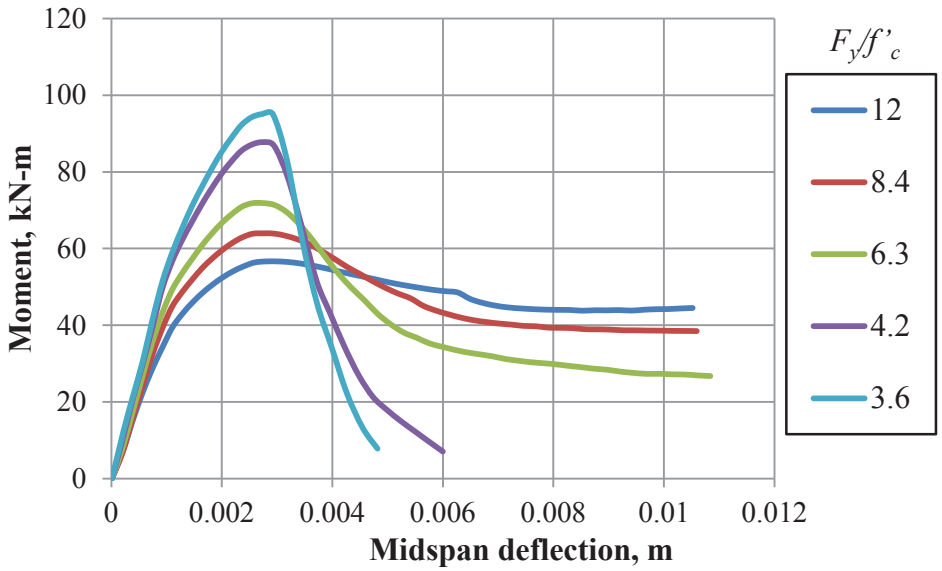

Figure 6.25 Effect of Material Strength Ratios on the Moment-Midspan Deflection Responses of Rectangular CFT Beam-Columns at Different Axial Load Ratios (P/P_n = 0.6) (B = 201.5 mm, t_f = 2.8 mm, b/t_f = 70.0, L/B = 3.0, and F_y = 253 MPa)

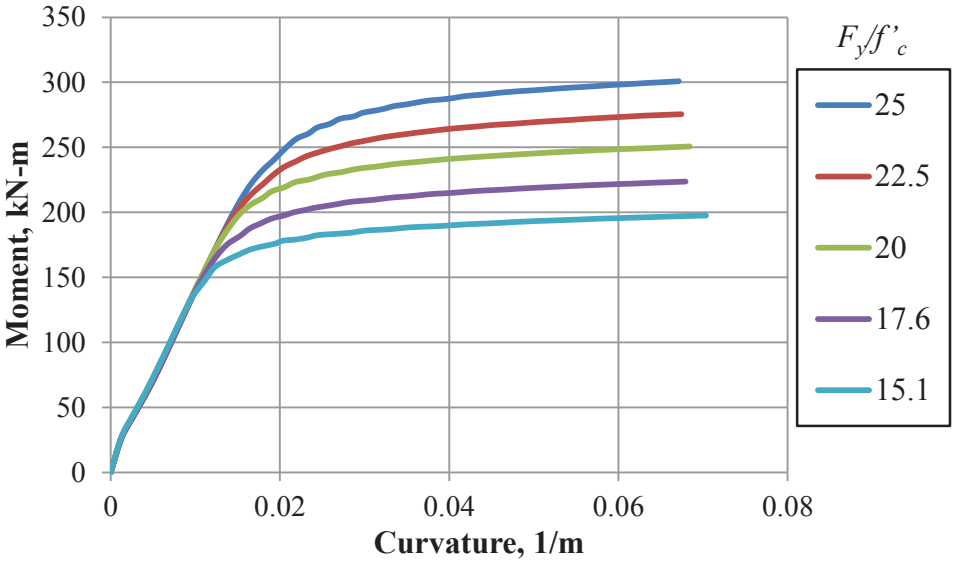

Figure 6.26 Effect of Material Strength Ratios on the Moment-Curvature Responses of Circular CFT Beam-Columns at Different Axial Load Ratios (P/P_n = 0) (D = 299.7 mm, t = 5.7 mm, D/t = 52.6, L/D = 6.7, and $f'c$ = 21 MPa)

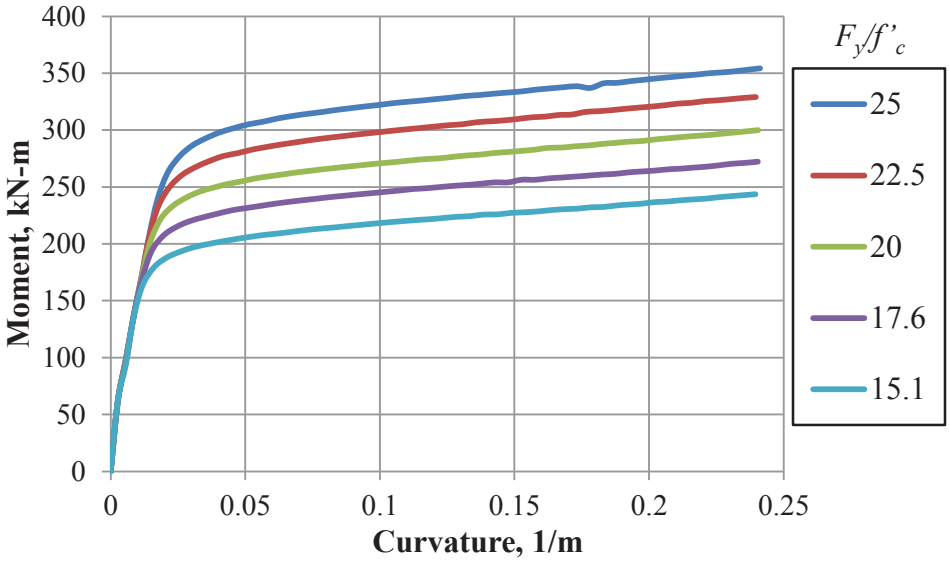

Figure 6.27 Effect of Material Strength Ratios on the Moment-Curvature Responses of Circular CFT Beam-Columns at Different Axial Load Ratios (P/P_n = 0.2) (D = 299.7 mm, t = 5.7 mm, D/t = 52.6, L/D = 6.7, and $f'c$ = 21 MPa)

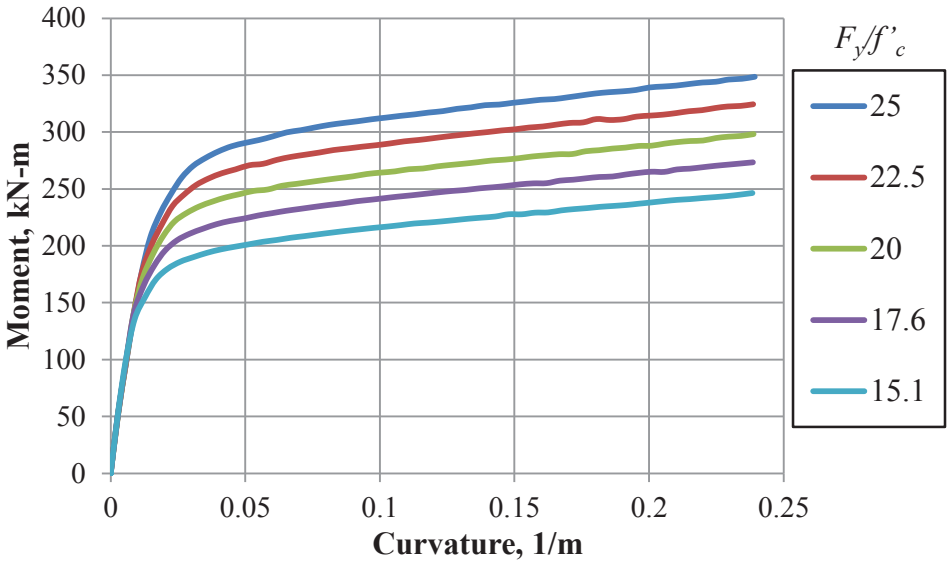

Figure 6.28 Effect of Material Strength Ratios on the Moment-Curvature Responses of Circular CFT Beam-Columns at Different Axial Load Ratios (P/P_n = 0.4) (D = 299.7 mm, t = 5.7 mm, D/t = 52.6, L/D = 6.7, and $f'c$ = 21 MPa)

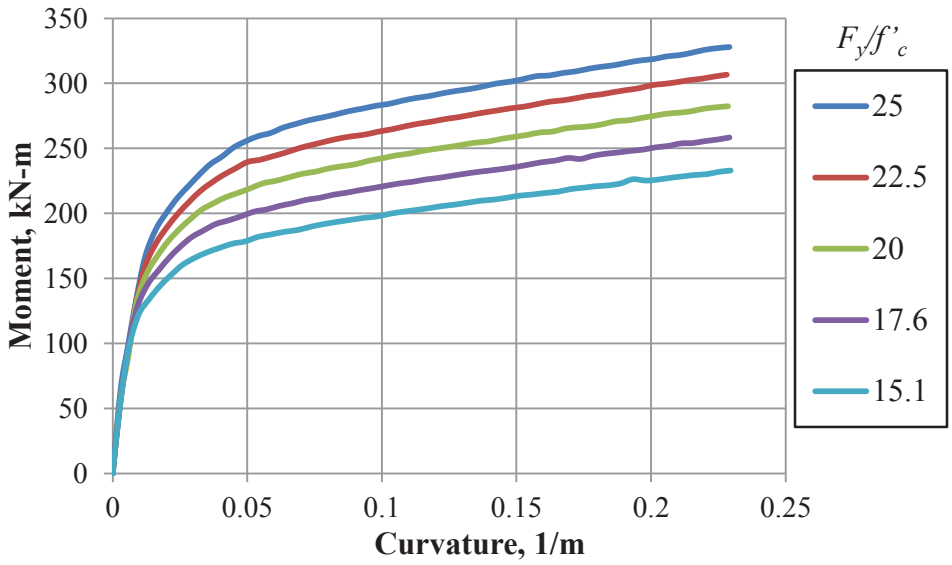

Figure 6.29 Effect of Material Strength Ratios on the Moment-Curvature Responses of Circular CFT Beam-Columns at Different Axial Load Ratios (P/P_n = 0.6) (D = 299.7 mm, t = 5.7 mm, D/t = 52.6, L/D = 6.7, and $f'c$ = 21 MPa)

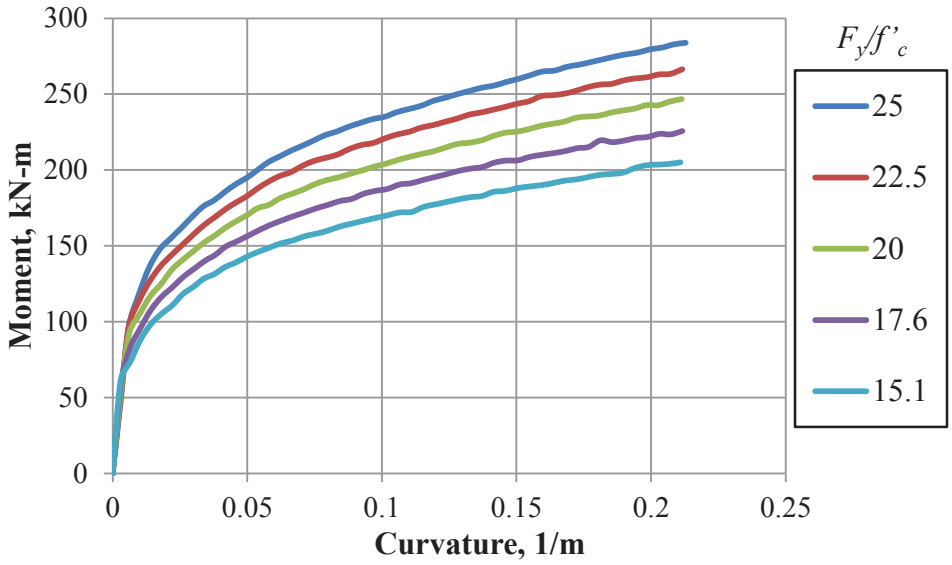

Figure 6.30 Effect of Material Strength Ratios on the Moment-Curvature Responses of Circular CFT Beam-Columns at Different Axial Load Ratios (P/P_n = 0.8) (D = 299.7 mm, t = 5.7 mm, D/t = 52.6, L/D = 6.7, and $f'c$ = 21 MPa)

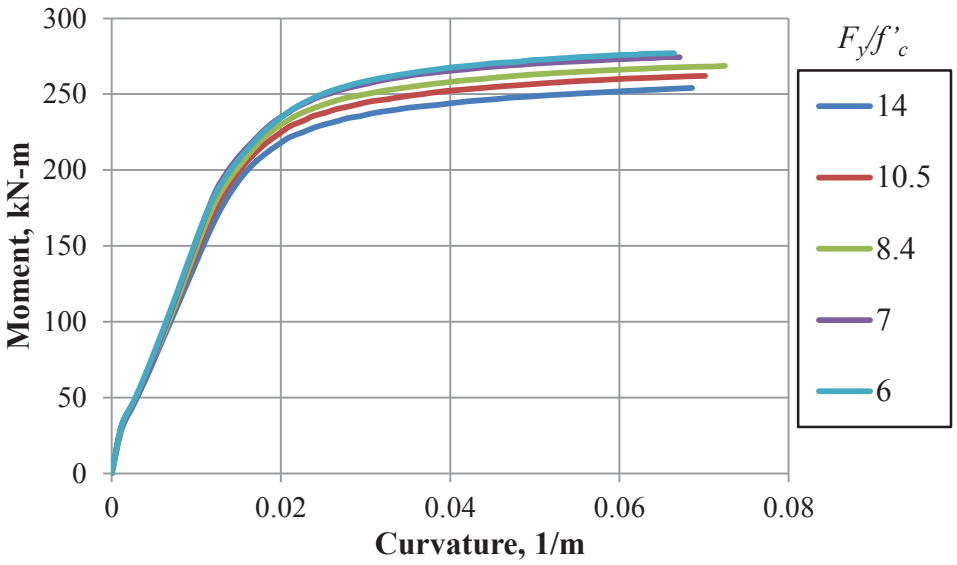

Figure 6.31 Effect of Material Strength Ratios on the Moment-Curvature Responses of Circular CFT Beam-Columns at Different Axial Load Ratios ($P/P_n = 0$) (D = 299.7 mm, t = 5.7 mm, D/t = 52.6, L/D = 6.7, and F_y = 420 MPa)

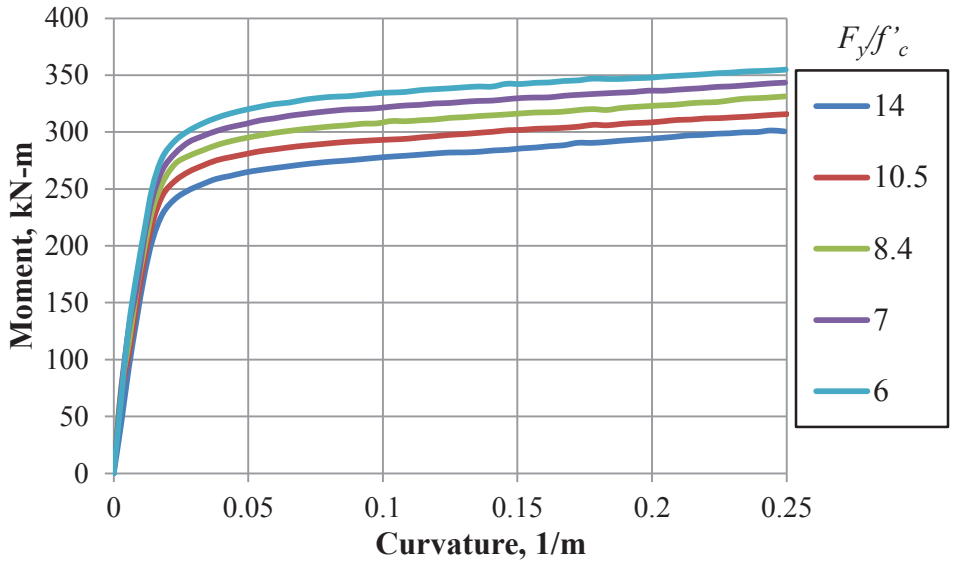

Figure 6.32 Effect of Material Strength Ratios on the Moment-Curvature Responses of Circular CFT Beam-Columns at Different Axial Load Ratios ($P/P_n = 0.2$) (D = 299.7 mm, t = 5.7 mm, D/t = 52.6, L/D = 6.7, and F_y = 420 MPa)

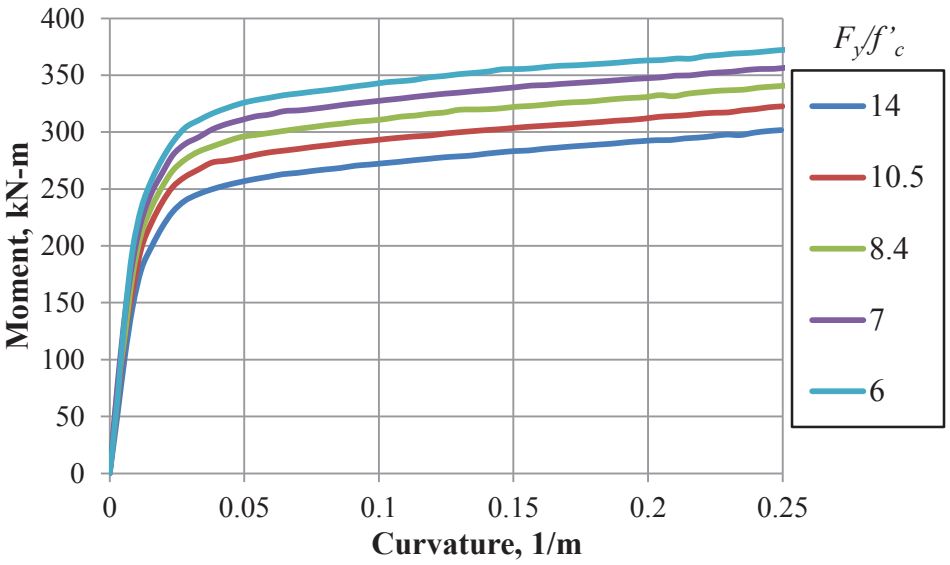

Figure 6.33 Effect of Material Strength Ratios on the Moment-Curvature Responses of Circular CFT Beam-Columns at Different Axial Load Ratios (P/P_n = 0.4) (D = 299.7 mm, t = 5.7 mm, D/t = 52.6, L/D = 6.7, and F_y = 420 MPa)

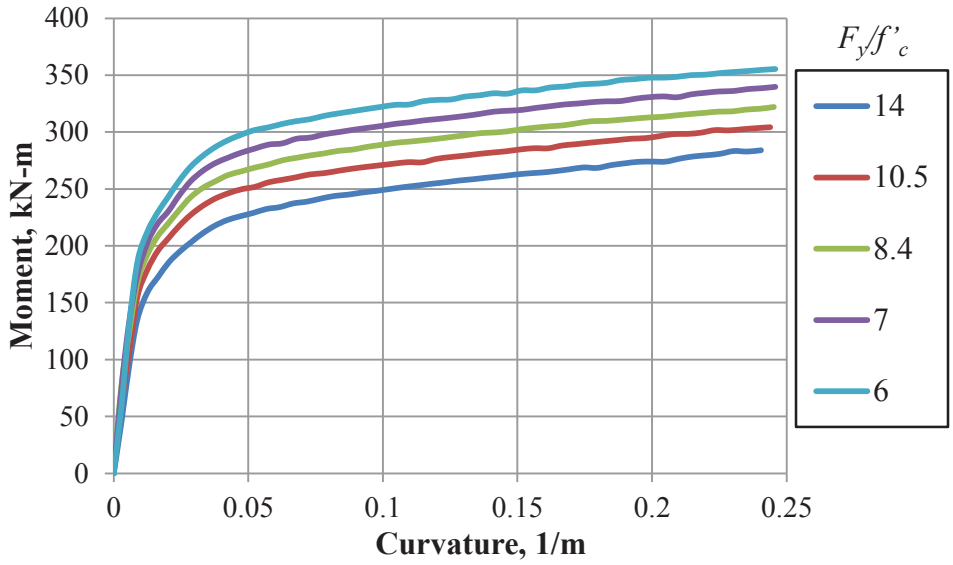

Figure 6.34 Effect of Material Strength Ratios on the Moment-Curvature Responses of Circular CFT Beam-Columns at Different Axial Load Ratios (P/P_n = 0.6) (D = 299.7 mm, t = 5.7 mm, D/t = 52.6, L/D = 6.7, and F_y = 420 MPa)

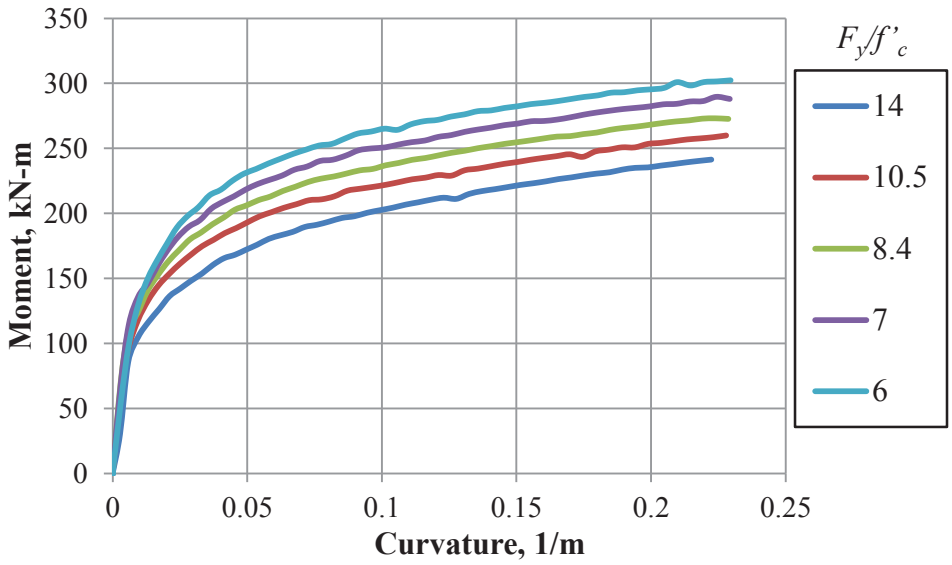

Figure 6.35 Effect of Material Strength Ratios on the Moment-Curvature Responses of Circular CFT Beam-Columns at Different Axial Load Ratios (P/P_n = 0.8) (D = 299.7 mm, t = 5.7 mm, D/t = 52.6, L/D = 6.7, and F_y = 420 MPa)

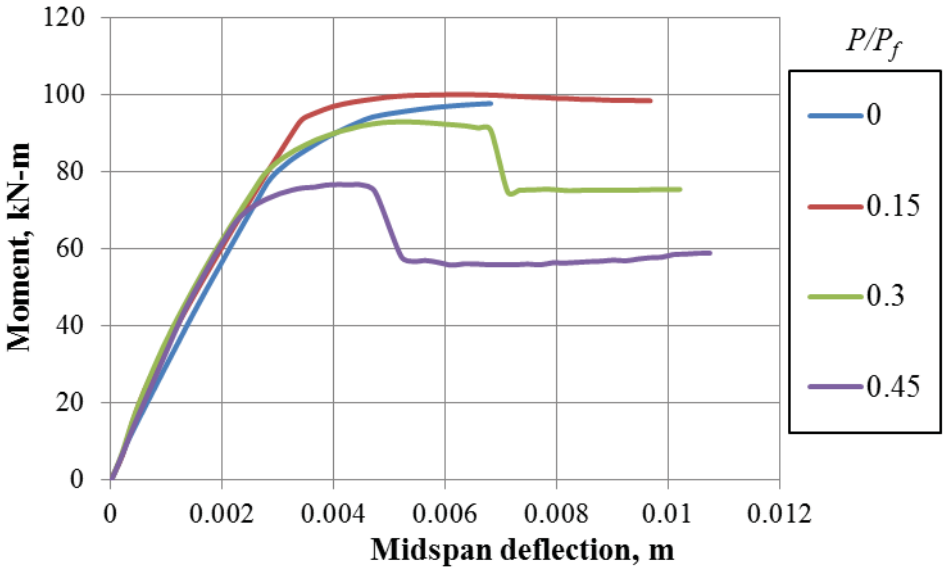

Figure 6.36 Effect of Axial Load Ratio on the Moment-Midspan Deflection Responses of Rectangular CFT Beam-Columns with Material Strength Ratio (F_y/F'_c) of 25.0 (B = 201.5 mm, t_f = 5.7 mm, b/t_f = 70.0, L/B = 3.0, and f'_c = 21 MPa)

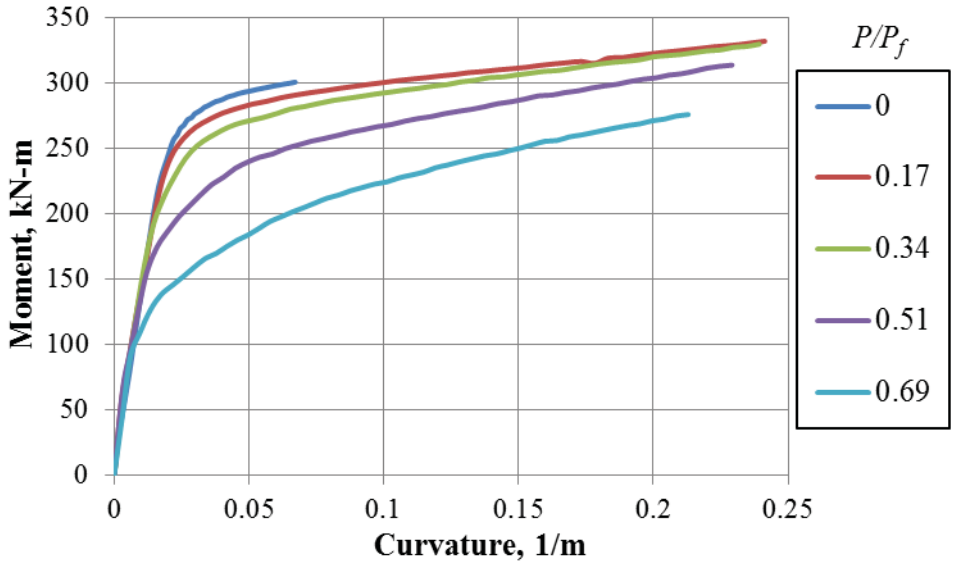

Figure 6.37 Effect of Axial Load Ratio on the Moment-Curvature Responses of Circular CFT Beam-Columns with Material Strength Ratio (F_y/F'_c) of 25.0 (D = 299.7 mm, t = 5.7 mm, D/t = 52.6, L/D = 6.7, and f'_c = 21 MPa)

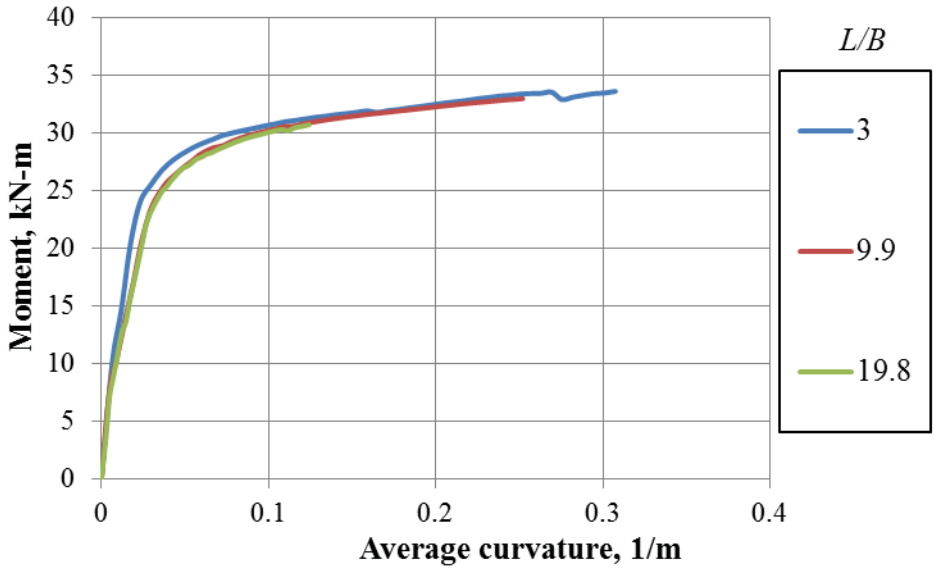

Figure 6.38 Effect of Member Length-to-Depth Ratio on the Moment-Midspan Deflection Responses of Rectangular CFT Beam-Columns at Different Axial Load Ratios (P/P_n = 0) (B = 201.5 mm, t = 1.4 mm, b/t_f = 139.9, F_y = 243 MPa, f'_c = 47.6 MPa, and F_y/f'_c = 5.3)

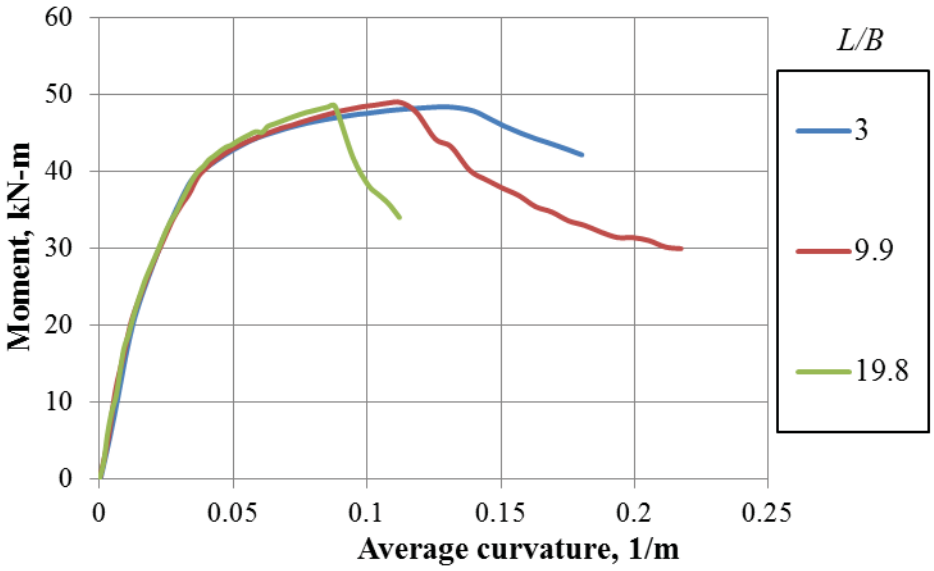

Figure 6.39 Effect of Member Length-to-Depth Ratio on the Moment-Midspan Deflection Responses of Rectangular CFT Beam-Columns at Different Axial Load Ratios (P/P_n = 0.2) (B = 201.5 mm, t_f = 1.4 mm, b/t_f = 139.9, F_y = 243 MPa, f'_c = 47.6 MPa, and F_y/f'_c = 5.3)

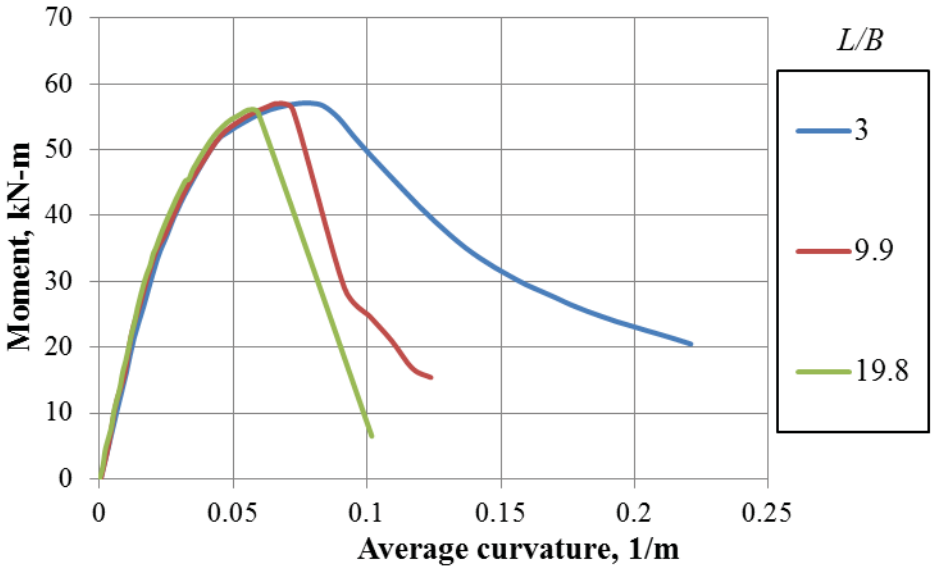

Figure 6.40 Effect of Member Length-to-Depth Ratio on the Moment-Midspan Deflection Responses of Rectangular CFT Beam-Columns at Different Axial Load Ratios (P/P_n = 0.4) (B = 201.5 mm, t_f = 1.4 mm, b/t_f = 139.9, F_y = 243 MPa, f'_c = 47.6 MPa, and F_y/f'_c = 5.3)

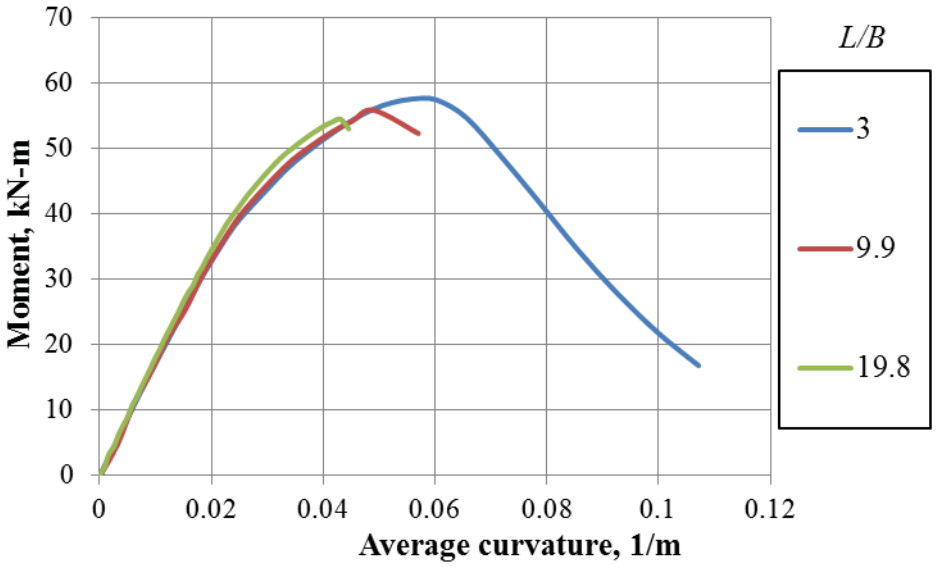

Figure 6.41 Effect of Member Length-to-Depth Ratio on the Moment-Midspan Deflection Responses of Rectangular CFT Beam-Columns at Different Axial Load Ratios ($P/P_n = 0.6$) ($B = 201.5$ mm, $t_f = 1.4$ mm, $b/t_f = 139.9$, $F_y = 243$ MPa, $f'_c = 47.6$ MPa, and $F_y/f'_c = 5.3$)

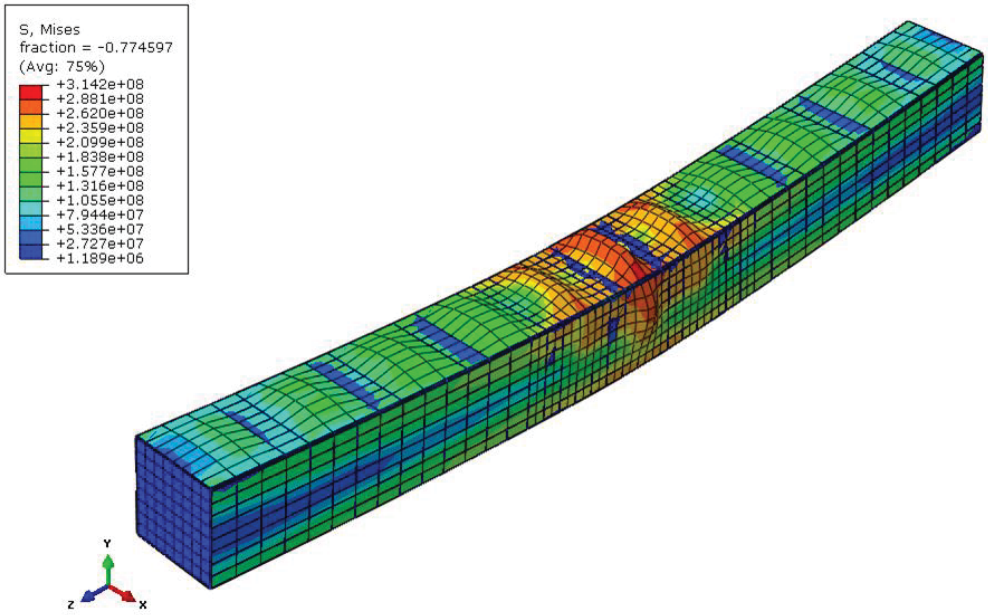

Figure 6.72 Propagation of the Local Buckling into the Webs (R-140-5-4-10)

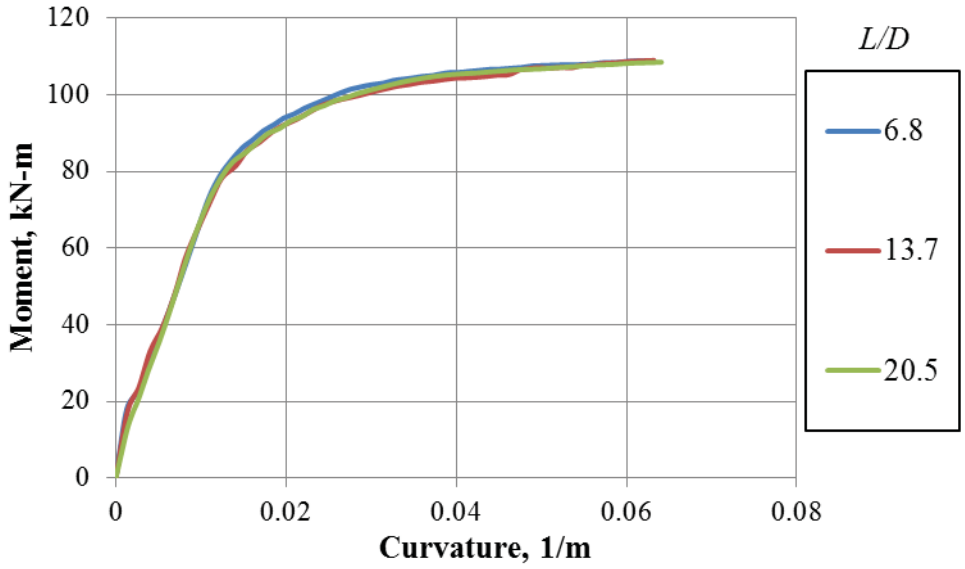

Figure 6.43 Effect of Member Length-to-Depth Ratio on the Moment-Curvature Responses of Circular CFT Beam-Columns at Different Axial Load Ratios ($P/P_n = 0$) (D = 292.3 mm, t = 2.0 mm, D/t = 146.2, F_y = 420 MPa, f'_c = 64.3 MPa, and F_y/f'_c = 6.5)

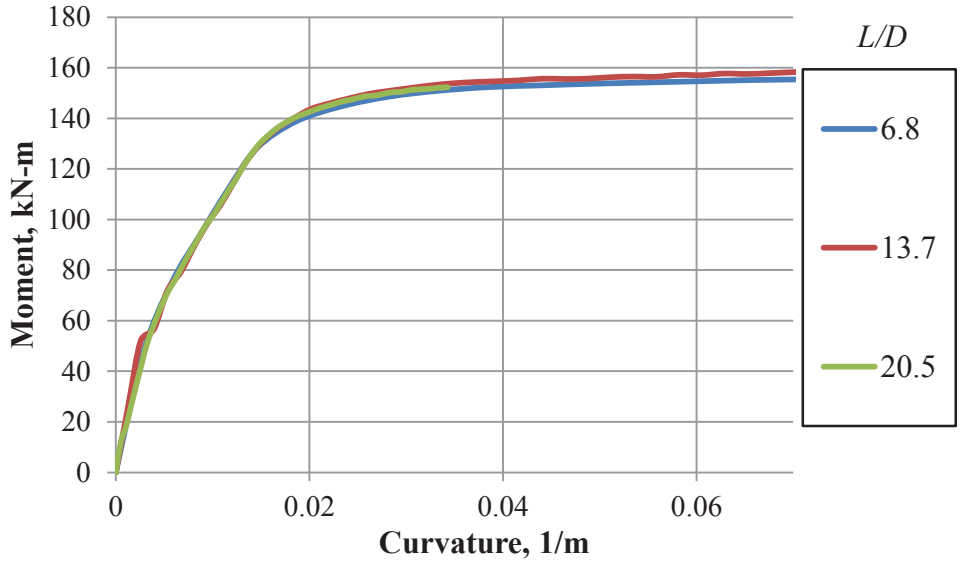

Figure 6.44 Effect of Member Length-to-Depth Ratio on the Moment-Curvature Responses of Circular CFT Beam-Columns at Different Axial Load Ratios ($P/P_n = 0.2$) (D = 292.3 mm, t = 2.0 mm, D/t = 146.2, F_y = 420 MPa, f'_c = 64.3 MPa, and F_y/f'_c = 6.5)

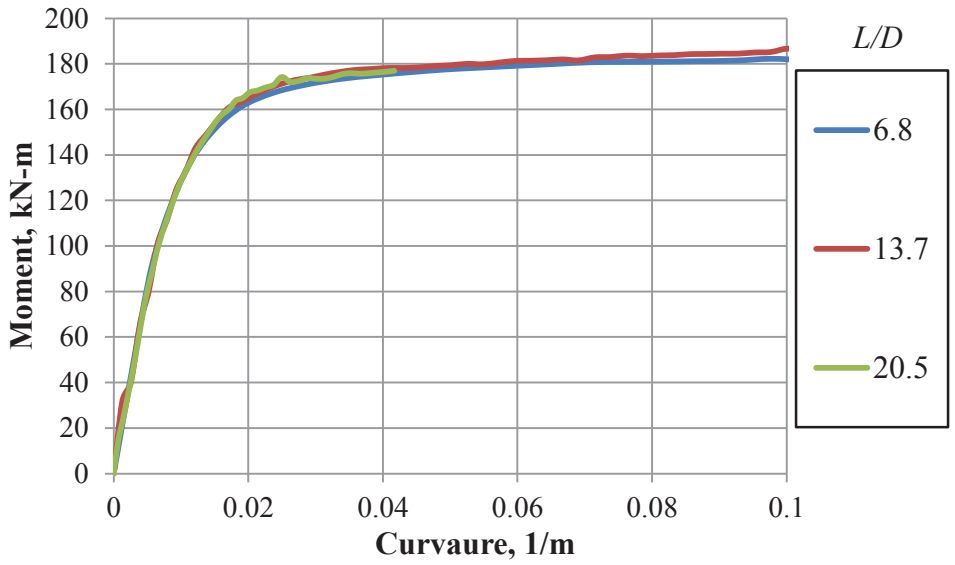

Figure 6.45 Effect of Member Length-to-Depth Ratio on the Moment-Curvature Responses of Circular CFT Beam-Columns at Different Axial Load Ratios (P/P_n = 0.4) (D = 292.3 mm, t = 2.0 mm, D/t = 146.2, F_y = 420 MPa, f'_c = 64.3 MPa, and F_y/f'_c = 6.5)

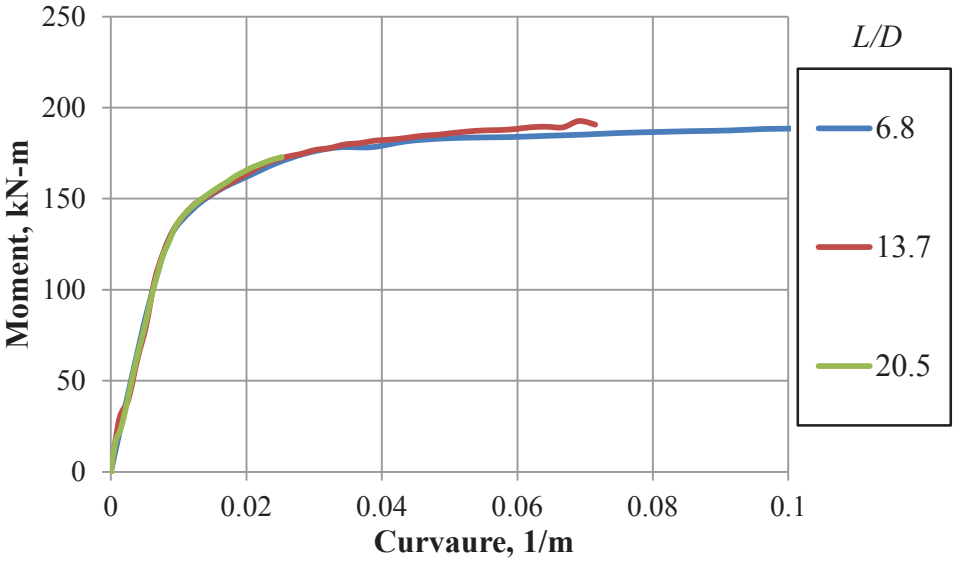

Figure 6.46 Effect of Member Length-to-Depth Ratio on the Moment-Curvature Responses of Circular CFT Beam-Columns at Different Axial Load Ratios (P/P_n = 0.6 (D = 292.3 mm, t = 2.0 mm, D/t = 146.2, F_y = 420 MPa, f'_c = 64.3 MPa, and F_y/f'_c = 6.5)

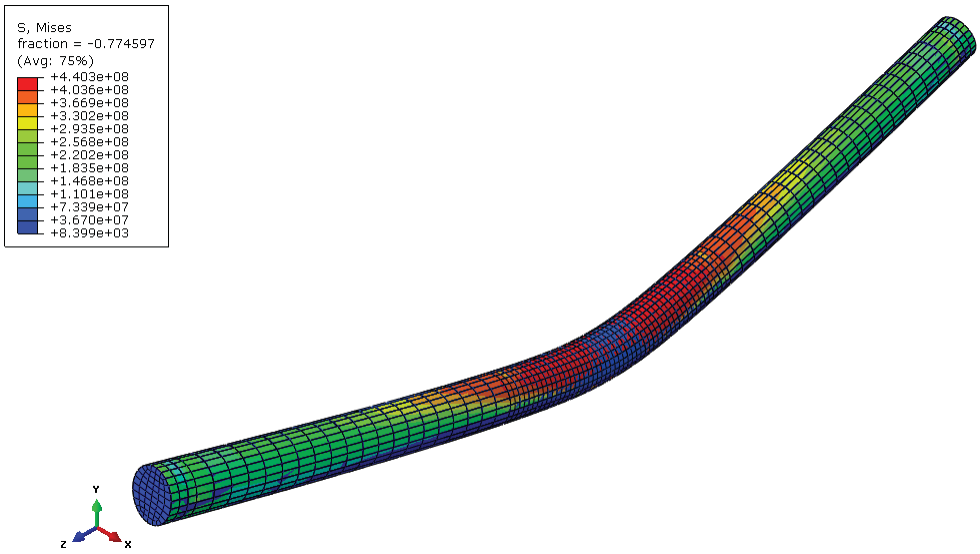

Figure 6.47 Deformed Shape of the Circular Beam-Column (C-146-7-6-21)

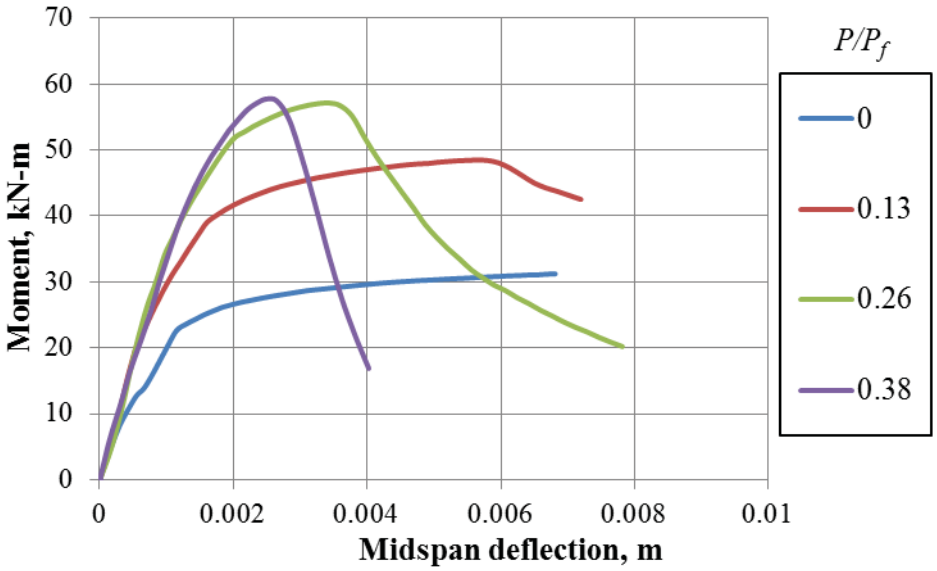

Figure 6.48 Effect of Axial Load Ratio on the Moment-Midspan Deflection Responses of Rectangular CFT Beam-Columns with Length-to-Depth Ratio (L/B) of 3.0 (B = 201.5 mm, t_f = 1.4 mm, b/t_f = 139.9, F_y = 243 MPa, f'_c = 47.6 MPa, and F_y/f'_c = 5.3)

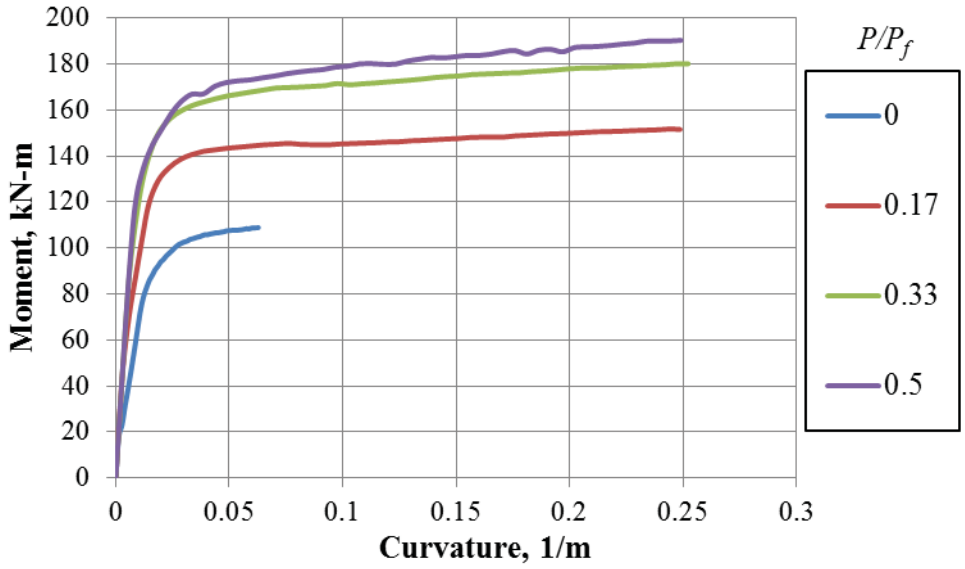

Figure 6.49 Effect of Axial Load Ratio on the Moment-Curvature Responses of Circular CFT Beam-Columns with Length-to-Depth Ratio (L/D) of 6.8 (D = 292.3 mm, t = 2.0 mm, D/t = 146.2, F_y = 420 MPa, f'_c = 64.3 MPa, and F_y/f'_c = 6.5)

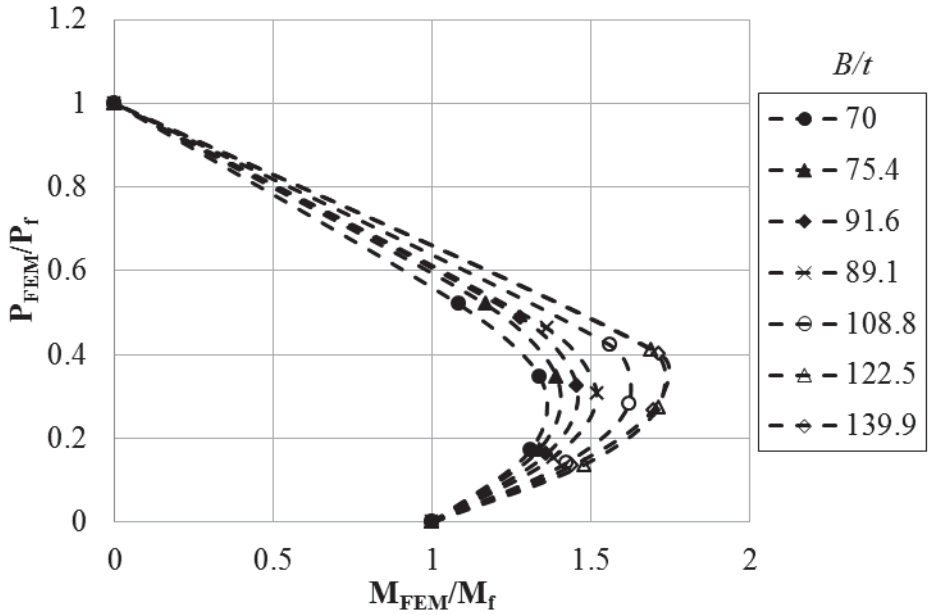

Figure 6.50 Effect of Tube Slenderness Ratio on the P-M Interaction Curve for Rectangular Noncompact and Slender CFT Beam-Columns (L/B = 3.0, and F_y/f'_c = 5.3)

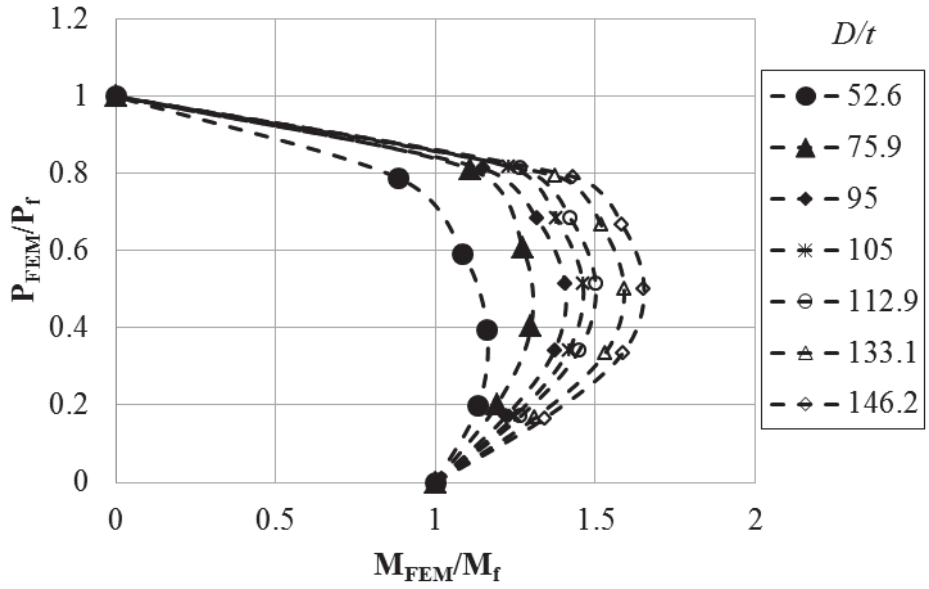

Figure 6.51 Effect of Tube Slenderness Ratio on the P-M Interaction Curve for Circular Noncompact and Slender CFT Beam-Columns (L/D = 6.7, and F_y/f'_c = 6.5)

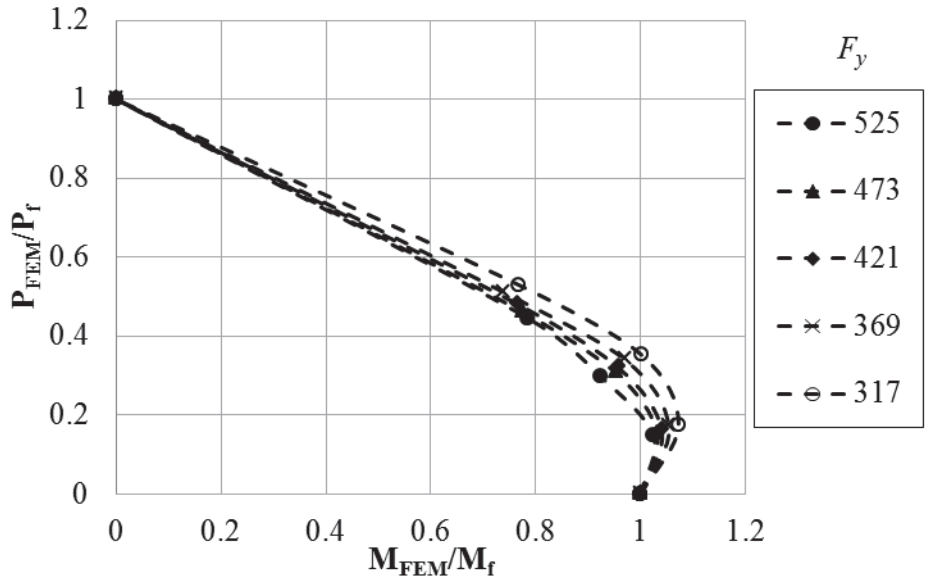

Figure 6.52 Effect of Steel yield stress on the P-M Interaction Curve for Rectangular Noncompact and Slender CFT Beam-Columns (b/t_f = 70.0 and L/B = 3.0)

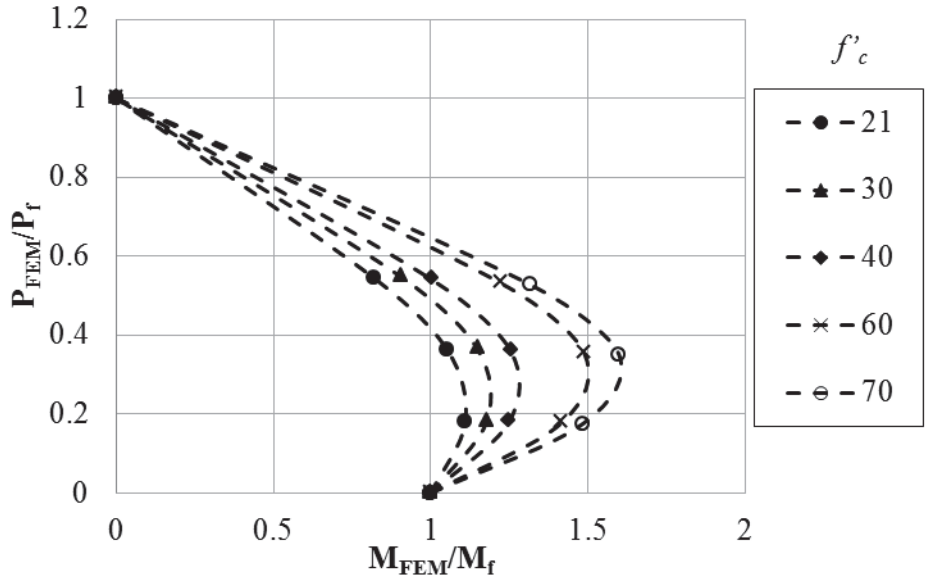

Figure 6.53 Effect of Concrete Compressive Strength on the P-M Interaction Curve for Rectangular Noncompact and Slender CFT Beam-Columns (b/t_f = 70.0 and L/B = 3.0)

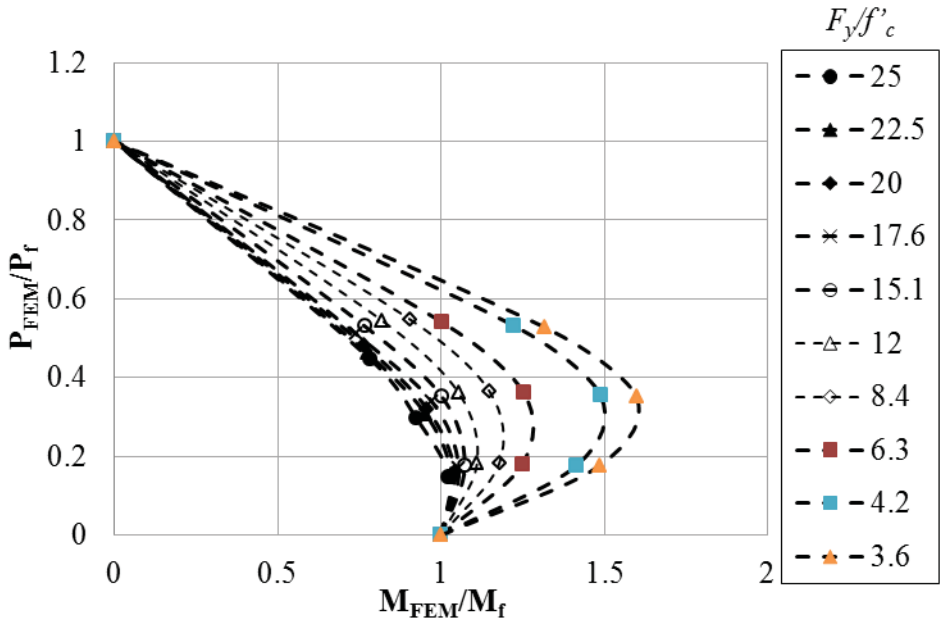

Figure 6.54 Effect of Material Strength Ratio on the P-M Interaction Curve for Rectangular Noncompact and Slender CFT Beam-Columns (b/t_f = 70.0 and L/B = 3.0)

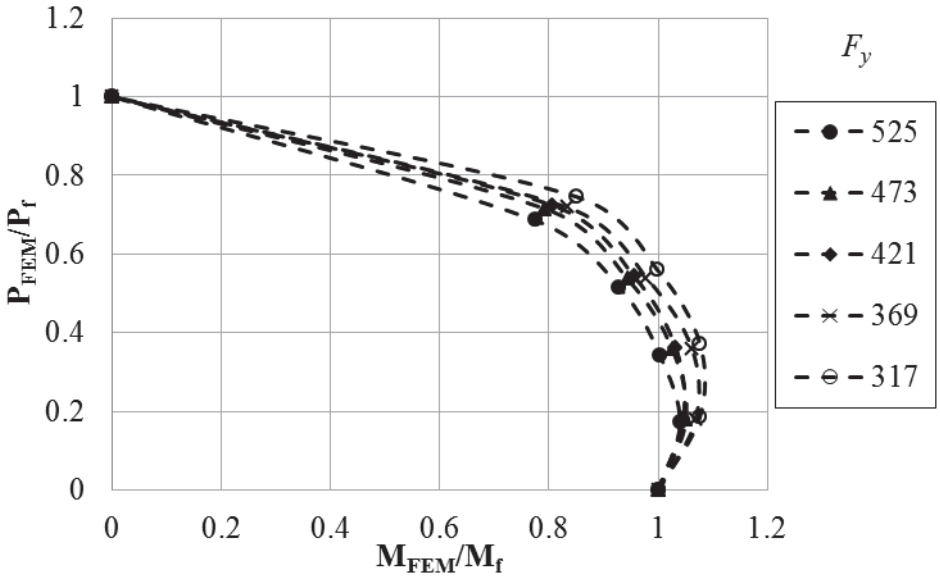

Figure 6.55 Effect of Steel yield stress on the P-M Interaction Curve for Circular Noncompact and Slender CFT Beam-Columns (D/t = 52.6 and L/D = 6.7)

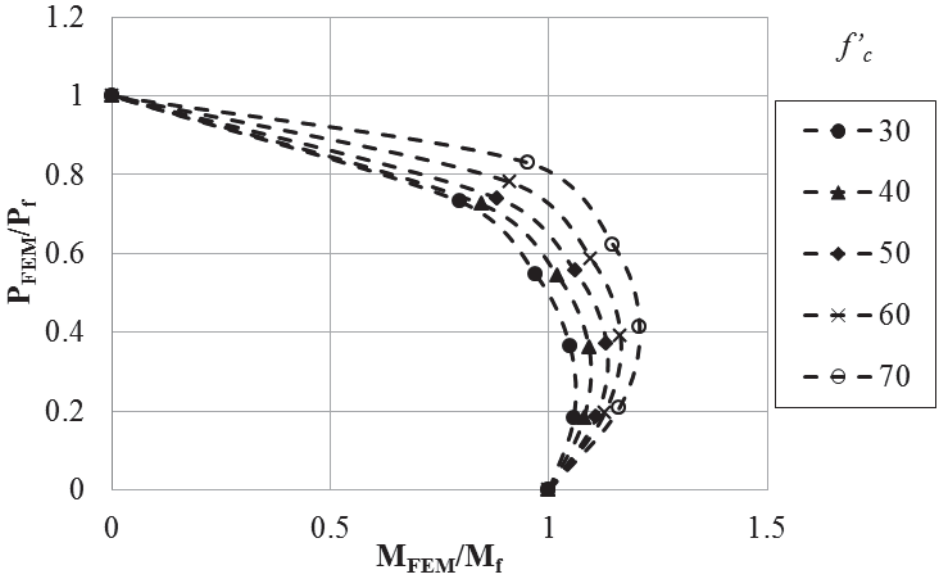

Figure 6.56Effect of Concrete Compressive Strength on the P-M Interaction Curve for Circular Noncompact and Slender CFT Beam-Columns (D/t = 52.6 and L/D = 6.7)

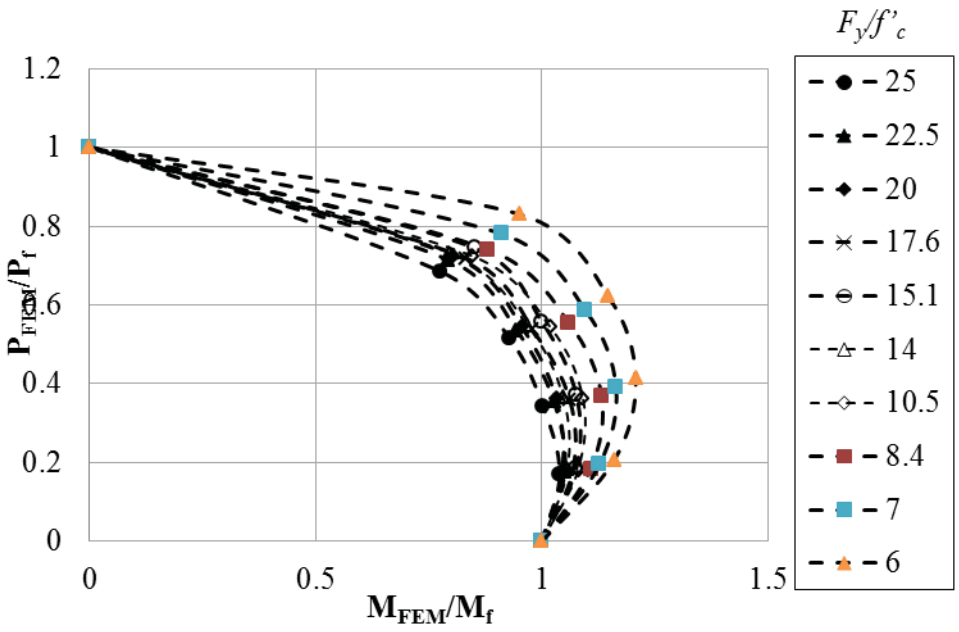

Figure 6.57 Effect of Material Strength Ratio on the P-M Interaction Curve for Circular Noncompact and Slender CFT Beam-Columns (D/t = 52.6 and L/D = 6.7)

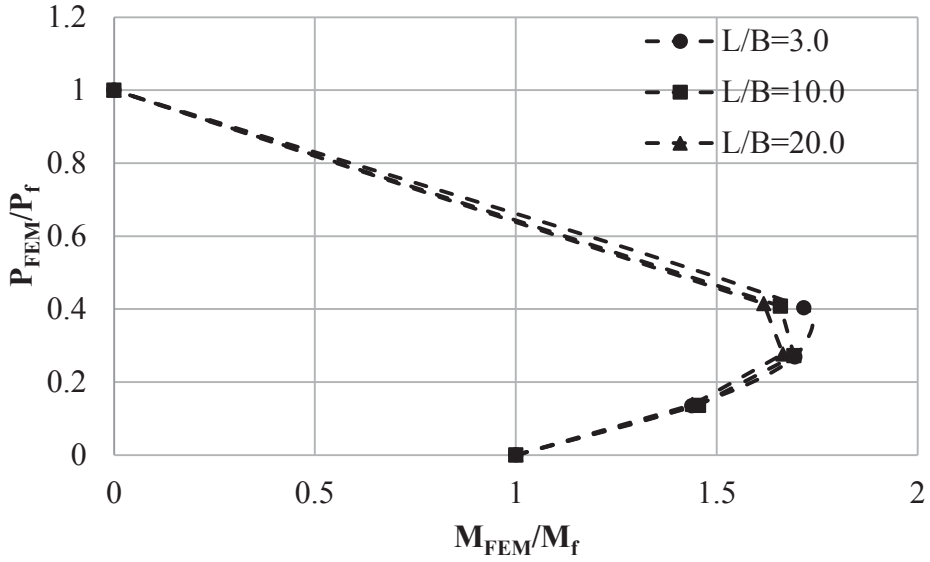

Figure 6.58 Effect of Length-to-Depth Ratio on the P-M Interaction Curve for Rectangular Noncompact and Slender CFT Beam-Columns (b/t_f = 70.0 and F_y/f'_c = 5.3)

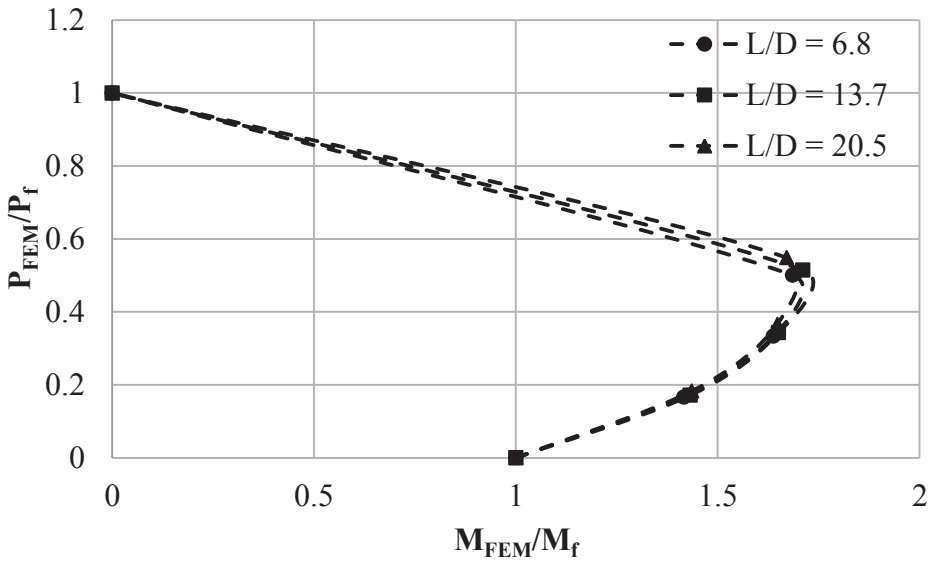

Figure 6.59 Effect of Length-to-Depth Ratio on the P-M Interaction Curve for Circular Noncompact and Slender CFT Beam-Columns (D/t = 52.6 and F_y/f'_c = 6.5)

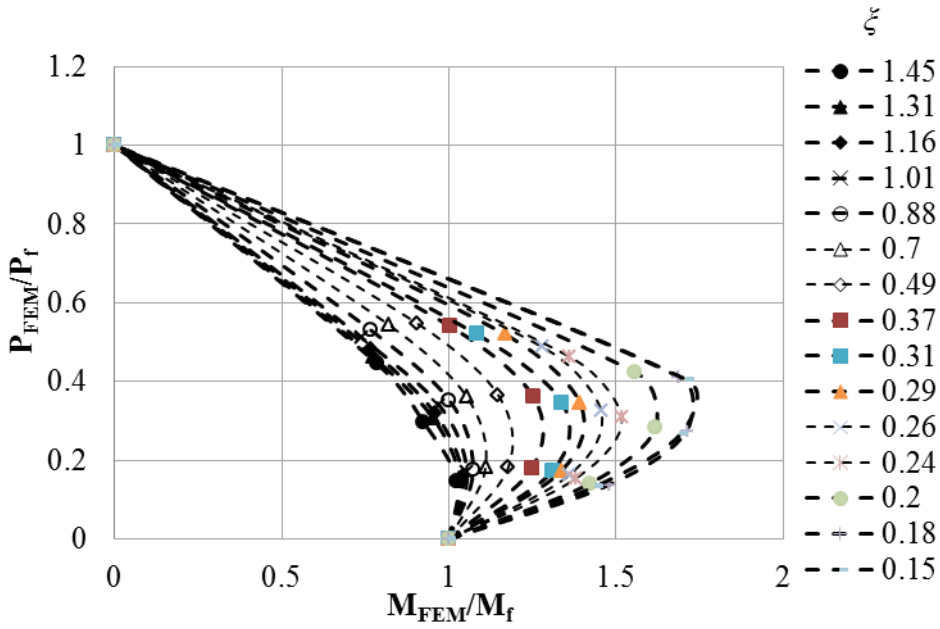

Figure 6.60 Effect of the Relative strength ratio on the Shape of P-M Interaction Curves for Rectangular Noncompact and Slender Beam-Columns

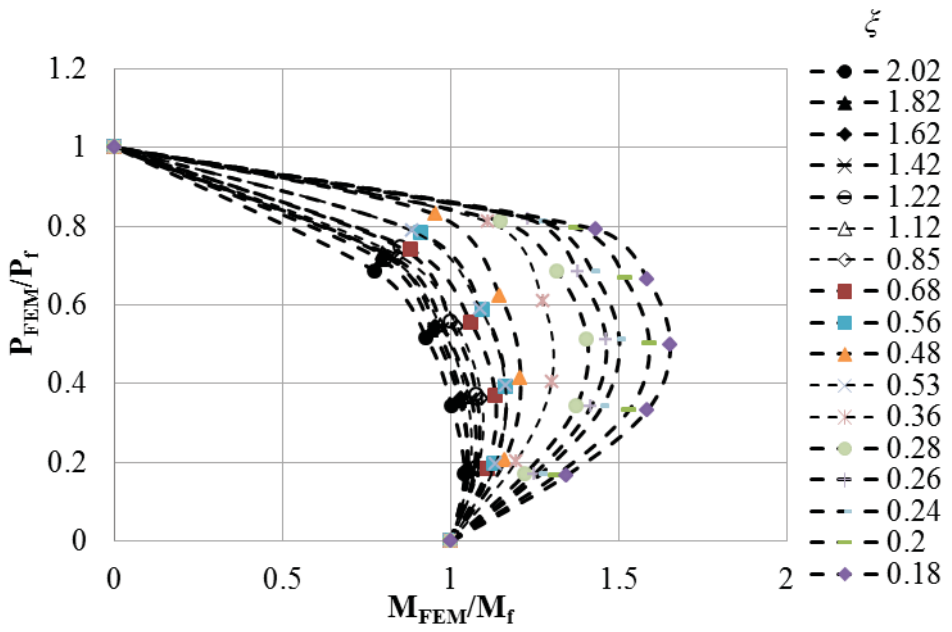

Figure 6.61 Effect of the Relative strength ratio on the Shape of P-M Interaction Curves for Circular Noncompact and Slender Beam-Columns

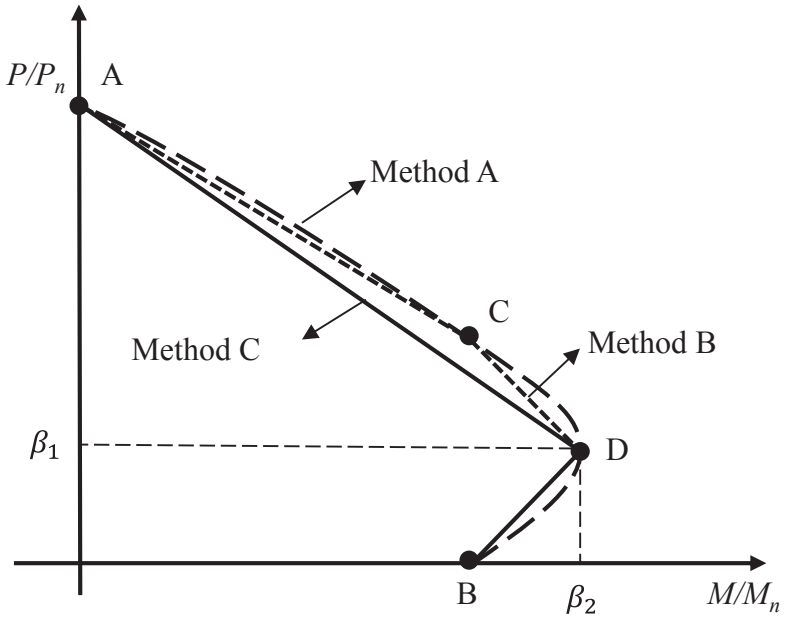

Figure 6.62 Different Design Methods for Defining Beam-Column Interaction Curve

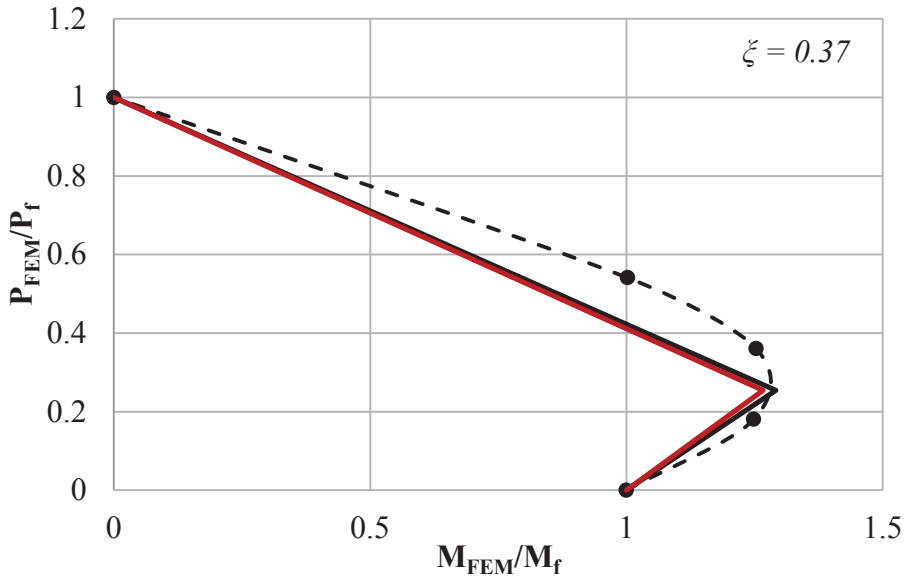

Figure 6.63 Comparisons of the Updated Interaction Curves (Solid Curve) Obtained Using Equations with Interaction Curves (Dashed Curves) from Analysis for Rectangular CFT Beam-Columns with Relative strength ratio of (ξ) 0.37 (b/t_f = 70.0, F_y = 253 MPa, and f'_c = 40 MPa)

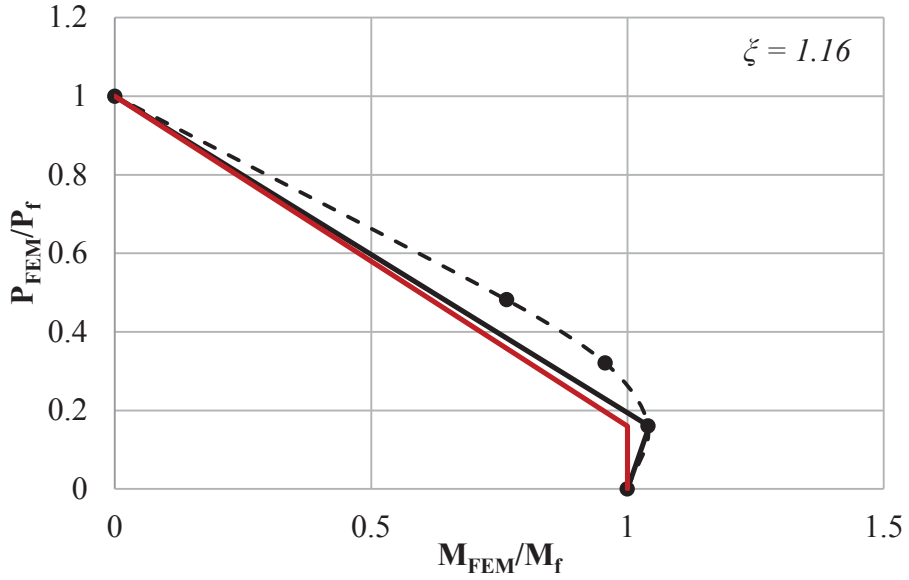

Figure 6.64 Comparisons of the Updated Interaction Curves (Solid Curve) Obtained Using Equations with Interaction Curves (Dashed Curves) from Analysis for Rectangular CFT Beam-Columns with Relative strength ratio of (ξ) 1.16 (b/t_f = 70.0, F_y = 421 MPa, and f'_c = 21 MPa)

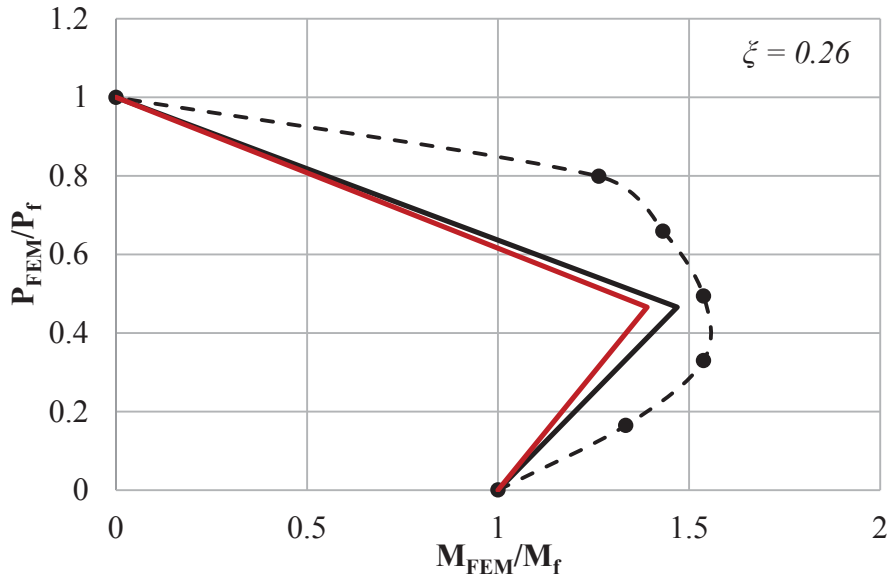

Figure 6.65 Comparisons of the Updated Interaction Curves (Solid Curve) Obtained Using Equations with Interaction Curves (Dashed Curves) from Analysis for Circular CFT Beam-Columns with Relative strength ratio of (ξ) 0.26 (D/t = 105.0, F_y = 420MPa, and f'_c = 64.3 MPa)

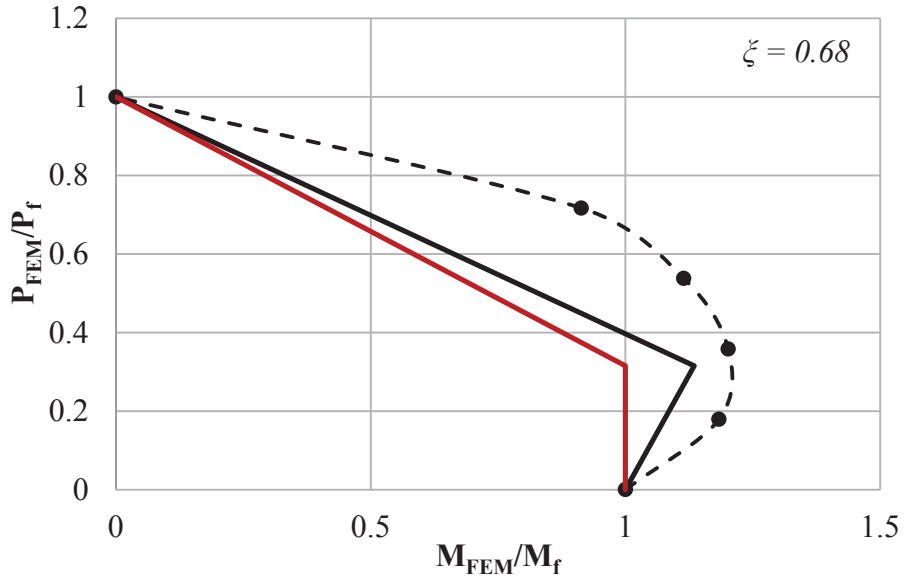

Figure 6.66 Comparisons of the Updated Interaction Curves (Solid Curve) Obtained Using Equations with Interaction Curves (Dashed Curves) from Analysis for Circular CFT Beam-Columns with Relative strength ratio of (ξ) 0.68 (D/t = 52.6, F_y = 420MPa, and f'_c = 50 MPa)

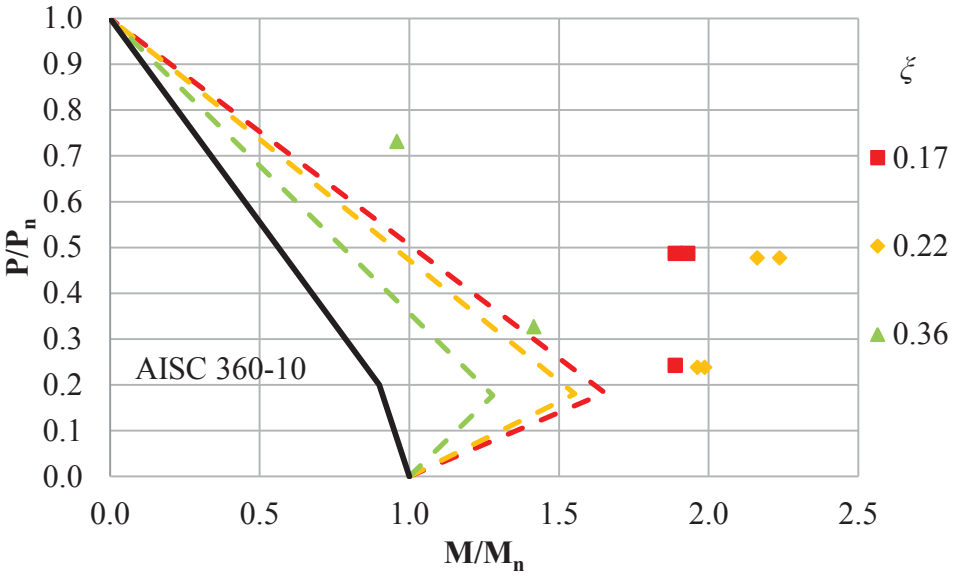

Figure 6.67 Comparisons of the updated interaction curve with experimental results for all rectangular specimens (except the specimens with high strength steel) in the database

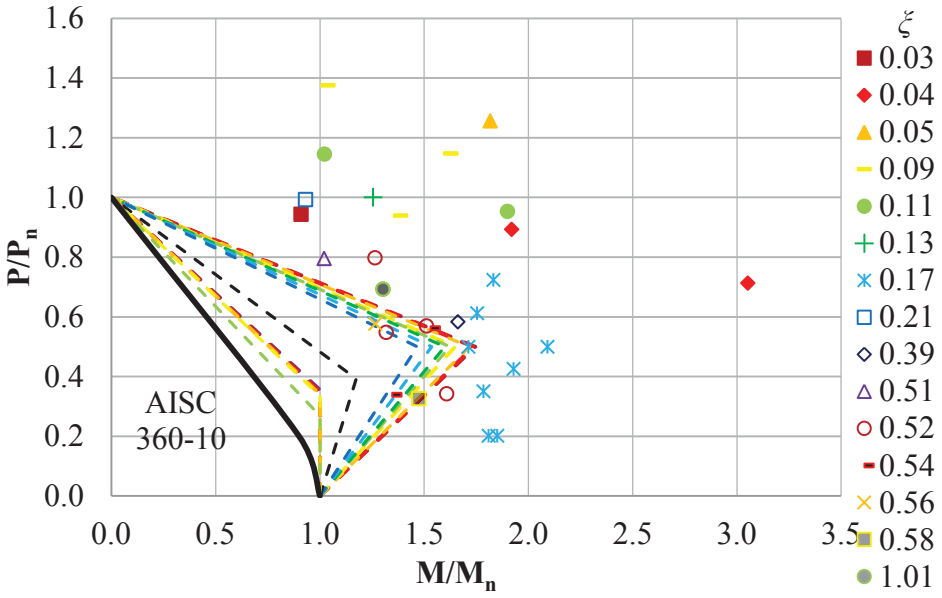

Figure 6.68 Comparisons of the updated interaction curve with experimental results for all circular specimens in the database

CHAPTER 7. DEVELOPMENT AND VALIDATION OF THE EFFECTIVE STRESS-STRAIN CURVES

As discussed in Section 1.3, several analytical methods are available for investigating the behavior of CFT members. For example, fiber analysis based macro models, concentrated-plasticity based FEM models, and distributed-plasticity based FEM models. Several commercial nonlinear structural analysis programs (such as Drain-2Dx, OpenSees) are also available to analyze composite (CFT) structural systems. The accuracy of these analytical methods and structural analysis programs for predicting the behavior of CFT members or structural systems depends largely on the uniaxial stress-strain curves assumed for the steel tube and concrete materials of the CFT sections.

This chapter presents the development of effective stress-strain curves of the steel tube and concrete infill for noncompact and slender CFT. These effective stress-strain curves are developed using results from comprehensive analytical studies conducted using the benchmarked FEM models presented earlier in Chapter 3. The FEM models accounted for the effects of geometric imperfections, steel tube local buckling, steel hoop stresses and concrete confinement from transverse and longitudinal interaction between the steel tube and concrete infill. The chapter also presents the validation of the conservatism of the effective stress-strain curves. The conservatism of these curves is validated by

implementing them in a nonlinear fiber analysis based macro model. This model was developed by Lai et al. (2013) and modified here in this chapter to analyze CFT members.

7.1 Development of the Effective Stress-Strain Curves

7.1.1 Basic Principles

The behavior of CFT members as columns, beams or beam-columns is different, as discussed previously in Chapters 4-6. For example, the behavior of CFT beam-columns depends on several parameters, such as the tube slenderness ratio (*b/t* or *D/t*), material strength ratio (F_y/f'_c) and axial load ratio (α). When the axial load ratio (α) is low, i.e., below the balance point on the P-M interaction curve, flexural behavior dominates the response. When α is high, i.e., above the balance point, axial compression behavior dominates the response. It is therefore impractical to propose effective stress-strain curves that accurately represent the behavior of the steel tube (or concrete infill) in all loading cases (axial compression, flexure, combined axial loading and flexure). Instead, the following three principles were applied in the development of the effective stress-strain curves:

(i). The effective stress-strain curves should capture the fundamental behavior and failure modes of CFT members.

(ii). The effective stress-strain curves should be conservative for all loading cases.

(iii). The effective stress-strain curves should be simple and straightforward to use and implement.

The implementation of the first two principles (Principle (i) and Principle (ii)) governs the choice of the type of CFT member (i.e., column, beam, or beam-column) for developing the effective stress-strain curves. In this research, the stress-strain behavior of the steel tube in tension was assumed to be bilinear (as shown in Figure 3.3), and the stress-strain behavior of the concrete in tension was assumed to be linear elastic until the tensile strength (f'_t) was reached. Once the tensile strength (determined according to the CEB-FIB model showed in Figure 3.4(b)) is reached, the concrete is assumed to lose its tensile strength completely (as will be shown later in Figure 7.55 and Figure 7.57). The primary purpose of the parametric studies is to investigate the compressive stress-strain behavior of the steel tube and concrete infill, and develop the corresponding effective stress-strain curves. Similar to Varma (2000) and Huang (2005), CFT stub columns (with length-to-depth ratio of 3.0) were selected (instead of CFT beams or beam-columns) to perform such parametric studies. The reasoning is explained as follows.

For rectangular noncompact and slender CFT members, the governing failure mode usually involves the local buckling of the steel tube wall, and there is limited confinement provided to the concrete infill. Therefore it is important for the effective stress-strain curves to capture the local buckling stress of the steel tube and limited confinement of the concrete infill. As compared to rectangular beams or beam-columns: (i) the local buckling stress of the steel tube for rectangular columns is most critical (i.e., smallest), because all tube walls are subjected to compressive loading, and (ii) the confinement of the concrete infill is less significant (i.e., smaller) than that of the concrete infill in the compressive region of beams or beam-columns (which has significant volumetric

dilation). Therefore, the effective stress-strain curves developed from stub column analysis are conservative, while capturing the fundamental failure mode and behavior of rectangular CFT members (i.e., steel tube local buckling and limited concrete confinement).

For circular noncompact and slender CFT members, local buckling of the steel tube is not that evident. The failure usually involves reaching of the material strengths of both the steel tube and concrete infill. However, the longitudinal stress capacity of the materials is influenced by the transverse interaction between the steel tube and concrete infill. These transverse interactions produce hoop stresses in the steel tube wall and confinement of the concrete infill. Therefore it is important for the effective stress-strain curves to capture: (i) the reductions in the longitudinal (axial) stress capacity required to cause yielding of the steel in compression, and (ii) the increase of the compressive strength of the concrete infill. As compared to circular CFT beams or beam-columns: (i) the effect of hoop stresses are more critical for the steel tube (i.e., greatest) because all tube walls are subjected to compressive loading, and (ii) the confinement of the concrete infill is less significant (i.e., smaller) for circular CFT columns because it has less volumetric dilation. Consequently, the effective stress-strain curves developed from stub column analysis are conservative, while capturing the fundamental failure mode and behavior of circular CFT members (i.e., steel tube hoop stresses and concrete confinement).

The implementation of the second and third principles (Principle (ii) and Principle (iii)) governs the interpretation of the analytical results and the development of the idealized effective stress-strain curves. This will be explained in detail later in Section 7.1.3.

7.1.2 Effective Stress-Strain Curves

The behavior and strength of CFT columns and the resulting effective stress-strain curves depend on several parameters, such as the tube slenderness ratio (*b/t* or *D/t*), the steel yield stress (F_y) and the concrete compressive strength (f'_c). In this section, comprehensive analyses using benchmarked FEM models were conducted to determine the effects of these parameters. Prototype specimens were selected from the experimental database. Parametric studies were performed using the benchmarked models of these prototype CFT specimens by varying the tube slenderness ratio (*b/t* or *D/t*), the steel yield stress (F_y) or the concrete compressive strength (f'_c). The tube slenderness ratio was varied by changing the tube thickness (t).

The prototype selected for rectangular CFT columns was Specimen E10 by Lin (1988), and the prototype selected for circular CFT columns was Specimen D2 by Lin (1988). For both prototype specimens, a total of 45 analyses were conducted with: (i) five tube slenderness ratios, (ii) three steel yield stress (317 MPa, 421 MPa, and 525 MPa), and three concrete compressive strength (21 MPa, 45 MPa, and 70 MPa). For all CFT columns analyzed in these parametric studies, the length-to-depth ratio was kept constant at 3.0. Details of these CFT columns are shown in Table 7.1 (for rectangular columns) and Table 7.2 (for circular columns). The nomenclature used in these two tables (for

example, R-60-317-21, D-60-317-21) consists of the cross section type (R represents a rectangular column while C represents a circular column), tube slenderness ratio (b/t_f for rectangular CFT columns and D/t for circular CFT columns), steel yield stress (F_y) and concrete compressive strength (f'_c).

The axial stresses in the steel tube were extracted from the results of the FEM analyses as follows. The corresponding axial force (SF) in each steel element of the midspan cross-section (where local buckling occurred) was extracted first. The axial force carried by the steel tube (P_s) was calculated as the sum of the axial forces carried by all steel elements in the cross-section at the midspan, and the axial force carried by the concrete infill (P_c) was calculated by subtracting P_s from the total applied axial load (P). Then the steel tube stress was estimated as P_s divided by the steel tube cross-sectional area (A_s), and the concrete stress was estimated as P_c divided by the concrete infill cross-sectional area (A_c). The axial strains in both the steel tube and concrete infill were estimated as the average axial strains of the column, which were calculated by dividing the axial shortening with the member length (L).

7.1.2.1 Rectangular CFT members

Figures 7.1-7.9 show the normalized axial stress-strain curves for the steel tubes for rectangular CFT columns (F_y is the steel yield stress, and ε_y is the steel yield strain). These figures indicate that: (i) the steel critical buckling stress decreases with increasing tube slenderness ratios (b/t_f) and increasing steel yield stress (F_y); this observation is

similar to the findings by Bradford et al. (1998), (ii) the steel post-buckling stress is influenced by the tube slenderness ratio (b/t_f), steel yield stress (F_y) and concrete compressive strength (f'_c), and (iii) the post-buckling stress-strain behavior is unstable; this is due to the fact that the local buckling in the midspan may propagate from the compression flanges to the webs (as shown in Figure 7.10), or shift from the midspan to other locations (as shown in Figure 7.11). A trilinear curve as shown in Figure 7.12 was proposed as the idealized effective stress-strain curve for the steel tube under compressive loading. This simplified curve follows the rule of Principle (iii) discussed in Section 7.1.1, and requires only two anchor points (ε_p, σ_p and $2\varepsilon_y$, σ_2) to define it. The peak strain (ε_p) can be calculated as:

$$\varepsilon_p = \frac{\sigma_p}{E_s} \tag{7.1}$$

Based on the results shown in Figures 7.1-7.9, multiple regression analysis was performed to define the parameter σ_p and σ_2, and the resulting equations are given by Equation 7.2 and Equations 7.3.

$$\frac{\sigma_u}{F_y} = 1.13 - 0.1\lambda_{coeff} \le 1.0 \tag{7.2}$$

$$\frac{\sigma_{2.0}}{F_y} = 0.87 - 0.0055\left(\frac{b}{t} - \frac{F_y}{f'_c}\right) \tag{7.3}$$

where λ_{coeff} is the slenderness coefficient:

$$\lambda_{coeff} = \frac{b/t}{\sqrt{E_s/F_y}} \tag{7.4}$$

Figures 7.13-7.21 show the normalized axial stress-strain curves for the concrete infill for rectangular CFT columns (f'_c is the concrete compressive strength, and ε_c is the concrete peak strain corresponding to f'_c). In these figures, the normalized unconfined stress-strain curves (black dashed lines, by Popovics 1973) that were used to define the uniaxial compressive behavior of the concrete infill in the FEM models are also included. These figures indicate that the concrete peak stress (f'_{cp}) is influenced by the tube slenderness ratio (b/t), steel yield stress (F_y) and concrete compressive strength (f'_c). For example, the peak stress (f'_{cp}) increases as the tube slenderness ratio (b/t_f) or the steel yield stress (F_y) increases. These figures also indicate that the concrete post-peak behavior is softer than the specified stress-strain behaviors for specimens with f'_c of 45 MPa and 70 MPa. For these specimens, the concrete has more contribution to the axial strength of the CFT column. When the concrete compressive strength was reached, the significant volumetric dilation cannot be captured due to the limitation of the concrete model (the CDP model does not adequately account for the beneficial effects of confinement on strain ductility) in ABAQUS, and the resulting average post-peak behavior is unstable (i.e., softer than the specified behavior). Therefore it is reasonable for an idealized stress-strain curve to focus on the changes of the concrete peak stress only, while keeping the post-peak responses the same as that of the unconfined stress-strain curve. This also follows the rule of Principle (iii) discussed in Section 7.1.1.

Figure 7.22 shows the proposed idealized stress-strain curve for the concrete infill under compressive loading. This formulation of this curve is the same as that of Popovics's

curve, except that the concrete compressive strength f'_c in the Popovics's equation (Equation 7.5, in psi) is replaced by the concrete peak stress f'_{cp}.

$$f_c = f_c' \frac{\varepsilon}{\varepsilon_c} \frac{n}{n-1+(\varepsilon/\varepsilon_0)^n} \tag{7.5 a}$$

$$\varepsilon_c = \frac{f_c'}{E_c} \frac{n}{n-1} \tag{7.5 b}$$

$$n = 0.0004 f_c' + 1.0 \tag{7.5 c}$$

Based on the results shown in Figures 7.13-7.21, multiple regression analysis was performed to define f'_{cp}, and the resulting equation is given by Equation 7.6. The maximum f'_{cp}/f'_c ratio was limited to 1.10 to avoid the overestimation of the concrete peak stress (f'_{cp}) when the tube slenderness ratio (b/t) or material strength ratio (F_y/f'_c) is relatively high.

$$\frac{f_{cp}}{f_c'} = 0.8 + 0.18\left(\frac{b/t}{100} + \frac{F_y / f_c'}{30}\right) \le 1.10 \tag{7.6}$$

With the concrete peak stress (f'_{cp}) given by Equation 7.6, Equation 7.7 (in MPa) can be updated from Equation 7.5 to define the effective stress-strain curve of the concrete infill in compression for rectangular CFT members.

$$f_c = f_{cp}' \frac{\varepsilon}{\varepsilon_c} \frac{n}{n-1+(\varepsilon/\varepsilon_0)^n} \tag{7.7 a}$$

$$\varepsilon_c = \frac{f_c'}{E_c} \frac{n}{n-1} \tag{7.7 b}$$

$$n = 0.058 f_c^{'} + 1.0 \quad (7.7\text{ c})$$

where the concrete elastic modulus (E_c) is evaluated according to ACI 318-11 as $4700\sqrt{f_c^{'}}$ (in MPa).

7.1.2.2 Circular CFT members

Figures 7.23-7.31 show the normalized axial stress-strain curves for the steel tubes for circular CFT columns (F_y is the steel yield stress, and ε_y is the steel yield strain). These figures indicate that: (i) the steel peak stress (σ_p) is approximately equal to 0.9 in all circular CFT columns, and (ii) the steel post-peak stress decreases with increasing axial strain. This decrease is due to the fact that: (i) the bending stresses produced by the second-order moment reduce the average compressive stress in the steel tube, and (ii) extensive hoop stresses was developed in the steel tube to confine the concrete and mitigate the unstable behavior (due to the limitation of the concrete model, as discussed in the previous section for rectangular CFT columns) when the concrete compressive strength was reached. These hoop stresses further reduces the average compressive stress in the steel tube. For a short column in reality, the decrease of steel post-peak stress is less significant or even disappeared. Therefore, the effective stress strain-curve for the steel tube for circular CFT members under compressive loading can be idealized to the bilinear curve as shown in Figure 7.32. This formulation follows the rule of Principle (iii) discussed in Section 7.1.1. As shown in Figure 7.32, the steel peak stress (σ_p) is given by Equation 7.8 as:

$$\sigma_p = 0.9 F_y \quad (7.8)$$

Figures 7.33-7.41 show the normalized axial stress-strain curves for the concrete infill for circular CFT columns (f'_c is the concrete compressive strength, and ε_c is the concrete peak strain corresponding to f'_c). In these figures, the normalized unconfined stress-strain curves (black dashed lines, by Popovics 1973) that were used to define the uniaxial compressive behavior of the concrete infill in the FEM models are also included. These figures indicate that the concrete stress (f'_{cp}) at ε_c is influenced by the tube slenderness ratio (D/t), steel yield stress (F_y) and concrete compressive strength (f'_c). For example, f'_{cp} decreases as the tube slenderness ratio (D/t) increases. This is reasonable because steel tubes with more compact sections (i.e., smaller D/t ratio) can provide better confinement.

These figures also indicate that the concrete post-peak behavior depends on the tube slenderness ratio (D/t), steel yield stress (F_y) and concrete compressive strength (f'_c). For example, the post-peak behavior becomes softer as the concrete compressive strength (f'_c) increases. For CFT columns with f'_c of 21 MPa, the concrete strength keeps increasing with increasing axial strain. For CFT columns with f'_c of 45 MPa, the concrete strength decreases suddenly at first, and then increases again with increasing axial strain. For CFT columns with f'_c of 70 MPa, the concrete strength also decreases suddenly at first, and then increases again with increasing axial strain. For CFT columns with f'_c of 45 MPa and 70 MPa, the sudden decrease of the concrete strength is due to the limitation of the concrete model in accounting for the beneficial effects of confinement on strain ductility (as discussed previously in Section 7.1.2.1 for rectangular CFT columns). This limitation is more significant as the concrete compressive strength (f'_c of 45 MPa) increases. Also,

as discussed in Section 3.1.5, elastic perfectly plastic curve was used to specify the uniaxial compressive stress-strain behavior of circular beam-columns. It is therefore reasonable for an idealized stress-strain curve be elastic perfectly plastic, and focus on the changes of the concrete stress (f'_{cp}) at ε_c. This also follows the rule of Principle (iii) discussed in Section 7.1.1.

Figure 7.42 shows the proposed idealized stress-strain curve for the concrete infill for circular CFT members under compressive loading. Based on the results shown in Figures 7.33-7.41, multiple regression analysis was performed to define f'_{cp}, and the resulting equation is given by Equation 7.9.

$$\frac{f_{cu}}{f_c'} = 1.0 - 0.11\left(\frac{D/t}{100} + \frac{F_y / f_c'}{9}\right) \tag{7.9}$$

7.2 Validation of the Effective Stress-Strain Curves

Figures 7.12, 7.22, 7.32 and 7.42 along with equations 7.1-7.4 and equations 7.6-7.8 show the idealized effective stress-strain curves for the steel tube and concrete infill for CFT members. The development of these stress-strain curves followed the three basic principles (Principles (i), (ii) and (iii), as presented in Section 7.1.1) to be simple, conservative, and capture fundamental behavior and failure modes of CFT members in all loading scenarios (i.e., axial compression, flexure, and combined axial compression and flexure). In a separate research, Lai et al. (2013) developed a macro model in terms of a nonlinear fiber-based analysis code implemented in Matlab. In this section, this model is modified to analyze CFT members. The effective stress-strain curves are implemented in

the fiber analysis model to analyze the behavior of noncompact and slender beam-columns. Comparisons of the P-M interaction curves obtained from the fiber analyses and the finite element analyses are then used to evaluate the conservatism of the proposed effective stress-strain curve. This chapter presents representative comparisons; comprehensive reporting of all key comparisons is presented in companion analytical database (Lai, 2014).

7.2.1 Details of the Nonlinear Fiber Analysis Based Macro Model

The validity of fiber analysis based macro models for CFT members have been proved by several researchers (Tomii and Sakino 1979a, 1997b; Hajjar and Gourley 1996; Inai and Sakino 1996, Morino et al. 1996; Zhang and Shahrooz 1997, Varma et al. 2005, and Liang 2008). In these models, the cross-sectional behavior of the member is calculated by fiber analysis, and then the member behavior is evaluated by integrating the sections along the member length. The accuracy of these models depends largely on the accuracy of the stress-strain curves assumed for the steel and concrete fibers of the CFT cross-section. In a separate research (Lai et al. 2013), the author has developed a benchmarked nonlinear fiber analysis based macro model to study the behavior of built-up steel compression member. In this section, this benchmarked model is modified to analyze CFT members. With given geometric and material information for a CFT member, this model is able to: (i) calculate the axial strength (P_{cr}), (ii) calculate the flexural strength, (iii) calculate the P-M interaction curve, (iv) calculate the moment-curvature (M-ϕ) responses, (v) calculate the deformed shape, and (iv) plot the stress-strain distributions of

any cross section along the member length. Details (i.e., algorithms) of this modified model are presented as follows.

Three assumptions are made in this fiber analysis based macro model: (i) the plane section remains plane, (ii) full bond is assumed between the steel tube and concrete infill, (iii) the tensile strength of the concrete infill is ignored, and (iv) geometric imperfections with the sinusoidal shape were implemented, and the magnitude was assumed to be $L/1500$.

In this fiber analysis model, axial loading was applied incrementally (and monotonically) to a CFT member until the axial strength (P_{cr}) was reached. For each load increment (P_i,), two analysis subroutines were applied consecutively: the $P-M-\phi$ subroutine and the Δ subroutine to calculate displacement. The $P-M-\phi$ subroutine was implemented to calculate the axial load-moment-curvature ($P-M-\phi$) curve using cross-section fiber analysis. The Δ subroutine was implemented to calculate converged member deflections using corresponding $P-M-\phi$ curves. Based on the applied axial load (P_i) and the calculated deflections, external moments including the secondary moments were calculated. The column failure was assumed to occur (i.e., the P_{cr} is reached) when the calculated external moment is greater than the section moment capacity obtained from the $P-M-\phi$ subroutine. Details of these two subroutines are presented as follows.

7.2.1.1 $P-M-\phi$ Subroutine

In this subroutine, both the steel tube and concrete infill in the cross section of a CFT member was first discretized into layers of fibers, as shown in Figure 7.43 (for rectangular CFT members) and Figure 7.44 (for circular CFT members). For both rectangular and circular sections, two layers of fibers were used for the steel tube wall, and sixteen layers of fibers were used through the depth. For each fiber, the area (A_{fib}), moment of inertia with respect to the centroid of the cross section (I_{fib}), and centroid distance (distance from the center of the fiber to the centroid of the cross section, y_{fib}) was calculated. The following procedures were then applied to obtain the $P-M-\phi$ curve for each load increment (P_i):

1) Increase the curvature ϕ from 0 to $10\varepsilon_y/h$ in increment of 0.001, where ε_y is the steel yield strain, and h is the depth of the existing section.

2) For each increment of ϕ, perform the following sub-procedures to obtain the corresponding value of M.

2.1) assume the strain value at the centroid (ε_{cntd}) based on the converged value from previous curvature increment.

2.2) calculate the total strain in each fiber (ε_{strc}). As shown in Figure 7.45, the total strain is calculated as the summation of the centroid strain (ε_{cntd}) and the bending strain (ε_b). Residual strains are also included if presented.

2.2) calculate the stress in each fiber (σ_{fib}) based on the total strain (ε_{strc}) and the idealized steel stress-strain curve.

2.4) calculate the axial force in each fiber (f_{fib}) as:

$$f_{fib} = \sigma_{fib} A_{fib}$$

2.5) calculate the cross-section internal moment by summing the moments from all fibers together:

$$M = \sum f_{fib} y_{fib}$$

2.6) calculate the cross-section internal axial force by summing the forces from all fibers together:

$$P_{cal} = \sum f_{fib}$$

2.7) if $P_{cal} - P_i \leq$ tolerance, go to the next increment of curvature until the limiting maximum curvature value ($10\varepsilon_y/h$) is reached. The tolerance is assumed to be $0.01P_i$.

2.8) if $P_{cal} - P_i \geq$ tolerance, change the value of ε_{cntd} using Newton's Method and restart this sub-procedure until converges.

3) The $P-M-\phi$ curve is obtained if the converged values of the curvatures and the corresponding moments for each load increment (P_i) are calculated.

7.2.1.2 Δ Subroutine to Calculate Displacement

In this subroutine, the CFT member was first discretized into segments as shown in Figure 7.46. This resulted in stations along the length. The number of the segments was approximately equal to the column length-to-depth ratio (L/h). The following iterations were then used to calculate the member deflections for each load increment (P_i):

1) Assume the lateral displacement at iteration j to be the same as the corrected displacement ($Y_k^{i,j}$, as discussed later) from previous iteration j-1. For the first iteration (j=1), the lateral displacement is assumed to be the same as the converged shape from

previous load increment (i.e., the converged shape from P_{i-1}), as shown in Figure 7.46. For the first load increment (i=1), the lateral displacement is assumed to be the same as the sinusoidal imperfection.

2) Calculate the external moment at each station (Station k) as:

$$M_k^{i,j} = P_i y_k^{i,j}$$

3) Obtain the curvature $\phi_k^{i,j}$ at each station using the calculated $P-M-\phi$ curve, and calculate the rotation at each station as:

$$\theta_k^{i,j} = \theta_{k-1}^{i,j} + \phi_k^{i,j} \Delta x$$

4) Calculate the displacement at each station as:

$$y_k^{i,j} = y_{k-1}^{i,j} + \phi_k^{i,j} \Delta x^2$$

5) Because of the fixity assumed at one end, all the rotations collected at the other end. This leaded to the complication shown in Figure 7.47. The calculated displacement was not the same as the deflection; therefore it was corrected as follows:

$$Y_k^{i,j} = (k/n) y_n^{i,j} - y_k^{i,j}$$

6) Compare the corrected displacements at each station ($Y_k^{i,j}$) with that from the previous iteration: if $Y_k^{i,j} - Y_k^{i,j-1} \leq$ tolerance, the converged displacements are found; if $Y_k^{i,j} - Y_k^{i,j-1} \geq$ tolerance, use the corrected displacements ($Y_k^{i,j}$) as the initial lateral displacement for the next iteration (j+1) and restart the iterations. The tolerance is assumed to be h/6000.

7.2.1.3 Axial Strength

Once the converged deflections ($Y_k^{i,j}$) were found, calculate the applied moment (M_k) at each station (Station k) as the product of applied axial force (P_i) and the deflections ($Y_k^{i,j}$). Check if the moment at any station (probably the center) has become greater than the moment capacity (M_i) obtained from the corresponding $P-M-\phi$ subroutine. If so, then the column has failed due to column buckling, and P_i is the axial strength (P_{cr}). Otherwise, increase the axial load from P_i to the next load increment P_{i+1} and restart the two subroutines ($P-M-\phi$ subroutine and Δ subroutine) presented above until column buckling occurs.

7.2.1.4 Outputs

For each increment, the following values (properties) are recorded: applied axial load (P_i), flexural strength (M_i), moment-curvature (M-ϕ) responses, axial deformations and lateral deflections, and cross-section stress and strain distributions at any station. Once the axial strength is reached, the P-M interaction curve is constructed using the recorded axial load value (P_i) and moment value (M_i) in each increment. As an example, figure 7.48 shows the stress and strain distributions at the midspan when the axial capacity is reached for circular CFT members.

7.2.2 Validation of the Effective Stress-Strain Curves

In Section 6.4, 187 finite element analyses were conducted on 34 CFT members (17 rectangular CFT beam-columns and 17 circular CFT beam-columns) to investigate the

effects of tube slenderness ratio, material strength ratio and axial load ratio. Details of these 34 beam-columns were summarized before in Tables 6.1-6.4. In this part, the effective stress-strain curves are implemented in the fiber analysis based macro model to perform beam-column analysis for all of these 34 specimens. Comparisons of the P-M interaction curves obtained from the fiber analyses and the finite element analyses are then used to evaluate the conservatism of the proposed effective stress-strain curve.

Representative comparisons are shown in Figure 7.50 and Figure 7.51 for rectangular CFT beam-columns, and Figure 7.52 and Figure 7.53 for circular CFT beam-columns. Other comparisons are shown in the companion analytical database (Lai, 2014). The beam-column for each figure is identified in figure caption (for example R-70-5, C-51-7) using the same nomenclature used in Tables 6.1-6.4 (since they are the same members) except that only the cross section type, tube slenderness ratio and material strength ratio are included. In these figures, the P-M interaction curves obtained from the fiber analysis are labeled as “Fiber”, and the P-M interaction curves from the finite element analysis are labeled as “FEM” (the “FEM” curves were also shown before in Figures 6.63 and Figure 6.64 for the rectangular CFT beam-columns, and Figures 6.65 and Figure 6.66 for the circular CFT beam-columns). These comparisons indicate that the proposed effective stress-strain curves are conservative for estimating the axial strength, flexure strength, and beam-column strength of noncompact and slender CFT members. For example, the “Fiber” curves are bounded by the “FEM” curves and the shape of the “Fiber” curves are similar to that of the “FEM” curves).

7.3 Summary and Conclusions

This chapter presented the development and validation of the effective stress-strain curves for the steel tube and concrete infill for noncompact and slender CFT members. These effective stress-strain curves were developed following the three basic principles presented in Section 7.1.1 (i.e., capturing the basic behavior, conservative and simple), and they were developed using results from comprehensive analytical studies (90 analyses) conducted using the benchmarked FEM models. These effective stress-strain curves include the effects of geometric imperfections, steel tube local buckling, and steel hoop stresses and concrete confinement from the transverse interaction between the steel tube and concrete infill.

The effective stress-strain curves to model the compressive behavior of the steel tube and concrete infill were shown in Figures 7.12, 7.22, 7.32, and 7.42. The equations required to define these curves are given in Equations 7.1-7.4 and 7.6 for rectangular CFT members, and Equation 7.7 and Equation 7.8 for circular CFT members. The tensile behavior of the steel tube was assumed to be bilinear (as shown in Figure 3.3), and the tensile behavior of the concrete infill was assumed to be linear elastic until the tensile strength (determined according to the CEB-FIB model showed in Figure 3.4(b)) was reached; once the tensile strength of the concrete is reached, the concrete is assumed to lose its tensile strength completely. The complete effective stress-strain curves for the steel tube and concrete infill are summarized here in Figure 7.54 and Figure 7.55 for rectangular CFT members and Figure 7.56 and Figure 7.57 for circular CFT members.

Details of a benchmarked fiber analysis based macro model were presented. The effective stress-strain curves were then evaluated by implementing them in the fiber analysis based macro model to predict the P-M interaction curve of the 34 beam-columns analyzed before in Section 6.4 (i.e., the parametric studies using benchmarked FEM models). The evaluation indicated that the proposed effective stress-strain curves are conservative, and they capture the basic behavior of CFT beam-columns.

Table 7.1Analysis Matrix for Rectangular CFT Stub Columns

ID.	B (mm)	t_f (mm)	b/t_f	λ_{coeff}	F_y (MPa)	f'_c (MPa)
R-60-317-21	413.3	6.7	60	2.39	317	21
R-70-317-21	411.4	5.7	70	2.79	317	21
R-80-317-21	410.0	5.0	80	3.18	317	21
R-90-317-21	408.9	4.4	90	3.58	317	21
R-100-317-21	408.0	4.0	100	3.98	317	21
R-60-421-21	413.3	6.7	60	2.75	421	21
R-70-421-21	411.4	5.7	70	3.21	421	21
R-80-421-21	410.0	5.0	80	3.67	421	21
R-90-421-21	408.9	4.4	90	4.13	421	21
R-100-421-21	408.0	4.0	100	4.59	421	21
R-60-525-21	413.3	6.7	60	3.07	525	21
R-70-525-21	411.4	5.7	70	3.59	525	21
R-80-525-21	410.0	5.0	80	4.10	525	21
R-90-525-21	408.9	4.4	90	4.61	525	21
R-100-525-21	408.0	4.0	100	5.12	525	21
R-60-317-45	413.3	6.7	60	2.39	317	45
R-70-317-45	411.4	5.7	70	2.79	317	45
R-80-317-45	410.0	5.0	80	3.18	317	45
R-90-317-45	408.9	4.4	90	3.58	317	45
R-100-317-45	408.0	4.0	100	3.98	317	45
R-60-421-45	413.3	6.7	60	2.75	421	45
R-70-421-45	411.4	5.7	70	3.21	421	45
R-80-421-45	410.0	5.0	80	3.67	421	45
R-90-421-45	408.9	4.4	90	4.13	421	45
R-100-421-45	408.0	4.0	100	4.59	421	45
R-60-525-45	413.3	6.7	60	3.07	525	45
R-70-525-45	411.4	5.7	70	3.59	525	45
R-80-525-45	410.0	5.0	80	4.10	525	45
R-90-525-45	408.9	4.4	90	4.61	525	45
R-100-525-45	408.0	4.0	100	5.12	525	45
R-60-317-70	413.3	6.7	60	2.39	317	70
R-70-317-70	411.4	5.7	70	2.79	317	70
R-80-317-70	410.0	5.0	80	3.18	317	70
R-90-317-70	408.9	4.4	90	3.58	317	70
R-100-317-70	408.0	4.0	100	3.98	317	70
R-60-421-70	413.3	6.7	60	2.75	421	70
R-70-421-70	411.4	5.7	70	3.21	421	70

Table 7.1 continued.

R-80-421-70	410.0	5.0	80	3.67	421	70
R-90-421-70	408.9	4.4	90	4.13	421	70
R-100-421-70	408.0	4.0	100	4.59	421	70
R-60-525-70	413.3	6.7	60	3.07	525	70
R-70-525-70	411.4	5.7	70	3.59	525	70
R-80-525-70	410.0	5.0	80	4.10	525	70
R-90-525-70	408.9	4.4	90	4.61	525	70
R-100-525-70	408.0	4.0	100	5.12	525	70

Table 7.2 Analysis Matrix for Circular CFT Stub Columns

ID.	D (mm)	t_f (mm)	D/t	λ_{coeff}	F_y (MPa)	f'_c (MPa)
D-60-317-21	413.8	6.9	60	0.10	317	21
D-75-317-21	411.0	5.5	75	0.12	317	21
D-90-317-21	409.1	4.5	90	0.14	317	21
D-105-317-21	407.8	3.9	105	0.17	317	21
D-120-317-21	406.8	3.4	120	0.19	317	21
D-60-421-21	413.8	6.9	60	0.13	421	21
D-75-421-21	411.0	5.5	75	0.16	421	21
D-90-421-21	409.1	4.5	90	0.19	421	21
D-105-421-21	407.8	3.9	105	0.22	421	21
D-120-421-21	406.8	3.4	120	0.25	421	21
D-60-525-21	413.8	6.9	60	0.16	525	21
D-75-525-21	411.0	5.5	75	0.20	525	21
D-90-525-21	409.1	4.5	90	0.24	525	21
D-105-525-21	407.8	3.9	105	0.28	525	21
D-120-525-21	406.8	3.4	120	0.32	525	21
D-60-317-45	413.8	6.9	60	0.10	317	45
D-75-317-45	411.0	5.5	75	0.12	317	45
D-90-317-45	409.1	4.5	90	0.14	317	45
D-105-317-45	407.8	3.9	105	0.17	317	45
D-120-317-45	406.8	3.4	120	0.19	317	45
D-60-421-45	413.8	6.9	60	0.13	421	45
D-75-421-45	411.0	5.5	75	0.16	421	45
D-90-421-45	409.1	4.5	90	0.19	421	45
D-105-421-45	407.8	3.9	105	0.22	421	45
D-120-421-45	406.8	3.4	120	0.25	421	45
D-60-525-45	413.8	6.9	60	0.16	525	45
D-75-525-45	411.0	5.5	75	0.20	525	45
D-90-525-45	409.1	4.5	90	0.24	525	45
D-105-525-45	407.8	3.9	105	0.28	525	45
D-120-525-45	406.8	3.4	120	0.32	525	45
D-60-317-70	413.8	6.9	60	0.10	317	70
D-75-317-70	411.0	5.5	75	0.12	317	70
D-90-317-70	409.1	4.5	90	0.14	317	70
D-105-317-70	407.8	3.9	105	0.17	317	70
D-120-317-70	406.8	3.4	120	0.19	317	70
D-60-421-70	413.8	6.9	60	0.13	421	70
D-75-421-70	411.0	5.5	75	0.16	421	70

Table 7.2 continued.

D-90-421-70	409.1	4.5	90	0.19	421	70
D-105-421-70	407.8	3.9	105	0.22	421	70
D-120-421-70	406.8	3.4	120	0.25	421	70
D-60-525-70	413.8	6.9	60	0.16	525	70
D-75-525-70	411.0	5.5	75	0.20	525	70
D-90-525-70	409.1	4.5	90	0.24	525	70
D-105-525-70	407.8	3.9	105	0.28	525	70
D-120-525-70	406.8	3.4	120	0.32	525	70

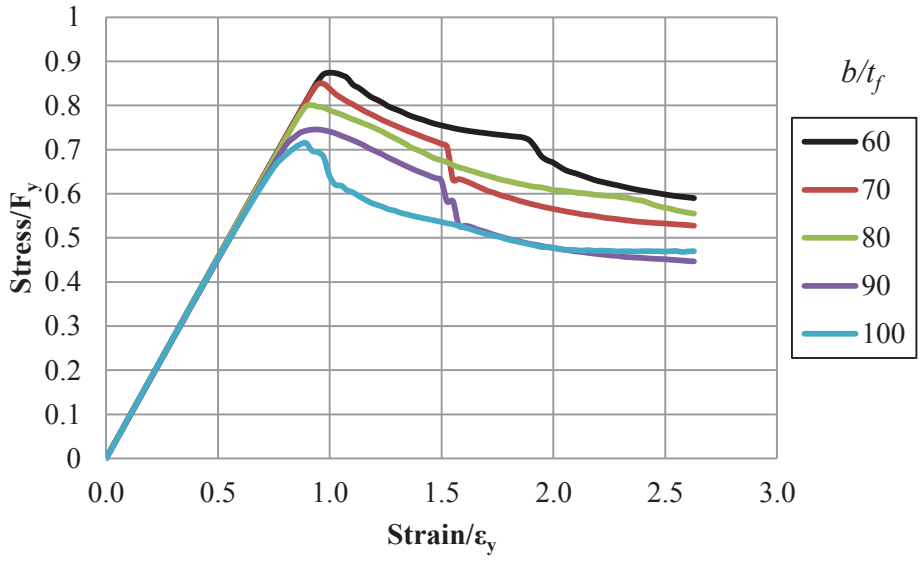

Figure 7.1 Normalized Axial Stress-Strain Curves for the Steel Tubes for Rectangular CFT Columns (F_y=317 MPa, f'_c=21 MPa)

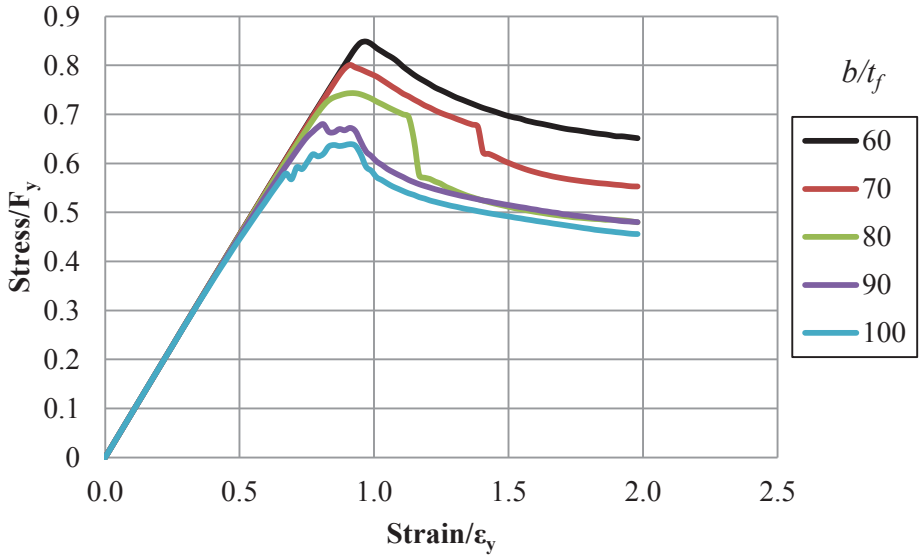

Figure 7.2 Normalized Axial Stress-Strain Curves for the Steel Tubes for Rectangular CFT Columns (F_y=421 MPa, f'_c=21 MPa)

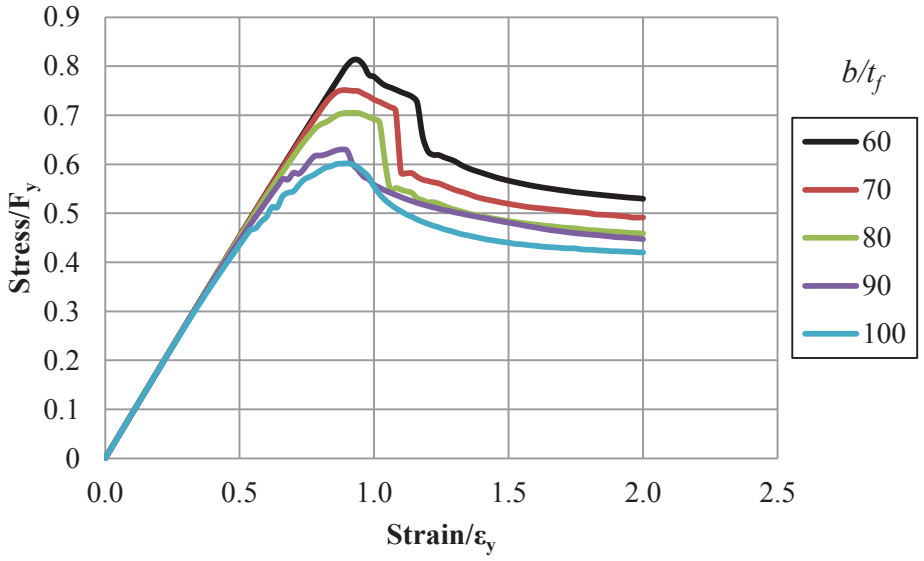

Figure 7.3 Normalized Axial Stress-Strain Curves for the Steel Tubes for Rectangular CFT Columns (F_y=525 MPa, f'_c=21 MPa)

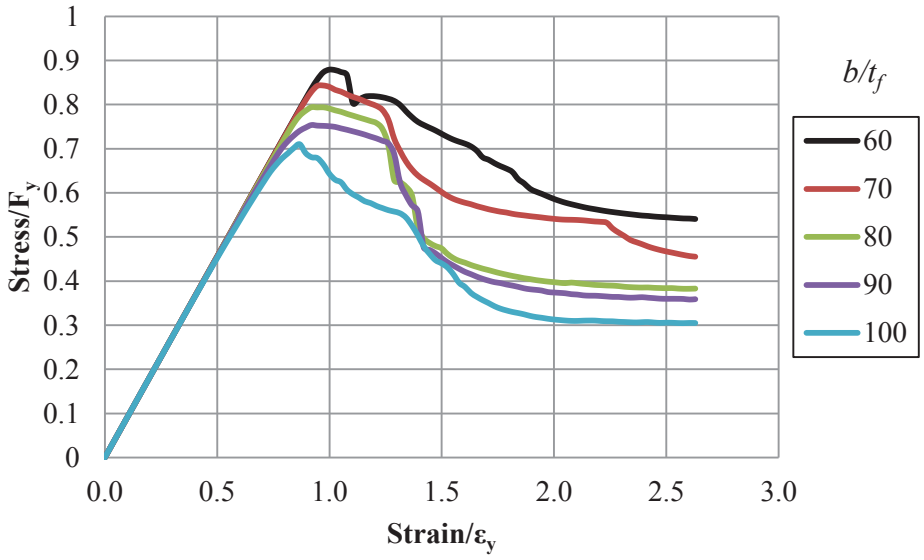

Figure 7.4 Normalized Axial Stress-Strain Curves for the Steel Tubes for Rectangular CFT Columns (F_y=317 MPa, f'_c=45 MPa)

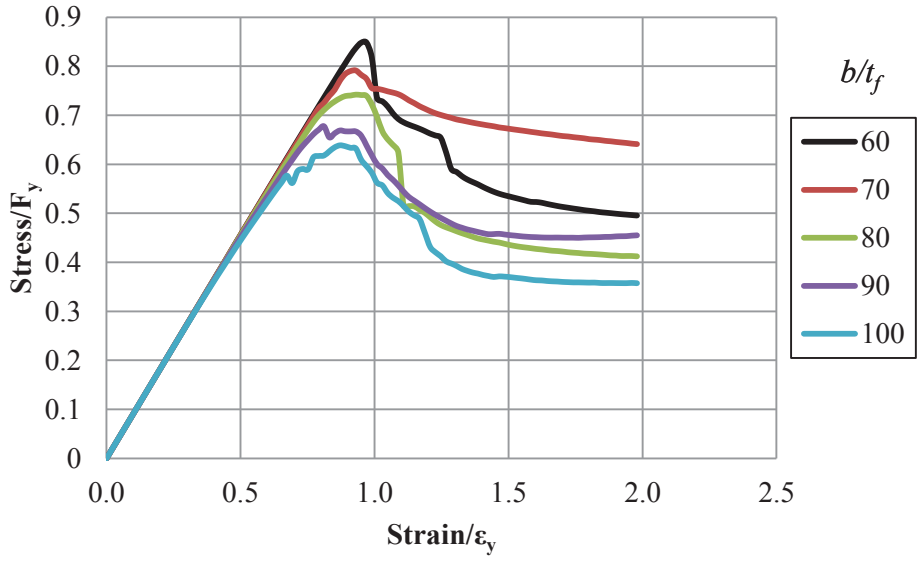

Figure 7.5 Normalized Axial Stress-Strain Curves for the Steel Tubes for Rectangular CFT Columns (F_y=421 MPa, f'_c=45 MPa)

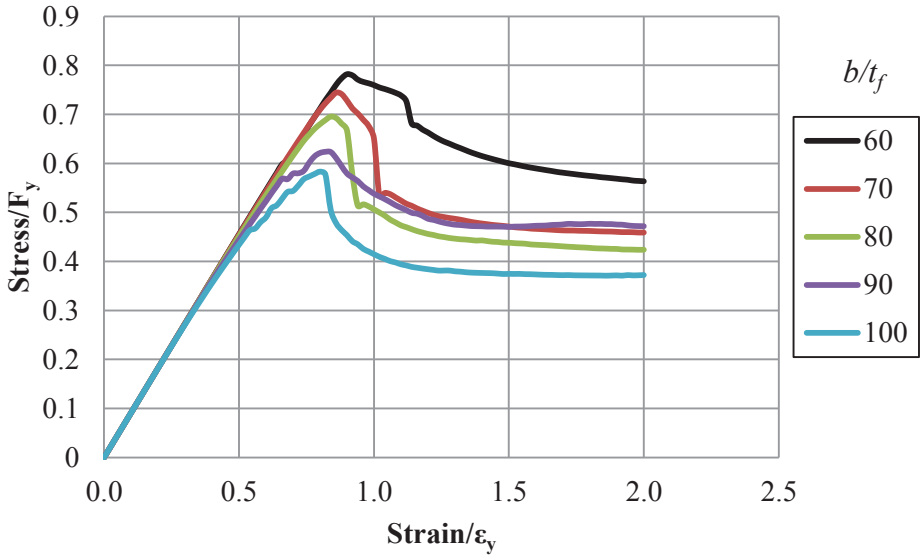

Figure 7.6 Normalized Axial Stress-Strain Curves for the Steel Tubes for Rectangular CFT Columns (F_y=525 MPa, f'_c=45 MPa)

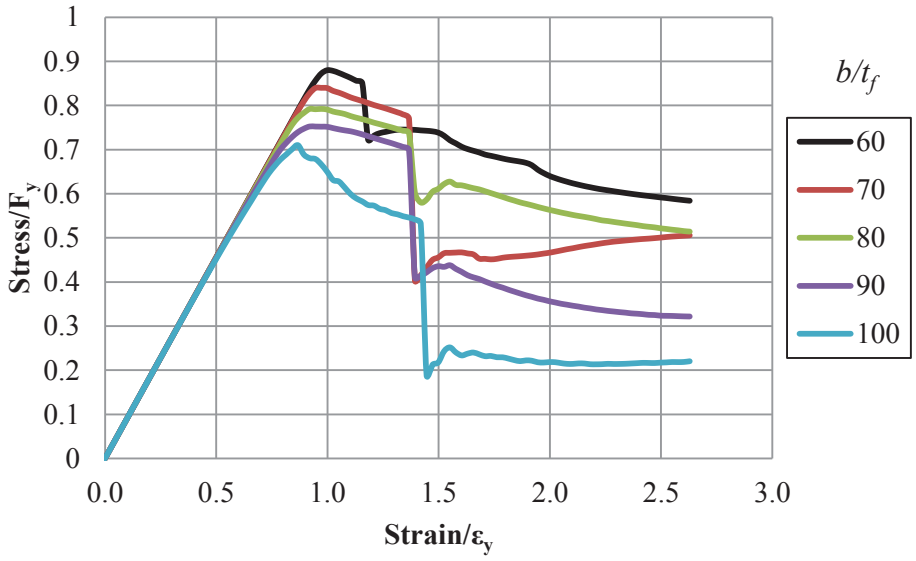

Figure 7.7 Normalized Axial Stress-Strain Curves for the Steel Tubes for Rectangular CFT Columns (F_y=317 MPa, f'_c=70 MPa)

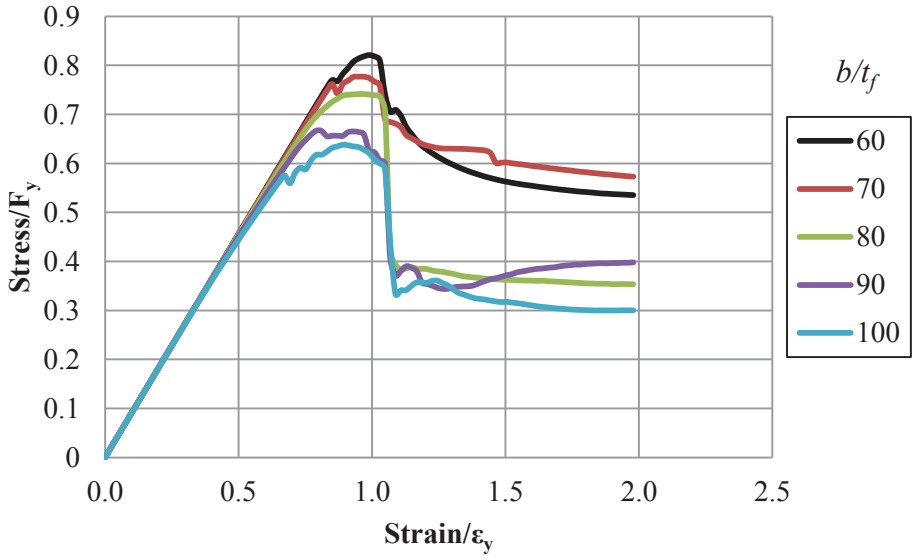

Figure 7.8 Normalized Axial Stress-Strain Curves for the Steel Tubes for Rectangular CFT Columns (F_y=421 MPa, f'_c=70 MPa)

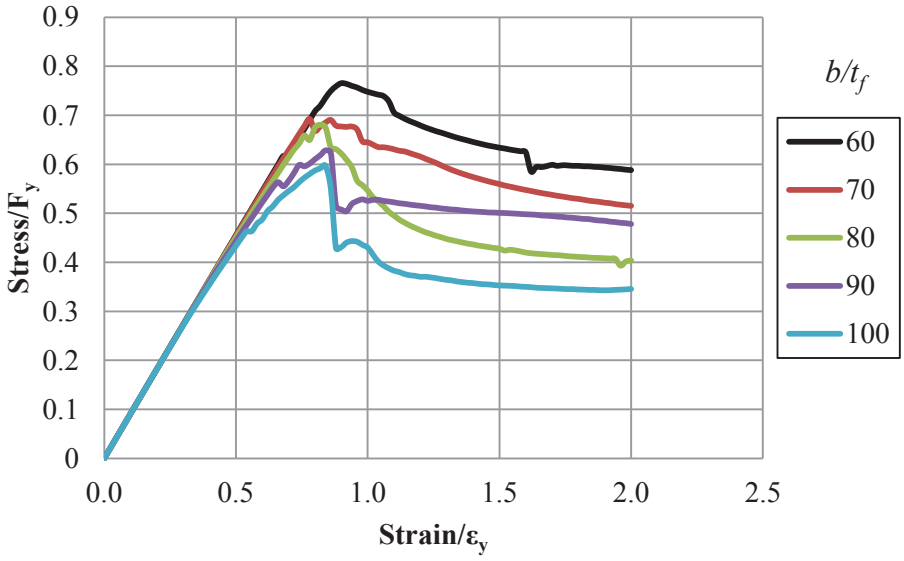

Figure 7.9 Normalized Axial Stress-Strain Curves for the Steel Tubes for Rectangular CFT Columns (F_y=525 MPa, f'_c=70 MPa)

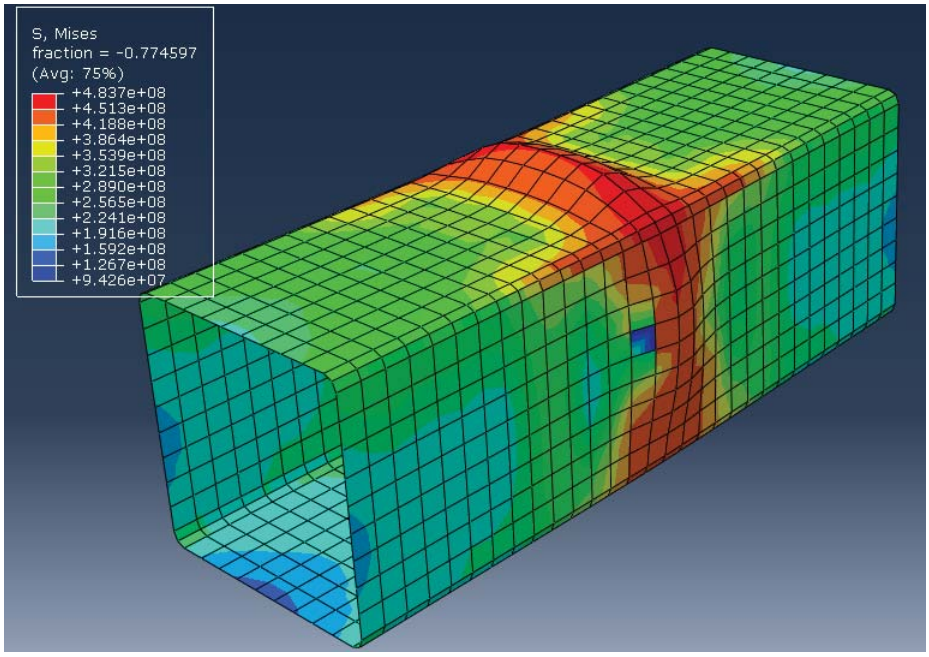

Figure 7.10 Propagation of the Local Buckling to the Webs

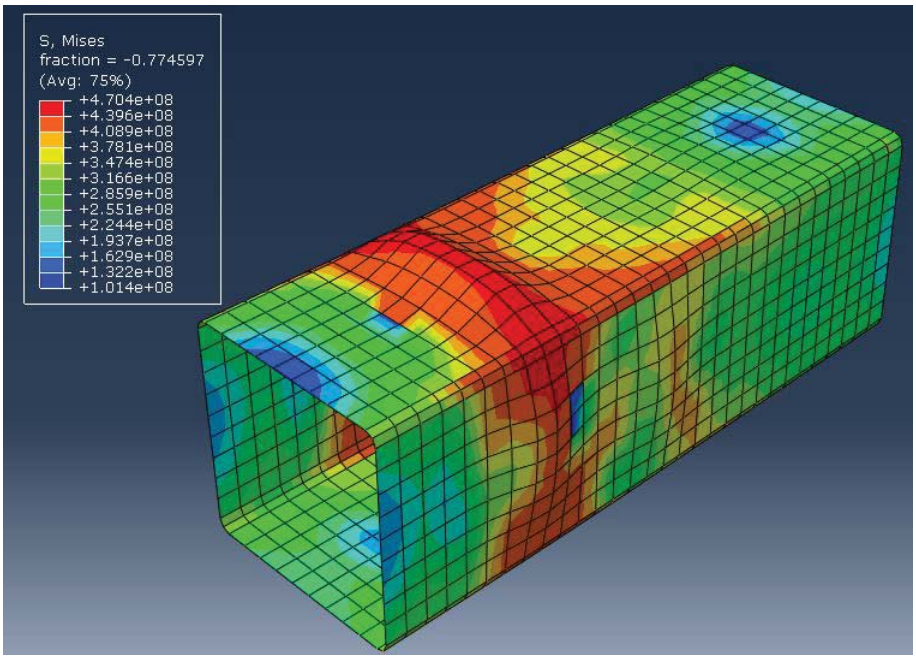

Figure 7.11 Shifting of the Local Buckling from the Midspan to Other Location

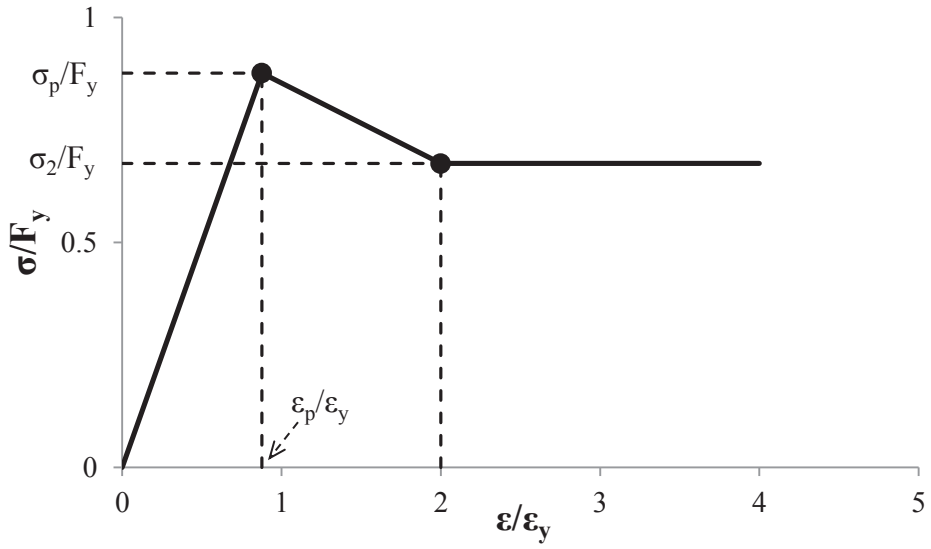

Figure 7.12 Idealized Effective Stress-Strain Curve for the Steel Tube in Compression for Noncompact and Slender Rectangular CFT members

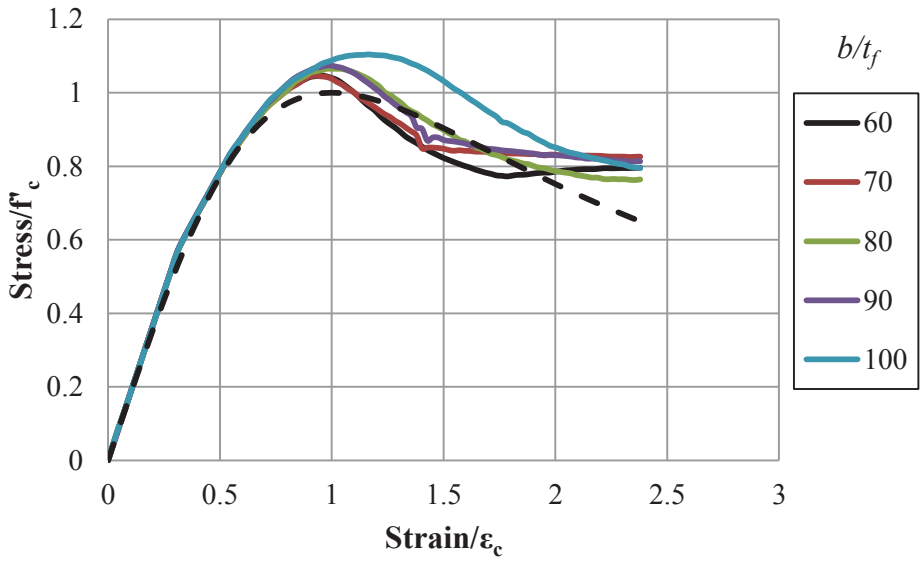

Figure 7.13 Normalized Axial Stress-Strain Curves for the Concrete Infill for Rectangular CFT Columns (F_y=317 MPa, f'_c=21 MPa)

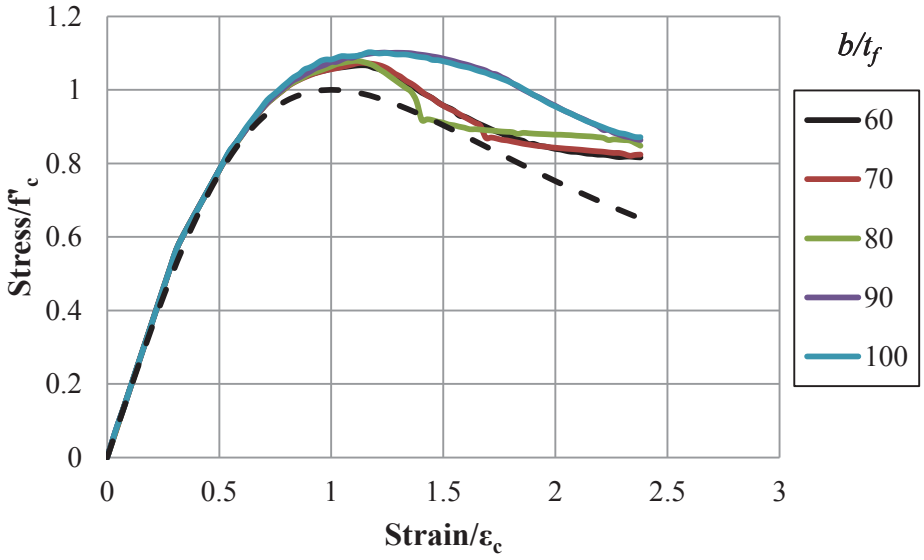

Figure 7.14 Normalized Axial Stress-Strain Curves for the Concrete Infill for Rectangular CFT Columns (F_y=421 MPa, f'_c=21 MPa)

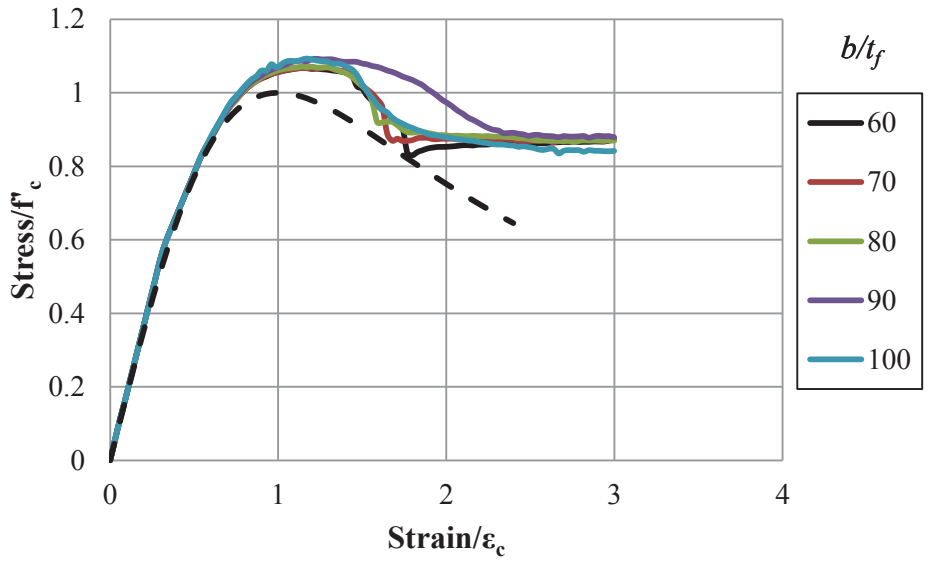

Figure 7.15 Normalized Axial Stress-Strain Curves for the Concrete Infill for Rectangular CFT Columns (F_y=525 MPa, f'_c=21 MPa)

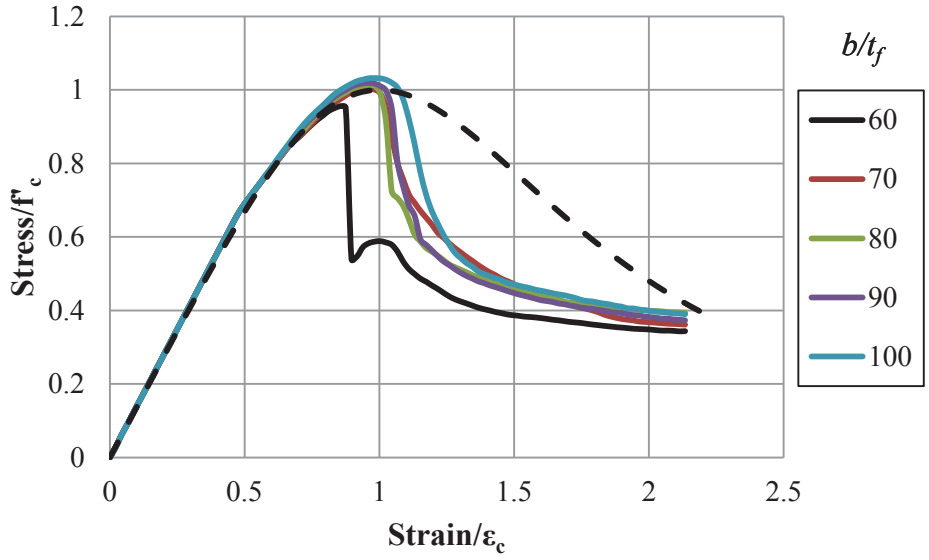

Figure 7.16 Normalized Axial Stress-Strain Curves for the Concrete Infill for Rectangular CFT Columns (F_y=317 MPa, f'_c=45 MPa)

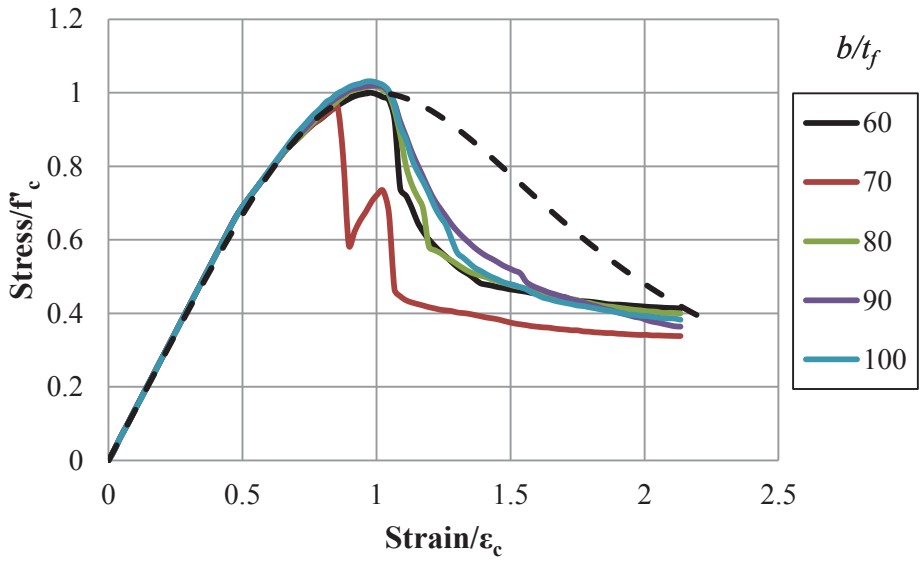

Figure 7.17 Normalized Axial Stress-Strain Curves for the Concrete Infill for Rectangular CFT Columns (F_y=421 MPa, f'_c=45 MPa)

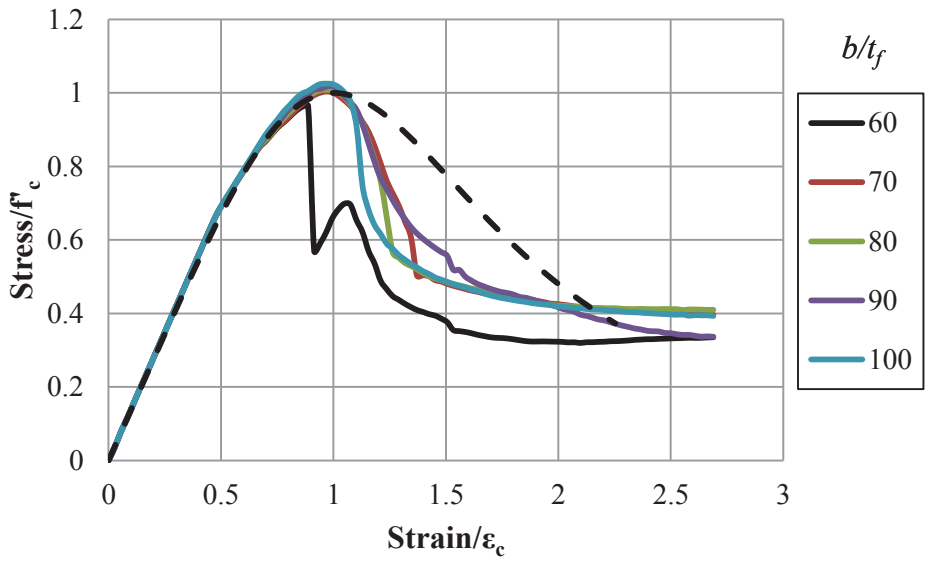

Figure 7.18 Normalized Axial Stress-Strain Curves for the Concrete Infill for Rectangular CFT Columns (F_y=525 MPa, f'_c=45 MPa)

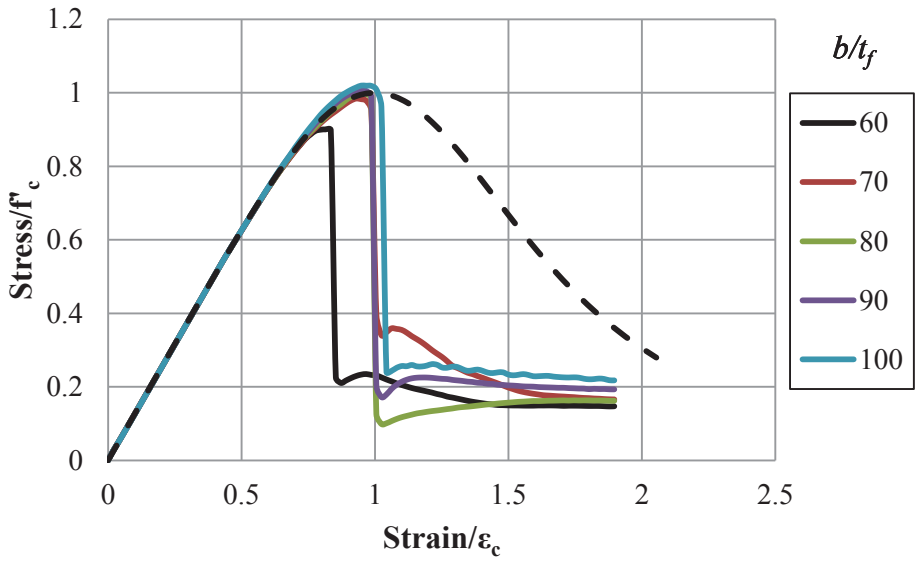

Figure 7.19 Normalized Axial Stress-Strain Curves for the Concrete Infill for Rectangular CFT Columns (F_y=317 MPa, f'_c=70 MPa)

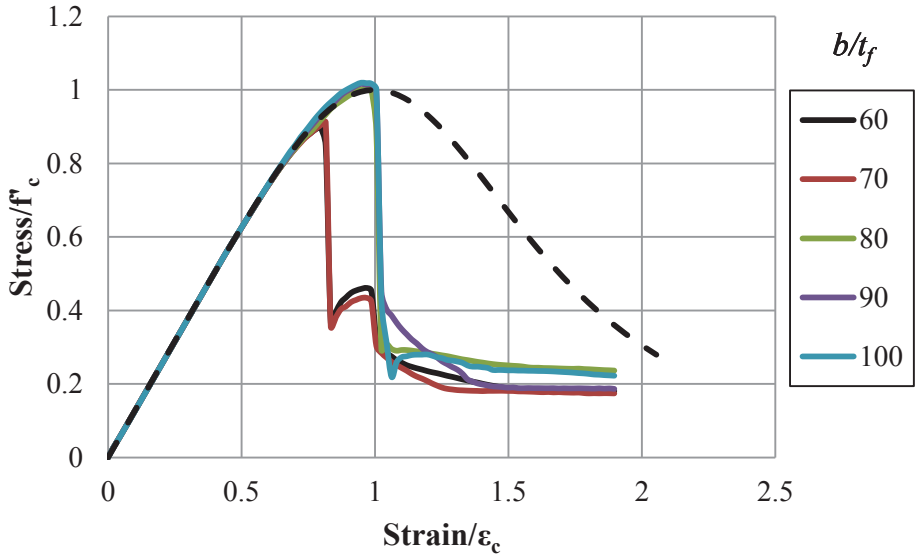

Figure 7.20 Normalized Axial Stress-Strain Curves for the Concrete Infill for Rectangular CFT Columns (F_y=421 MPa, f'_c=70 MPa)

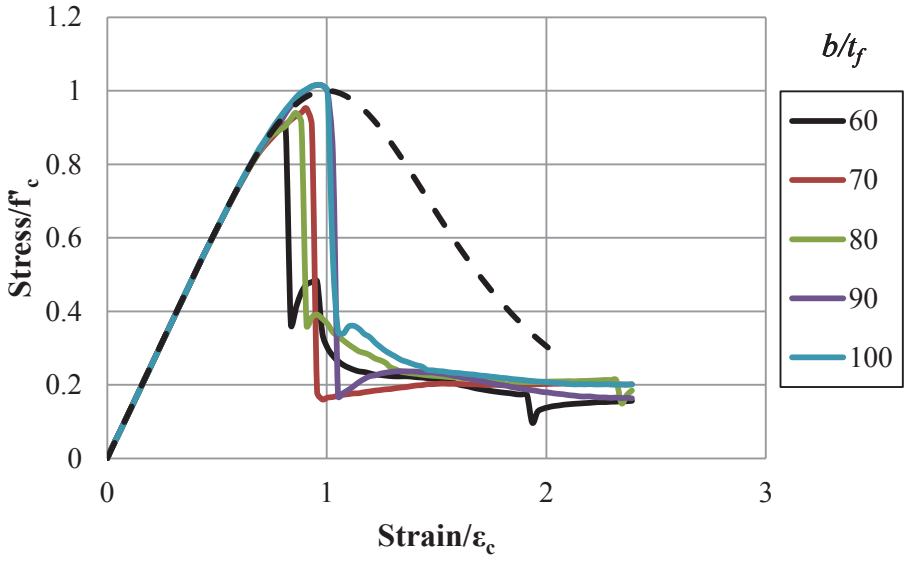

Figure 7.21 Normalized Axial Stress-Strain Curves for the Concrete Infill for Rectangular CFT Columns (F_y=525 MPa, f'_c=70 MPa)

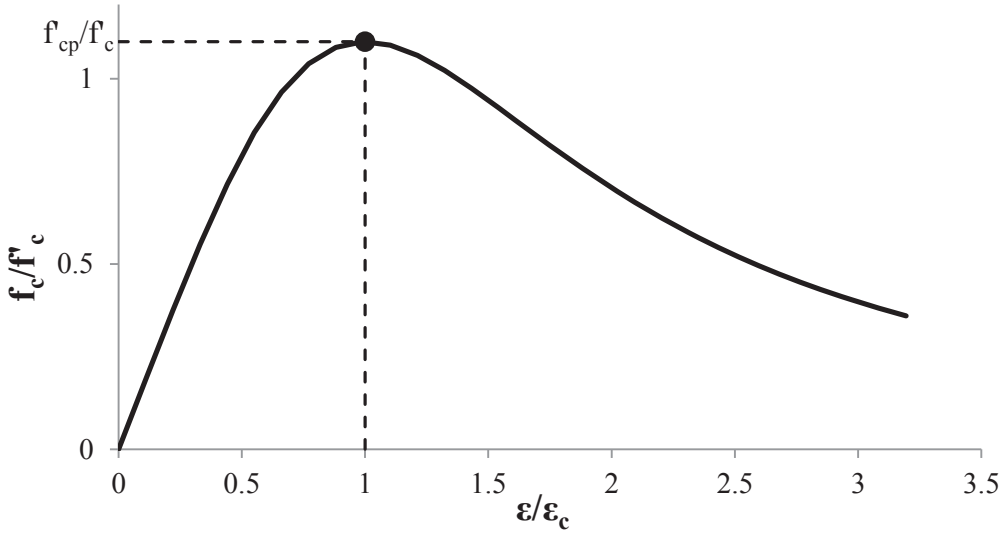

Figure 7.22 Idealized Effective Stress-Strain Curve for the Concrete Infill in Compression for Noncompact and Slender Rectangular CFT members

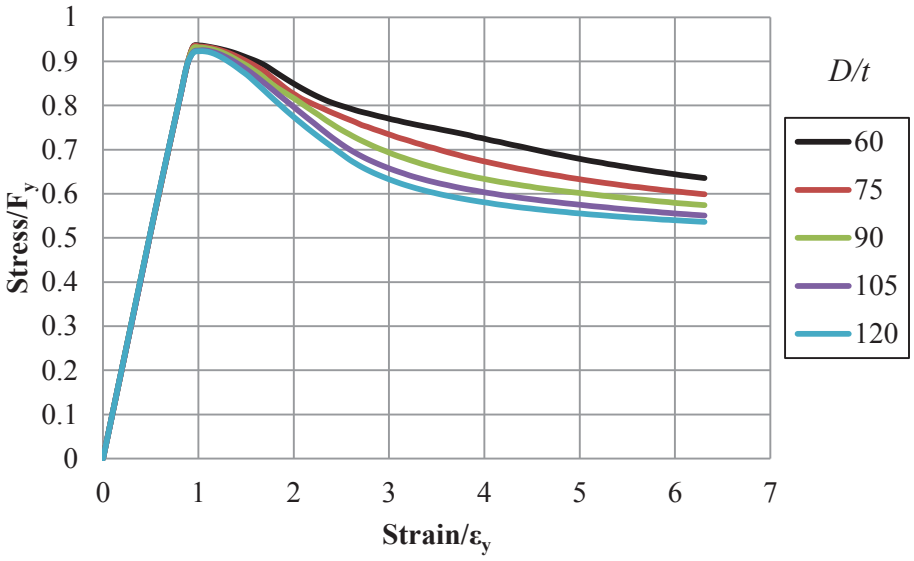

Figure 7.23 Normalized Axial Stress-Strain Curves for the Steel Tubes for Circular CFT Columns (F_y=317 MPa, f'_c=21 MPa)

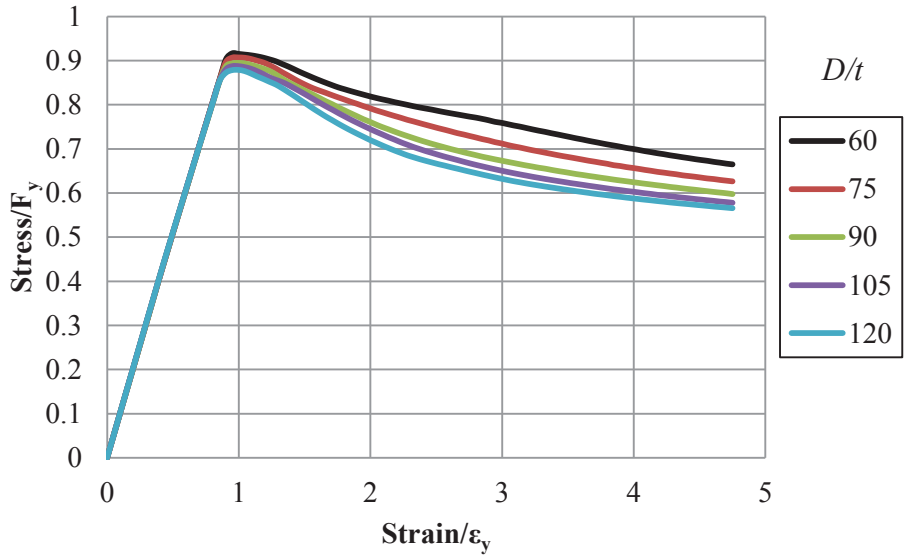

Figure 7.24 Normalized Axial Stress-Strain Curves for the Steel Tubes for Circular CFT Columns (F_y=421 MPa, f'_c=21 MPa)

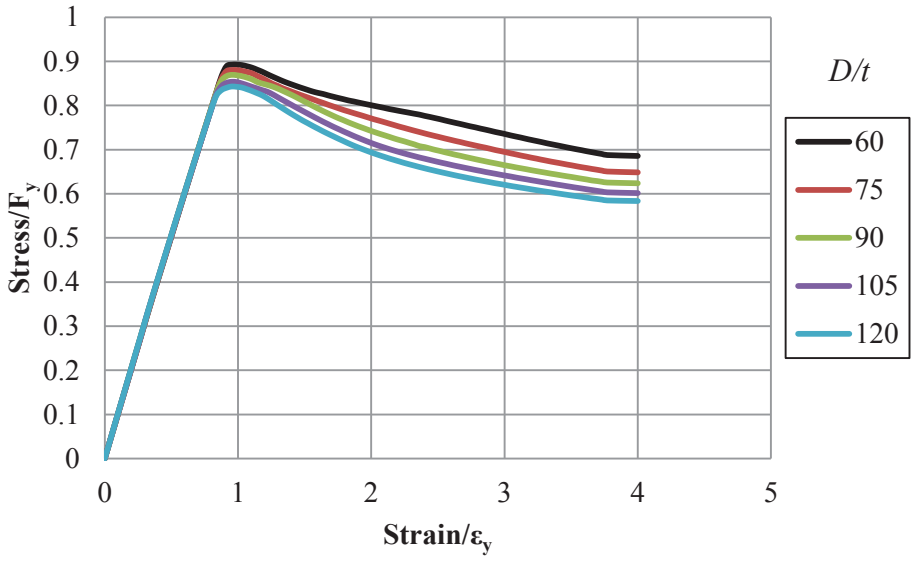

Figure 7.25 Normalized Axial Stress-Strain Curves for the Steel Tubes for Circular CFT Columns (F_y=525 MPa, f'_c=21 MPa)

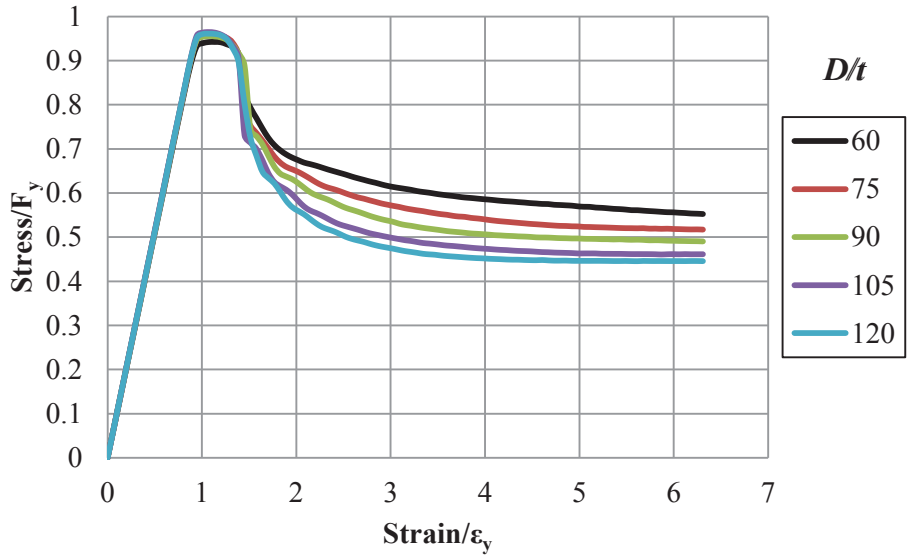

Figure 7.26 Normalized Axial Stress-Strain Curves for the Steel Tubes for Circular CFT Columns (F_y=317 MPa, f'_c=45 MPa)

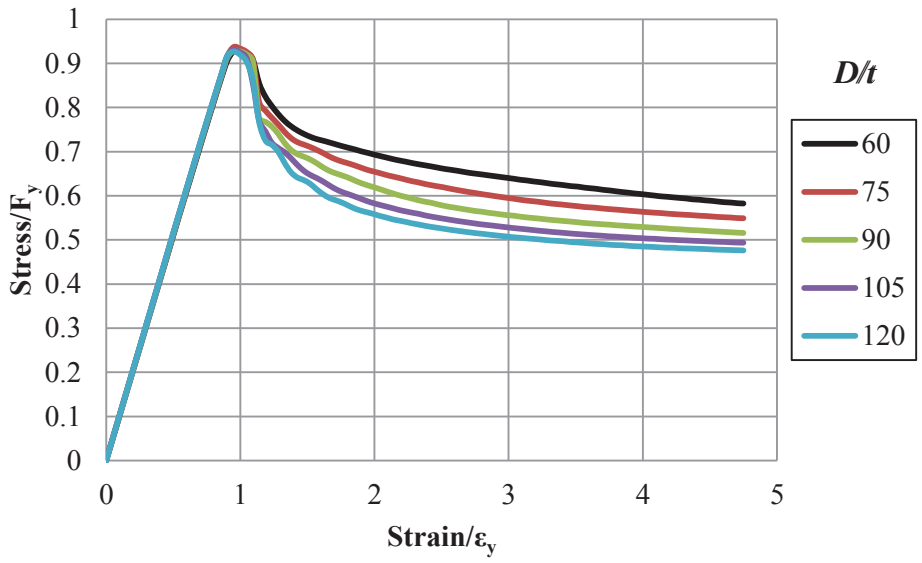

Figure 7.27 Normalized Axial Stress-Strain Curves for the Steel Tubes for Circular CFT Columns (F_y=421 MPa, f'_c=45 MPa)

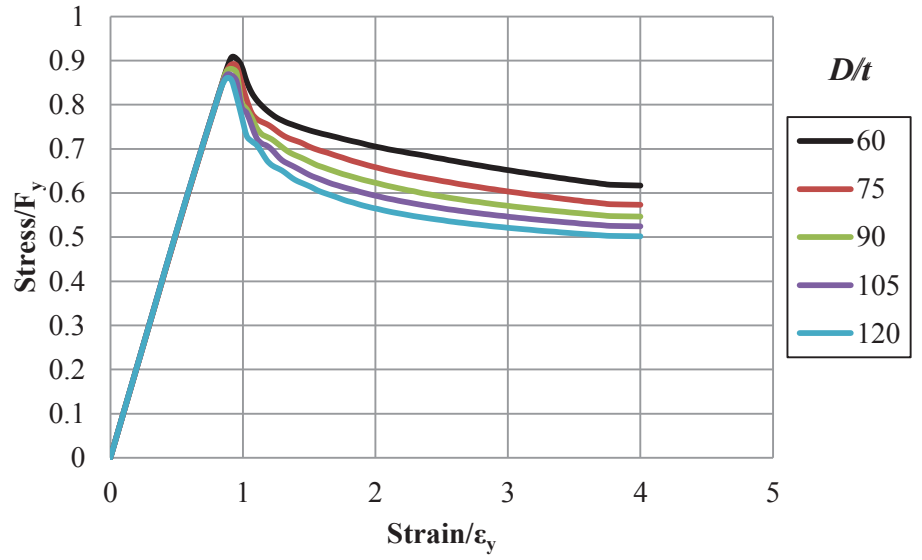

Figure 7.28 Normalized Axial Stress-Strain Curves for the Steel Tubes for Circular CFT Columns (F_y=525 MPa, f'_c=45 MPa)

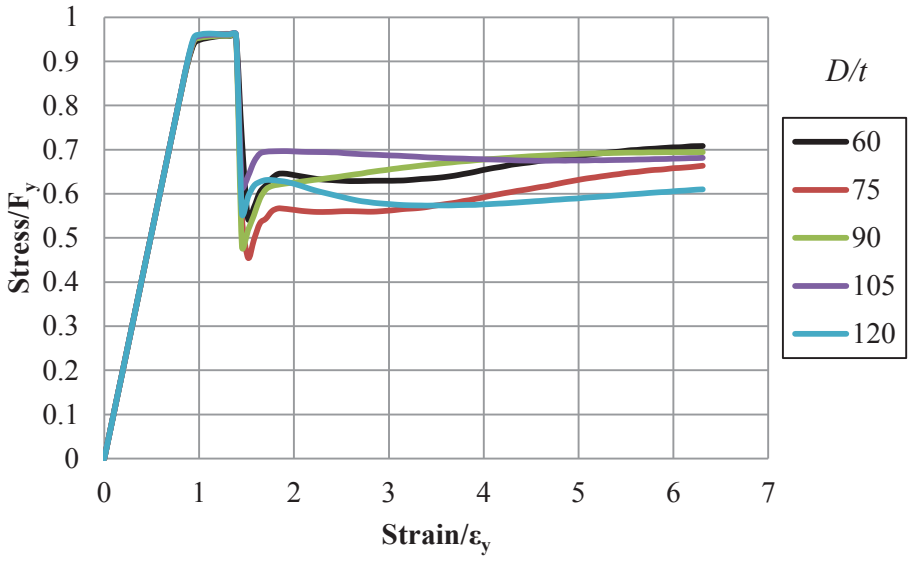

Figure 7.29 Normalized Axial Stress-Strain Curves for the Steel Tubes for Circular CFT Columns (F_y=317 MPa, f'_c=70 MPa)

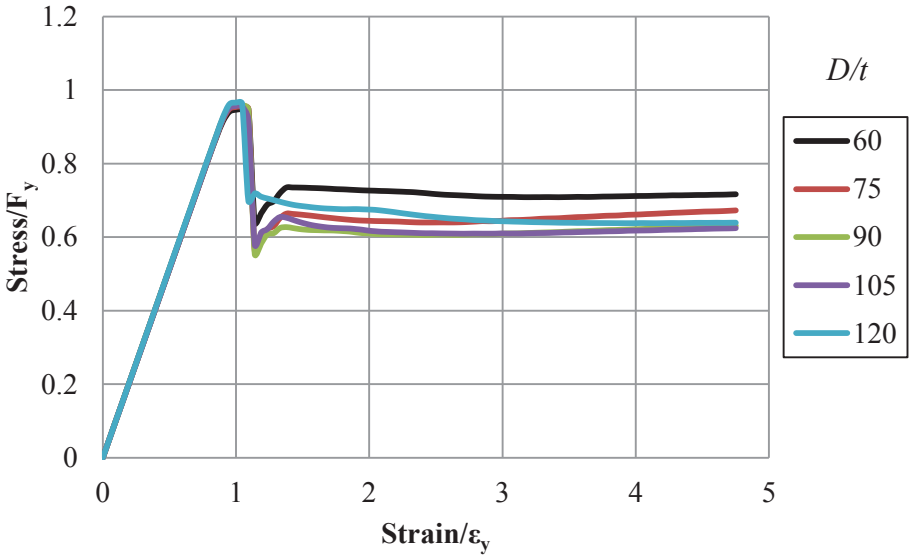

Figure 7.30 Normalized Axial Stress-Strain Curves for the Steel Tubes for Circular CFT Columns (F_y=317 MPa, f'_c=21 MPa)

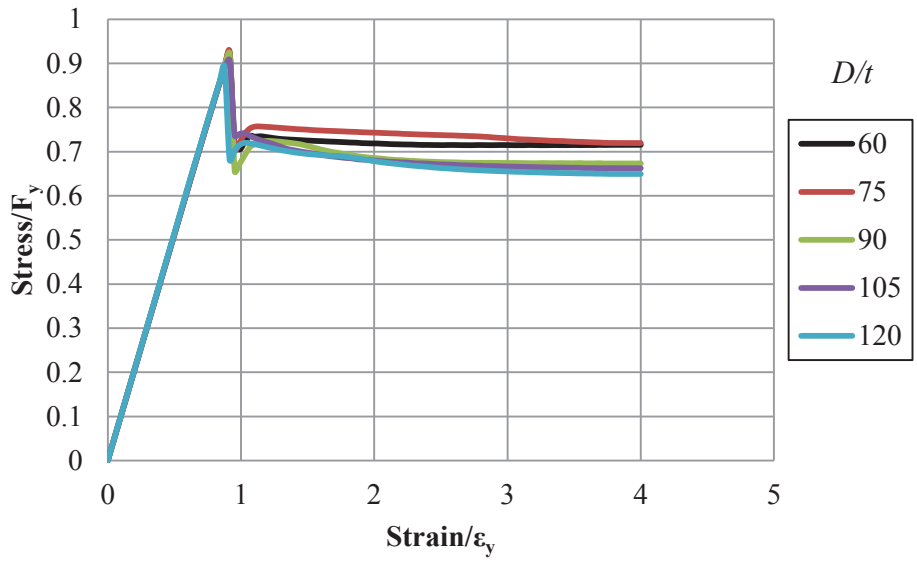

Figure 7.31 Normalized Axial Stress-Strain Curves for the Steel Tubes for Circular CFT Columns (F_y=525 MPa, f'_c=70 MPa)

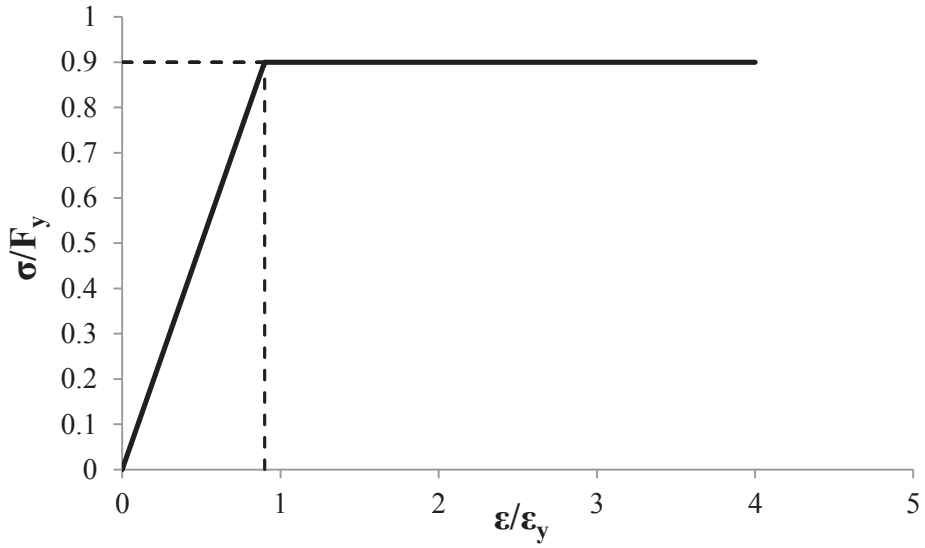

Figure 7.32 Idealized Effective Stress-Strain Curve for the Steel Tube in Compression for Noncompact and Slender Circular CFT members

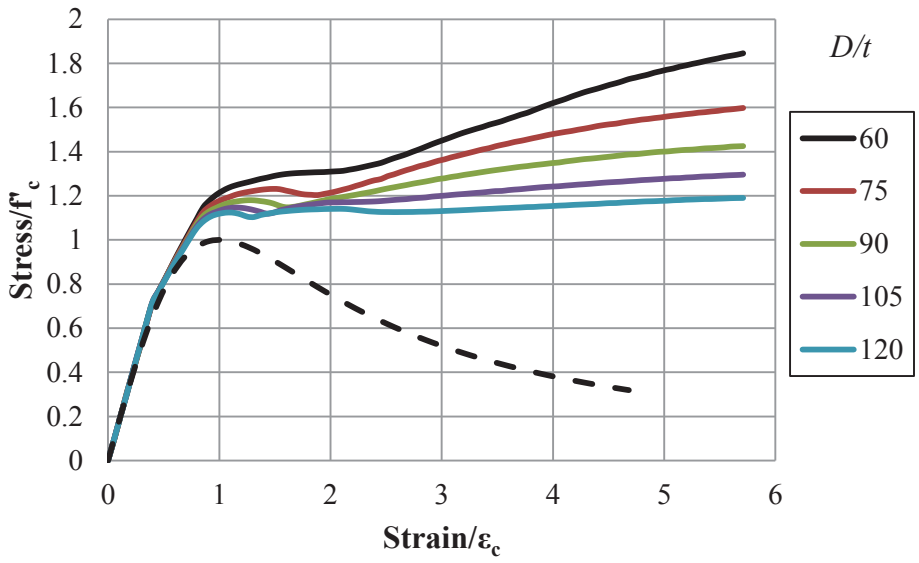

Figure 7.33 Normalized Axial Stress-Strain Curves for the Concrete Infill for Circular CFT Columns (F_y=317 MPa, f'_c=21 MPa)

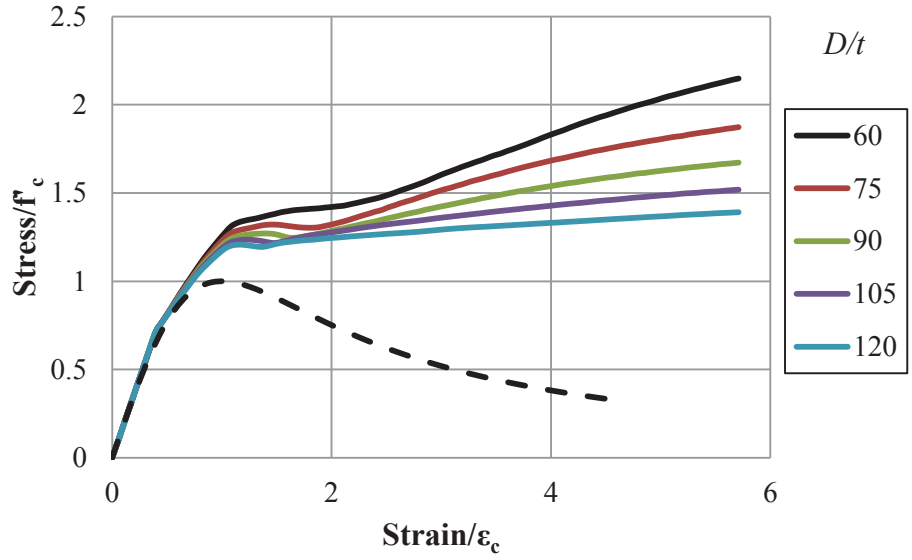

Figure 7.34 Normalized Axial Stress-Strain Curves for the Concrete Infill for Circular CFT Columns (F_y=421 MPa, f'_c=21 MPa)

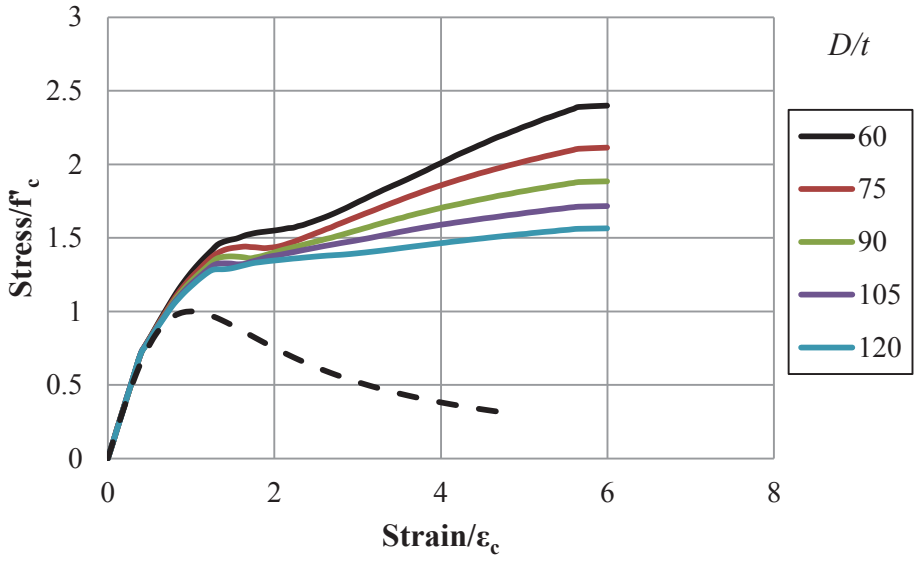

Figure 7.35 Normalized Axial Stress-Strain Curves for the Concrete Infill for Circular CFT Columns (F_y=525 MPa, f'_c=21 MPa)

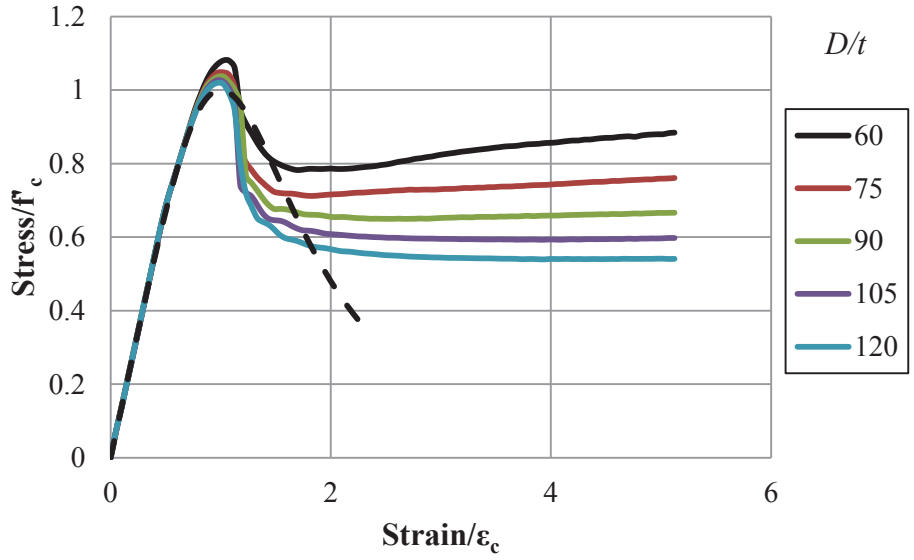

Figure 7.36 Normalized Axial Stress-Strain Curves for the Concrete Infill for Circular CFT Columns (F_y=317 MPa, f'_c=45 MPa)

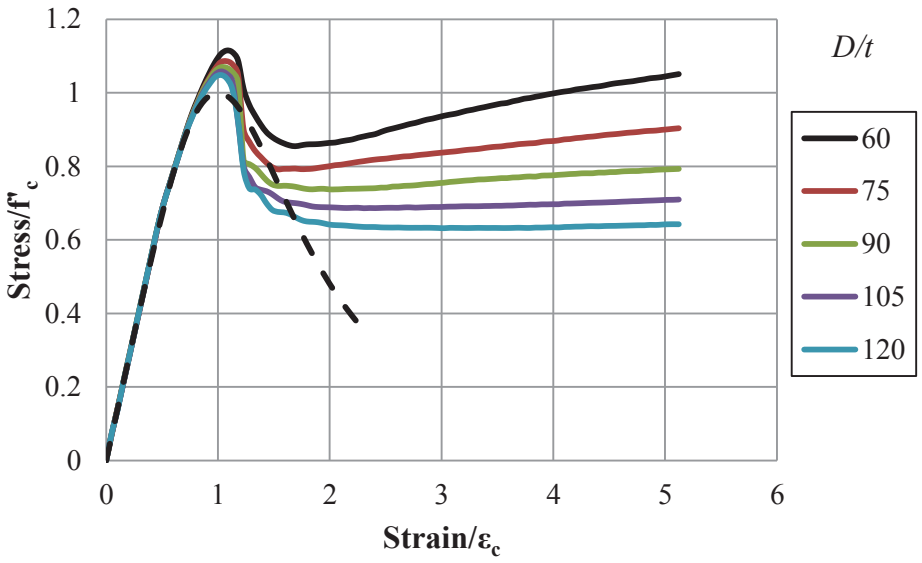

Figure 7.37 Normalized Axial Stress-Strain Curves for the Concrete Infill for Circular CFT Columns (F_y=421 MPa, f'_c=45 MPa)

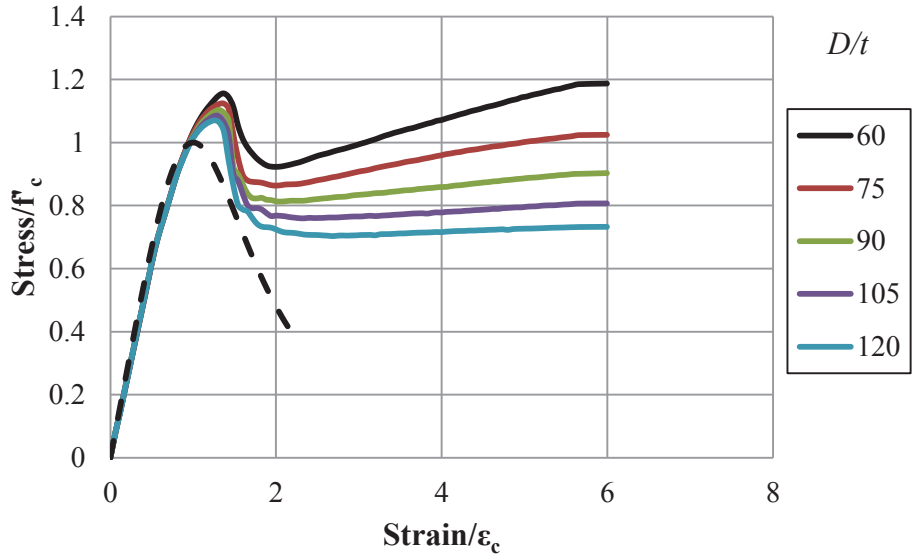

Figure 7.38 Normalized Axial Stress-Strain Curves for the Concrete Infill for Circular CFT Columns (F_y=525 MPa, f'_c=45 MPa)

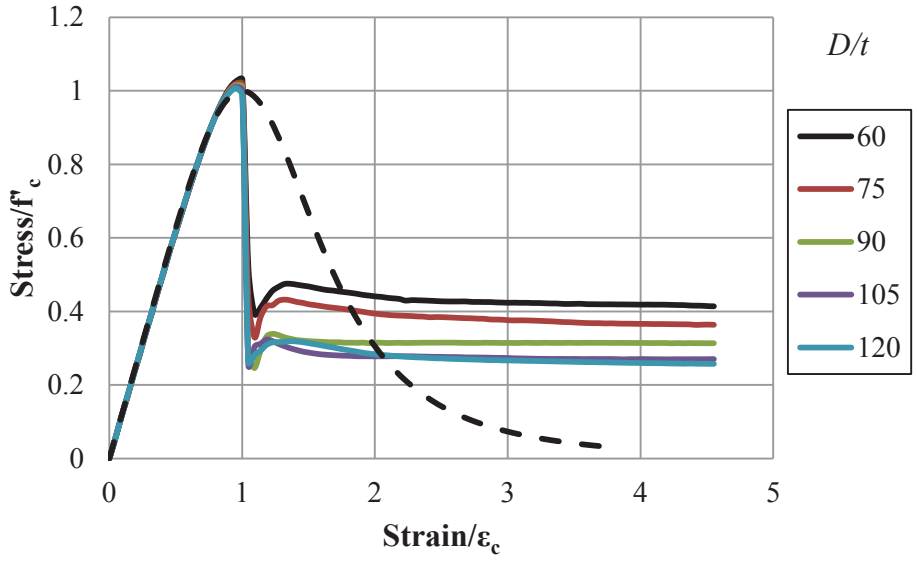

Figure 7.39 Normalized Axial Stress-Strain Curves for the Concrete Infill for Circular CFT Columns (F_y=317 MPa, f'_c=70 MPa)

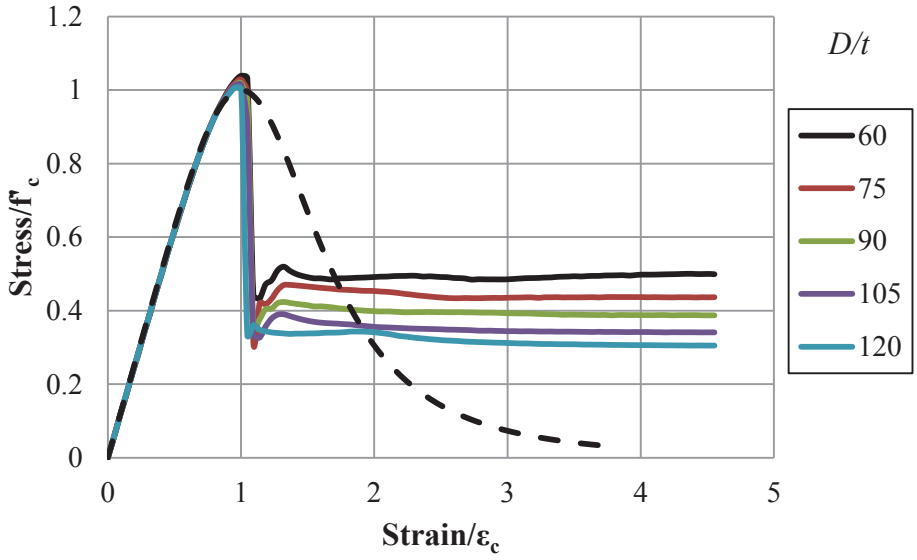

Figure 7.40 Normalized Axial Stress-Strain Curves for the Concrete Infill for Circular CFT Columns (F_y=421 MPa, f'_c=70 MPa)

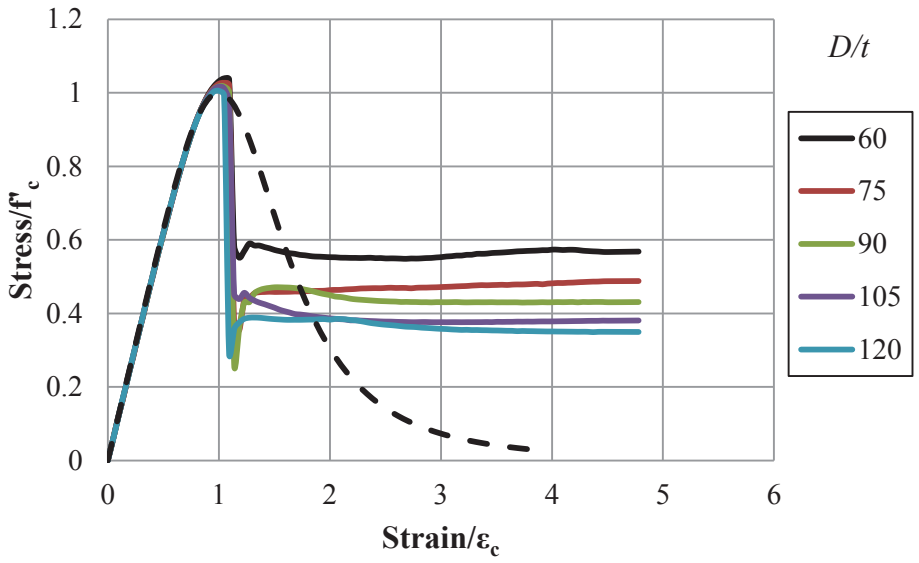

Figure 7.41 Normalized Axial Stress-Strain Curves for the Concrete Infill for Circular CFT Columns (F_y=525 MPa, f'_c=70 MPa)

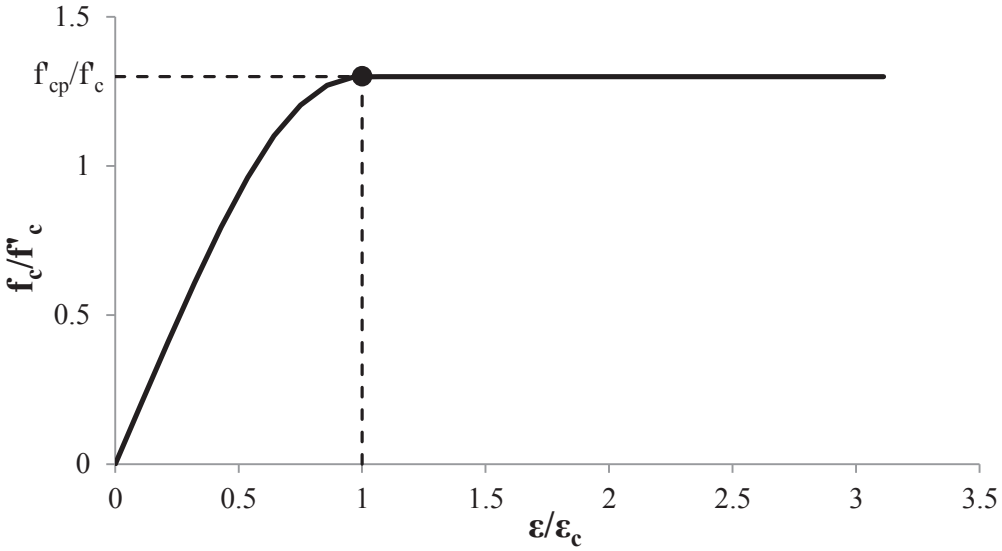

Figure 7.42 Idealized Effective Stress-Strain Curve for the Concrete Infill in Compression for Noncompact and Slender Circular CFT members

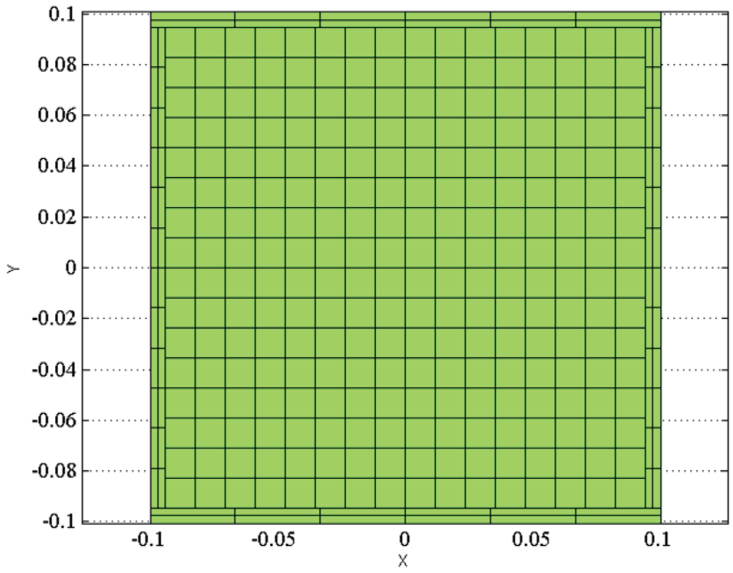

Figure 7.43 Fiber Discretization of Rectangular CFT Members

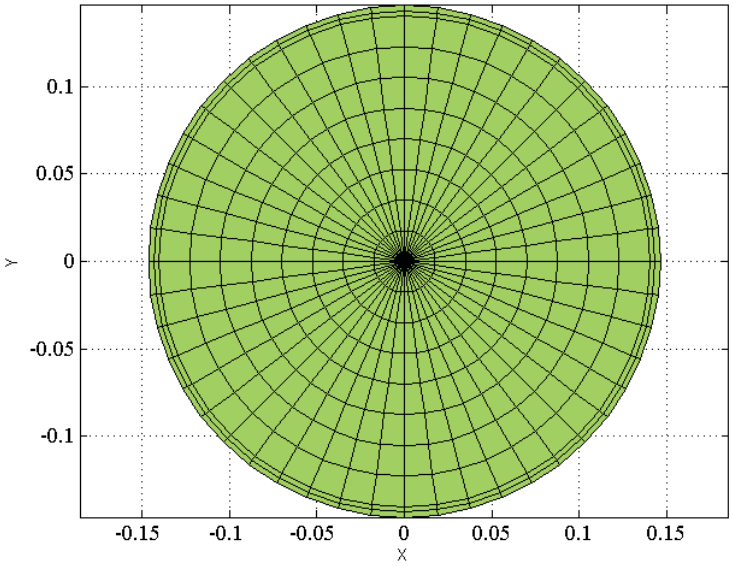

Figure 7.44 Fiber Discretization of Circular CFT Members

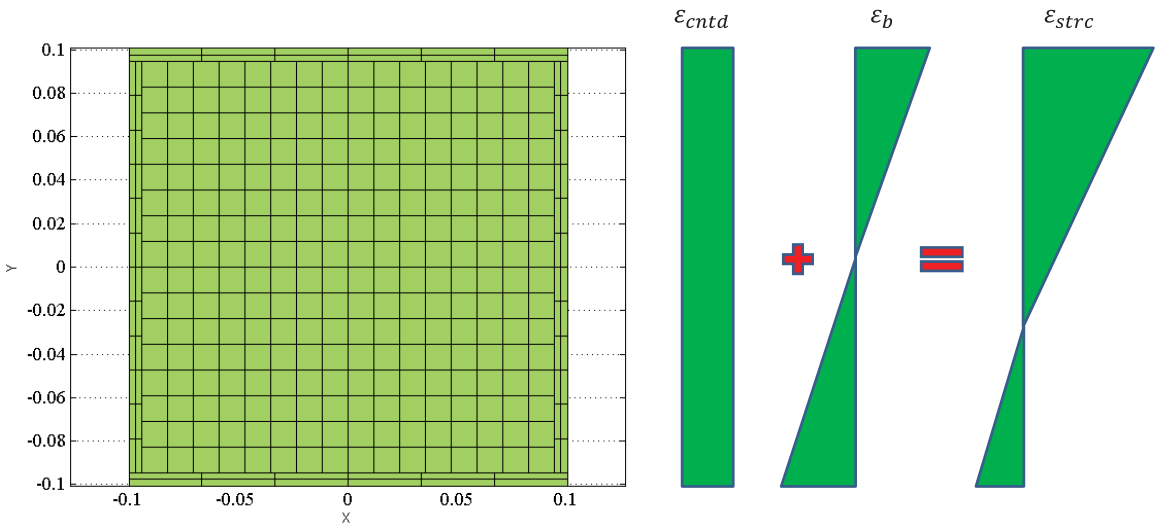

Figure 7.45 Summations of the Strain Components

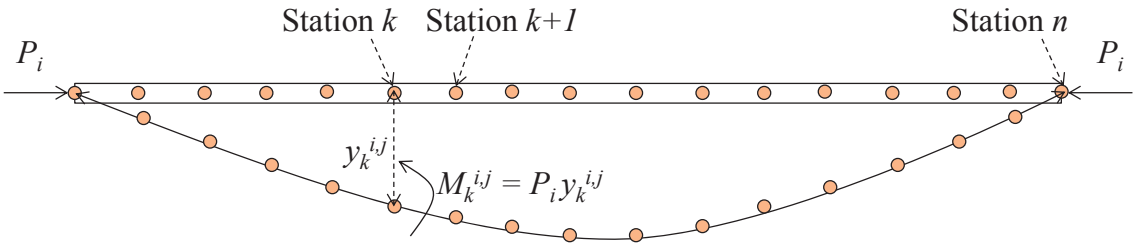

Figure 7.46 Discretization of Segments along the Member Length

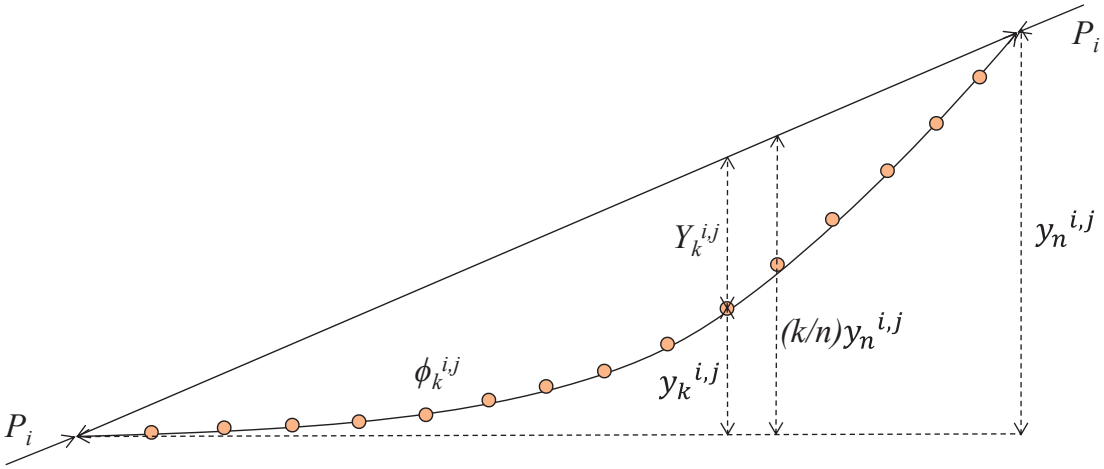

Figure 7.47 Calculation of Deflections

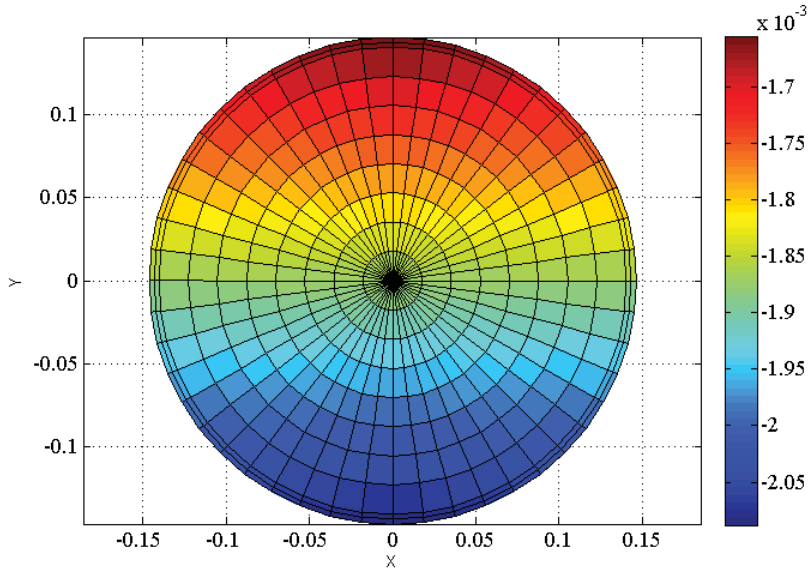

Figure 7.48 Example of Strain Distributions

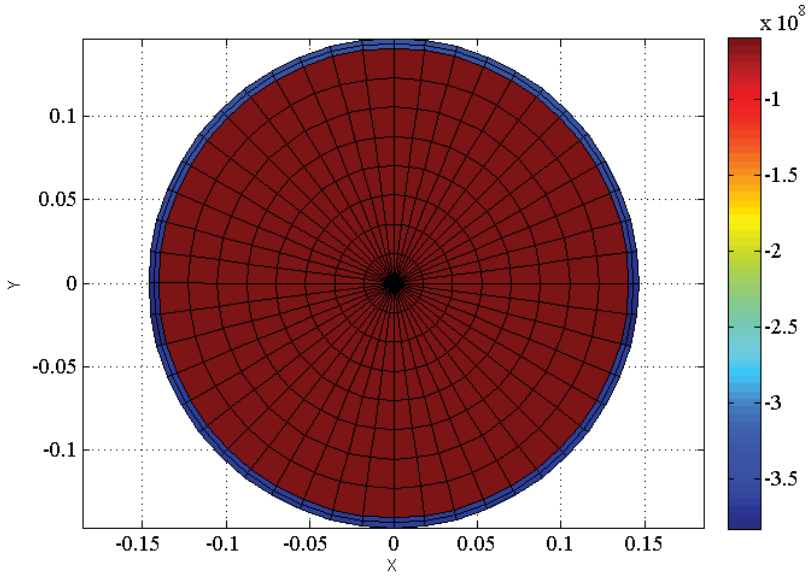

Figure 7.49 Example of Stress Distributions

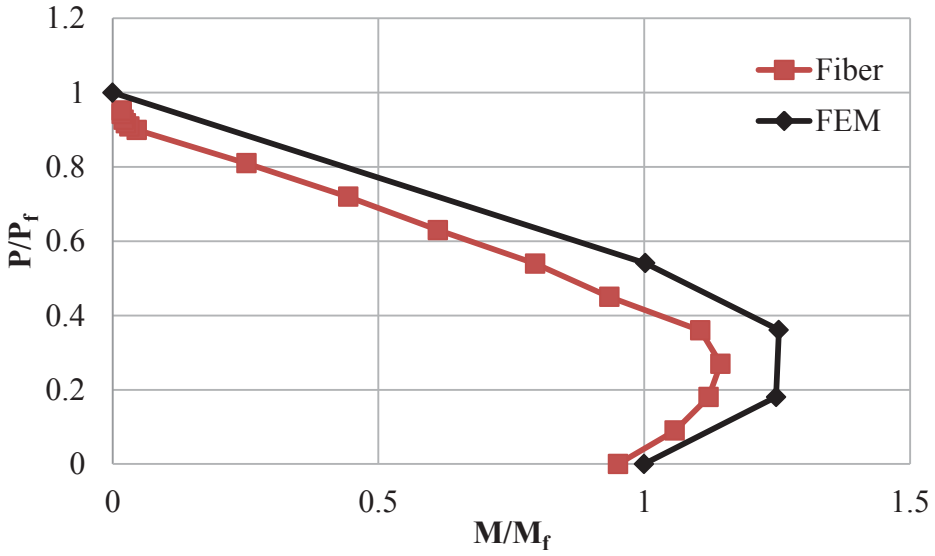

Figure 7.50Comparison of the P-M Interaction Curve for Rectangular CFT Beam-Columns (R-70-6)

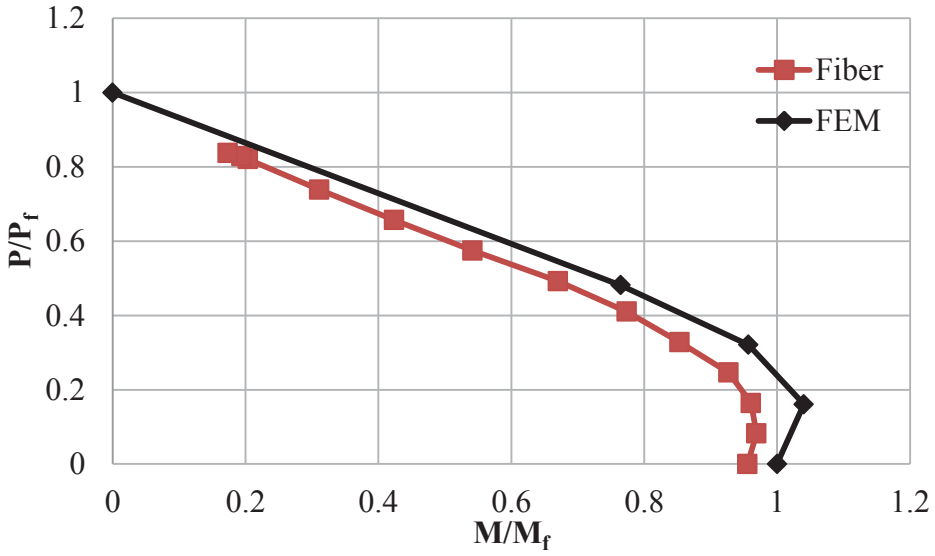

Figure 7.51 Comparison of the P-M Interaction Curve for Rectangular CFT Beam-Columns (R-70-20)

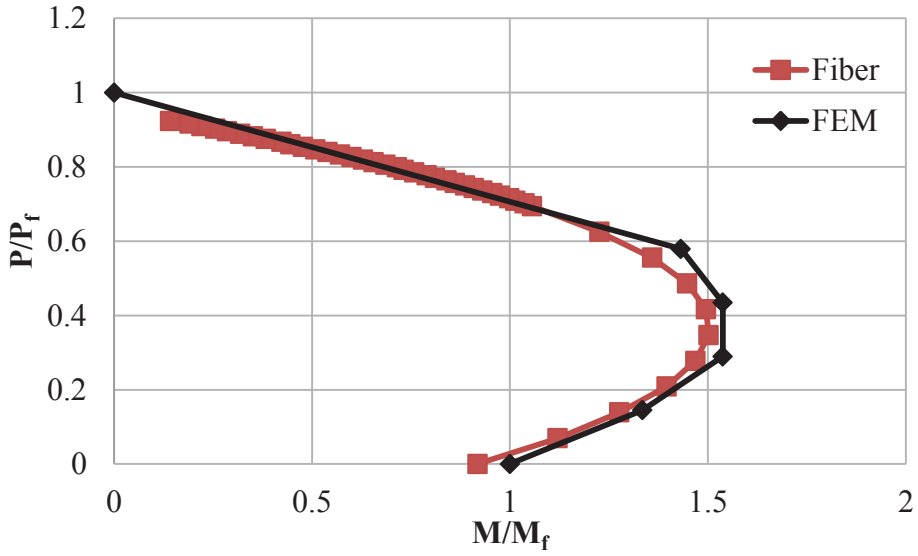

Figure 7.52 Comparison of the P-M Interaction Curve for Circular CFT Beam-Columns (C-105-7)

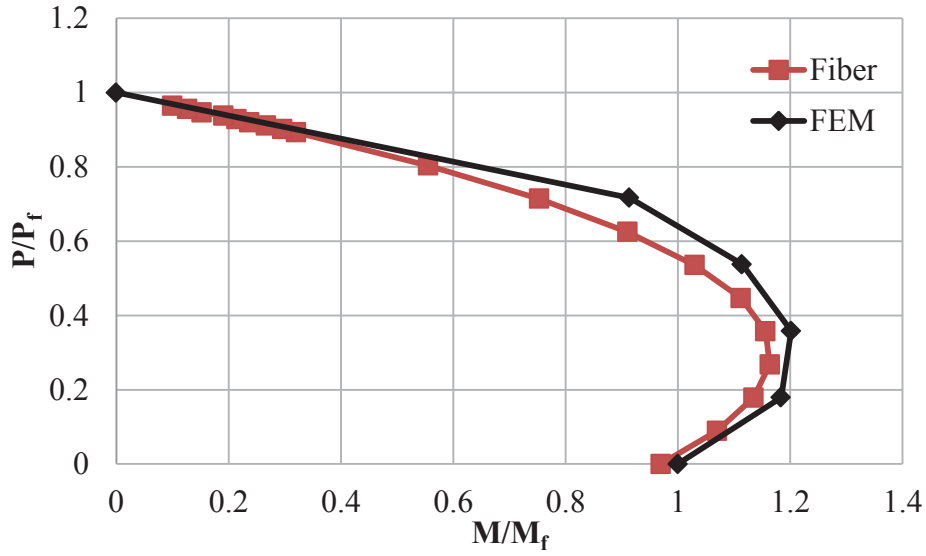

Figure 7.53 Comparison of the P-M Interaction Curve for Circular CFT Beam-Columns (C-53-8, f'_c =60 MPa)

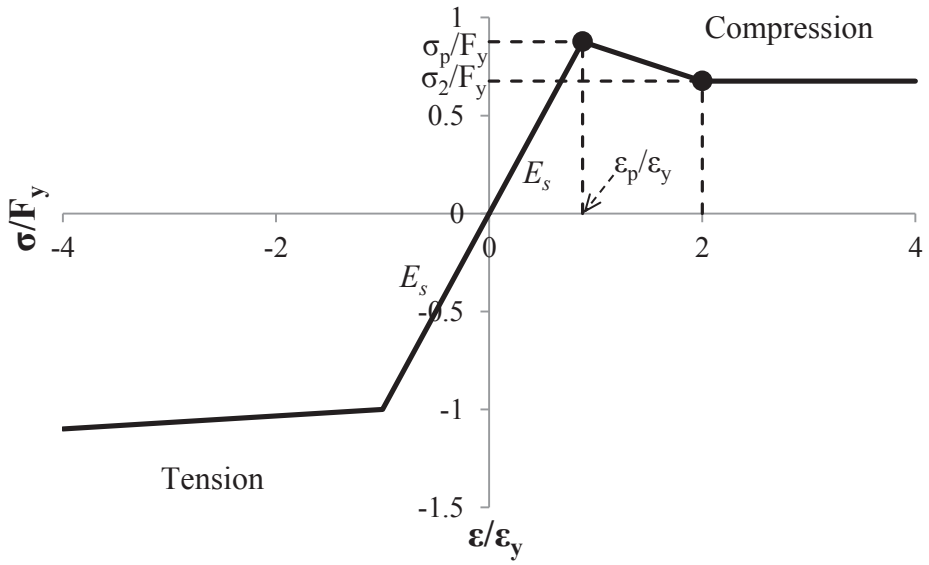

Figure 7.54 Idealized Effective Stress-Strain Curve for the Steel Tube for Noncompact and Slender Rectangular CFT members

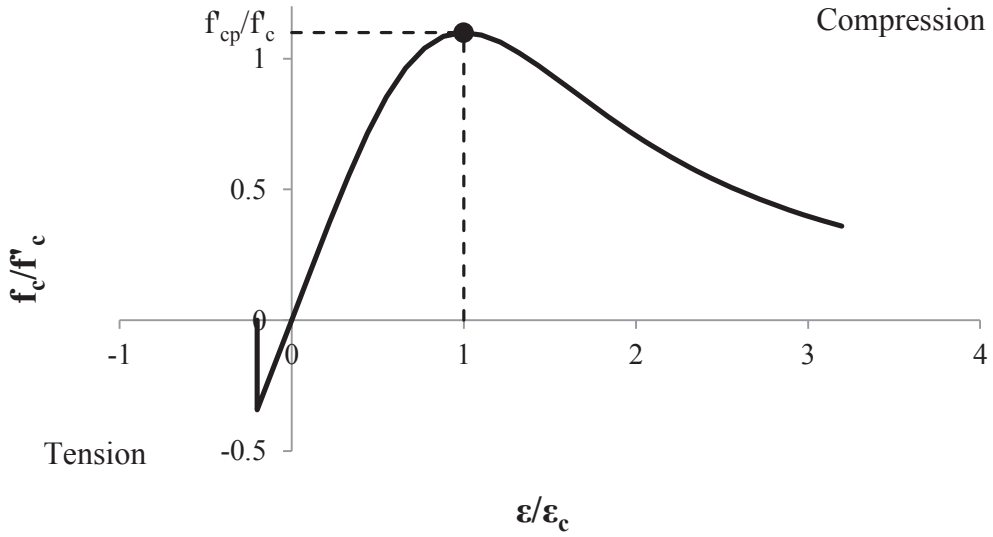

Figure 7.55 Idealized Effective Stress-Strain Curve for the Concrete Infill for Noncompact and Slender Rectangular CFT members

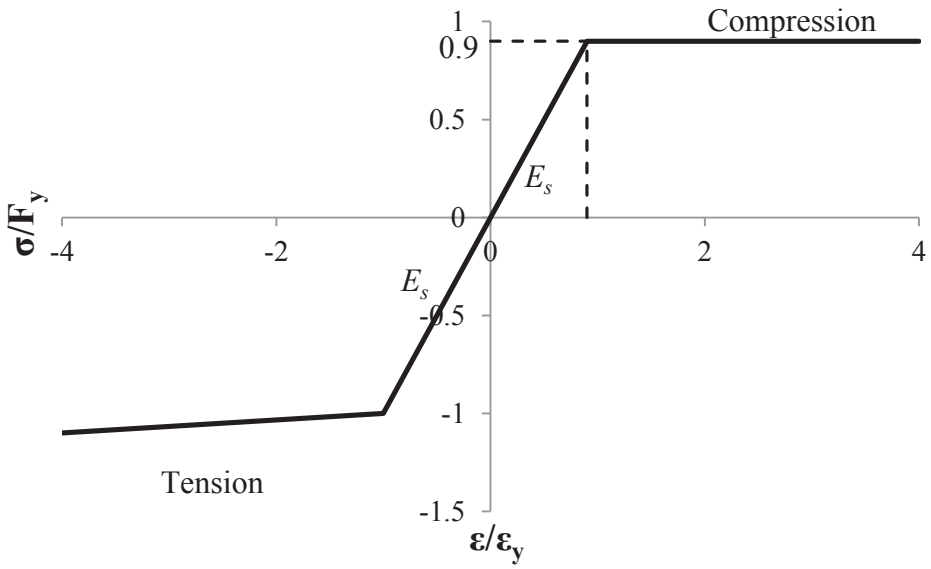

Figure 7.56 Idealized Effective Stress-Strain Curve for the Steel Tube for Noncompact and Slender Circular CFT members

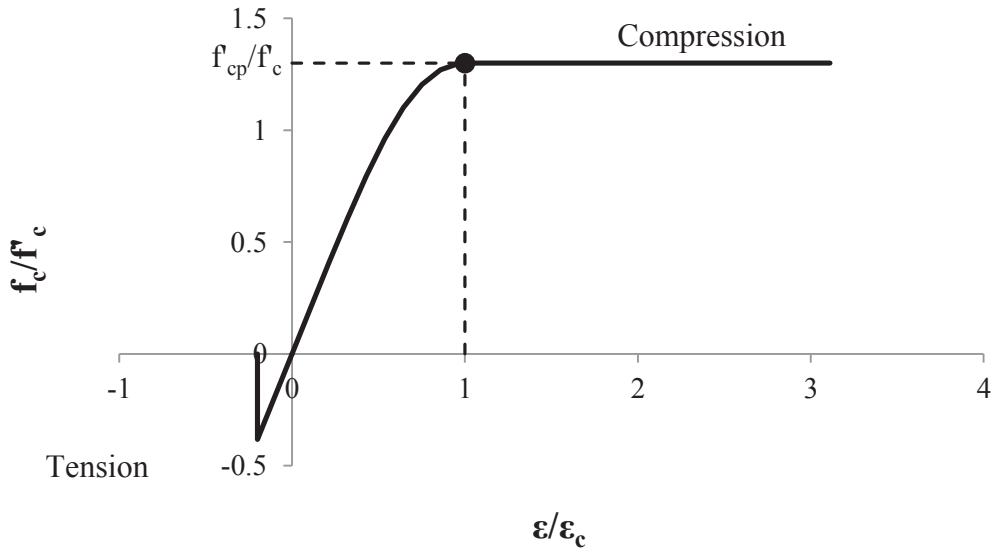

Figure 7.57 Idealized Effective Stress-Strain Curve for the Concrete Infill for Noncompact and Slender Circular CFT members

CHAPTER 8. SUMMARY, CONCLUSIONS AND FURTHER WORK

8.1 Summary

Concrete-filled steel tube beam-columns are categorized as compact, noncompact or slender depending on the governing tube slenderness ratio. AISC 360-10 specifies the provisions for designing noncompact and slender rectangular and circular CFT members under axial compression, flexure, and combined axial and flexural loading. The experimental database of tests conducted on noncompact and slender CFT members was compiled. Detailed 3D finite element method (FEM) models were developed for noncompact and slender CFT members, and benchmarked using experimental results. The AISC 360-10 design provisions for noncompact and slender CFT members were then evaluated by both the experimental test results and additional FEM analysis that address the gaps in the experimental database. The current AISC 360-10 P-M interaction equations were updated, using the results from comprehensive parametric studies conducted using the benchmarked FEM models. Effective stress-strain curves for the steel tube and concrete infill were also developed. The conservatism of these effective stress-strain curves were confirmed by implementing them in the benchmarked nonlinear fiber analysis based macro model.

8.1.1 Summary of Experimental Database

The experimental database of tests conducted on noncompact and slender CFT members subjected to axial compression, flexure, and combined axial compression and flexure was compiled. This database contains a total of 187 tests, including 88 column tests (41 tests on rectangular CFT columns, and 47 tests on circular CFT columns), 46 beam tests (four tests on rectangular CFT beams, and 42 tests on circular CFT beams), and 53 beam-column tests (17 tests on rectangular CFT beam-columns, and 36 tests on circular CFT beam-columns). Details of these test specimens were included in the database (as shown in Tables 2.1-2.6) where reported. For rectangular CFT members, these details include the length (L), width (B), depth (H), flange thickness (t_f), web thickness (t_w), steel yield stress (F_y), concrete strength (f'_c), experimental axial load capacity (P_{exp}) and the experimental flexural capacity (M_{exp}). For circular CFT members, these details include length (L), diameter (D), tube thickness (t), steel yield stress (F_y), concrete strength (f'_c), experimental axial load capacity (P_{exp}) and the experimental flexural capacity (M_{exp}). Gaps in the database were identified. The database was used to: (i) evaluate the AISC 360-10 design provisions for designing CFT columns, beams, and beam-columns, and (ii) benchmark the FEM models.

8.1.2 Summary of FEM Models and Finite Element Analysis

Detailed 3D finite element method (FEM) models were developed and analyzed using ABAQUS (Version 6.12). Details of the FEM models were presented. These details include the element types, contact interactions, geometric imperfections, boundary

conditions, material model for the steel tube and concrete infill in compression and tension, and the analysis method.

The steel tubes of the CFT members were modeled using a fine mesh of 4-node S4R shell elements. The concrete infill of CFT members was modeled using eight-node solid elements with reduced integration (C3D8R). The contact interactions between the steel tube and concrete infill of CFT members were modeled in both the normal and tangential directions. Geometric imperfections were defined to initiate local buckling in the steel tube. The shape of the geometric imperfection was developed by conducting eigenvalue buckling analysis and the amplitude (magnitude) of the geometric imperfection was set equal to 0.1 times the tube thickness. The boundary conditions used for the FEM models were defined by kinematic coupling constrains, and they were designed to simulate those achieved in the experiments. The steel material multiaxial behavior was defined using the Von Mises yield surface, associated flow rule, and kinematic hardening. An idealized bilinear curve as shown in Figure 3.3 was used to specify the uniaxial stress-strain behavior of steel. The elastic modulus (E_s) was assumed to be 200 GPa, and the post-yield hardening modulus (E_t) was assumed to be E_s/100. The concrete material multiaxial behavior was modeled using the concrete damaged plasticity (CDP) material model developed by Lee and Fenves (1998). Two types of stress-strain curve (EPP and Popovics's curve) were used to specify the uniaxial compressive behavior of the concrete infill, as summarized in Table 3.2. The smeared cracking behavior in tension was specified using a stress-crack opening displacement curve that is based on fracture energy

principles and empirical models developed by CEB-FIB (2002), as shown in Figure 3.4(b). The explicit dynamic analysis method was selected as the analysis method.

The developed FEM models were benchmarked by using them to predict the behavior of 92 test specimens in the experimental database. These 92 tests include 33 column tests, 20 beam tests, and 39 beam-column tests. The resulting comparisons indicate that the FEM models predict the behavior and strengths of CFT members reasonably well.

The benchmarked FEM models were used to conduct: (i) additional analyses to evaluate the AISC 360-10 design provisions by addressing gaps in the experimental database, (ii) comprehensive parametric studies on noncompact and slender beam-columns to improve the current AISC 360-10 P-M interaction curve, and (iii) comprehensive parametric studies on noncompact and slender stub columns to develop effective stress-strain curves.

A total of 20 additional FEM analyses were conducted to evaluate the design provisions for noncompact and slender CFT columns. These 20 analyses include 13 analyses for rectangular columns and 7 analyses for circular columns. A total of 24 additional analyses were conducted to evaluate the design provisions for noncompact and slender CFT beams. These 24 analyses include 14 analyses for rectangular beams and 10 analyses for circular beams. These additional FEM analyses addressed gaps in the experimental database, and further confirmed the conservatism of the AISC design provisions in estimating the axial and flexural strength of CFT members.

A total of 207 beam-column analyses were conducted to improve the AISC P-M interaction curve for designing noncompact and slender CFT beam-columns. These 207 analyses include 95 analyses for rectangular beam-columns and 112 analyses for circular beam-columns. Parameters investigated in these analyses include the tube slenderness ratio, material strength ratio, axial load ratio, and member length-to-depth ratio. The results from these parametric studies indicate that the shape of the P-M interaction curve depends on the relative strength ratio (which includes the effect of both the tube slenderness ratio and material strength ratio), and that the shape is not influenced by the member length-to-depth ratio (up to 20.0). The results from the parametric studies were also used to develop the equations for factors β_1 and β_2, which were used to improve the current AISC 360-10 P-M bilinear interaction curve.

A total of 90 stub column analyses were conducted to develop the effective stress-strain curves for the steel tube and concrete infill for noncompact and slender CFT beam-columns. These 90 analyses include 45 analyses for rectangular columns and another 45 analyses for circular columns. Parameters investigated in these analyses include the tube slenderness ratio, steel yield strength and concrete compressive strength.

8.1.3 Summary of the Design of Noncompact and Slender CFT Members

The AISC 360-10 specifies the slenderness limits for classifying CFT members, and the provisions for calculating the strength of noncompact and slender CFT members. The slenderness limits were summarized in Table 1.1, and they are proposed by Varma and

Zhang (2009), based on the research of Schilling (1965), Winter (1968), Tsuda et al. (1996), Bradford et al. (1998, 2002), Leon (2007) and Ziemian (2010).

8.1.3.1 Noncompact and Slender CFT Columns

The design equations to calculate the axial strength of CFT members were given in Equations 4.2-4.13. CFT columns with slenderness ratios less than or equal to λ_p are classified as compact sections. CFT columns with compact sections can develop yielding before local buckling and provide adequate confinement of the concrete infill to develop its compressive strength up to $0.85f'_c$ for rectangular CFT columns and $0.95\ f'_c$ for circular CFT columns. CFT columns with steel tube slenderness ratio greater than λ_p but less than or equal to λ_r are classified as noncompact. Noncompact CFT sections can reach the yield stress (F_y) of the steel tube with local buckling, but cannot provide adequate confinement to the concrete infill to reach its full compressive strength. CFT columns with tube slenderness ratio greater than λ_r are classified as slender. Slender CFT sections undergo elastic local buckling, and the buckled tube wall cannot provide adequate confinement to the concrete infill to reach its full compressive strength. The concrete compressive strength of both noncompact and slender sections is limited to $0.70\ f'_c$.

The AISC 360-10 design equations (Equations 4.2-4.13) were used to calculate the strength of CFT columns, and these calculated axial strengths were compared to both the experimental test results and the additional FEM analysis results. These comparisons

indicate that the AISC 360-10 design equations are conservative in estimating the axial strength of noncompact and slender CFT members.

8.1.3.2 Noncompact and Slender CFT Beams

The design equations to calculate the flexural strength of CFT members were given in Equations 5.1-5.7, along with: (i) the stress blocks showed in Figures 5.1-5.3 (for rectangular CFT members) and Figure 5.4 and Figure 5.5 (for circular CFT members), and (ii) the fiber analysis procedure showed in Figure 5.7 (for circular CFT members).

For rectangular CFT members subjected to flexure, the tube slenderness ratios are defined by the *b/t* ratio of the flanges and the *h/t* ratio of the webs. Depending on the governing tube slenderness ratio, rectangular CFT members subjected to flexure may have: (i) compact, noncompact, or slender flanges, but (ii) only compact or noncompact webs. However, CFT members with slender flanges and noncompact webs are still classified as slender for flexure.

Circular CFT beams with tube slenderness ratio less than or equal to λ_p are classified as compact, while circular CFT beams with tube slenderness ratio greater than λ_p but less than or equal to λ_r are classified as noncompact. Circular CFT beams with tube slenderness greater than λ_r are classified as slender. However, no slender section is allowed for circular CFTs in flexure in the AISC 360-10.

The AISC 360-10 design equations (Equations 5.1-5.7) were used to calculate the strength of CFT beams, and these calculated flexural strengths were compared to both the experimental test results and the additional FEM analysis results. These comparisons indicate that the AISC 360-10 design equations are conservative in estimating the flexural strength of noncompact and slender CFT members.

8.1.3.3 Noncompact and Slender CFT Beam-Columns

The updated design equations to estimate the beam-column strength of noncompact and slender CFT members were given in Equation 6.13 and Equation 6.14, along with: (i) Equation 6.6 and Equation 6.12 to calculate β_1 and β_2 for rectangular CFT members, and (ii) Equation 6.9 and Equation 6.13 to calculate β_1 and β_2 for circular CFT members. Factors β_1 and β_2 are the ordinate and abscissa for the balance point (Point D) in the updated bilinear interaction curve.

These updated beam-column design equations (Equation 6.13 and Equation 6.14) improve the current AISC 360-10 beam-column design equations (Equation 6.1 and Equation 6.2), which are over-conservative as shown by the comparisons with experimental results from the database complied by the authors.

The updated beam-column design equations were developed using the results from parametric studies focusing on the effects of relative strength ratio (which includes the effect of both the tube slenderness ratio and material strength ratio) and member length-

to-depth ratio. Of these, the relative strength ratio determines the shape of the interaction curve, while the member length-to-depth ratio was found to have negligible effect on the shape of the interaction curve, up to *L/B* or *L/D* ratio of 20.

The updated P-M interaction curve preserves the bilinear form of the current AISC 360-10 interaction curve, while capturing the basic behavior of noncompact and slender CFT beam-columns. Comparisons with the both analysis and experimental results showed that the updated P-M interaction equations were able to predict the strength of noncompact and slender CFT beam-columns quite well.

8.1.4 Summary of the Effective Stress-Strain Curves

The complete effective stress-strain curves for the steel tube and concrete infill were summarized in Figure 7.54 and Figure 7.55 for rectangular CFT members and Figure 7.56 and Figure 7.57 for circular CFT members. The equations required to define the compressive behavior of these curves were given in Equations 7.1-7.4 and 7.6 for rectangular CFT members, and Equation 7.7 and Equation 7.8 for circular CFT members. The tensile behavior of the steel tube were assumed to be bilinear (as shown in Figure 3.3), and the tensile behavior of the concrete infill was assumed to be linear elastic until the tensile strength (determined according to the CEB-FIB model showed in Figure 3.4(b)) was reached; once the tensile strength of the concrete is reached, the concrete is assumed to loss its tensile strength completely.

The effective stress-strain curves to specify the compressive behavior of the steel tube and concrete infill were developed following the three basic principles presented in Section 7.1.1 (i.e., capturing the basic behavior, conservative and simple), and they were developed using results from comprehensive analytical studies (90 analyses) using the benchmarked FEM models. These effective stress-strain curves include the effects of geometric imperfections, steel tube local buckling, and steel hoop stresses and concrete confinement from the transverse interaction between the steel tube and concrete infill.

These effective stress-strain curves were validated by implementing them in a benchmarked fiber analysis based macro model to predict the P-M interaction curve of the 34 beam-columns analyzed before in Section 6.4 (i.e., the parametric studies using benchmarked FEM models). Comparisons with FEM results indicated that the effective stress-strain curves are conservative, and they capture the basic behavior of CFT beam-columns.

8.2 Conclusions

The following conclusions can be made based on this research:

(1) The experimental database compiled in this research provides fundamental information to benchmark the FEM models, and to evaluate the AISC 360-10 design equations.

(2) The benchmarked FEM models can be used to predict and evaluate the behavior of noncompact or slender rectangular and circular CFT columns, beams, and beam-columns.

(3) The AISC 360-10 equations are appropriate for classifying CFT members into compact, noncompact or slender sections for axial compression or flexure.

(4) The AISC 360-10 equations can be used to conservatively calculate the axial and flexural strengths of CFT members.

(5) The AISC 360-10 equations are over-conservative in estimating the beam-column strengths of noncompact and slender CFT members.

(6) The updated P-M interaction equations can be used to estimate the beam-column strengths of noncompact and slender CFT members.

(7) The developed effective stress-strain curves can be used to conservatively evaluating the behavior of noncompact and slender CFT members.

8.3 Further Work

Evaluation of the current AISC 360-10 P-M interaction equations for noncompact and slender rectangular and circular CFT members indicate that these equations are over-conservative. The over-conservatism of these design equations is due to the conservative evaluation of axial and flexural strength, and the use of bilinear P-M interaction curve for steel beam-columns. To improve these design equations, both the design equations for calculating the axial and flexural strength, and the bilinear P-M interaction curve need to be improved.

In this research, effective stress-strain curves for the steel tube and concrete infill were developed. Therefore, further work can be conducted to improve the equations for

calculating the axial and flexural strength of noncompact and slender CFT members, using the developed effective stress-strain curves.

In this research, the bilinear interaction curve was already improved. However, the current AISC 360-10 uses the direct analysis method as the primary mean to address the stability requirements for the design of steel structures. Therefore further work needs to be conducted to calibrate and verify the applicability of these equations in estimating the available strengths of noncompact and slender CFT members in the direct analysis.

REFERENCES

REFERENCES

ABAQUS. (2012). *ABAQUS Version 6.12 Analysis User's Manuals*. Dassault Systemes Simulia Corporation, Providence, RI, USA.

AIJ. (2008). *Recommendations for Design and Construction of Concrete Filled Steel Tubular Structures*. Architectural Institute of Japan, Tokyo, Japan.

AISC 360-05. (2005). *Specification for Structural Steel Buildings*. AISC, Chicago, IL, USA.

AISC 360-10. (2010). *Specification for Structural Steel Buildings*. AISC, Chicago, IL, USA.

AS. (2012). *Australian Standard for Steel Structures*. ABCB, Canberra, Australia.

Bergmann, R. (1994). "Load Introduction in Composite Columns Filled with High Strength Concrete." *Tubular Structures VI, Proceedings of the Sixth International Symposium on Tubular Structures*, P. Grundy, A. Holgate, and B. Wong, eds., Taylor & Francis, Melbourne, Australia, 373–380.

Bradford, M. A., Loh, H. Y., and Uy, B. (2002). "Slenderness Limits for Filled Circular Steel Tubes." *Journal of Constructional Steel Research*.

Bradford, M. A., Loh, H. Y., and Uy, B. (2002). “Slenderness Limits for Filled Circular Steel Tubes.” *Journal of Constructional Steel Research*.

Bradford, M. A., Wright, H. D., and Uy, B. (1998). “Local Buckling of the Steel Skin in Lightweight Composites Induced by Creep and Shrinkage.” *Advances in Structural Engineering*, 2(1), 25–34.

Bridge, R. Q. (1976). “Concrete Filled Steel Tubular Columns", Report no. 283, School of Civil Engineering. *University of Sydney*, University of Sydney.

Bridge, R. Q., and O’Shea, M. D. (1998). “Behaviour of Thin-Walled Steel Box Sections with or without Internal Restraint.” *Journal of Constructional Steel Research*, 47(1-2), 73–91.

Bridge, R. Q., and Webb, J. (1993). “Thin Walled Circular Concrete Filled Steel Tubular Columns.” *Composite Construction in Steel and Concrete II, Proceedings of the Engineering Foundation Conference*, W. S. Easterling and W. M. Roddis, eds., ASCE, Potosi, Missouri, 634–649.

Bruneau, M., Uang, C.-M., and Sabelli, R. (2011). *Ductile Design of Steel Structures*. McGraw-Hill Professional, New York, 928.

Cai, S. (1991). “Influence of Moment Distribution Diagram on Load-Carrying Capacity of Concrete-Filled Steel Tubular Columns.” *Proceedings of the Third International Conference on Steel-Concrete Composite Structures*, M. Wakabayashi, ed., Association for International Cooperation and Research in Steel-Concrete Composite Structures, Fukuoka, Japan, 113–118.

Chen, W. F., and Han, D. (2007). *Plasticity for Structural Engineers*. (Reprint, ed.), J. Ross Publishing, Plantation, FL, USA.

Choi, Y. H. (2004). “A Modified AISC P-M Interaction Curve for Square Concrete Filled Tube Beam-Columns.” University of Illinois at Urbana-Champaign.

Comité Euro International du Béton (CEB)-Fédération Internation alede la Précontrainte (FIP). (2010). *Model Code for concrete structures. (CEB-FIP MC 2010)*. Thomas Telford, London, U.K.

Denavit, M. D. (2012). “Characterization of Behavior of Steel-Concrete Composite Members and Frames with Applications for Design [Dissertation].” University of Illinois at Urbana-Champaign.

Elchalakani, M., and Zhao, X. (2008). “Concrete-Filled Cold-Formed Circular Steel Tubes Subjected to Variable Amplitude Cyclic Pure Bending.” *Engineering Structures*, 30, 287–299.

Elchalakani, M., Zhao, X. L., and Grzebieta, R. H. (2001). "Concrete-Filled Circular Steel Tubes Subjected to Pure Bending." *Journal of Constructional Steel Research*, 57, 1141–1168.

Elchalakani, M., Zhao, X.-L., and Grzebieta, R. (2004). "Concrete-Filled Steel Circular Tubes Subjected to Constant Amplitude Cyclic Pure Bending." *Engineering Structures*, 26, 2125–2135.

Eurocode. (2004). *Eurocode 4 : Design of Composite Steel and Concrete Structures Part 1-1 : General Rules And Rules For Buildings*. CEN, Brussels, Belgium, 1–117.

Fujimoto, T., Nishiyama, I., Mukai, A., and Baba, T. (1995). "Test Results of Eccentrically Loaded Short Columns - Square CFT Columns." *Proceedings of the Second Joint Technical Coordinating Committee Meeting, U.S.-Japan Cooperative Research Program, Phase 5: Composite and Hybrid Structures*, National Science Foundation, Honolulu.

Furlong, R. W. (1967). "Strength of Steel-Encased Concrete Beam Columns." *Journal of the Structural Division, ASCE*, 93(ST5), 113–124.

Goto, B. Y., Wang, Q., and Obata, M. (1998). "FEM Analysis for Hysteretic Behavior of Thin-Walled Columns." *Journal of Structural Engineering*, 124(11), 1290–1301.

Goto, Y., Kumar, G. P., and Kawanishi, N. (2010). "Nonlinear Finite-Element Analysis for Hysteretic Behavior of Thin-Walled Circular Steel Columns with In-Filled Concrete." *Journal of Structural Engineering*, 136(11), 1413–1422.

Goto, Y., Kumar, G. P., and Seki, K. (2011). “Finite Element Analysis for Hysteretic Behavior of Thin-Walled CFT Columns with Large Cross Sections.” *Procedia Engineering*, 14, 2021–2030.

Gourley, B. C., Cenk, T., Denavit, M. D., Schiller, P. H., and Hajjar, J. F. (2008). “A Synopsis Of Studies of the Monotonic and Cyclic Behavior of Concrete-Filled Steel Tube Members, Connections, And Frames." Report No. NSEL-008, Department of Civil and Enviromental Enginnering. University of Illinois at Urbana-Champaign, Champaign, IL, USA.

Guo, L., Zhang, S., Kim, W.-J., and Ranzi, G. (2007). “Behavior of Square Hollow Steel Tubes and Steel Tubes Filled With Concrete.” *Thin-Walled Structures*, 45(12), 961–973.

Haijar, J. F., and Gourley, B. C. (1997). “A Cyclic Nonlinear Model for Concrete-Filled Tubes. I: Formulation.” *Journal of Structural Engineering*, 123(6), 736–744.

Hajjar, J. F., and Gourley, B. C. (1996). “Representation of Concrete-Filled Steel Tube Cross-Section Strength.” *Journal of Structural Engineering*, 122(11), 1327–1336.

Hajjar, J. F., Gourley, B. C., Tort, C., Denavit, M. D., and Schiller, P. H. (2013). “Steel-Concrete Composite Structural Systems.” *Department of Civil and Environmental Engineering, Northeastern University*, Northeastern University.

Hajjar, J. F., Molodan, A., and Schiller, P. H. (1998). "A Distributed Plasticity Model for Cyclic Analysis of Concrete-Filled Steel Tube Beam-Columns and Composite Frames." *Engineering Structures*, 20(4-6), 398–412.

Hajjar, J. F., Schiller, P. H., and Molodan, A. (1998). "A Distributed Plasticity Model for Concrete-Filled Steel Tube Beam-Columns with Interlayer Slip." *Engineering Structures*, 20(8), 663–676.

Han, L.-H. (2004). "Flexural Behaviour of Concrete-Filled Steel Tubes." *Journal of Constructional Steel Research*, 60(2), 313–337.

Han, L.-H., Lu, H., Yao, G.-H., and Liao, F.-Y. (2006). "Further Study on the Flexural Behaviour Of Concrete-Filled Steel Tubes." *Journal of Constructional Steel Research*, 62(6), 554–565.

Han, L.-H., and Yan, S. . (2000). "Experimental Studies on The Strength with High Slenderness Ratio Concrete Filled Steel Tubular Columns." *Proceedings of the Sixth ASCCS International Conference on Steel-Concrete Composite Structures*, Y. Xiao and S. . Mahin, eds., Association for International Cooperation and Research in Steel-Concrete Composite Structures, Los Angeles, 419–426.

Han, L.-H., and Yang, Y. . (2007). *The State-of-the-Art-Technology of Concrete Filled Steel Tubes*. China Architecture & Press, Beijing, China.

Huang, J., Dai, S., and Liu, J. (2011). "Study on Earthquake Resistance Test of L-Shaped Concrete-Filled Rectangular Composite Steel Tubular Columns." *2011 International Conference on Electrical and Control Engineering (ICECE)*, Institute of Electrical and Electronics Engineers (IEEE), Beijing, China, 2589–2593.

Huang, Z. (2005). "Seismic Behavior of Moment Resisting Frames with High-Strength Square CFT Columns [Dissertation]." Michigan State University.

Ichinohe, Y., Matsutani, T., Nakajima, M., Ueda, H., and Takada, K. (1991). "Elasto-Plastic Behavior of Concrete Filled Steel Circular Columns." *Proceedings of 3rd International conference on steel-concrete composite structures*, M. Wakabayashi, ed., Association for International Cooperation and Research in Steel-Concrete Composite Structures, Fukuoka, Japan, 131–136.

Inai, E., and Sakino, K. (1996). "Simulation of Flexural Behavior of Square Concrete Filled Steel Tubular Columns." *Proceedings of the Third U.S.-Japan Joint Technical Coordinating Committee on Composite and Hybrid Structures*, Hong Kong.

Janss, J., and Anslijn, R. (1974). "Le Calcul des Charges Ultimes des Colonnes Métalliques Enrobés de Béton." *Rapport CRIF, MT*, 89, (Bélgica).

Jiang, A., Chen, J., and Jin, W. (2013). "Experimental Investigation and Design of Thin-Walled Concrete-Filled Steel Tubes Subject to Bending." *Thin-Walled Structures*, Elsevier, 63, 44–50.

Kang, C. H., Oh, Y. S., and Moon, T. S. (2001). "Strength of Axially Loaded Concrete-Filled Tubular Stub Column." *International Journal of Steel Structures*, 13(3), 279–287.

Kim, D. K. (2005). "A Database for Composite Columns [Thesis]." Georgia Institute of Technology.

Klöppel, K., and Goder, W. (1957). "Traglastversuche mit ausbetonierten Stahlrohen und Aufstellung einer Bemessungsformel." *Der Stahlbau, Berlin*, 26(1).

Knowles, R. B., and Park, R. (1969). "Strength of Concrete Filled Steel Tubular Columns." *Journal of the Structural Division, ASCE*, 95(ST12), 2565–2587.

Kupfer, H. B., and Gerstle, K. H. (1973). "Behavior of Concrete under Biaxial Stresses." *Journal of the Engineering Mechanics Division*, 99(4), 853–866.

Lai, Z. (2014). "Analytical Database on Noncompact and Slender CFT Members." Purdue University Research Repository. doi: 10.4231/R7QC01DR

Lai, Z., Varma, A. H., Connor, R. J., and Liu, J. (2013). "Retrofit Analysis of Steel Built-Up Members for Bottom Chords of Bayonne Bridge." Bowen Laboratory Research Report (BLRR), Purdue University, West Lafayette, IN, USA, 2, 1–60.

Lee, J., and Fenves, G. L. (1998). "Plastic-Damage Model for Cyclic Loading of Concrete Structures." *Journal of Engineering Mechanics*, 124(8), 892–900.

Lennie, A. G. R., Mervyn, J. K., Jim, N., and Tasnim, H. (2008). "Reversal Cyclic Testing of Full Scale Pipe Piles,Technical." Report No. IS-08-13, Constructed Facilities Laboratory, North Carolina State University, Raleigh, NC, USA.

Leon, R. T., Kim, D. K., and Hajjar, J. F. (2007). "Limit State Response of Composite Columns and Part 1 : Formulation Of Design Provisions for the 2005 AISC Specification." *Engineering Journal*, 05, 341–358.

Liang, Q. Q. (2008). "Nonlinear Analysis of Short Concrete-Filled Steel Tubular Beam–Columns under Axial Load and Biaxial Bending." *Journal of Constructional Steel Research*, 64(3), 295–304.

Lin, C. Y. (1988). "Axial Capacity of Concrete Infilled Cold-Formed Steel Columns." *Ninth International Specialty Conference on Cold-Formed Steel Structures*, W.-W. Yu and H. S. Joseph, eds., University of Missouri - Rolla, St. Louis, 443–457.

Lu, H., Han, L.-H., and Zhao, X.-L. (2009). "Analytical Behavior of Circular Concrete-Filled Thin-Walled Steel Tubes Subjected to Bending." *Thin-Walled Structures*, 47(3), 346–358.

Lu, Y. Q., and Kennedy, L. D. J. (1994). "The Flexural Behaviour of Concrete-Filled Hollow Structural Sections." *Canadian Journal of Civil Engineering*, 21(1), 111–130.

Lubliner, J., Oliver, J., Oller, S., and Onate, E. (1988). "A Plastic-Damage Model for Concrete." *International Journal of Solids and Structures*, 25(3), 299–326.

Moon, J., Roeder, C. W., Lehman, D. E., and Lee, H.-E. (2012). "Analytical Modeling of Bending of Circular Concrete-Filled Steel Tubes." *Engineering Structures*, Elsevier Ltd, 42, 349–361.

Morino, S., Sakino, K., Mukai, A., and Yoshioka, A. (1996). "U.S.-Japan Cooperative Earthquake Research Program on CFT Column Systems." *Proc. Of 5th International Colloquium on Stability of Metal Structures*, Chicago, IL, USA, 83–92.

Mursi, M., and Uy, B. (2004). "Strength of Slender Concrete Filled High Strength Steel Box Columns." *Journal of Constructional Steel Research*, 60(12), 1825–1848.

Nakahara, H., and Sakino, K. (2000). "Flexural Behavior of Concrete Filled Square Steel Tubular Beam-Columns." *Proceedings of the Twelfth World Conference on Earthquake Engineering*, New Zealand Society for Earthquake Engineering, Auckland, New Zealand, 441–448.

Nishiyama, I., Morino, S., Sakino, K., Nakahara, H., Fujimoto, T., Mukai, A., Inai, E., Kai, M., Tokinoya, H., Fukumoto, T., Mori, K., Yoshioka, K., Mori, O., Yonezawa, K., Uchikoshi, M., and Hayashi, Y. (2002). *Summary of Research on Concrete-Filled Structural Steel Tube Column System Carried Out under the U.S.-Japan Cooperative Research on Composite and Hybrid Structures*. Ibaraki Prefecture, Japan.

O'Shea, M. D., and Bridge, R. Q. (1996). "Circular Thin-Walled Tubes with High Strength Concrete." *Composite Construction in Steel and Concrete III, Proceedings of the Engineering Foundation Conference*, C. D. Buckner and B. M. Shahrooz, eds., American Society of Civil Engineers, Irsee, Germany, 780–793.

O'Shea, M. D., and Bridge, R. Q. (1997). "Tests on Circular Thin-Walled Steel Tubes Filled with Very High Strength Concrete." Research Report No. R755, School of Civil Engineering, University of Sydney, Sydney, Australia.

O'Shea, M. D., and Bridge, R. Q. (1997). "Behaviour of Thin-Walled Box Sections with Lateral Restraint." Research Report No. R739, School of Civil Engineering, University of Sydney, Sydney, Australia.

O'Shea, M. D., and Bridge, R. Q. (2000). "Design of Circular Thin-Walled Concrete Filled Steel Tubes." *Journal of Structural Engineering*, 126(November), 1295–1303.

O'Shea, M. D. O., and Bridge, R. Q. (1997). "Local Buckling of Thin-Walled Circular Steel Sections with or without Internal Restraint." *Journal of Constructional Steel Research*, 41(2), 137–157.

Popovics, S. (1973). "A Numerical Approach to the Complete Stress-Strain Curve of Concrete." *Cement and Concrete Research*, 3, 583–599.

Prabhu, M., Varma, A., and Buch, N. (2009). "Analytical Investigation of the Effects of Dowel Misalignment on Concrete Pavement Joint Opening Behaviour." *International Journal of Pavement*, 10(1), 49–62.

Prion, H. G. L., and Boehme, J. (1994). "Beam-column Behaviour of Steel Tubes Filled with High Strength Concrete." *Canadian Journal of Civil Engineering*, 21, 207–213.

Sakino, K., and Hayashi, H. (1991). "Behavior of Concrete Filled Steel Tubular Stub Columns under Concentric Loading." *Proceedings of the Third International Conference on Steel-Concrete Composite Structures*, M. Wakabayashi, ed., Association for International Cooperation and Research in Steel-Concrete Composite Structures, Fukuoka, Japan, 25–30.

Sakino, K., and Nakahara, H. (2000). "Practical Analysis for High-Strength CFT Columns under Eccentric Compression." *Proceedings of the Sixth ASCCS International Conference on Steel-Concrete Composite Structures*, Y. Xiao and S. . Mahin, eds., Los Angeles, California, 473–480.

Schilling, C. G. (1965). "Buckling Strength of Circular Tubes." *Journal of the Structural Division, ASCE*, 91(ST5), 325–348.

Schneider, S. P. (1998). "Axially Loaded Concrete-Filled Steel Tubes." *Journal of Structural Engineering*, 124(October), 1125–1138.

Sherman, D. R. (1976). *Tentative Criteria for Structural Applications of Steel Tubing and Pipe*. American Iron and Steel Institute, Washington, DC.

Sherman, D. R., and Tanavde, A. S. (1984). "Report on Comparative Study of Flexural Capacity of Pipes." Internal Report,Internal Report, Department of Civil Engineering, University of Wisconsin- Milwaukee, Milwaukee, WI, USA.

Song, J. Y., and Kwon, Y. . (1997). "Structural Behavior of Concrete-Filled Steel Box." *Composite Construction-Conventional and Innovative, International Conference*, International Association for Bridge and Structural Engineering, Innsbruck, Austria, 795–800.

Soundararajan, A., and Shanmugasundaram, K. (2008). "Flexural Behaviour of Concrete-Filled Steel Hollow Sections Beams." *Journal of Civil Engineering and Management*, 14(2), 107–114.

Tao, Z., Wang, Z.-B., and Yu, Q. (2013). "Finite Element Modelling of Concrete-Filled Steel Stub Columns under Axial Compression." *Journal of Constructional Steel Research*, Elsevier Ltd, 89, 121–131.

Tomii, M., and Sakino, K. (1979a). "Experimental Studies on the Ultimate Moment of Concrete Filled Square Steel Tubular Beam-Columns." *Transactions of the Architectural Institute of Japan*, 275, 55–63.

Tomii, M., and Sakino, K. (1979b). "Elasto-Plastic Behavior of Concrete Filled Square Steel Tubular Beam-Columns." *Transactions of the Architectural Institute of Japan*, 280, 110–120.

Tsuda, K., Matsui, C., and Mino, E. (1996). "Strength and Behavior of Slender Concrete Filled Steel Tubular Columns." *Proceeding 5th International Colloquium on Structural Stability*, Structural Stability Council, Chicago, IL, USA, 489–497.

Uy, B. (1998). “Local and Post-Local Buckling of Concrete Filled Steel Welded Box Columns.” *Journal of Constructional Steel Researchournal of Constructional Steel Research*, 47, 47–72.

Uy, B. (2000). “Strength of Concrete Filled Steel Box Columns Incorporating Local Buckling.” *Journal of Structural Engineering*, 126(March), 341–352.

Uy, B. (2001). “Strength of Short Concrete Filled High Strength Steel Box Columns.” *Journal of Constructional Steel Research*, 57(2), 113–134.

Varma, A. H. (2000). “Seismic Behavior, Analysis and Design of High Strength Square Concrete Filled Steel Tube (CFT) Columns [Dissertation].” Lehigh University.

Varma, A. H., Ricles, J. M., Sause, R., and Lu, L. (2004). “Seismic Behavior and Design of High-Strength Square Concrete-Filled Steel Tube Beam Columns.” *Journal of Structural Engineering*, 130(February), 169–179.

Varma, A. H., Ricles, J. M., Sause, R., and Lu, L.-W. (2002a). “Experimental Behavior of High Strength Square Concrete-Filled Steel Tube Beam-Columns.” *Journal of Structural Engineering*, 128(March), 309–318.

Varma, A. H., Ricles, J. M., Sause, R., and Lu, L.-W. (2002b). “Seismic Behavior and Modeling of High-Strength Composite Concrete-Filled Steel Tube (CFT) Beam–Columns.” *Journal of Constructional Steel Research*, 58, 725–758.

Varma, A. H., Sause, R., Ricles, J. M., and Li, Q. (2005). "Development and Validation of Fiber Model for High-Strength Square Concrete-Filled Steel Tube." *ACI Structural Journal*, 102(1), 73–84.

Varma, A. H., and Zhang, K. (2009). "Slenderness Limits for Noncompact / Slender Filled Members, Bowen Laboratory." Research Report School of Civil Engineering, Purdue University, West Lafayette, IN, USA

Wheeler, A., and Bridge, R. Q. (2004). "The Behavior of Circular Concrete-Filled Thin-Walled Steel Tubes in Flexure." *Proceedings of the fifth international conference on Composite Construction in Steel and Concrete*, R. T. Leon and J. Lange, eds., American Society of Civil Engineers, Kruger National Park, Berg-en-Dal, Mpumalanga, South Africa, 412–423.

Winter, G. (1968). *Commentary on the Specification for the Design of Cold-Formed Steel Members*. American Iron and Steel Institute, Washington, DC., USA.

Yonezawa, K., Hiroyoshi, T., Sekine, S., and Yoshioka, K. (1996). "Three Dimensional FEM Analysis of CFT Columns." *Proceedings of the Third U.S.-Japan Joint Technical Coordinating Committee on Composite and Hybrid Structures*, Hong Kong.

Yoshioka, K., Inai, E., Hukumoto, N., Kai, M., Murata, Y., Noguchi, T., Tanaka, Y., Tokinoya, H., and Mukai, A. (1995). "Compressive Tests on CFT Short Columns. Part 1: Circular CFT Columns." *Proceedings of the Second Joint Technical Coordinating Committee (JTCC) on Composite and Hybird Structures, Phase 5: Composite and Hybrid Structures*, National Science Foundation, Honolulu,Hawaii.

Zhang, W., and Shahrooz, B. M. (1997). "Analytical and Experimental Studies into Behavior of Concrete-Filled Tubular Columns, College of Engineering." *Report No. UC-CII 97/01*, University of Cincinnati.

Ziemian, R. D. (Ed.). (2010). *Guide to stability design criteria for metal structures*. John Wiley & Sons, Inc., Hoboken, NJ.

VITA

VITA

Zhichao Lai was born to Mr. Congming Lai and Mrs. Suxia Huang on November 5, 1986. He graduated with a B.S. degree in Civil Engineering from Tongji University in June 2009. He attended Purdue University, West Lafayette, in August 2009. He will receive his Ph.D. degree in Civil Engineering from Purdue University in December, 2014. His research interests include analysis and design of concrete-filled steel tube (CFT) members, retrofit analysis and design of built-up compression members, and analysis of steel-concrete composite structures.